Towards high-fidelity microwave driven multi-qubit gates on microfabricated surface ion traps

Tomas Navickas

Submitted for the degree of Doctor of Philosophy

University of Sussex, Brighton, United Kingdom. September 2017

Declaration

I hereby declare that this thesis has not been and will not be submitted in whole or in part to another University for the award of any other degree.

Signature:

Tomas Navickas

UNIVERSITY OF SUSSEX

Tomas Navickas, Doctor of Philosophy

Towards high-fidelity microwave driven multi-qubit gates on microfabricated surface ion traps

Abstract

For quantum computers to become a reality, high-fidelity logic gates are required to be implemented on a scalable architecture. The IQT group follows an approach based on using a magnetic field gradient and microwave radiation to implement the required operations. To demonstrate their scalability to many quantum bit systems, these operations need to be implemented on micro-fabricated surface ion traps. In this thesis I describe the technologies I developed for surface ion traps with magnetic field gradients. This entailed the design, assembly and operation of two surface ion trap systems with permanent magnets for generating large magnetic field gradients of 140 T/m, novel in-vacuum radio-frequency and microwave emitters for implementing high-speed quantum state manipulation and development of robust and reliable laser control systems required for stable long-term experimental operation.

General acknowledgements

I would like to thank my supervisor Prof. Winfried Hensinger for giving me the opportunity to work in the Ion Quantum Technology (IQT) group. The excitement and vigour he displays for everything to do with quantum computing will, in my opinion, remain unmatched for many year to come. Next, I would like to thank Dr. Seb Weidt for his unwavering support and encouragement inside and outside the lab. His patience and dedication to our work has always pushed me forward. Thanks go to Dr. David Murgia, Dr. Joe 'Chips' Randall, Anna Webb for keeping the banter going and reminding me that that it can be fun spending time outside the lab. Thanks go to Dr. Simon Webster for providing me with knowledge of everything from physics related to obscure music and cross country running. Thanks go to Adam Lawrence for reading all of the chapters of this thesis and providing a constant stream of IQT related memes. Thanks go to Ethan Potter, Anton Grounds, Weikang Fan, Nick Johnson, Zak Romaszko, Foni Le Brun-Ricalens, Altaf Nizamani and Harry Bostock making the general work in the lab fun. Thanks go to people who were there from the beginning, Dr. Darren De Motte, Dr. Marcus Hughes, Dr. Gouri Giri, Dr. Eamon Standing, Dr. James Siverns.

Most importantly I would like to thank my family. Without their constant support and comforting I would have never lasted all these years. Aciu Mama, Teti ir Indre.

Author contributions

During this thesis I have developed a laser locking system capable of stabilising all required lasers in the group for the use on Yb and Ba ions. As part of this work I have rebuilt and significantly improved the Rb spectroscopy setup used for stabilising laser frequencies, which included improving the electronic feedback circuits and optimising the optical layout of a saturated absorption spectroscopy setup. The system provides a stability of 100 kHz for averaging times of several hours. In order to expand the systems capabilities, I have designed and constructed additional stabilisation schemes. One of them is based on a laser frequency offset lock, for which I have designed and built the high bandwidth photodiode circuit and the required phase lock loop for generating the required control signal. This system provides a frequency stability of 100 Hz for averaging times of several hours and is capable of having offsets of several gigahertz. The second system is a tunable low-drift optical cavity capable of simultaneously stabilising four different laser frequencies. I have designed and built the cavity which consists of a block of ultra-low expansion

glass and piezoelectric transducers. To isolate the setup from convection, the cavity is housed in a vacuum system built by myself. This setup has shown to be more robust and stable than the saturated spectroscopy scheme. To make these systems more user friendly, I have developed a control unit based on FPGA technology, which simplifies control parameter tuning and allows for large bandwidth feedback. These systems are now used in all of the experimental setups in the lab and have been instrumental in implementing a novel high fidelity two qubit gate. One of the major current goals in the group is to implement high fidelity gates on a microchip. To this end I have also co-led and led the development and operation of two experimental systems aimed to implement a high-fidelity two qubit entangling gate on a micro-fabricated surface ion trap using a static magnetic field gradient and long wavelength radiation. The first system included a modular PCB-based ion trap mounting system, in-vacuum permanent magnets for large magnetic field gradient generation and a liquid nitrogen cooling system for reducing the trapped ion heating rate. My contribution included the assembly of the vacuum system, design and assembly of the various low noise electronic circuits for delivering the DC and radio-frequency signals to the trap electrodes, and optical setups for shaping and launching the required laser beams for ion trapping, cooling, state preparation and detection. I have successfully trapped ions on a microchip setup producing a static magnetic field gradient of 140 T/m. I have also identified the shortcomings of the experimental system. Following this, I have led on a second experimental setup, which removes these shortcomings. The work included the design and assembly of a new vacuum system, featuring an optimised and more robust ion trap, an in-vacuum microwave emitter setup and a 20 bar heat exchanger for cooling the trap structure to 70 K. My contribution included the design choices for the simplified electrode geometry, which is easier to produce and carries a smaller risk of fabrication error. To minimise the ion heating rate a new cooling system was designed to provide helium gas based cooling. To mount the heat exchanger into the vacuum system, I have designed a titanium based mounting structure which features a minimal thermal load and robustness against unwanted relevant mechanical vibrations. I have performed detailed simulations to carefully analyse and characterise the vibrational and thermal performance of the heat exchanger and mounting structure. As part of the goal of operating at cryogenic temperatures, the magnet mounting structure was designed by me to withstand cryogenic environments, providing good thermal conductivity and minimised strain on the ion trap due to different thermal expansion coefficients. In order to reduce gate infidelities, the individual coherent operations on the qubits must be carried

out as fast as possible. This can be achieved by increasing the microwave field intensity and can be implemented in two ways. The first one includes the use of an external emitter connected to carefully stabilised high power microwave amplifiers, while the second one includes developing an in-vacuum emitter setup as close as possible to the qubits. I have developed and constructed systems for both cases. I have designed, simulated and assembled an in-vacuum emitter, which is expected to increase Rabi frequencies by an order of magnitude compared to similar powers applied to the conventional external emitter setups. As a mitigating strategy and since in-vacuum emitters are not always feasible, I have also developed a feedback system capable of reducing the comparably large level of noise present in high power amplifiers by actively controlling the power level with a voltage variable attenuator. The combination of the above provides a promising platform for the successful implementation of high fidelity multi qubit gates on a scaleable architecture.

Detailed acknowledgements

The theoretical description of the entangling gate using magnetic field gradients was developed by Dr. Sebastian Weidt, Dr. Simon Webster and Dr. Joseph Randall.

The first system was designed by Dr. David Murgia and Dr. Bjoern Lekitsch. The ion traps used in the first experimental setup were designed and fabricated by Dr. Bjoern Lekitsch. The first set of magnets used for generating the gradient were designed and assembled by Dr. Eamon Standing.

The ion traps used on the second system were designed and made by Dr. Bjoern Lekitsch, Weikang Fan and Zak Romaszko.

The second heat exchanger was designed by me, based on the previous work of Foni Le Brun-Ricalens. The system was assembled with assistance from Adam Lawrence.

Publications

Efficient preparation and detection of microwave dressed-state qubits and qutrits with trapped ions

J. Randall, S. Weidt, E. D. Standing, K. Lake, S. C. Webster, D. F. Murgia, T. Navickas, K. Roth, and W. K. Hensinger

Phys. Rev. A, 91:012322, Jan 2015

Trapped-Ion Quantum Logic with Global Radiation Fields

S. Weidt, J. Randall, S. C. Webster, K. Lake, A. E. Webb, I. Cohen, T. Navickas, B. Lekitsch, A. Retzker and W. K. Hensinger

Phys. Rev. Lett., 117:220501, Nov 2016

Contents

List of Tables

List of Figures

Chapter 1

Introduction

Quantum information processing has gained significant interest and attention in many areas of research and industry, promising to solve problems intractable using classical computers. With emerging technologies, whose operation relies on the laws of quantum mechanics being already in use [1], a universal quantum processor is expected to be demonstrated in the next few decades. In the meantime, demonstration of quantum supremacy over classical machines [2, 3] is within reach and is expected to have a significant impact in the development of realistic quantum processors. Whichever the case it might be, the engineering of these devices still remains a challenge.

1.1 Quantum bit

The basic constituent of a computing machine is the bit, which has a physical meaning, such as holes in a tape machine or voltages in electrical circuits. The same principle can be applied to a two level quantum system, whose state is described using the laws of quantum mechanics, hence called the qubit. The state of a qubit is represented can be the wavefunction $|\psi\rangle$, given by

$$|\psi\rangle = a\,|0\rangle + b\,|1\rangle\,, \tag{1.1}$$

where a and b are complex coefficients. The state of the qubit can be changed by using different unitary operators U, which are the equivalent to the logic gates in classical computing. In this case, the universal set of gates is composed out of different operators acting on the wavefunction. One of the fundamental operations of this set, is the two qubit entagling controlled-not (CNOT) gate [4], whose operator is given by

$$U_{CNOT} = |00\rangle\langle 00| + |01\rangle\langle 01| + |10\rangle\langle 11| + |11\rangle\langle 10|\,. \tag{1.2}$$

The operation of this gate can be described by calling one qubit the 'control', while the other one is the 'target'. The control qubit determines if the target undergoes a transition or not. By applying the CNOT gate on an input of $(1/\sqrt{2})(|0\rangle + |1\rangle)$ this creates a highly correlated state $(1/\sqrt{2})(|00\rangle + |11\rangle)$ known as a Bell state, with no equivalent classical counterpart. The state indicates that a measurement of one qubit will determine the state of the other one with unit certainty. These states expand the computational basis of computing, compared to the non-entangled classical state. The access to these quantum states has been shown to have more favourable resource scaling for several complex algorithms [5, 6].

The demonstration of qubit entanglement forms one of the building blocks of a quantum processing architecture, with great effort dedicated to increasing the number of entangled qubits and the fidelity of the operation.

1.2 DiVincenzo criteria

In order to build a useful quantum processing platform, several requirements must be met by the selected qubit architecture, known as the DiVincenzo criteria [7]:

1. A scalable physical system with well characterised qubits.
2. The ability to initialise the state of the qubits to a simple fiducial state.
3. Long relevant decoherence times, compared to the qubit manipulation time.
4. A 'universal' set of quantum gates.
5. A qubit-specific measurement capability.

The first requirement corresponds to the ability of assembling a large scale system using many qubits, whose characteristics are easily replicated across a large architecture and is easy to address. The second point requires the state to be purified in order to be used for coherent operations, this means preparing all of the qubits in a known state before any operation. The third point captures the fact that these are highly sensitive systems, which are perturbed by the surrounding environment. This sets the practical limit of how long the qubit can be used for, before large errors become relevant. The fourth point was described in the previous section as the requirement for total qubit control. The last point touches on the fact that the state is required to be read out, in order to measure the outcome of the applied gates. All of these requirements seek to capture the description

of a quantum computing scheme, which is unavoidably affected by real world limitations, therefore operating with errors and finite resources.

There are many possible qubit systems, which can be used for quantum information processing. These include photons [8], superconducting circuits [9, 10], diamond NV centres [11] and quantum dots [12], trapped ions [13]. Currently, superconducting circuits and trapped ions are the most likely candidates, both having successfully shown high operation fidelities and the basic requirements for scalability.

1.3 Trapped ion quantum computer

Charged particles can be confined with the use of static and oscillating electromagnetic fields, which 'levitate' ions in a deep potential well. Placed in a vacuum system for isolation, the ion can remain trapped for several weeks.

Several early ion trap experiments were concerned with the analysis of the internal atom structure and its use as a frequency standard for defining the second [14]. A single trapped ion possesses a highly distinct energy level scheme, unperturbed by collisions and interaction with other particles. The qubit levels of the ion then, can be encoded in the energy levels of the outer shell electron, with radiation used to transfer the ion from one state to another. This and the development of laser cooling [15], has resulted in the ability to control the ion state to an arbitrary level [16]. The use of laser radiation to address the energy levels of the ion, fulfils the requirement of initialisation of the qubit into a fiducial state, whereas the detection of ion fluorescence provides a method of reading the qubit state. With these capabilities, the trapped ions provided a test-bed for investigating the most basic quantum systems [17, 18]. The first proposal of using trapped ions as a platform for quantum computing came from Cirac and Zoller [13], which required the ions to be cooled to their motional ground state in order to perform a two-qubit entangling CNOT gate. Although the complexity of the method prevented high fidelity performance [19], it did introduce the use of ion motional modes as the information 'bus'. The purpose of this bus is to provide a method of controlling the internal state of the target qubits but only when addressing the control qubit. This idea was later expanded on by Mølmer and Sørensen [20], where the requirement of having ground state cooled ions was alleviated. The first Mølmer-Sørensen gate was implemented in [21] and later improved in [22, 23, 24, 25] reporting fidelities as high as >99%. Further development of these initial results for ion qubit preparation, detection and entanglement has provided lowest reported infidelities, which are unrivalled by other quantum computing platforms.

The state of the art ion trap quantum processors have already demonstrated algorithms with the use of several ions to perform small-scale calculations [26].

The last DiVincenzo criteria that requires consideration is the demonstration of a scaleable architecture, which can contain millions of qubits for processing. So far, the largest number of ions that have been used to demonstrate the universal set of gates is 14 [27], implemented on a centimetre scale ion trap system with a pair of laser beams aligned onto a pair of ions. Owing to the physical size of the required optical devices, the addressability of the individual ions is limited due to photon scattering from the adjacent ions. A solution to this is the development of microfabricated ion traps, which allow for the control of the individual ion potential and the ability to move the ions deterministically through the laser beams without perturbing the nearest neighbours [28].

The main challenge of the aforementioned systems is the reliance on complex laser systems, which are vital for implementing high-fidelity two-qubit gates. These systems could be minimised using microfabricated laser and optical devices [29], but these technologies still require further development. As an alternative to this, the hyperfine levels of the trapped ion qubits can be addressed using microwave radiation, which is easy to generate using devices developed in the well established field of microwave and RF engineering. It was decided to pursue the latter method, due to the ease of using long-wavelength radiation sources and emitters and the ability to easily incorporate them on a microfabricated surface ion trap.

1.4 High fidelity two-qubit gates using long-wavelength radiation

All of the listed results on high-fidelity quantum operations using trapped ions rely on the use of laser beams to address the ions in a linear chain. However, to address a single ion, without perturbing its neighbours, requires tightly focused Raman laser beams to be positioned within $\approx$1 µm of the target ion. Any misalignment of these beams will produce interference of the neighbouring ions with the laser beam. In addition to this, the use of laser beams introduces additional errors due to non-negligible spontaneous emission of the excited state of the ion [22]. The technical requirements for minimising these errors have been addressed for a few ion systems [25], however a practical system is likely to consist of thousands of trapped ions [30, 31, 32]. A more scaleable approach to trapped ion quantum state manipulation is therefore required.

An alternative to using laser based manipulation is to use the hyperfine states of the trapped ion, which are typically separated by microwave frequencies. In this case, instead of using laser beams for addressing the qubits, the radiation is emitted through a microwave horn or antenna. Owing to the inherent stability of the microwave sources, the radiation system requires standard off-the-shelf devices, which are easy to integrate into an experiment. The only caveat is that the microwave radiation does not carry sufficient momentum to affect the motional state of the ion, which results in no appreciable effect on the motional information bus. A solution to this issue was pointed out by [33] and [34], which requires a static or an oscillating magnetic field gradient at the vicinity of the ion. This increases the coupling strength between the ion motion and the applied microwave radiation and is described in chapter 2. First implemented by [35] and [36], both methods have demonstrated two-qubit entanglement. The complication of the gradient schemes is the requirement of using the magnetic field sensitive states, which are susceptible to magnetic field fluctuations. This severely limits the coherence time of the qubit, therefore a more intricate method of coherent qubit manipulation is required.

To decouple the qubit from the noisy environment, a dressed scheme was implemented by [37], which requires the magnetic field sensitive states to be dressed with microwave radiation. This results in obtaining a new energy level diagram with three eigenstates, two of which can be used as the qubit states. The obtained qubit is robust against magnetic field fluctuations and can be manipulated using radio-frequency (RF) pulses. This was further improved by [38], which minimises the number of required frequencies for ion addressing during an entangling gate.

The continuous research into aforementioned methods of using the hyperfine qubit with magnetic field gradients and microwave radiation radiation instead of lasers have resulted in the demonstration of high-fidelity two-qubit gates [39, 40], which are comparable with the laser-based implementations.

1.5 Scaleable architecture using global radiation fields

The methods described in the previous section provide an elegant solution for implementing entanglement with the use of easy to generate global RF and microwave signals. However, in order to increase the number of ions used in computational tasks, the ion trap system must be able to provide a means of confining many ions on a small scale device. A proposal for such a system was presented by [28], where the architecture of the ion trap system requires many ions to be controlled individually. To do this, the size of the

electrodes must be reduced to several micrometres. Proof-of-principle experiments such as [41, 42], have demonstrated first use of micro-electromechanical system (MEMS) methods for fabricating an ion trapping structure, which was successfully used to demonstrate the capability of manufacturing ion traps with systems which are used for mass production of modern electronics. Recently, these systems have demonstrated high-fidelity operation [40, 43].

The success of using microfabricated ion traps has culminated in the foreseeable realisation of scalable quantum computing architectures. Several proposals for such systems have been made, one of which relies on constructing ion trap modules which are later interconnected with optical fibres [44] to distribute information between the individual units. The scheme heavily relies on entangling two distant ions by using entangled photons, a process which is inherently probabilistic and therefore has a limited entanglement rate. In addition to this, each module requires an individual laser system for cooling and manipulation of the trapped ions, making the footprint of each module large and costly to scale up. An alternative to this, is the proposal by [45], where the architecture is built up by ion trap modules, which are positioned next to each other and allow to be shuttled across. The design also incorporates the two-qubit gate scheme presented in [39], which makes the architecture highly attractive due to the simplified ion addressing using global radiation fields. This replaces many laser beams with a handful of microwave and RF fields.

The focus of this thesis is the development of the experimental setup capable of demonstrating a fault-tolerant two-qubit gate using the static magnetic field gradient scheme on a microfabricated surface trap. This work forms an important building block for the realisation of large scale devices of the sort prescribed in [45].

1.6 Thesis summary

The outline of this thesis is given below.

Chapter 2 contains the theoretical background and description of the requirements for trapping and manipulating Yb ions. It also presents the static magnetic field gradient scheme for improving internal-motional state coupling and the use of a microwave dressing scheme to obtain a highly robust qubit. The chapter concludes with a description of a two-qubit gate and the requirements for reducing gate infidelities due to various sources of noise.

Chapter 3 includes the fundamentals of active feedback systems and the implementa-

tion of a laser frequency stabilisation system capable of providing multiple laser systems with a low-maintenance control setup. This entails the description of the various optical references and their control systems. The performance of each optical reference is evaluated and an outline of the possible improvements is given.

Chapter 4 describes the assembly and operation of an experimental setup for demonstrating high-fidelity two-qubit gates using a microfabricated surface ion trap with permanent magnets. The description of the system includes the use of a modular in-vacuum PCB system for interfacing the ion trap with external voltage sources, optimisation of microwave and RF delivery systems and the use of a heat exchanger for reducing the ion trap temperature to 80 K.

Chapter 5 describes the assembly of a second experimental setup with improvements for implementing a fault-tolerant two qubit gate. This includes a high-pressure cooling system for reducing the trapped ion heating rate by an order of magnitude, and in-vacuum and external microwave and RF emitters for generating high intensity fields at the vicinity of the ion, used for improving the two-qubit gate parameters. The chapter concludes with the description of active feedback systems used to stabilise the power of different RF and microwave systems.

Chapter 2

Ion trapping and coherent manipulation for quantum computation

2.1 Introduction

Confinement of charged particles has led to development of precision chemical analysis [46, 47], time and frequency standards [48, 49, 50], and research into basic quantum systems [51, 52, 53]. In addition to this the ability to isolate, control and analyse single particles has resulted in this being one of the leading platforms for quantum technologies with near fault-tolerant performance [25, 23, 24, 45]. Despite the technological advancements over the last several decades, the basic principles of trapping have remained relatively unchanged from the first principles outlined in the Nobel prize winning work of Dehmelt and Paul [54, 55]. This chapter describes these principles and their application to microfabricated surface ion traps. In addition to this, the chapter contains the description of using trapped ion qubits and the principles behind coherent manipulation of their internal and motional states using a static magnetic field gradient. Particular attention is given to preparing a robust dressed state qubit and performing single- and multi-qubit operations with long-wavelength radiation. The chapter concludes with a description of an entangling two-qubit gate and the requirements for its fault-tolerant operation.

2.2 Ion traps

To confine a free particle, it has to be placed in a 3-dimensional potential well, where the barrier height must be larger than its kinetic energy. For charged particles such as ions, this potential well can be formed with electromagnetic fields, which interact with the particle through the Coloumb force. However, the confining field has to obey Earnshaws theorem, which states that a potential minimum cannot be formed with static electric fields alone. Two possible solution to this was given by [54] and [55], where a strong magnetic field or a radio-frequency (RF) field were used in conjunction with static electric fields to confine ions. The first type is called a Penning trap [54] and has been established as the most precise metrological tool for measuring the electron mass [56] and magnetic moment of the proton [57], and to test various aspects of the standard particle model [58] and as a platform for investigating quantum phenomena [59, 60]. On the other hand, the Paul trap [55] has been successfully used for several decades in the field of mass spectrometry [61]. The latter method is used in this thesis, therefore only the Paul-type ion trap will be described in detail.

2.2.1 RF trap

An example of a common RF trap is given in fig. 2.1a. The trap consists of four hyperbolic electrodes, with two opposite electrodes driven with an RF signal out-of phase with the other. The resultant voltage arrangement is illustrated by a cross-sectional view in 2.1b, where $2r_0$ is the surface-to-surface distance between the opposite electrodes. This produces a hyperbolic electric field seen in 2.1c, also known as a saddle potential, which has a minimum in one dimension, but is unstable in the orthogonal axis. The application of an oscillating voltage will interchange these axes after a half of the period of the applied RF angular frequency. For an RF drive signal of $V_{RF}(t) = V_0 \cos(\Omega_D t)$, where Ω_D is the angular frequency and V_0 is the amplitude, the potential is given by [62]:

$$\phi_{RF}(x, y, t) = \eta_{RF} V_{RF}(t) \left(\frac{x^2 - y^2}{2r_0^2} \right). \tag{2.1}$$

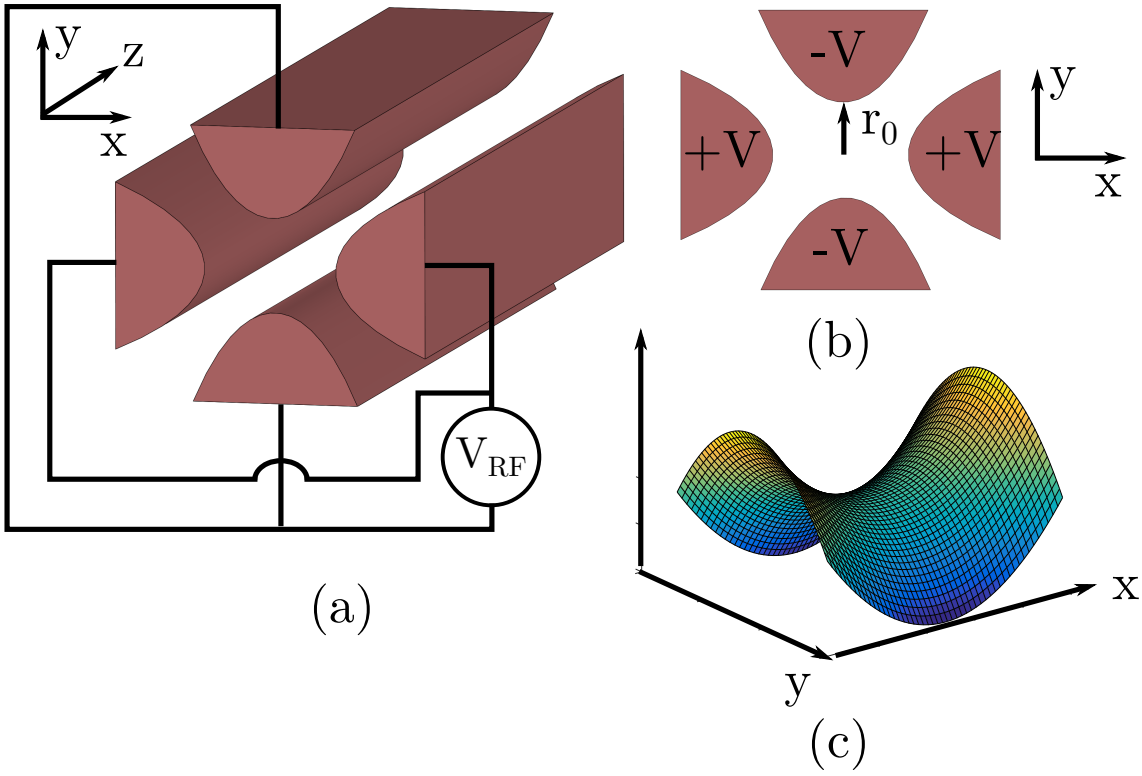

Figure 2.1: (a) The arrangement of four rods of length l and applying equal voltages for the opposite electrodes in (b), results in a saddle like potential (c).

The geometric factor η_{RF} describes the deviation of the RF electrodes from a perfect hyperboloid, for which $\eta_{RF} = 1$. Intuitively, if the ion motion is much slower at the centre of the trap compared to the applied radio-frequency signal, the potential can be time averaged over to obtain an effective well in both x and y axes. This is known as the potential well model detailed in [63], which for an ion of mass m can be written as

$$\psi(x,y) = \frac{e^2}{4m\Omega_D^2}|\nabla\phi_{RF}(x,y)|^2, \tag{2.2}$$

where the time dependence is removed by averaging and e is the electron charge. Plugging in equation 2.1 into 2.2, the effective potential can be written as

$$\psi(x,y) = \frac{e^2\eta_{RF}^2 V_0^2}{4m\Omega_D^2 {r_0}^2}\left(x^2+y^2\right), \tag{2.3}$$

which, as required, produces a global minimum in the $x-y$ plane. The motional frequency of the ion within the potential well is given by [63]:

$$\omega_{x,y} = \frac{eV_0\eta}{\sqrt{2}m\Omega_D r_0^2}. \tag{2.4}$$

The motion at the frequency calculated by 2.4 is called the secular motion of the ion, which for both x and y-axes is equal.

Due to symmetry, the resultant potential is uniform along the z direction, which means that an ion will move at a constant velocity along this axis. This is a particular interest for mass spectrometry, where the ions are collected at one end for analysis. For the purpose of obtaining a trapping field in all axes, another pair of hyperboloid electrodes (endcaps) are placed at $z = 0$ and $z = z_0$ to provide confinement along the axial direction with the use of DC voltages. The electric potential is determined by the distance between the two electrodes z_0 and the applied voltage V_{DC} and is given by [64]:

$$\phi_{DC}(x, y, z) = \eta_{DC} V_{DC} \left(\frac{2z^2 - (x^2 + y^2)}{2z_0^2} \right). \tag{2.5}$$

The secular frequency of the z-axis motion is then:

$$\omega_z = \frac{\sqrt{2} e \eta_{DC} V_{DC}}{m {z_0}^2}. \tag{2.6}$$

One of the interests of using the potential well model, is to estimate the trap depth. The trap depth is defined as the energy needed for the ion to escape the trap. Ions with a kinetic energy larger than the trap depth will propagate through, which would require a method of slowing them down first. To avoid this as much as possible, a large trap depth is desirable. Ions trapped in a deep well are also less susceptible to perturbations due to background particle collisions and stray electric fields. The trap depth can be calculated by finding the difference in the potential energy from eq. 2.3 for the ion to move from the trap 'nil' at $x^2 + y^2 = 0$ to the edge of the trap, set by the electrode distance r_0 such that $x^2 + y^2 = r_0^2$. This can be easily calculated to be [63]

$$U = \frac{e^2 \eta_{RF}^2 V_0^2}{4 m \Omega_D^2}. \tag{2.7}$$

A typical linear trap will be operated at a depth of $\approx$1 eV, which guarantees the trapping of ions with a temperature of $\leq$7000 K. The ions produced by a metallic vapour source have temperatures of 673 K to 1173 K, which are significantly smaller.

Although the potential well treatment does not describe the complete dynamics of the trapped ion, it serves as a useful model when designing traps and estimating the motional frequencies. In fact, all of the simulations and analysis performed on the traps used in this thesis were carried out using this model.

Trapped ion trajectories

The motion of a trapped ion described in the previous section assumed a time-averaged potential due to the ion undergoing only small excursion from the trap centre. A more detailed treatment of the motion of the ion requires solving the Mathieu equation [63]. The complete potential of an ion trap can be written by summing the individual components of the RF and DC potentials eq. 2.1 and eq. 2.5 to obtain

$$\begin{aligned}\phi(x,y,z,t) =& \phi_{RF}(x,y,t) + \phi_{DC}(x,y,z) = \\ & \eta_{RF} V_0 \cos(\Omega_D t)\left(\frac{x^2-y^2}{2r_0^2}\right) + \eta_{DC} V_{DC}\left(\frac{2z^2-(x^2+y^2)}{2z_0^2}\right).\end{aligned} \tag{2.8}$$

The force exerted on the ion $\vec{F} = -e\nabla\phi$ can be equated to its acceleration multiplied by the mass of the ion. Considering the motion along the x-axis, the ion follows a trajectory set by

$$\begin{aligned}\frac{\mathrm{d}^2x}{\mathrm{d}t^2} &= -\frac{e}{m}\left(\frac{\partial\phi(x,y,z,t)}{\partial x}\right) \\ \frac{\mathrm{d}^2x}{\mathrm{d}t^2} &= -\frac{e}{m}\left(\frac{\eta_{RF}V_0\cos(\Omega_D t)}{r_0^2} - \frac{\eta_{DC}V_{DC}}{z_0^2}\right)x.\end{aligned} \tag{2.9}$$

To simplify the analysis, the following substitutions are used

$$a_x = \frac{4e\eta_{DC}V_{DC}}{mz_0^2{\Omega_D}^2}; \qquad q_x = \frac{2e\eta_{RF}V_0}{mz_0^2{\Omega_D}^2}; \qquad \Omega_D t = 2\zeta \tag{2.10}$$

in eq. 2.9 and rearranged to obtain

$$\frac{\mathrm{d}^2x}{\mathrm{d}\zeta^2} + (a_x - 2q_x\cos(2\zeta))x = 0. \tag{2.11}$$

Equation 2.11 has the form of a canonical Mathieu equation [65], solved with the use of Floquet theorem [66]. The a and q parameters determine if the solution to the Mathieu equation results in stable or unstable trajectories. The same type of equation is obtained for the y-axis, but with a minus sign instead on the second term. The stability of the trap can be visualised with a stability diagram given in fig. 2.2, where the choice of parameters results in confined motion for both axes.

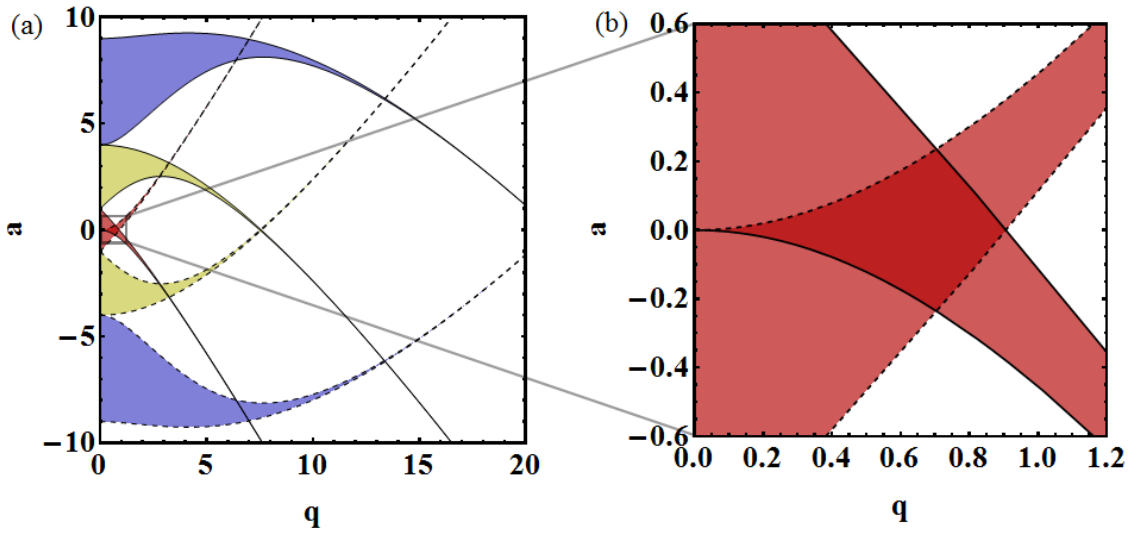

Figure 2.2: Stability diagram for a linear quadrupole ion trap. (a) The shaded areas correspond to a set of values for a and q where the motion is stable along a particular axis. (b) In order to have stable motion in both axes, the stability region is limited to the deep red area. Adapted from [64].

The deep red in fig. 2.2b indicates a set of parameters for the ion to undergo stable motion and not escape the trap. Setting $a = 0$, the solution to eq. 2.11 is given by [67]

$$x(t) = x_0 \cos(At)[1 + B\cos(\Omega_D t)], \tag{2.12}$$

where the coefficients A and B determining the amplitude and frequency of the motion, equate to

$$A = \frac{q_x}{\sqrt{2}}; \qquad B = \frac{q_x}{2}. \tag{2.13}$$

The particle undergoes a trajectory composed out of two frequencies, the larger secular $\frac{q_2}{\sqrt{2}} = \omega_x$ and the smaller amplitude oscillation at the drive frequency Ω_D, called micromotion, see fig. 2.3. The same is true for the orthogonal y axis, therefore obtaining a closed trajectory in the $x - y$ plane.

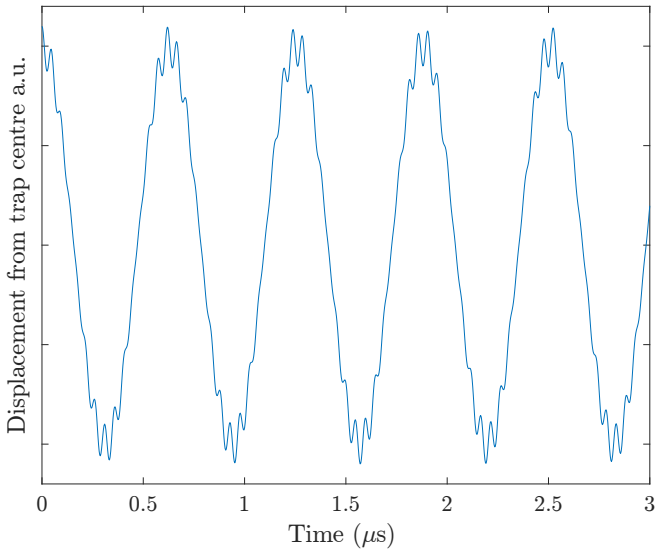

Figure 2.3: Plot of a trapped ion trajectory along the x-axis. The drive frequency was set to $\Omega_D/2\pi = 21\,\mathrm{MHz}$ with an amplitude of $V_0 = 300\,\mathrm{V}$ for an ion electrode distance of $r_0 = 0.3\,\mu\mathrm{m}$. The secular frequency can be clearly seen as the larger amplitude oscillation, whereas the micromotion is mostly pronounced at the point furthest from the trap centre.

The presence of micromotion disturbs the ion from perfect harmonic motion and therefore needs to be minimised as much as possible. This is achieved by setting a small q parameter of the applied radio-frequency voltage, however the presence of stray electric fields or misalignment from the field nil can also induce excess micromotion. The effect of the micromotion can be understood as a perturbation to the ion motion, which increases the amplitude and hence the kinetic energy of the ion, causing the ion to escape the trap. Furthermore, the uncompensated micromotion leads to poor laser cooling [68] and noise in the qubit energy level scheme composed out of magnetic field sensitive states, described in section 2.9.4. Micromotion is corrected for by optimising static the potential and minimising the field seen by the ion with the use additional DC voltages on the electrodes. To minimise stray electric fields, the ion must be isolated from any potential sources of noise with electric shielding. This requires placement of meshes and shields around the experimental setup.

2.2.2 Trapped ion normal modes of motion

As mentioned in the introduction, the ion motion is used as the information bus for trapped ion quantum information processing. To describe the motion and interaction of multiple ions in a single potential well, the Coloumb forces between them need to be considered.

A single trapped ion oscillates around the potential minimum with secular frequencies

$\omega_{x,y,z}$, which can be easily calculated using equations 2.4 and 2.6. When trapping more than one ion, the trapped particles will be trapped along the weaker z-axis, resulting in a linear chain of ions. The shape of the potential well along this axis is modified by the Coulomb interaction between the ions, which is proportional to $|z_n - z_m|^{-1}$, where z_n and z_m are the positions of the two ions. The equation for the potential energy of a two ion chain can be written as [69]:

$$V = \frac{1}{2}m\omega_z^2(z_m(t)^2 + z_n(t)^2) + \frac{e^2}{8\pi\epsilon_0}\frac{1}{|z_n - z_m|}. \tag{2.14}$$

The potential well representing this case is illustrated in fig. 2.4.

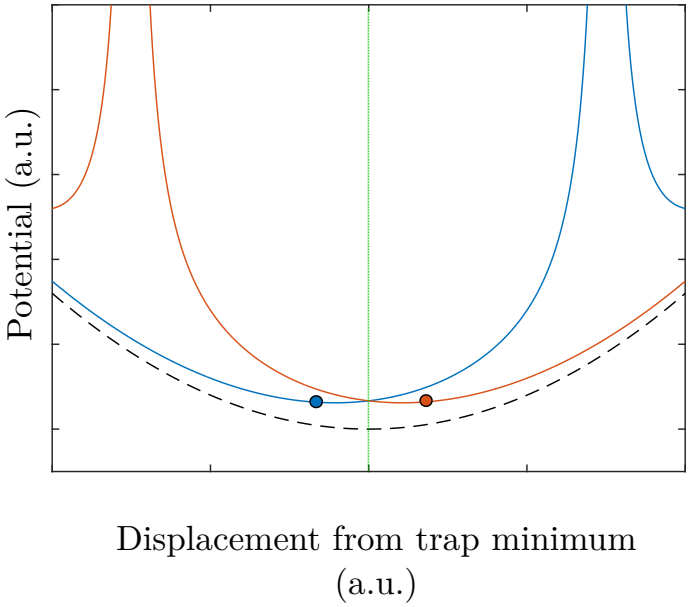

Figure 2.4: The potential well for a two ion chain. The axial potential well (black dashed line) is set by the endcap voltages has a quadratic dependence on the displacement from the trap centre (green line). The blue and red lines correspond to the potential energy barriers seen by each ion according to its colour.

Since the ions are in constant motion in the trap, this potential minimum oscillates with the motion of the ions. However, this motion can be decomposed into eigenvalue modes, with each having a distinct oscillation frequency and fixed minimum positions. These modes are called the normal modes of the chain, which correspond to all of the ions undergoing common motion of equal frequency. Although, the example is given for the axial modes of motion, the same is true for the radial components, but with larger frequencies, due to the stronger radial confinement.

The minimum ion spacing is calculated using equation [70]

$$z_s = \left(\frac{e^2}{4\pi\epsilon_0 M{\omega_z}^2}\right)\frac{2.018}{N^{0.559}}, \tag{2.15}$$

where N is the number of ions in the chain. The eigenvalue frequencies for a two ion chain are

$$\nu_1 = \omega_z; \qquad \nu_2 = \sqrt{3}\omega_z. \tag{2.16}$$

The modes are named after the type of motion the ions undergo within the potential well. The lowest frequency mode is referred to as the centre-of-mass mode (COM), where the ions oscillate in phase within the potential with the angular frequency ω_z. Whereas the out of phase higher frequency mode in is called the stretch mode, which oscillates at the frequency $\sqrt{3}\omega_z$. The stretch mode frequency is larger due to the ion-ion distance averaged over the period of the oscillation being shorter, therefore having a larger contribution to the Coulomb term in equation 2.14. Both modes are illustrated in fig. 2.5. The ion spacing in a linear chain is typically several microns, set by equation 2.15.

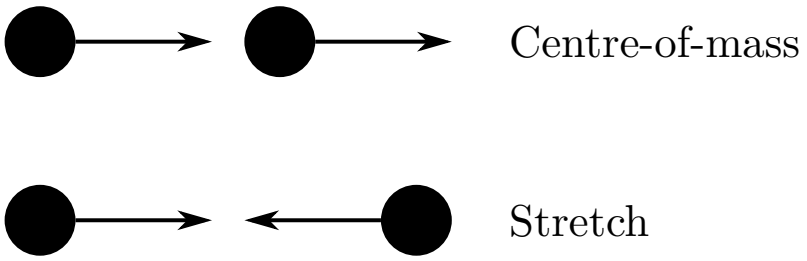

Figure 2.5: Illustration of the axial modes of motion, with the arrows showing the direction of motion for each ion.

To quantize the normal motional modes, the position and momentum of the two ion chain can be replaced with the quantum harmonic oscillator operators, which gives the motional contribution to the total Hamiltonian

$$\hat{H}_m = \hbar\nu_k {\hat{a}_i}^\dagger \hat{a}_i, \tag{2.17}$$

where the zero point energy is ignored and ν_k is the normal mode of the ion chain and ${\hat{a}_i}^\dagger$ and $\hat{a}_i$ are the creation and annihilation operators.

2.3 Micro-fabricated ion traps

The DiVincenzo criteria described in chapter 1 introduced the requirement of a scalable architecture for implementing efficient quantum information processing. For ion trap de-

vices, this translates to the manufacture of small ion trap structures which can be periodically placed on reasonable size modules [28, 45]. Trapping zones in these architectures are dedicated for specific purposes, such as ion trapping, cooling, coherent manipulation and state readout, with ions moved from one zone to another by changing the axial confinement minimum, referred to as 'shuttling' [71, 72]. An additional purpose of shuttling is to create the two ion chains by moving two ions into a single potential well, where they can be entangled and later separated for further operation. An equivalent scaleable approach is entanglement of the ion state over large distances with photons [44]. Although, the architecture is simplified to building individual modules and connecting them with optical fibres, the system suffers from slow entanglement rates (several hertz) and significant infidelities due to unavoidable photon scatter. A scalable design for an ion trap quantum computing architecture was proposed in [45], which relies on entanglement using global long-wavelength radiation [39], which promise fault-tolerant entangling gates. In order to implement the architecture, the ion trap zones are produced using methods in microelectromechanical system (MEMS) production, which allow to reduce the trap electrodes to several micrometers. To understand the effect of scaling down the trap features, it is important to investigate the generated electric potential.

2.3.1 Trap geometry

Microfabricated ion traps can be divided into two groups, determined whether the RF electrode placement is symmetric or not around the trap centre [73]. The asymmetric designs are commonly referred to as 'surface traps', with a few examples of both types given in fig. 2.6.

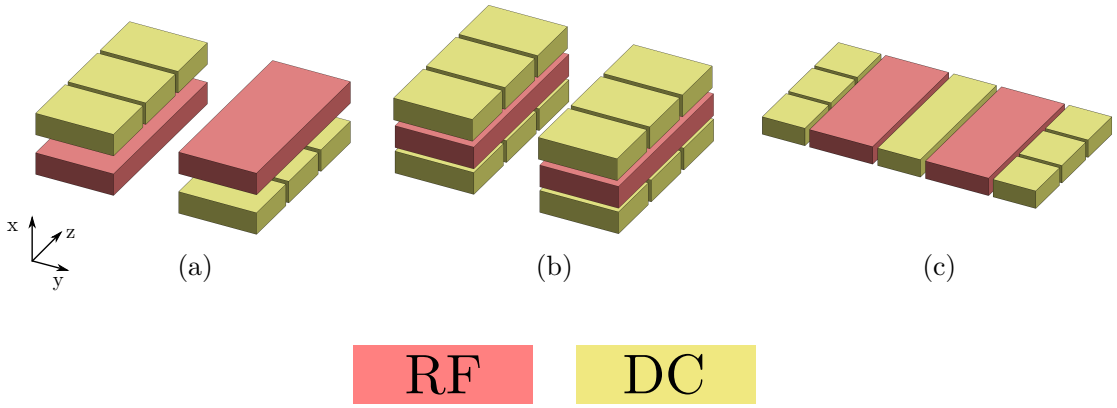

Figure 2.6: Types of traps fabricated using MEMS methods. Trap geometries in (a) and (b) are similar to the linear trap shown in fig. 2.1a, where the RF electrodes are placed symmetrically around the trap centre. The fabrication of multiple layer traps is more complex, due to the requirement of keeping the different layers of RF and DC electrodes separated. Constraining the electrode geometry to a single layer as illustrated in (c) simplifies the process. These traps are often referred to as asymmetric surface traps. Adapted from [73].

The symmetric designs are the closest example to the linear trap pictured in fig. 2.1a, therefore the shape of the potential well is comparable to the given example in section 2.2.1, with slight deviations determined by the geometric factor η_{RF}. Due to the electrode placement, the generated potential is symmetric, which confines the ion equally along the principal axes. In this case the trap depth is equal as well, which cannot be said about the surface trap seen in fig. 2.6c. The placement of the electrodes in a single plane, introduces a weakness in one of the radial axes, normal to the surface, which makes the ion more likely to escape. However, the benefits gained from a single layer design greatly outweighs the reduced trap depth. These include the simple single-layer trapping geometry, unobstructed access to the ion for manipulation and the ability to easily incorporate optical and electronic systems.

Surface ion traps

The layout of the electrodes of the surface ion trap can be visualised as a projection of the linear ion trap onto a plane. A typical surface trap will have a five wire design, for which an analytic model of the potential was developed in the work of [74]. The electrode layout of the trap and a cross section of the potential can be seen in fig. 2.7.

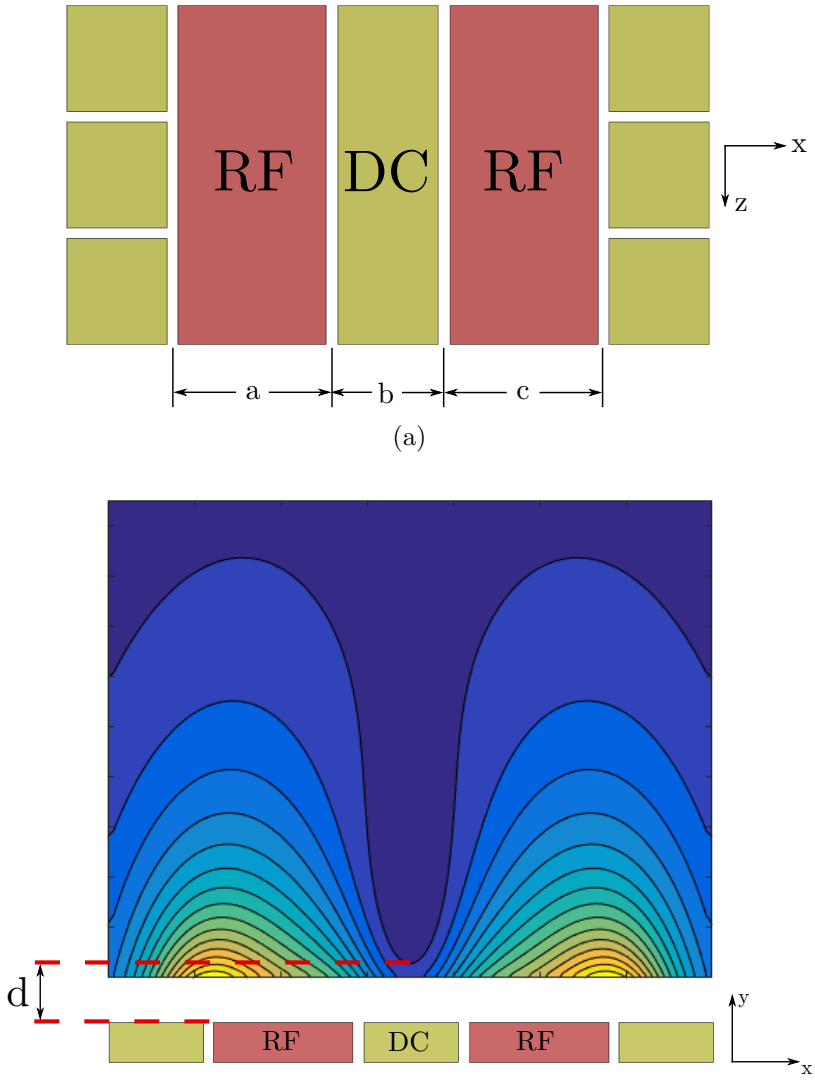

Figure 2.7: (a) The five wire design of a surface ion trap, with the parameters a, b and c determining the shape of the potential well in (b). The size of the gaps is assumed to be negligible compared to the size of the electrodes.

The contour plot of the potential indicates a minimum at a certain distance above the surface, which is commonly referred to as the ion height d. The ion height is independent of the applied voltage can be calculated by [74]:

$$d = \frac{\sqrt{abc}(a+b+c)}{a+c}. \tag{2.18}$$

The position of the minimum can be controlled by changing the width (a, c) and separation (b) of the RF electrodes. Reducing the RF separation, lowers the ion height, which according to equation 2.7, results in larger trap depths and secular frequencies. Despite these benefits, there are numerous disadvantages of trapping ions close to the surface of

the electrodes. One of the most significant is the anomalous heating rate, documented in the work of [75]. This heating rate refers to the gain in the trapped ion kinetic energy over time, which eventually allows the ion to escape the trap. Although there is no strong theory of how it occurs, studies of trap surfaces indicate that the presence of carbon contaminants modifies the trap potential [76]. Additionally, there is evidence supporting that the anomalous heating rate is not linearly proportional with the number of contaminants [77]. Whatever the case might be, there has been a lot of effort put into minimising these effects with the use of laser cleaning [78], ion sputtering [76] and cryogenic cooling [79], with different levels of success. Despite not having a definite answer for the origins of the heating rate, it's dependence on the ion height is documented in the work of [80, 81] as being proportional to $\approx d^{-4}$. Balancing the requirements of trap depth and secular frequencies with the anomalous heating rate, the typical ion heights for surface ion traps are in the range of 50 µm to 150 µm.

RF electrodes confine the ion motion along the x and y-axes, while DC electrodes are used the for the z axis confinement. However, a more general description of the principal axes can be used instead to describe the direction of the trapped ion motion. The principal axes of a trapped ion refer to the independent axes of the motion, and they are determined by the RF electrode position. The ability to control this parameter is important for laser Doppler cooling, which is described in the later section of this chapter. To rotate the principal axes, the trap illustrated in fig. 2.7a is modified to include additional DC electrodes, called the rotation electrodes. An example of such a trap can be seen in fig. 2.9.

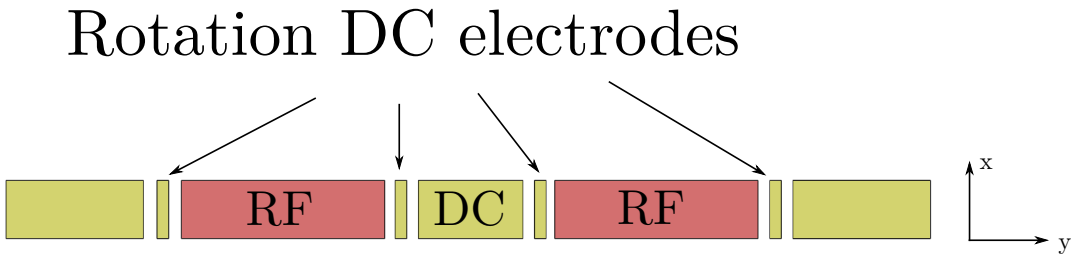

Figure 2.8: The four rotation DC electrodes are placed around the RF electrodes to be able to rotate the principal axes of the trapped ion.

The operation of the rotation electrodes can be imagined as adding another quadrupole potential generated with static voltages. By choosing alternating voltages going from left to right, a weak quadrupole potential is generated, which modifies the principal axes set

by the RF electrodes. The largest possible angle of rotation is set by the width of the rotation electrodes. A ratio of 1:10 between the widths of the rotation and RF electrodes can produce rotation angles of ≈10° [82].

These surface ion traps are not significantly different from macroscopic traps. However, the small scales and the low ion-electrode distances introduce additional complications arising due to the asymmetrical design and the effect of the surface on the trapped ion. Furthermore, the methods used in fabricating these devices are complex and often the results are unpredictable. Multiple different traps were used in this thesis, with their fabrication method described in their respective chapters.

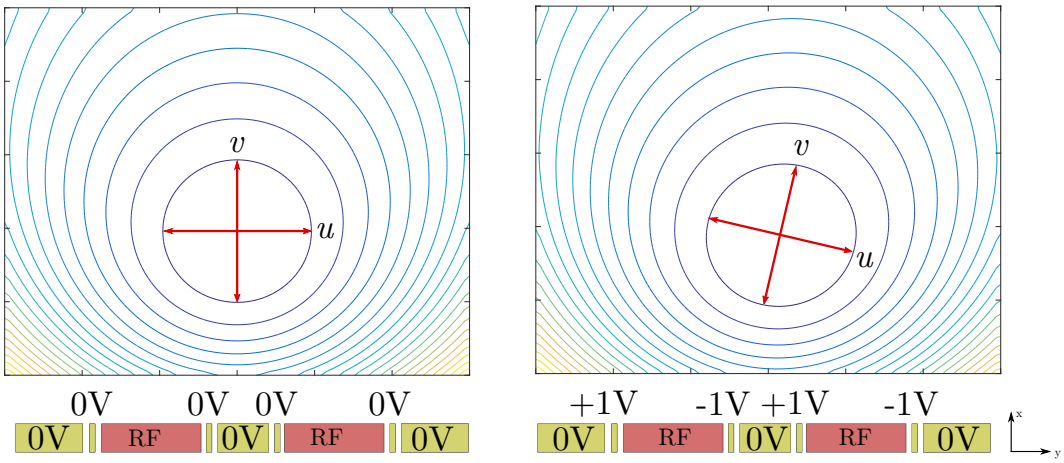

Figure 2.9: The principal axes u and v with and without the added rotation by applying the voltages indicated on the rotation DC electrodes.

2.4 Vacuum system

In order to isolate ions from background gases, stray electromagnetic fields and other perturbations, the ion trap is placed inside a vacuum system. The vacuum system is evacuated to reach ultra-high vacuum (UHV) conditions, with absolute pressures of 1×10^{-11} mbar. The two systems that were used in the experiments described in this thesis were based on the design pictured in fig. 2.10.

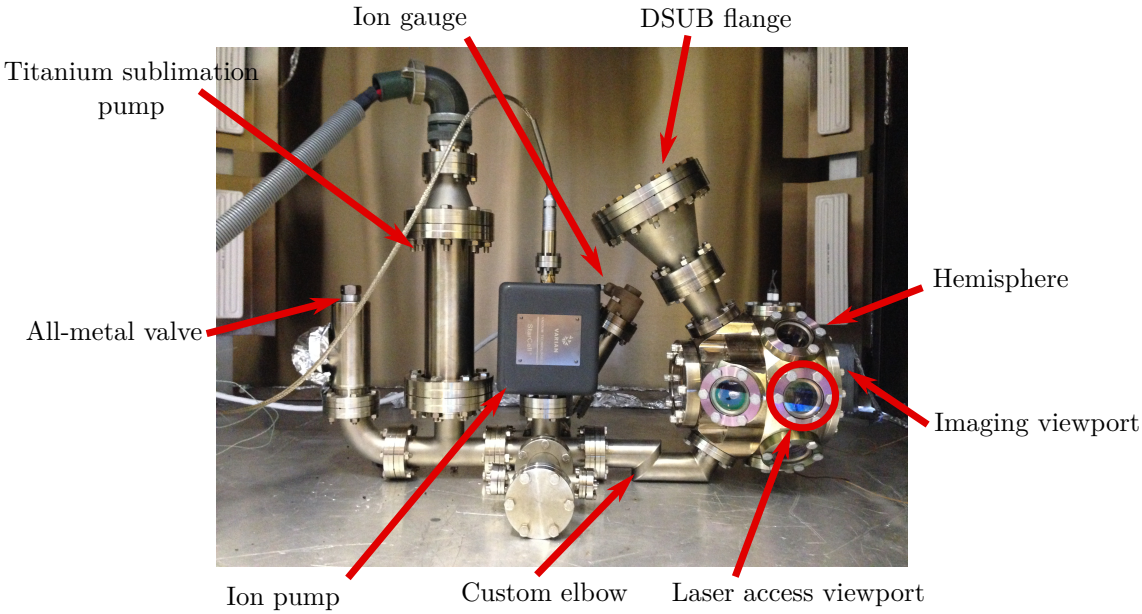

Figure 2.10: Ion trap vacuum system. The whole assembly can be divided into two sections, one containing the trap inside the hemisphere and the pump section to the left of it.

The ion trap is contained within the hemisphere[1]. It has one DN100CF port which holds the imaging viewport[2], one DN63CF port for holding the mounting structure of the ion trap and twelve additional DN40CF ports, which are used for performing various functions. Eight of these ports are placed on an octagon around the imaging viewport. Several of them are dedicated for laser access windows[3], which are coated with an anti-reflective coating for the photoionisation, cooling and repumping lasers to optimise transmission and minimise scatter inside the vacuum system. One of the octagon flanges contains the SMA connection for applying the trapping RF voltage. The flange at the base of the octagon is sealed off with a blank flange, which acts as the support point for the hemisphere. The DSUB connector flange[4] is used for DC voltage delivery to the ion trap electrodes, to fit the flange on the hemisphere, two reducing flanges[5] are used to go from DN100CF to DN40CF.

The pumping section of the vacuum system is placed behind the hemisphere, such that the generated electric fields do not interfere with the ion trapping potential. The pumps and the hemisphere are connected via a five-way cross piece[6] and a custom-shaped elbow [83], whose additional purpose is to set the correct height of the laser access viewports

[1]Kimball Physics MCF600-SphOct-F2C8 and MCF450-WeldClstr-E1C4
[2]Kurt J. Lesker VPZL-275Q
[3]Kurt J. Lesker VPZL-275Q
[4]Kurt J. Lesker IFDGG501056AX
[5]Kurt J. Lesker CRN337X275 and CRN600X337
[6]Kurt J. Lesker C5-0275

to ≈12.5 cm above the optics table. The pumping section includes an ion pump[7], ion gauge[8], titanium sublimation pump[9] and an all-metal valve[10] for connecting a detachable turbomolecular pump[11].

To reach the required UHV pressure, the vacuum system requires a bakeout at a temperature of ≈190 °C, which evaporates gases absorbed by the stainless steel walls of the vacuum system. The procedure starts by connecting the turbomolecular pump. After several days of pumping the chamber reaches a pressure of 10^{-6} mbar. The system is then wrapped in several layers of foil and heated to the required temperature inside an oven [84]. The rate of temperature change has to be kept small, in order to avoid the windows and ceramic components from cracking under thermal stress. Therefore, the oven is controlled by an active feedback system, implemented by Nikolaus Lorenz, which controls the heating rate of the oven. After several weeks of baking at the required temperature, the pressure of the system drops to a pressure of 10^{-7} mbar, at which point the ion pump and the ion gauge is turned on. Since the turbomolecular pump cannot go lower in pressure, the baking oven is briefly opened to close the all-metal valve. From this point, the ion pump is relied upon to reduce the pressure, to a value of 10^{-8} mbar. Once the pressure of the chamber does not change appreciably, the temperature is gradually brought down to room temperature. If the bake is successful, the system reaches a pressure of $\approx 10^{-10}$ mbar, which is further improved by using the titanium sublimation pump. The pump works on the principle of heating a titanium filament until the outer layer liquefies and becomes an excellent absorbent of any background gasses. The final pressure of the system is $\approx 10^{-11}$ mbar.

Despite the simple procedure of reaching UHV pressures, the assembly of an ion trap inside a vacuum system carries the risk of contaminating the chamber with materials which have slow evaporation rates. These contaminants are referred to as virtual leaks, due to them preventing the vacuum system from going down to the required pressure. Therefore, the assembly of the vacuum system takes place in a clean room with protective clothing to minimise the risk of contamination.

During the work described in this thesis, several modifications were made to the basic vacuum system described in fig. 2.10, the purpose of which will be described in the following chapters. The details of the setup inside the hemisphere will also be described

[7] Varian 9191145
[8] Agilent Technologies UHV-24p
[9] Varian 9160050
[10] Kurt J. Lesker VZCR40R
[11] Oerlikon Leybold Vacuum TURBOLAB

in the relevant chapters.

2.5 Yb ion

The choice of the species of ion to trap determines several key experimental parameters. The most important one is the energy level diagram, which determines the qubit energy gap between the ground and excited states. Ideally these states have long lifetimes and can be addressed with easy to generate signals. One such element is Ytterbium, which is a metal with an atomic number of 70, part of the lanthanide category of elements. Natural ytterbium is composed of the stable isotopes of ^{168}Yb, ^{170}Yb, ^{171}Yb, ^{172}Yb, ^{173}Yb, ^{174}Yb and ^{176}Yb. The 174 isotope is the most abundant one, making up a third of the found resources. In this thesis, isotopes 174 and 171 are used as the main trapped ions. This is largely due to the simplicity of the photoionisation and Doppler cooling laser setups and the favourable qubit transitions in the microwave frequency regime, described in the following sections.

2.5.1 Atomic oven

An atomic oven is a device used for generating a cloud of atoms, which can be ionised and trapped at the vicinity of the ion trap electric potential minimum. This is achieved by heating a small sample of Yb to large temperatures, at which the atoms have enough energy to break the bonds in the crystal and travel towards the ion trap. The design of the ovens is described in chapter 4.

2.5.2 Photoionisation

To ionise an atom, an electron needs to be excited enough to be ripped out of its orbital and into the continuum. In the early days of ion trapping experiments, an electron gun was used to provide enough energy. These devices not only ionise the atoms of interest, but everything else within the atomic sample, making isotope selectivity impossible. Furthermore, the heat generated by the gun disturbs the electric potentials of the trap, which requires downtime for the temperature to stabilise. An alternative to this method is the use photoionisation[85, 86], where the atoms are selectively excited using optical radiation.

In our photoionisation scheme, the neutral atom is firstly excited into an isotope dependent level from where a second photon transfers the electron into the continuum. The scheme for Yb isotopes is given in fig. 2.11. This method of ionisation consists of a two different wavelength photon excitation process, where the first photon excites the right

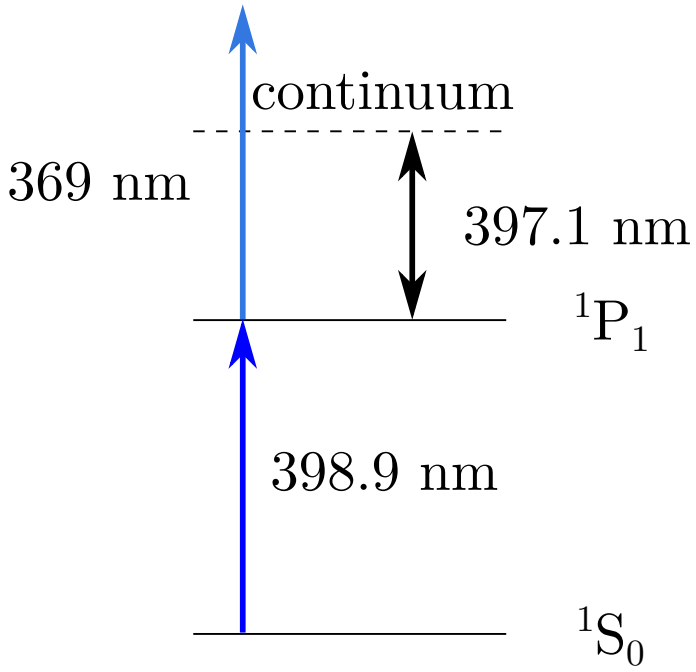

Figure 2.11: Isotope selective ionisation scheme for Yb. The isotope is selected by tuning the 398.9 nm wavelength to excite the transition of the sixth shell ($^1S_0 \rightarrow {}^1P_1$).

isotope into the $^1P_1$ level, from which the next photon must have a wavelength shorter than ≈397.1 nm to produce an ion. A 369 nm laser used for Doppler cooling the trapped ion can be used for the second ionisation step. The requirements for the ionisation laser includes the linewidth being narrow such that it does not excite the unwanted isotopes, where transitions are separated by several hundreds of megahertz, as shown in table 2.1. The exact values for each isotope is documented in [87]. The transitions are shifted by the Doppler effect caused by the thermal motion of the atoms. Knowing the angle between the atoms leaving the oven and the laser, the shift in frequency Δf can be calculated by

$$\Delta f = \frac{v \cos\theta}{c} f_0, \tag{2.19}$$

where $v \cos\theta$ is the projection of the atom velocity onto the $\vec{k}$-vector of the photoionising beam and f_0 is the Doppler free transition frequency, as given in [87] for Yb.

Table 2.1: Table for the ${}^1S_0 \leftrightarrow {}^1P1$ transition line of different Yb isotopes as listed in [87].

Yb isotope	Transition	Absolute frequency (THz)
170	${}^1S_0 \leftrightarrow {}^1P_1$	751.52779(120)
171	${}^1S_0(F = 1/2) \leftrightarrow {}^1P_1(F = 3/2)$	751.52760(60)
172	${}^1S_0 \leftrightarrow {}^1P_1$	751.52714(120)
173	${}^1S_0(F = 1/2) \leftrightarrow {}^1P_1(F = 3/2)$	751.52714(120)
173	${}^1S_0(F = 1/2) \leftrightarrow {}^1P_1(F = 7/2)$	751.52714(120)
176	${}^1S_0 \leftrightarrow {}^1P_1$	751.52615(60)

2.5.3 Laser Doppler cooling

The lifetime of an ion in a trap is dependent on the heating rate of the ion and the trap depth. As mentioned previously the heating rate refers to the kinetic energy gain over time, which is caused not only by the anomalous heating rate mentioned in section 2.3.1, but is also dependent on the amount of ambient electric field noise and collisions with background gases. The electric noise level can be minimised by heavily filtering and shielding of the electronic components used in the laboratory which has shown significant improvement of the ion heating rate [88]. A long standard of improving ion lifetimes was the use of buffer gas cooling [89], where gas such as helium is injected into the trap. The gas particles collide with the trapped ion and reduce its temperature. The technique is most effective for cooling down hot ions, which have a kinetic energy above the surrounding environment temperature. This technique is rarely used, due to the efficiency and effectiveness of laser cooling to dampen the trapped ion motion.

The use of laser cooling for reducing the ion temperature was proposed and implemented by David Wineland in [15] and later developed for neutral atoms by Steven Chu [90], William D Phillips [91] and Claude Cohen-Tannoudji [92]. The interaction of a two-level particle with energy separation of frequency ω_0, moving with a velocity v, with monochromatic light of frequency w can be described using a semi-classical approach of the particle scattering the incoming photons [93]. The photons scattered by the particle result in a net force, which can be used to slow down the particle. This scattering rate is given as [94]:

$$\gamma_{scatt} = \frac{\Gamma}{2} \frac{I/I_{sat}}{1 + I/I_{sat} + 4\delta^2/\Gamma^2}, \tag{2.20}$$

where Γ is the linewidth of the transition and the saturation parameter is the ratio of the

intensity of the light I and the saturation intensity I_{sat}, calculated as

$$I_{sat} = \frac{\hbar\Gamma\omega_0^2}{6c}. \tag{2.21}$$

The frequency detuning from resonance δ includes the Doppler shift kv,where $k = \omega/c$ is the wavenumber. The scattering force is then given as

$$F_{scatt} = \hbar k \frac{\Gamma}{2} \frac{I/I_{sat}}{1 + I/I_{sat} + 4\delta^2/\Gamma^2}, \tag{2.22}$$

which is the scattering rate multiplied by the photon momentum $\hbar k$. Equation 2.22 has a dependence on the frequency detuning δ, which is determined by the ion velocity v due to the Doppler effect. The velocity oscillates with the ion motion in the potential well set by the secular motion of the ion. By setting the frequency slightly bellow resonance (red detuned), the ion will scatter more photons when going towards the laser rather than backwards. This difference in the scattering force slows the ion motion down, therefore the method is also known as laser Doppler cooling. Since it relies on momentum transfer, the limit on laser cooling is known as the recoil limit given as $\hbar\Gamma/2$.

In order to cool the ion, several requirements must be met. One of these is that the radiation wavevector $\vec{k}$ needs to have a component in all of the principal axes of motion, so that there is momentum transfer along them. This amounts to having the laser cooling beam crossing the ion at an angle relative to its motion. Furthermore, a trapped ion has more than two energy levels, with decay channels leading to states which stop the cooling cycle. To be able to cool the ion, the cooling cycle must be closed with additional repumping lasers, which depopulate these 'dark' states. The energy level diagram for ^{174}Yb for a closed cooling cycle is given in fig. 2.12. All of the transitions are easily addressed with lasers, with exact wavelengths detailed in [64]. The 369.5 nm transition is referred to as the Doppler transition laser since the ion scatters the most photons for the transition $^2S_{1/2} \rightarrow {}^2P_{1/2}$, which has a natural linewidth of 19.6 MHz [95]. The repumper laser light 935.2 nm and 638.6 nm keeps the ion state within the cooling cycle.

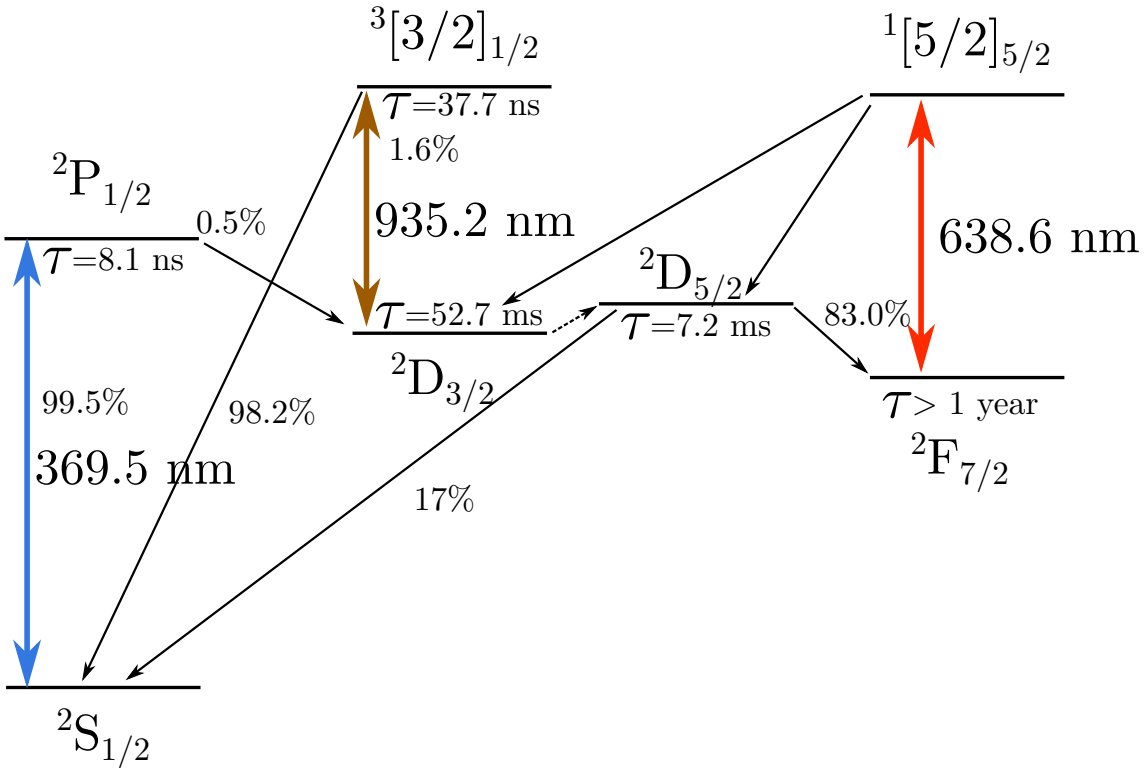

Figure 2.12: The reduced energy level scheme of $^{174}Yb^+$. The strongest transition is the $^2S_{1/2} \leftrightarrow {}^2P_{1/2}$ scatters the most photons, but the ion can occasionally, with a probability of 0.5%, decay into the $^2D_{3/2}$ state, from where 935.2 nm light is used to excite it to the $^3[3/2]_{1/2}$ state where it eventually decays back into the $^2S_{1/2}$ ground state. The dashed line representing the transition $^2D_{3/2} \leftrightarrow {}^2D_{5/2}$ can be excited through collision with background gases. This happens approximately once per hour. A 638.6 nm repumper is used to bring back the ion into the cooling cycle. Linewidths, branching ratios and lifetimes taken from [96, 97].

The cooling cycle for $^{174}Yb^+$ is relatively simple due to the nuclear spin having a value of zero, which is different for the $^{171}Yb^+$ with a nuclear spin of 1/2. The half integer spin introduces hyperfine splitting into the energy levels of different total angular momentum values F [94], which slightly complicates the cooling scheme with the requirement of addressing all of the split levels and selection rules. The energy level diagram for $^{171}Yb^+$ is given in fig. 2.13.

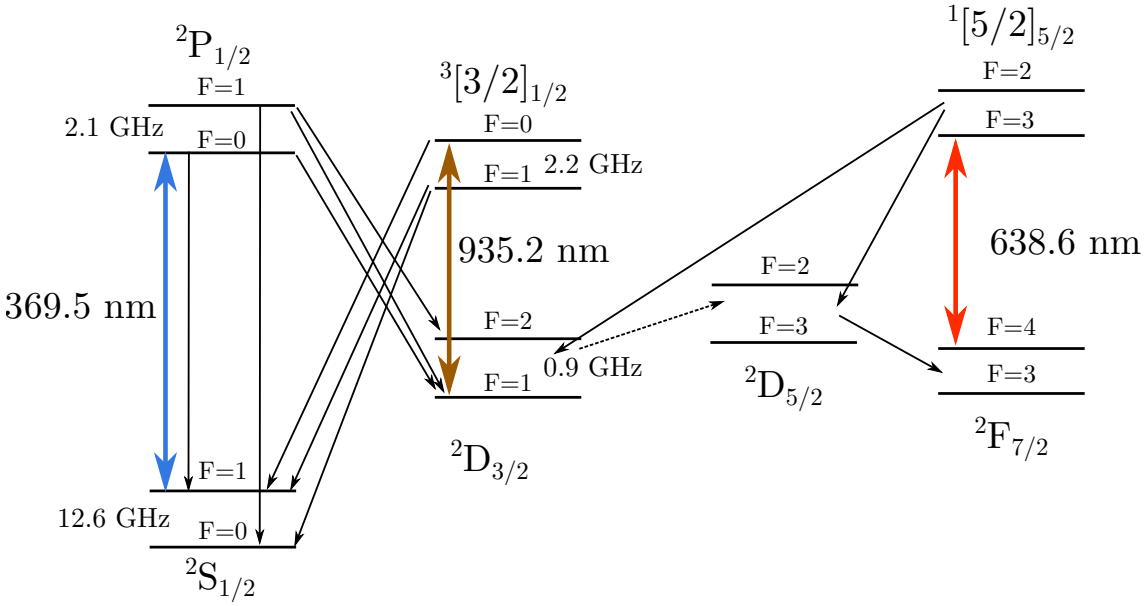

Figure 2.13: The energy level scheme for $^{171}Yb^+$ Doppler cooling cycle. For this isotope the scheme is complicated by the hyperfine splitting, with the amount indicated next to the energy level. Due to selection rules, the Doppler cooling laser can only address the transition $^2S_{1/2}F = 1 \rightarrow {}^2P_{1/2}F = 1$. To keep the ion in the cooling cycle, microwave radiation is required to address the $F = 0 \rightarrow F' = 1$ transitions in the $^2S_{1/2}$ and $^2P_{1/2}$ manifolds.

The nuclear spin of 1/2 splits the $^2S_{1/2}$ and $^2P_{1/2}$ manifolds into two possible states with total angular momentum $F = 0$ and $F = 1$. The frequency splitting for the ground state $^2S_{1/2}$ state is equal to ≈12.64 GHz, whereas it is ≈2.1 GHz for the excited state $^2P_{1/2}$. These splittings can cause the ion to decay into states which are off resonant to the 369 nm laser, therefore to keep the ion in the cooling cycle, these shifts need to addressed with additional frequencies. Setting the 369 nm laser to excite the transition $^2S_{1/2}, (F = 1) \leftrightarrow {}^2P_{1/2}, (F = 0)$, it is possible for the ion to be off-resonantly excited into the $^2P_{1/2}, (F = 1)$ state. The ion can then decay into the $^2S_{1/2}(F = 0)$ state, where it is not addressed by the cooling laser. To excite the ion back into the $^2S_{1/2}, (F = 1)$ state, microwave radiation set to the splitting of 12.64 GHz is applied. There is a 0.5% probability of the ion decaying into the $^2D_{3/2}$ manifold instead of the $^2S_{1/2}$ ground state. As in the case for $^{174}Yb^+$, the repumping 935 nm and 638 nm wavelengths are used. All of the D and F state frequencies are shifted as well due to the nuclear spin, however these transitions are typically power broadened by several gigahertz by setting the beam intensity much larger than the saturation intensity [64]. Linewidths of such magnitude cover the hyperfine splitting, therefore avoiding the requirement for additional frequencies.

The $^2S_{1/2}, F = 1$ manifold contains the different projected angular momentum states $m_f = -1, 0, +1$, which are degenerate in a zero magnetic field. These states are all

resonant to the applied 369 nm laser light and microwave field at 12.64 GHz. However, the depopulation of these states requires the σ_+,σ_- and π polarisation, which is set with polarisation waveplates. If the polarisation of the laser beam and the microwaves is not set accurately, the ion will be 'trapped' in the unaddressed m_f states. To avoid this, the degeneracy of the states is lifted using an applied magnetic field, which shifts the states due to the Zeeman effect. The splitting of these states is in the range of 10 MHz to 20 MHz for applied weak magnetic fields of 7 G to 14 G.

2.5.4 Laser systems

The multitude of lasers used for photoionisation, Doppler cooling and repumping are required to have narrow linewidths and accurate frequency control. This guarantees isotope selectivity and efficient cooling. The lasers used in this work are based on the extended laser diode cavity designs described in [64] and high-power diode-pumped frequency doubling laser systems, detailed in [67].

The extended cavity laser diode system (ECDL) (pictured in fig. 2.14) generates several milliwatts of light from a light-emitting diode, whose emission wavelength is determined by the temperature and the applied current. The spectrum of the emitted light spans several nanometres, which can be minimised with the use of a diffraction grating. The diffraction grating reflects the impinging light back into the diode, where it interferes with the incoming light. At certain wavelengths, the interference suppresses the spectrum of the diode to only permit specific frequencies of light to propagate. The linewidth of a typical ECDL laser is ≈5 MHz, which makes them excellent for exciting the wanted transitions. The lasers are tuned with the use of a piezoeletric transducer, which is mounted to change the angle of the diffraction grating and the cavity length. This method allows the laser frequency to be set with an accuracy of ≈1 MHz. Commercial and homebuilt ECDL systems are used for the 399 nm, 935 nm and 638 nm wavelengths, which each outputting laser beams with power of ≈30 mW.

The 369 nm light used for Doppler cooling is provided by several frequency doubling systems. This is due to the poor performance of laser diodes in deep UV, which make the ECDL laser assembly complicated and difficult to maintain in operating condition. To obtain sufficient power in the UV, large 739 nm beam powers are required due to the limited conversion efficiency of the doubling process. Two types of commercial laser doubling systems are used in the lab, one using a high-power diode pump beam with a

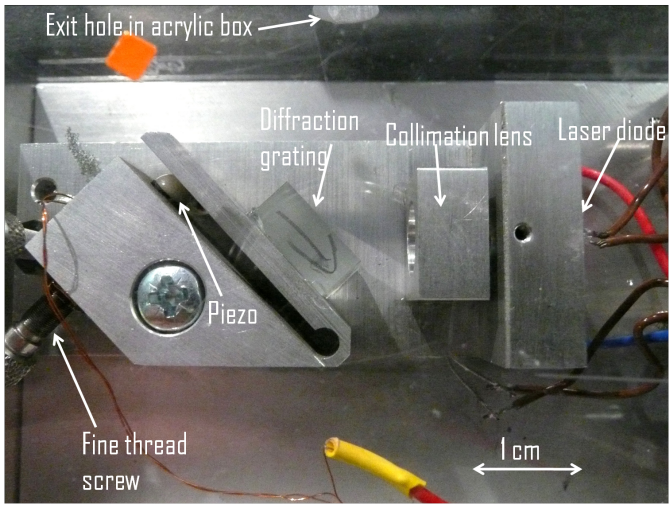

Figure 2.14: Picture of an ECDL laser system with highlighted components. The output light of the diode is collimated with a lens to obtain a non-diverging beam. The temperature of the system is controlled by a Peltier element, mounted under the laser diode. Image taken from [83].

titanium sapphire crystal [12] and the other relying on an amplified ECDL system[13].

The diode pumped system operates by using a 532 nm pump beam and a titanium sapphire cavity to generate 10 W at 739 nm, which is later used in the frequency doubling process. To control the wavelength of the 369 nm light, the titanium sapphire cavity contains a birefringent filter, whose angle can be changed to tune the output frequency of the red wavelength. The linewidth of the output beam is specified to have a linewidth of $<$1 MHz and an output power of $\approx$1.2 W, which can be used for supplying power to multiple ion trapping setups.

The amplified ECDL system contains the ECDL unit and an optical amplifier. The optical amplifier increases the output power of the ECDL unit to a power of $\approx$400 mW, which is used for frequency doubling. The amplified ECDL system outputs a weaker 40 mW beam, which is sufficient for up to three ion trap systems. The linewidth of the output beam is $<$1 MHz.

Even though the lasers used in ion trapping experiments are specified to have a narrow linewidth, they are still susceptible to frequency drift caused by the ambient environment of the laboratory. To obtain a long term stable laser frequency, active stabilisation is required to correct for the unpredictable fluctuations. The methods and techniques of these systems is described in chapter 3.

[12] MSquared SolsTis
[13] Toptica Photonics AG TA-SHG 36

2.6 Laser beam optical setup

To ionise the neutral atoms and cool the trapped ion, laser beams enter the vacuum system and propagate above the surface of the trap, with beams centred on the ion height of the chip. The beam diameters and position need to be controlled with an accuracy of ≈10 µm. To achieve this, an optical layout was set up with the additional goal of easily trapping different isotopes, see fig. 2.15.

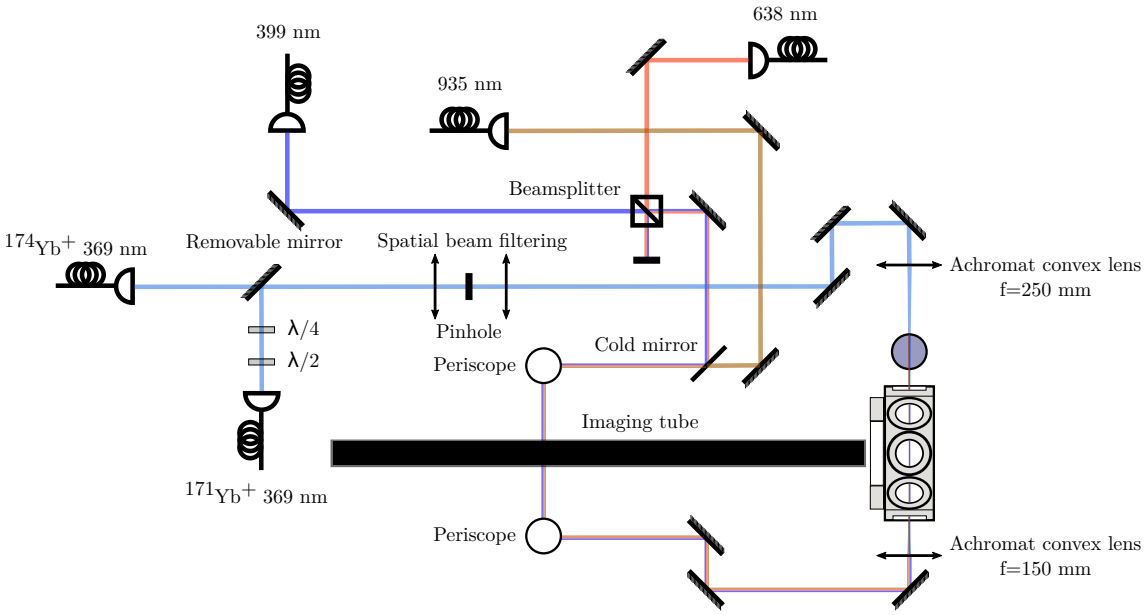

Figure 2.15: The optical layout of the laser beams used for trapping ions on a surface trap.

The output beams of all the lasers are split into several arms with the use of beam-splitters. The split laser beams are used for wavemeter measurements and distributed to multiple experimental ion trap systems. The direct output beam from the laser does not possess a circular beam profile, which is corrected by fibre coupling all laser beams to single mode fibres, which outputs a beam with a TEM00 profile and a diameter set by the fibre type and the output coupler lens. The added benefit of using fibre couplers includes the ability to easily swap between lasers of the same wavelength and the increased alignment stability.

The pre-fibre beam path for the ^{171}Yb isotope contained an acousto-optic modulator (AOM) to precisely shift the frequency of the laser and an electric-optic modulator (EOM) for generating sidebands in the frequency spectrum. The layout of these components is pictured in fig. 2.16.

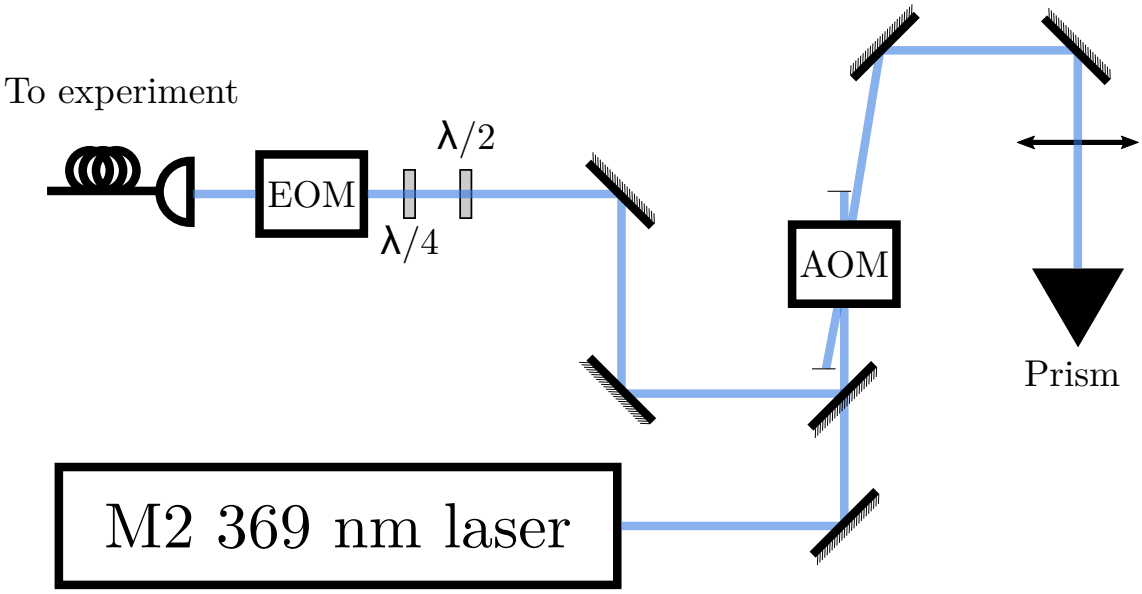

Figure 2.16: The optical layout of the ^{171}Yb isotope laser beam path. The 369 nm laser uses frequency doubling to obtain the required wavelength.

A single pass of the beam through the AOM will produce multiple diffracted beams, shifted by an angle proportional to the frequency applied to the AOM. To avoid this, the AOM is double-passed, which when aligned appropriately, corresponds to having the beam frequency shifted twice the frequency applied to the AOM. After the first pass, the first order diffracted beam is reflected back into the AOM with the use of a prism. Before being launched into the fibre, the beam passes a pair of polarisation waveplates, which are used to match the beam polarisation to the fast axis of a polarisation maintaining fibre[14]. Although the beams exit single-mode fibres, the beam profile of the 369 nm beam contained circular rings around the main beam, which causes additional scatter off the surface of the ion trap. The effect is reduced by using a higher quality collimating fibre coupler[15].

The Doppler cooling beam was given the largest priority in terms of beam shape control, due to its physical effect on the ion trap surface. The effect of UV beams on the trap can be explained by the photoelectric effect, where the UV photons have sufficient energy to free electrons in the gold electrodes and cause a significant current to cross into neighbouring conductors, causing severe burns to the surface of the trap, also know as voltage breakdown. The same electrons can move into the electrode gaps, where they accumulate and cause static charge build-up, which can take several days to decay [98]. In addition to this, the parasitic scatter of 369 nm light reduces the fluorescence detection fidelity of the

[14] PM-S350-HP
[15] Schafter+Kirchoff 60FC-4-A6.2S-52

Yb ion qubit which limits the final operation fidelity. To avoid these complications, the laser beam profile needs to be clean, well defined and of a small diameter to reduce the amount of scatter. Particular attention is given to beam alignment on the trap. The three laser beams with wavelengths of 399 nm, 638 nm and 935 nm were overlapped and shared the same beam path into the vacuum system. The optical setup then can be split into two groups, one for the 399 nm, 638 nm and 935 nm laser beams and the other dedicated to the 369 nm laser. Although present in the setup, the 638 nm beam was rarely used, due to the low probability of the ion decaying to the dark state $^2F_{7/2}$.

The overlap between 399 nm and 638 nm is achieved using a 30:70 ratio beamsplitter[16], which is then overlapped with the 935 nm light with the use of a cold mirror[17]. The combined beams are then guided along the optical table using broadband mirrors[18] capable of reflecting 99 % of the incident light. The alignment to the trap of this set of beams is optimised by observing the beam exiting the vacuum system. If a beam is set to have an angle to the ion trap, the reflective surface will produce two spots separated by a certain distance horizontally, one of them corresponding to the reflection from the trap. By beam walking the input light with two mirrors, the distance between the spots can be minimised, achieving a beam which propagates parallel to the trap surface. The alignment procedure is carried out with low beam powers of <10 µW to avoid charge build up.

The 369 nm laser light was provided by two different laser systems, one dedicated to ^{174}Yb and the other to ^{171}Yb. In order to easily switch between the two isotopes, a high accuracy removable mirror mount was used. Both beam paths were nearly identical, except for the 171 isotope requiring polarisation control to address the Zeeman shifted states. The half waveplate[19] was used to set the linear polarisation and the quarter waveplate[20] produced circular polarisation.

To check the beam quality, the profile of the fibre output was imaged with a beam profiler[21], which revealed a beam profile depicted in fig. 2.17a. Despite using a higher quality collimator, the output beam profile contained several rings around the central beam. To remove these parasitic features, the beam is passed through a spatial beam filtering setup, which consists of two convex lenses and a pinhole. The convex lenses act as a telescope, separated by the sum of their focal lengths, while the pinhole is positioned at the focal point of the first lens. The pinhole has a circular clearance of 75 µm, which

[16] Thorlabs BS019
[17] Thorlabs M254C45
[18] Newport 10B20BB.1
[19] Thorlabs WPH05M-355
[20] Thorlabs WPQ05M-355
[21] DataRay WinCamD XHR

means that features larger than this parameter do not propagate past the pinhole. The light that passes through the pinhole is then collimated with the second lens for further manipulation. Since the focal length of a lens can vary slightly due to chromatic aberration or a slightly divergent beam, the pinhole was mounted on a three-axis translation stage, which allowed the position to be set with micrometer precision. The second convex lens was also mounted on a single axis translation stage, to have a handle on the final beam diameter. The beam profile after spatial beam filtering can be seen in fig. 2.17b.

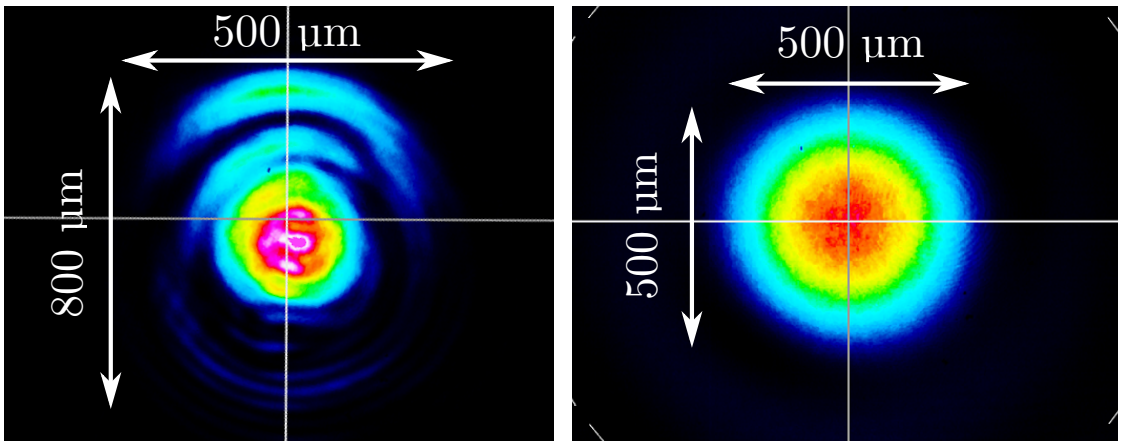

(a) (b)

Figure 2.17: The 369 nm laser beam before and after inserting a pinhole in the spatial filtering beam path.

The final optical element for all of the laser beams before entering the vacuum system is an achromatic convex lens, which is used to focus down the beam diameter smaller than the trap ion height, see fig. 2.18. In this thesis, the beam diameter is defined as twice of the $1/e^2$ radius. The lenses were mounted on a single-axis micrometer translation stage, which sets the height of the laser beam relative to the trap surface. The behaviour of a focused Gaussian beam is illustrated in fig. 2.18. The focused beam diameter is given by

$$2W_0' = \frac{2\lambda f}{\pi W_0} \tag{2.23}$$

where λ is the wavelength of the laser beam, f is the focal length of the lens and W_0 is the incident beam waist.

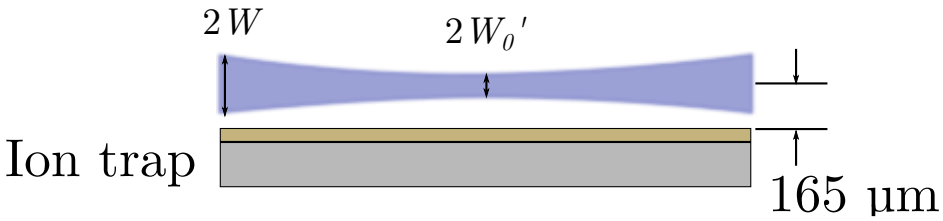

Figure 2.18: Beam waist expansion from the focal point of a convex lens.

The latter parameter is set by the boundary conditions of the fibre output beam and was found to be ≈ 1 mm to 3 mm for most laser beams. To calculate how much the beam diameter expands from the focal point to the edge of the chip, the following equation is used

$$2W(z) = 2W_0\sqrt{1 + (\frac{z}{M^2 z_0})^2}, \tag{2.24}$$

where $M = \frac{W_0'}{W_0}$ is the magnification factor and z is the distance from the beam waist and z_0 is the depth of focus of the input beam. The z_0 parameter indicates the distance at which the beam waist increases by a factor of $\sqrt{2}$. In this optical system, the input beam z_0 distances were measured to be approximately 1 m long.

It is clear that the size of the beam at the focal point is determined by the input beam diameter and divergence. Using these equations, the 399 nm and 935 nm beams having a waist of 0.5 mm and 1 mm respectively, were focused with a convex lens having a focal length of 150 mm, which results in equal beam diameters at the trap centre of 40 µm. The beam diameters at the edges of the trap (5 mm away from the focus) were found to be 150 µm for 399 nm beam and 280 µm for the 935 nm laser, which are small enough not to clip the surface trap, which lies at 165 µm below the beam.

The convex lens used for focusing the 369 nm beam has a focal length of 250 mm, which for an input beam waist of 0.5 mm results in a beam diameter of 117 µm, expanding to 120 µm at the edges.

Ion trapping relies heavily on cooling the ion motion so it does not escape the potential well. The angle of the propagating Doppler cooling beam relative to the trap axis determines how effectively the trapped ion scatters photons. In order to cool all of the motional modes of a trapped ion, the 369 nm beam must have a component in all of the three principal axes of the trapped ion, defined in section 2.3.1. To account for this, the beam was made to traverse the trap with a non-negligible angle relative to the RF rail electrodes, which was implemented by directing the cooling beam along one of the diagonal pairs of viewports as seen in fig. 2.19.

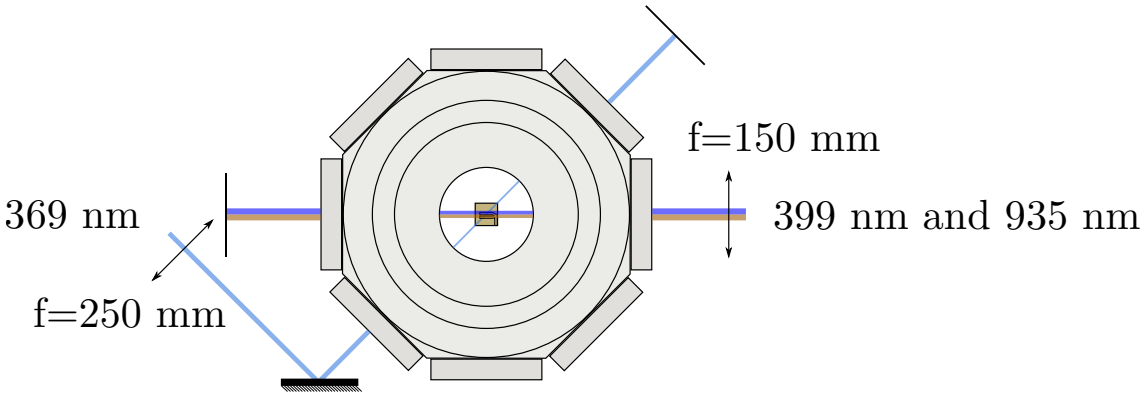

Figure 2.19: Beam propagation through the vacuum system. The collimated beams pass through focusing convex lenses (represented by arrows) placed close to the vacuum system.

To regularly check the beam diameter at the trap position for imperfections, a flipper mirror was installed after the achromat convex lens, which directed the 369 nm laser beam onto a beam profiler for analysis.

2.7 Imaging optics

To image a trapped ion, the ion must scatter a large enough number of photons, which can be detected with the use of highly sensitive charge-coupled devices (CCD) or photo-multiplier tubes (PMT). Although the PMT modules are more sensitive, the preferred choice for ion trapping is a CCD camera[22], which can resolve 2D images and identify trapped ions more easily. The light scattered by the trapped ion is detected through the imaging viewport coated with an anti-reflective coating for 369 nm light. The fused silica dielectric window has the risk of building up a static charge [98], which can prevent reliable trapping, therefore the ion trap is shielded from the window with the use of a stainless steel mesh fixed to the window with a stainless steel cable tie. The mesh is made using 25 µm wire with a spacing of 500 µm. A more detailed discussion of the issue can be found in the thesis of D. Murgia [67]. Although it would seem that the mesh could diminish the collection efficiency, only 10% of the light is blocked due to the mesh structure.

The scattered photons are collected with an imaging setup consisting of triplet and doublet optical systems mounted in a standard 1 inch optical tube, see fig. 2.20.

[22] Andor iXon Ultra 888, quantum efficiency of at least 30% for the 369 nm

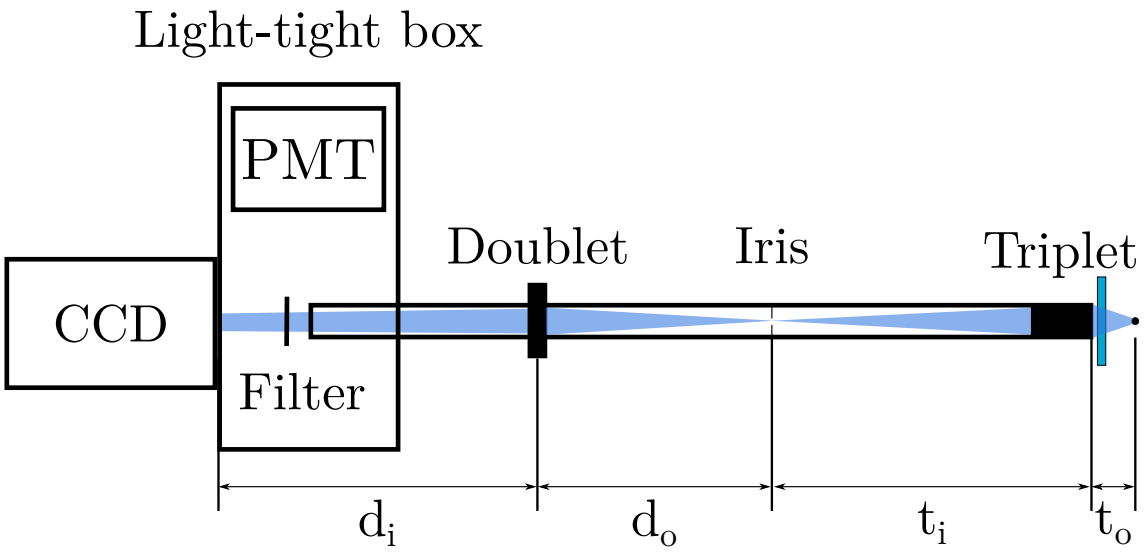

Figure 2.20: The ion imaging setup. Not included is the three-axis translation stage which holds the imaging tube and allows micrometre precision alignment.

The detailed design considerations of the system can be found in the thesis of Dr James Siverns [84]. The 369 nm photons scattered by the trapped ion are collected by the triplet[23] positioned next to the imaging viewport of the vacuum system. The triplet was set to have a working distance of 25 mm [99], which requires to have the ion positioned as close as possible to the imaging viewport. The triplet focuses the image at a distance $t_i + t_o$ from the ion with a magnification of $M_{tr} = 12.29$. At the focal point of the triplet lens, an iris is placed to block background light coming from the trap electrodes. In order to produce the required size image on the camera sensor, the magnification of the imaging setup can be tuned by including a doublet lens into the imaging path. The total magnification of the whole setup is given by

$$M_{tot} = M_{tr} M_{dbl}. \tag{2.25}$$

The total magnification was chosen to have a value of 14, which requires to have $M_{dbl} = 1.14$. The doublet is formed by two closely placed convex lenses of different focal lengths. The magnification is then calculated using

$$M_{dbl} = \frac{d_i}{d_o}, \tag{2.26}$$

where d_i and d_o are given by the relation

$$\frac{1}{f_{dbl}} = \frac{1}{d_o} + \frac{1}{d_i}. \tag{2.27}$$

[23] Special Optics 54-17-29-369

The distance $d_o + d_i \approx 400\,\text{mm}$ is fixed by the camera placement, therefore the equations are solved to obtain $f_{dbl} = 100\,\text{mm}$. The focal lengths for the doublet is the given by

$$\frac{1}{f_{dbl}} = \frac{1}{f_1} + \frac{1}{f_2}. \tag{2.28}$$

The lenses were chosen to have focal lengths $f_1 = 150\,\text{mm}$ and $f_2 = 300\,\text{mm}$, which achieves the required magnification. The triplet and doublet are then built up using 1 inch optics mounting tubes and placed on a translation stage for accurate position control.

The CCD camera sits in a light-tight box which also serve as housing for a photomultiplier tube (PMT). A flipper mirror placed in the imaging path is used to switch between the CCD and PMT. To block out ambient light, an optical filter[24] for 369 nm light is placed in the imaging path before the camera. The filter was mounted on an electronic flipper mirror, which permits the easy removal of the filter in cases where the trap needs to be imaged with background light.

2.8 Yb ion hyperfine qubit

The full hyperfine manifold of $^2S_{1/2}$ is illustrated in fig. 2.21. The state $|0\rangle \equiv |F = 0, m_f = 0\rangle$

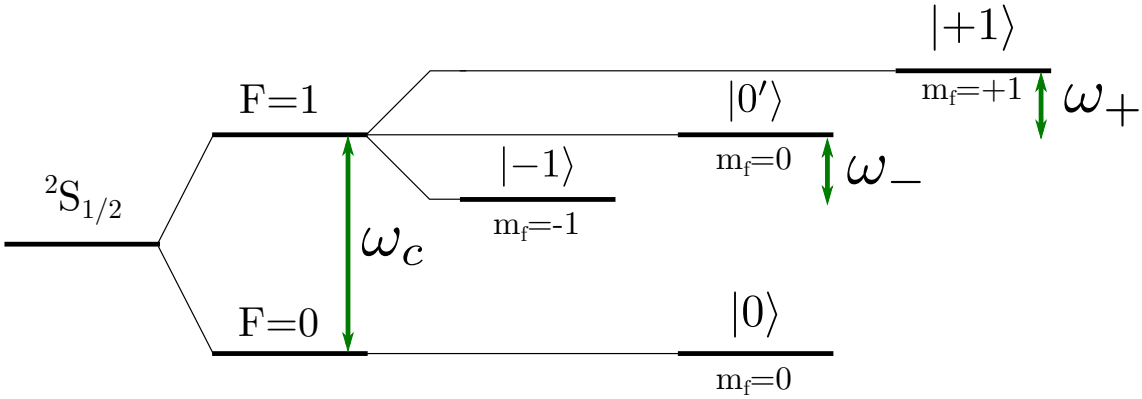

Figure 2.21: The hyperfine splitting of the $^2S_{1/2}$ manifold. The degeneracy of the $F = 1$ sub-manifold is lifted by the application of an offset magnetic field of several Gauss, which splits the different m_f states.

serves as the ground state of the qubit separated by $\omega_0 = 2\pi \times 12.642\,812\,1\,\text{GHz}$ from the $F = 1$ sub-manifold. The presence of a magnetic field B defines a quantization and lifts the degeneracy of the sub-manifold by splitting the different projected angular momentum states $m_f = -1, 0, 1$ labelled as $|-1\rangle \equiv |F = 1, m_f = -1\rangle$, $|0'\rangle \equiv |F = 1, m_f = 0\rangle$ and $|+1\rangle \equiv |F = 1, m_f = +1\rangle$. The applied magnetic field is limited to several Gauss and the

[24] Semrock FF01-370/36-25

frequency shifts from the clock transition are calculated using [100]

$$\omega_+ = \frac{\omega_0}{2}\left(1+\chi-\sqrt{1+\chi^2}\right), \tag{2.29}$$

$$\omega_- = -\frac{\omega_0}{2}\left(1-\chi-\sqrt{1+\chi^2}\right), \tag{2.30}$$

$$\omega_c = \omega_0\sqrt{1+\chi^2}, \tag{2.31}$$

where $\chi = g_J\mu_B B/\hbar\omega_0$. The g_J factor for the $^2S_{1/2}$ manifold is equal to 2 and μ_B is the Bohr magneton. For weak magnetic fields, the term χ^2 can be ignored, which simplifies the eqs. (2.29)–(2.31) to $\omega_c{\approx}\omega_0$ and $\omega_+{\approx}\omega_-{\approx}\mu_B B/\hbar$.

The states $|-1\rangle$ or $|+1\rangle$ can be used as the qubit state $|1\rangle$ and when combined with $|0\rangle$ will be referred to as the bare state qubits. The advantages of using the hyperfine states as the qubit logic levels are the long lifetimes of the excited state due to reduced spontaneous emission probability [94] and the easily generated radiation for manipulating the qubit state.

The application of the magnetic field not only introduces frequency shifts in the energy levels, but also makes the states more sensitive to magnetic field fluctuations, which can be calculated by differentiating eqs. (2.29)–(2.31) with respect to χ. This results in equations

$$\frac{\mathrm{d}\omega_+}{\mathrm{d}\chi} = \frac{\omega_0}{2}\left(1+\frac{\chi}{\sqrt{1+\chi^2}}\right), \tag{2.32}$$

$$\frac{\mathrm{d}\omega_-}{\mathrm{d}\chi} = -\frac{\omega_0}{2}\left(-1+\frac{\chi}{\sqrt{1+\chi^2}}\right), \tag{2.33}$$

$$\frac{\mathrm{d}\omega_c}{\mathrm{d}\chi} = -\omega_0\frac{\chi}{\sqrt{1+\chi^2}}. \tag{2.34}$$

The equations indicate that the $|-1\rangle$ and $|+1\rangle$ states are sensitive to magnetic field fluctuations to first order, due to the non-zero angular momentum. Therefore, the coherence time of these states is limited by the stray magnetic field fluctuations, which are difficult to shield or compensate for.

2.9 Coherent manipulation

2.9.1 Ion qubit initialisation and readout

To be able to use the trapped ion hyperfine qubit, it has to demonstrate the requirements given in [25]. One of them is initialisation of the qubit, which amounts to preparing the qubit in its ground state $|0\rangle$. This is done by setting the 369 nm laser frequency to be

resonant with the ${}^2S_{1/2}, F = 1 \leftrightarrow {}^2P_{1/2}, F = 1$ transition (seen in fig. 2.13), while the 12.6 GHz microwave radiation is turned off. This breaks the Doppler cooling cycle, due to the ${}^2S_{1/2}$ state not being depopulated with any radiation. After around 1 µs the ion will have a near unit probability of occupying the $|0\rangle \equiv \left|{}^2S_{1/2}, F = 0\right\rangle$.

In order to use the qubit as the basis for quantum information processing, it requires the ability to be read out to distinguish the two levels $|0\rangle$ and $|+1\rangle$. For the hyperfine qubit in fig. 2.21, the Doppler cooling cycle in fig. 2.13 serves as the method of measuring the state of the ion. The description of the method is detailed in the thesis of [101]. Setting the 369 nm laser frequency to be resonant with the ${}^2S_{1/2}, F = 1 \leftrightarrow {}^2P_{1/2}, F = 0$ transition and counting the scattered photons with a detector will produce different rates depending if the ion was in either $F = 0$ (dark) or $F = 1$ (bright) state. This is due to the off-resonant beam not exciting the ion when it is in the dark state due to a 14.7 GHz frequency difference. On the other hand the laser is resonant with the bright state. To infer which state is occupied, the detection system must count the photons for a certain amount of time until a threshold is reached to say with certainty if the ion is in state $|0\rangle$ or one of the states of $F = 1$ manifold. This detection time is typically on the order of a few hundred microseconds [101], which is mostly limited by the detection efficiency of the photon collecting system and the detector used, which can be a charge-coupled-detector (CCD) camera or a photomultiplier tube (PMT). The detection histograms for the dark and bright states can be seen in fig. 2.22. The two histograms have a small overlap for photon numbers 0 to 5, which limits the readout fidelity to 96.8%. Ideally, the two histograms have no overlap, which can be achieved with improved collection efficiency.

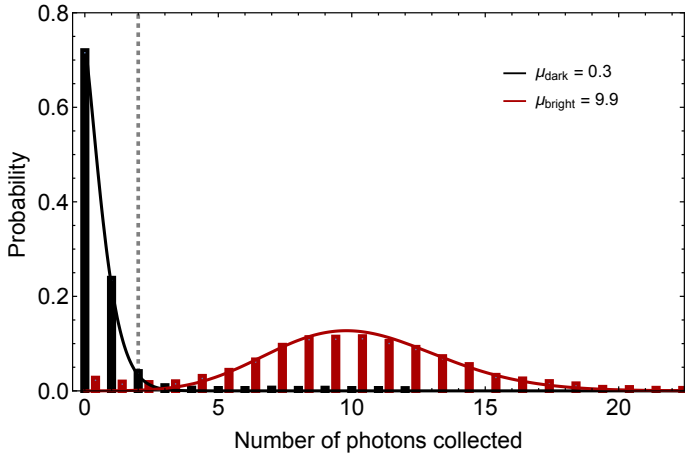

Figure 2.22: Typical histogram from [69], showing the different photon number distributions for different detected states, red -$F = 1$, black -$F = 0$. On average, the ion scatters 0.3 photons when in the state $F = 0$, and 9.9 when detected in the $F = 1$ state. Setting the threshold (marked with dashed line) to three photons, the ion state can be read out with a fidelity of 96.8%.

2.9.2 Single qubit operations

The Hamiltonian of a trapped ion qubit with a frequency gap ω_0 can be written as the sum of two terms,

$$\hat{H_0} = \frac{\hbar\omega_0}{2}\left(|0\rangle\langle 0| - |1\rangle\langle 1|\right) + \hbar\omega_z\left(\hat{a}^\dagger\hat{a} + \frac{1}{2}\right), \tag{2.35}$$

where the first is determined by the electronic state of the ion and the second term describes the quantum motion of the particle with secular frequency ω_z in a quadratic potential well described by number state $|n\rangle$. The $|1\rangle$ state represents one of the atomic states $|-1\rangle$,$|0'\rangle$ and $|+1\rangle$. The qubit internal state $|\psi\rangle$ is the superposition of the eigenstates of the Hamiltonian. The interaction of this qubit with applied radiation is described by the interaction of the ion magnetic moment $\vec{\mu}$ with the magnetic field component of the radiation $\vec{B}$ of frequency ω, given as

$$\hat{H_r} = -\vec{\mu}.\vec{B}. \tag{2.36}$$

Substituting the magnetic field for $\frac{B_z}{2}\left(e^{i(kz-\omega t+\phi)} + e^{-i(kz-\omega t+\phi)}\right)\hat{z}$, the Hamiltonian is expanded to

$$\hat{H_r} = -\vec{\mu}.\hat{z}\frac{B_z}{2}\left(e^{i(kz-\omega t+\phi)} + e^{-i(kz-\omega t+\phi)}\right), \tag{2.37}$$

where $k = 2\pi/\lambda$ is the wavenumber. The dot product $\vec{\mu}.\hat{z}$ can be written as [94]

$$\vec{\mu}.\hat{z} = \langle 0|\,\vec{\mu}.\hat{z}\,|1\rangle\left(|0\rangle\langle 1| + |1\rangle\langle 0|\right). \tag{2.38}$$

The term $\langle 0|\,\vec{\mu}.\hat{z}\,|1\rangle$ is defined as the Rabi frequency Ω. It describes the population oscillation frequency of a two level system between the states $|0\rangle$ and $|1\rangle$ when exposed to radiation resonant with the qubit energy gap. The Hamiltonian then can be written as

$$\hat{H_r} = \frac{\hbar\Omega}{2}\left(|0\rangle\langle 1| + |1\rangle\langle 0|\right)\left(e^{i(kz-\omega t+\phi)} + e^{-i(kz-\omega t+\phi)}\right). \tag{2.39}$$

Replacing the position operator with $z = \sqrt{\hbar/2m\omega_z}(\hat{a} + \hat{a}^\dagger)$, using the interaction picture transformation $\hat{H_I} = e^{i\hat{H_0}t/\hbar}\hat{H_r}e^{-i\hat{H_0}t/\hbar}$ and applying the rotating wave approximation (RWA) the Hamiltonian is then given by

$$\hat{H_I} = \frac{\hbar\Omega}{2}\left(|0\rangle\langle 1|\,e^{i(\eta(\hat{a}^\dagger e^{i\omega_z t} + \hat{a}e^{-i\omega_z t}) + \Delta + \phi)} + h.c.\right), \tag{2.40}$$

where Δ is the detuning from resonance. The Lamb-Dicke parameter, η, is defined as [102]

$$\eta = k\sqrt{\frac{\hbar}{2m\omega_z}} \tag{2.41}$$

which represents the ratio of the spread of the position to the wavelength of the applied radiation. Keeping the Lamb-Dicke parameter small such that,

$$\eta^2 (2n+1) \ll 1, \tag{2.42}$$

known as the Lamb-Dicke regime, allows the Hamiltonian in eq. 2.40 to be approximated to

$$\hat{H_I} = \frac{\hbar\Omega}{2}\left(|0\rangle\langle 1|\,(1 + i\eta(\hat{a}^\dagger e^{i\omega_z t} + \hat{a}e^{-i\omega_z t}))e^{i(\phi-\Delta t)} + h.c.\right). \tag{2.43}$$

Setting Δ to zero, the first term in equation 2.43 corresponds to driving the carrier transition with no interaction with the motion of the ion. This term can be written as

$$\hat{H_I}^c = \frac{\hbar\Omega}{2}\left(|0\rangle\langle 1|\,e^{i\phi} + |1\rangle\langle 0|\,e^{-i\phi}\right). \tag{2.44}$$

By appropriately setting the phase ϕ, different qubit operations can be implemented. A few examples include,

$$\begin{aligned}\hat{H_I}^c(\phi = 0) &= \frac{\hbar\Omega}{2}(|0\rangle\langle 1| + |1\rangle\langle 0|) = \frac{\hbar\Omega}{2}\hat{\sigma_x},\\ \hat{H_I}^c(\phi = \frac{\pi}{2}) &= i\frac{\hbar\Omega}{2}(|0\rangle\langle 1| - |1\rangle\langle 0|) = \frac{\hbar\Omega}{2}\hat{\sigma_y}.\end{aligned} \tag{2.45}$$

The σ_x and σ_y operators are the Pauli matrices, with $\sigma_z = -i\sigma_x\sigma_y$, which completes the possible set of operations in the Bloch sphere representation of a two-level system [103], illustrated in fig. 2.23. Applying any combination of the Pauli matrices on the qubit, the system can be steered into the required superposition defined by spherical coordinates. Moving out of the interaction picture and solving the time dependent Schrödinger equation shows that the rotation angles of the Bloch vector corresponds to applying pulses of radiation for a specific amount of time. A π-pulse corresponds to the transition $|0\rangle \rightarrow |1\rangle$ by applying a resonant frequency radiation for time of π/Ω, whereas a $\pi/2$-pulse prepares the even superposition state $\frac{1}{\sqrt{2}}(|0\rangle + |1\rangle)$. Applying constant radiation resonant with the energy splitting will make the ion state oscillate with the Rabi frequency, Ω, as illustrated in fig. 2.24. Performing many Rabi oscillations can be used to estimate the level of decoherence of the qubit system, where any noise on the qubit system will eventually

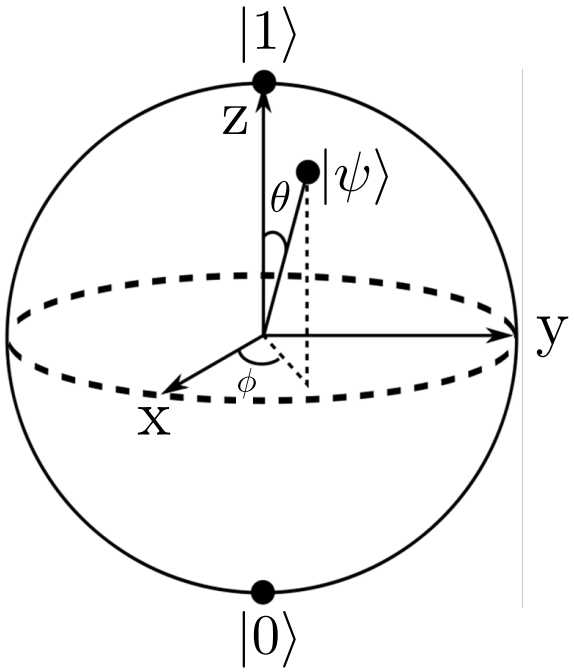

Figure 2.23: Bloch sphere representation of the qubit state $|\psi\rangle$. The state is defined as a unit vector where the two angles θ and ϕ describe the state completely. Single qubit operations are then commonly referred to as the change in these angles to obtain the required state. Adapted from [64].

diminish the oscillation amplitude.

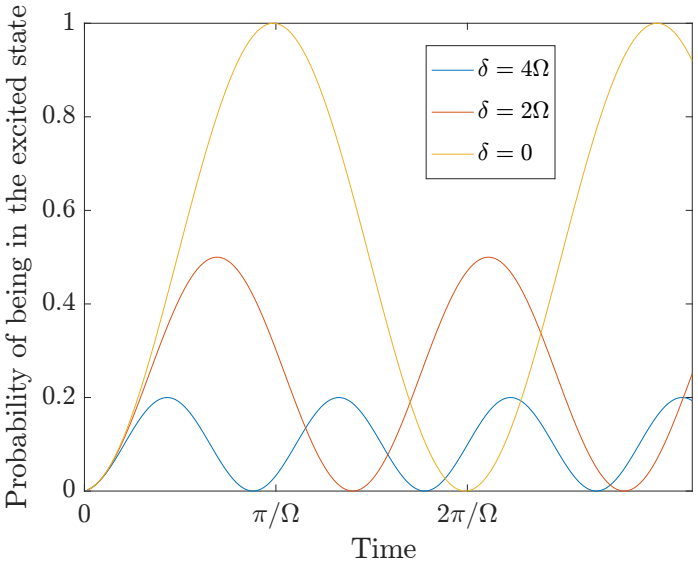

Figure 2.24: Population oscillations of the qubit state when exposed to radiation. If the radiation is resonant with the qubit energy gap, the probability of finding the qubit in the excited state undergo oscillations with with frequency Ω (yellow line). If the radiation frequency is detuned slightly from resonance, the resultant oscillation amplitude is significantly decreased (blue and red lines).

Although the description of these operations is simple, the actual implementation

is sensitive to different unwanted fluctuations in the environment, to which the qubit is sensitive to. This makes all operations imperfect, which can be quantified by measurement of fidelity, which is the overlap of the state that is wanted to be reached with the measured result $F = \langle\psi_{result}|\psi_{wanted}\rangle$. Fidelities for single qubit operations have shown a near unity performance, minimised with the improvement of the radiation delivery and photon detection systems [104].

The additional terms in equation 2.43 with the Lamb-Dicke parameter contain the creation and annihilation operators $\hat{a}^\dagger$ and $\hat{a}$ which operate on the motional energy levels of the ion. By setting Δ equal to one of the sidebands at frequency $+\omega_z$ and dropping the fast oscillation terms, the Hamiltonian in eq. 2.43 can be written as

$$\hat{H}_I^S = i\eta\frac{\hbar\Omega}{2}\left(|0\rangle\langle 1|\,\hat{a}^\dagger e^{i\phi t} + |1\rangle\langle 0|\,\hat{a}e^{i\phi t}\right). \tag{2.46}$$

By choosing different values of ϕ the Hamiltonian can be written as

$$\hat{H}_I^S(\phi = 0) = i\eta\frac{\hbar\Omega}{2}\left(|0\rangle\langle 1|\,\hat{a}^\dagger - |1\rangle\langle 0|\,\hat{a}\right), \tag{2.47}$$

which in addition to changing the internal state of the ion, also adds one phonon to the ion motion, therefore called the blue sideband. By setting $\Delta = -\omega_z$, a similar expression is obtained which removes one phonon, and is referred to the red sideband transition.

2.9.3 Internal-motional state coupling

The motional modes of a linear ion chain are used as the information 'bus' to couple the electronic states (internal) of two or more trapped ion qubits. This requires to be to able impart a state-dependent momentum kick to the ion, which excites the specific motional mode. In the previous section, the interaction Hamiltonian in equation 2.43 provides a means of controlling the motional state of the ion through excitation of the sideband transitions. The origin of these sidebands is the coupling between the secular motion of the ion and the applied radiation, with the strength of the interaction quantified by the Lamb-Dicke parameter in eq. 2.41. The Lamb-Dicke parameter determines the strength of the sidebands at frequencies $\omega_0 - \omega_z$ ('blue') and $\omega_0 + \omega_z$ ('red'). Applying radiation at the frequencies of the sidebands, will drive the qubit transition and the motional states $|0, n\rangle \leftrightarrow |1, n+1\rangle$ ('blue') and $|0, n\rangle \leftrightarrow |1, n-1\rangle$ ('red') respectively with Rabi frequencies

[101]

$$\Omega_{n\to n+1} = \sqrt{n+1}\eta\Omega, \tag{2.48}$$

$$\Omega_{n\to n-1} = \sqrt{n}\eta\Omega, \tag{2.49}$$

where Ω is the Rabi frequency defined in section 2.9.2.

The dependence of Ω_n on η indicates that, for the applied microwave radiation at 12.64 GHz and a Lamb-Dicke parameter $\eta = 1.4 \times 10^{-6}$, the sideband coupling is diminishingly small. However it is possible to increase this coupling with the use of a static magnetic field gradient, as will be shown in the next section.

2.9.4 Magnetic field gradient scheme

The scheme relies on generating a strong magnetic gradient at the ion trap position, which not only produces a non-negligible Lamb-Dicke parameter, but also allows to address ions individually in a linear chain. The method was proposed in [33] and first implemented in [35], with an alternative method developed in [34], and first implemented by [36]. Although the schemes are distinct, the recent work by [105] compares both methods and highlights many similarities. However, the use of an oscillating gradient has a few limitations. The main one is the requirement of generating large oscillating magnetic field gradients can only be achieved close to the electrode surface, which increases the anomalous heating rate of the ion. Furthermore, the electrodes can only run along the RF trapping electrodes and require to be impedance matched to the 50 Ω source. The scheme also does not lend itself to individual addressing, which hinders the possibility to be used on a large scale system. With these complications in mind, the static scheme was chosen to increase the required motional sideband coupling. The method of generating the magnetic field gradient will be discussed in section 4. The derivation of the main equations for coupling the motional and internal states follows [69, 101].

Internal-motional state coupling with a magnetic field gradient

The magnetic field gradient scheme relies on using a qubit made of two states with different magnetic moments, which also makes it sensitive to magnetic field fluctuations. In this description of the scheme only the magnetic field sensitive state $|+1\rangle$ of the qubit in fig. 2.21 is considered as the excited state $|1\rangle$, and the ground state is $|0\rangle$. The presence of a

weak magnetic field shifts this level in frequency, whose value can be calculated as

$$\omega_0 + \omega_+ \approx \omega_0 + \frac{\mu_B B}{\hbar} \tag{2.50}$$

where B is the magnetic field at the ion position and μ_B is the Bohr magneton. The magnetic field can be written as a sum of an offset field B_0 and a linear gradient along the z-axis as $B = B_0 + z\partial_z B$. This results in a position dependent shift, which can be expanded around the trapping position $z_0 = 0$ to give the position dependent frequency gap

$$\omega_0(z) = \omega_0(0) + z\partial_z\omega_0(z). \tag{2.51}$$

Substituting this expression and the position operator as $z = \sqrt{\hbar/2m\nu_z}(\hat{a} + \hat{a}^\dagger)$, where ν_z is the motional frequency of the ion, into eq. 2.35, the Hamiltonian can be written as

$$\hat{H}_0 = \frac{\hbar\omega_0}{2}\left(|0\rangle\langle 0| - |1\rangle\langle 1|\right) + \frac{\hbar\nu_z\epsilon_c}{2}(\hat{a} + \hat{a}^\dagger) + \hbar\nu_z\left(\hat{a}^\dagger\hat{a} + \frac{1}{2}\right), \tag{2.52}$$

with the parameter ϵ_c defined as

$$\epsilon_c = \frac{\partial_z\omega_0(z)}{\nu_z}\sqrt{\frac{\hbar}{2m\nu_z}}. \tag{2.53}$$

The Hamiltonian can be rewritten using the Polaron transformation, $\hat{H}_0' = \hat{U}\hat{H}_0\hat{U}^\dagger$, where $\hat{U} = e^{\epsilon_c(\hat{a}^\dagger - \hat{a})(|0\rangle\langle 1| - |1\rangle\langle 0|)/2}$. Once again the obtained Hamiltonian $\hat{H}_r'$ can be transformed to the interaction picture by finding $\hat{H}_I' = e^{i\hat{H}_0't/\hbar}\hat{H}_r'e^{-i\hat{H}_0't/\hbar}$. Making the RWA approximation results in the Hamiltonian,

$$\hat{H}_I' = \frac{\hbar\Omega}{2}(|0\rangle\langle 1| e^{i(\eta_{eff}(\hat{a}^\dagger e^{i\nu_z t} + \hat{a}e^{-i\nu_z t}))} + h.c), \tag{2.54}$$

which is equivalent to the one in equation 2.40 except for the factor η_{eff}, which is given by

$$\eta_{eff} \approx \epsilon_c. \tag{2.55}$$

The term is proportional to the applied gradient and secular frequency but not to the frequency of the applied radiation. Assuming no additional micromotion, this parameter for a typical axial secular frequency of $\nu_z = 2\pi \times 200\,\mathrm{kHz}$ and a gradient of $100\,\mathrm{T/m}$ results in $\epsilon_c = 0.086$, which is three orders of magnitude larger without the presence of a gradient. This makes manipulating the motional state with resonant radiation possible and, with an increase of the magnetic field gradient, provides an elegant method for manipulating

ion qubits with easy to generate microwave radiation.

Individual addressing

One of the prerequisites for performing high fidelity operations is the minimised cross-talk between different qubits when one of them is manipulated. Optical trapped ion qubit schemes suffer from cross-talk, due to unavoidable scatter of photons which can influence neighbouring ions. Although solutions to the problems have been proposed in [106], the methods used are complex and require significant technical overhead. Using the magnetic field gradient scheme, the ions trapped in a linear chain experience a different magnetic field at different positions. This results in position dependent qubit transition frequency, allowing qubits to be individually addressed in frequency space.

Despite that the magnetic field gradient scheme provides a method of manipulating the ion motion with microwave radiation, the magnetic field sensitive states are heavily susceptible to magnetic field noise, which is difficult to minimise. To obtain a qubit system resilient to ambient magnetic field fluctuations, a dressed state scheme is used to engineer a robust qubit which remains being sensitive to a static magnetic field gradient.

2.10 Dressed states

The internal-motional coupling provided by the magnetic field gradient allows to completely control the state of the trapped ion microwave qubit. However, the use of magnetic field sensitive states diminishes the coherence time of the qubit system caused by the magnetic field noise disturbing the splitting determined by eqs. (2.29)–(2.31). To circumvent this, the experimental system can be isolated with a magnetic field shielding system [107] or qubit decoupling schemes. Since the former method requires significantly more challenging engineering, the latter was implemented instead. In order to decouple the qubit from the environment, additional pulses and fields are synthesised and applied to the ion qubit, whose interaction is significantly stronger compared to the ambient noise. Multiple different methods have been designed and have demonstrated great success in protecting the qubit systems [108]. The scheme used in our research group was proposed and implemented by [37], which relies on forming a new qubit system with microwave dressed magnetic field sensitive states. This method was later improved in [100], which indicates an improvement by a factor of ≈ 300 of the coherence time. The description of the scheme follows the detailed explanation in [69], with the main results outlined in this thesis.

2.10.1 Microwave dressed state qubit

The dressed state scheme relies on forming a qubit system described by a Jaynes-Cummings Hamiltonian [109], where the total Hamiltonian of the system includes the qubit and the applied radiation. In the case for the the trapped ^{171}Yb ion, the qubit energy gap corresponds to the splitting of the fine levels of the $^2S_{1/2}$ manifold, equal to ≈12.64 GHz. By applying microwave radiation to the ion the energy scheme of the 'bare' ion is transformed into the dressed scheme, shown in 2.25a.

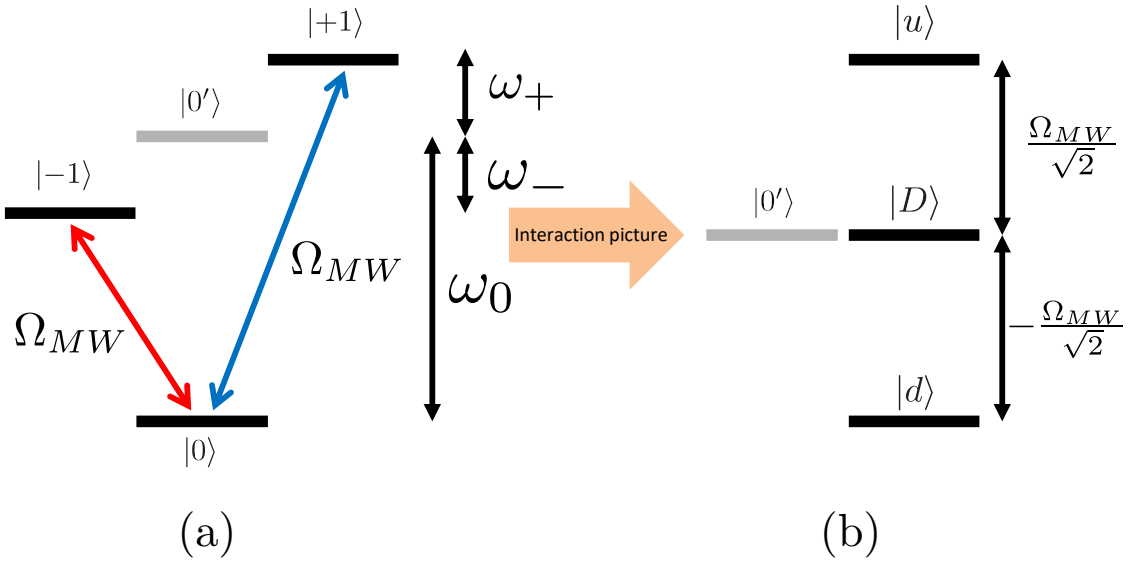

Figure 2.25: The microwave dressed state qubit scheme, where microwave fields resonant with the magnetic field sensitive state $|-1\rangle$ and $|+1\rangle$ in (a) form a new level diagram (b), which is less susceptible to magnetic field fluctuations. Adapted from [100].

Using the energy levels defined in section 2.8, the unperturbed Hamiltonian of the three level ion $\hat{H}_0$ is given by

$$\hat{H}_0 = -\hbar\omega_0 |0\rangle\langle 0| + \hbar\omega_+ \left(|+1\rangle\langle +1| - |-1\rangle\langle -1|\right), \tag{2.56}$$

where the energy level $|0'\rangle$ is set as the zero energy point. In the dressed state preparation method of [37, 38], microwave radiation of frequency $\omega_0 \pm \omega_+$ is applied with equal Rabi frequencies of Ω_{MW} with equal phase of 0, where the shift due to the weak magnetic field results in $\omega_- = \omega_+$. The interaction with the microwave field can be written as

$$\hat{H}_{MW} = \frac{\hbar\Omega_{MW}}{2}\left(e^{i(\omega_0+\omega_+)t}|0\rangle\langle 1| + e^{i(\omega_0-\omega+)t}|0\rangle\langle -1| + h.c.\right). \tag{2.57}$$

Rewriting the Hamiltonian in the interaction picture and applying the RWA, the Hamil-

tonian takes the form

$$\hat{H}^I_{MW} = \frac{\hbar\Omega_{MW}}{2}\left(|0\rangle\langle+1| + |0\rangle\langle-1| + |+1\rangle\langle 0| + |-1\rangle\langle 0|\right). \tag{2.58}$$

The eigenstates of this Hamiltonian are superpositions of the states $|0\rangle$,$|-1\rangle$,$|+1\rangle$ and are given by

$$\begin{aligned} |D\rangle &= \frac{1}{\sqrt{2}}\left(|+1\rangle - |-1\rangle\right) \\ |u\rangle &= \frac{1}{2}|+1\rangle + \frac{1}{2}|-1\rangle + \frac{1}{\sqrt{2}}|0\rangle \\ |d\rangle &= \frac{1}{2}|+1\rangle + \frac{1}{2}|-1\rangle - \frac{1}{\sqrt{2}}|0\rangle. \end{aligned} \tag{2.59}$$

Using these new states, the Hamiltonian of the microwave dressed system $\hat{H}^I_{MW}$ can be expressed as

$$\hat{H}^I_{MW} = \frac{\hbar\Omega_{MW}}{\sqrt{2}}\left(|u\rangle\langle u| - |d\rangle\langle d|\right). \tag{2.60}$$

The resultant energy level diagram is shown in fig. 2.25b, where the $|D\rangle$ state is separated from $|u\rangle$ and $|d\rangle$ by $\hbar\Omega_D/\sqrt{2}$. The robustness against magnetic field fluctuations is guaranteed by using $|0'\rangle$ and the $|D\rangle$ state as the new qubit system. To see this, the contribution of magnetic field noise to the Hamiltonian of the system can be written as

$$\begin{aligned} \hat{H}_{noise} &= \hbar\lambda(t)\left(|+1\rangle\langle+1| - |-1\rangle\langle-1|\right) \\ &= \frac{\hbar\lambda(t)}{\sqrt{2}}\left(|D\rangle\langle u| + |D\rangle\langle d| + |u\rangle\langle D|\right), \end{aligned} \tag{2.61}$$

which indicates that only noise at the dressed state energy splitting will cause depolarisation. Although it is possible to use the $|u\rangle$ and $|d\rangle$ states of the Hamiltonian in eq. 2.60, these states are sensitive to the Rabi frequencies of the microwave fields, which can fluctuate in power [100]. Instead the dressed state $|D\rangle$ is used for manipulation.

The motional coupling provided by the magnetic field described in 2.9.3 carries over for the $|D\rangle$ state, due to being a superposition of the magnetic field sensitive states $|-1\rangle$ and $|+1\rangle$. The description of how these states are initialised and read out is given in the next section.

2.10.2 Dressed-state qubit manipulation

The manipulation of the dressed state qubit follows the method of [38], where the second order shift in the eqs. (2.29)–(2.31) is taken into account. The procedure starts by initial-

isation of the ion in the state of $|0\rangle$, from which it is transferred to the state $|0'\rangle$ with the use of a π pulse at the frequency ω_0. The dressing fields are the turned on to form the dressed states. From this point, the excitations from the ground state $|0'\rangle$ are carried out by applying an RF field of frequency closely tuned to ω_+ or ω_- frequency. The interaction picture Hamiltonian after making the rotating wave approximation (RWA) has the form

$$\hat{H}_{RF} = \frac{\hbar\Omega_{RF}}{2}\left(|+1\rangle\langle 0'|\, e^{-i\Delta_+ t} + |-1\rangle\langle 0'|\, e^{i\Delta_- t} + h.c.\right), \tag{2.62}$$

where $\Delta_+ = \omega_{RF} - \omega_+$ and $\Delta_- = \omega_{RF} - \omega_-$. Rewriting equation 2.62 using the dressed state basis and moving to the interaction picture gives the Hamiltonian of the form

$$\begin{aligned}\hat{H}'_{RF} = &\frac{\hbar\Omega_{RF}}{2\sqrt{2}}(|D\rangle\langle 0'|\,(e^{-i\Delta_+ t} - e^{i\Delta_- t}) + h.c.)\\ &+ \frac{\hbar\Omega_{RF}}{4}(|u\rangle\langle 0'|\,(e^{-i(\Delta_+ - \frac{\Omega_{MW}}{\sqrt{2}})t} + e^{i(\Delta_- + \frac{\Omega_{MW}}{\sqrt{2}})t})\\ &+ |d\rangle\langle 0'|\,(e^{-i(\Delta_+ + \frac{\Omega_{MW}}{\sqrt{2}})t} + e^{i(\Delta_- - \frac{\Omega_{MW}}{\sqrt{2}})t}) + h.c.).\end{aligned} \tag{2.63}$$

The Hamiltonian can be used to drive transitions between the state $|0'\rangle$ and the dressed states $|D\rangle$,$|u\rangle$ and $|d\rangle$ by controlling the detunings Δ_+ and Δ_-. Setting $\Delta_+ = 0$ or $\Delta_- = 0$, the RF π pulse drives the transition to the $|D\rangle$ state, whereas setting $\Delta_+ = \Omega_{MW}/\sqrt{2}$ or $\Delta_- = -\Omega_{MW}/\sqrt{2}$ gives a transition between $|0'\rangle$ and $|u\rangle$ and with $\Delta_+ = -\Omega_{MW}/\sqrt{2}$ or $\Delta_- = +\Omega_{MW}/\sqrt{2}$ driving the transition $|0'\rangle \leftrightarrow |d\rangle$. The detection of population transfer to the dressed states is implemented by turning off the dressing fields and applying a π pulse on $|0\rangle \leftrightarrow |1\rangle$, same as in the dressed state initialisation. If any of the dressed states were populated, the pulse transfers the qubit state to the bare states in the ${}^2S_{1/2}, F = 1$ manifold, where the detection method described in section 2.9.1 will give a bright result. If the population is in $|0'\rangle$ state, the π pulse transfers the state to $|0\rangle$, which gives a dark result.

The dressed state manipulation scheme has shown significant improvement when compared to working with the bare state levels. Using the $|0'\rangle$ and $|D\rangle$ states as the qubit, the Hamiltonian is simplified to

$$\hat{H}'_{RF} = \frac{\hbar\Omega_{RF}}{2\sqrt{2}}(|D\rangle\langle 0'| + |0'\rangle\langle D|), \tag{2.64}$$

where the terms proportional to $\omega_+ - \omega_-$ where removed by constraining $\Omega_{RF} \ll \omega_+ - \omega_-$. Rabi oscillations of the two schemes are compared for long operation times, see fig. 2.26. It is clear that the amplitude of the dressed state oscillations show no significant

change, whereas in the case of the bare state qubit, a reduction in contrast is quickly noticeable. The measured coherence times are ≈700 ms and 2.2 ms respectively. The improved coherence makes the new qubit system an ideal system to be used for multi-qubit entangling gates.

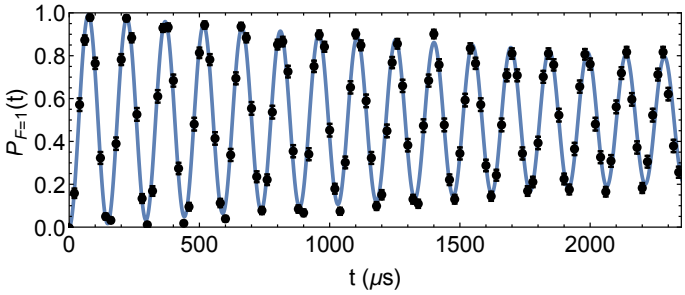

(a)

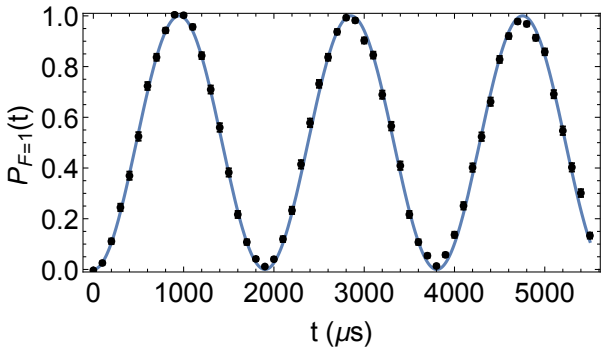

(b)

Figure 2.26: Rabi oscillations observed when using a resonant radiation field for the transitions (a) $|0\rangle \leftrightarrow |+1\rangle$, which is sensitive to magnetic field noise, and the dressed state qubit $|0'\rangle \leftrightarrow |D\rangle$ (b). The dressed state qubit case exhibitst no significant decay in the oscillation amplitude even after 5 ms, where the sensitive state amplitude diminishes after ≈0.5 ms. Obtained from [69].

2.10.3 Multi-qubit dressed state gates

A quantum computer must be able to perform logical operations on these qubits, similar to logic gates found in computational engineering. The first quantum gate for trapped ions was proposed by Cirac and Zoller [13] and experimentally observed with two ions by Schmidt-Kaler et al [110], with fidelities of 74%. The indication of a successful gates were parity oscillation measurements and quantum state tomography, which is a representation of the density matrix. The Cirac-Zoller gate relies on cooling the ion to its motional ground state using sideband cooling [111]. This makes the implementation of the gate particularly challenging.

To perform quantum gates with hot ions (motional state larger than n=0), Mølmer and Sørensen introduced a method of entangling ions, independent of their motional state [20], which was later expanded to performing logic gates [112]. The essence of the gate is coupling the two states of a two ion system with two fields with frequencies ω_1 and ω_2, where $\omega_1 = \omega_0 - \delta$ and $\omega_2 = \omega_0 + \delta$. The detuning, δ, has to be close, but not resonant with the motional mode of the two ion chain.

To demonstrate the viability of using the magnetic field gradient scheme, a high-fidelity two-qubit Mølmer-Sørensen was implemented using dressed states [39]. This section describes the theory behind the method and summarises the results. Furthermore, an optimum set of parameters is given for implementation using a surface ion trap.

2.11 Mølmer-Sørensen gates with a magnetic field gradient

The Hamiltonian of the two ion system placed in a magnetic field gradient can be written as a sum of three terms, which are

$$\hat{H}_{int} = \hbar \sum_{i=1,2} (-\omega_i^0 \left|0\right\rangle_i \left\langle 0\right|_i - \omega_i^- \left|-1\right\rangle_i \left\langle -1\right|_i + \omega_i^+ \left|+1\right\rangle_i \left\langle +1\right|_i) \tag{2.65}$$

$$\hat{H}_{mot} = \hbar\nu \hat{a}^\dagger \hat{a} \tag{2.66}$$

$$\hat{H}_{coupl} = \hbar \sum_{i=1,2} \nu\eta_i (\hat{a}^\dagger + \hat{a})\hat{\sigma}_{zi}. \tag{2.67}$$

$\hat{H}_{int}$ represents the internal energy states of the qubits (the zero point energy chosen as the $|0'\rangle$ state), which is different for the qubits due to the magnetic field gradient. The η_i term corresponds to the effective Lamb-Dicke parameter for each ion. The frequency shifts ω_i^- and ω_i^- have the same definition as in eqs. (2.29)–(2.31). The motional state term $\hat{H}_{mot}$

captures the contribution of the motional states to the total energy determined by the secular frequency ν. The possible motional modes were defined in section 2.2.2. The final term contains the spin-motion coupling, which is independent of the applied radiation, but is proportional to the effective Lamb-Dicke parameter η set by the magnetic field gradient. The Pauli matrix $\hat{\sigma}_{zi}$ represents the operation $|+\rangle_i \langle +|_i - |-1\rangle_i \langle -1|_i$.

As shown in the previous section, the dressed state qubit manipulation can be written using the Hamiltonian in eq. 2.64, which for two ions is

$$\hat{H}'_{RF} = \frac{\hbar\Omega_{RF}}{2\sqrt{2}}(|D\rangle_i \langle 0'|_i + |0'\rangle_i \langle D|_i), \tag{2.68}$$

where the indices correspond to ions 1 and 2. To implement the two qubit gate, the manipulation RF field frequency is set to be slightly detuned from the blue and red motional sidebands of the ions, which has the frequency $\omega_i^{RF} = \omega_i^+ \pm(\nu+\delta)$, where δ is the detuning. In this case equation 2.62 can be written as

$$\hat{H}_{RF} = \hbar\Omega_{RF} \sum_{i=1,2} (|+1\rangle_i \langle 0'|_i + |0'\rangle_i \langle +1|_i) \cos{(\nu+\delta)t}, \tag{2.69}$$

which can be rewritten using the Polaron transformation described in section 2.9.4, to obtain

$$\hat{H}^P_{RF} = \hbar\Omega_{RF}(|+1\rangle_i \langle 0'|_i e^{\eta_i(\hat{a}^\dagger - \hat{a})} + h.c.) \cos{(\nu+\delta)t}. \tag{2.70}$$

In the Lamb-Dicke regime, the term $e^{\eta_i(\hat{a}^\dagger - \hat{a})}$ can be expanded to first order. This allows the RF term to be written as

$$\begin{aligned}\hat{H}^P_{RF} = \Omega_{RF} \sum_{i=1,2} \eta_i \left[\frac{|u\rangle_i e^{i\Omega_{MW}/\sqrt{2}t} + |d\rangle_i e^{-i\Omega_{MW}/\sqrt{2}t}}{2} - \frac{|D\rangle_i}{\sqrt{2}}\right] \langle 0'|_i \\ \times (\hat{a}^\dagger e^{i\nu t} - \hat{a} e^{-i\nu t}) + h.c.) \cos{(\nu+\delta)t}.\end{aligned} \tag{2.71}$$

Making the assumption $\delta \ll \frac{\Omega_{MW}}{\sqrt{2}} \ll \nu$ and making the RWA, the RF term can be approximated to be equal to

$$\begin{aligned}\hat{H}_{MS} = &- \frac{\eta_1\Omega_0}{2}(|D\rangle_1 \langle 0'|_1 - |0'\rangle_1 \langle D|_1 \\ &- |D\rangle_2 \langle 0'|_2 + |0'\rangle_2 \langle D|_2)(\hat{a} e^{i\delta t} - \hat{a}^\dagger e^{-i\delta t}),\end{aligned} \tag{2.72}$$

which is the form of the Mølmer-Sørensen gate described in [20], with $\Omega_0 = \Omega_{RF}/\sqrt{2}$. By applying the gate for a time of $\tau = 2\pi/\delta$, where $\delta = 2\eta_1\Omega_0$, the different input qubit states

will undergo the transformations

$$\begin{aligned}
\left|0'\right\rangle\left|0'\right\rangle &\rightarrow \left(\left|0'\right\rangle\left|0'\right\rangle + i\left|D\right\rangle\left|D\right\rangle\right)/\sqrt{2} \\
\left|0'\right\rangle\left|D\right\rangle &\rightarrow \left(\left|0'\right\rangle\left|D\right\rangle + i\left|D\right\rangle\left|0'\right\rangle\right)/\sqrt{2} \\
\left|D\right\rangle\left|0'\right\rangle &\rightarrow \left(\left|0'\right\rangle\left|D\right\rangle - i\left|D\right\rangle\left|0'\right\rangle\right)/\sqrt{2} \\
\left|D\right\rangle\left|D\right\rangle &\rightarrow \left(\left|0'\right\rangle\left|0'\right\rangle - i\left|D\right\rangle\left|D\right\rangle\right)/\sqrt{2},
\end{aligned} \tag{2.73}$$

which result in obtaining maximally entangled Bell states.

Fig. 2.27a shows the successful implementation of this gate where the input states correspond to $\left|0'\right\rangle\left|0'\right\rangle$. Although the Mølmer-Sørensen gate does not require to have the ions occupying the lowest motional mode, the ions in the experiment are sideband cooled using a technique developed in [88]. To find the fidelity of the gate, parity oscillations were measured by applying a $\pi/2$ pulse after the gate with variable phase, with the result shown in fig. 2.27b. The fidelity was measured to be equal to 98.5(12)%, which is the highest reported for this particular scheme, but has room for improvement. This is detailed in the next section.

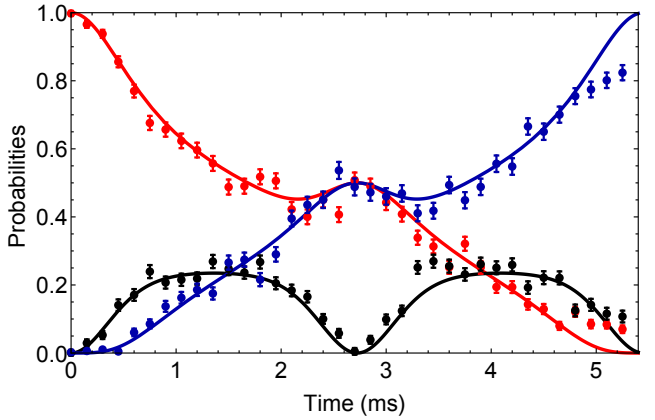

(a)

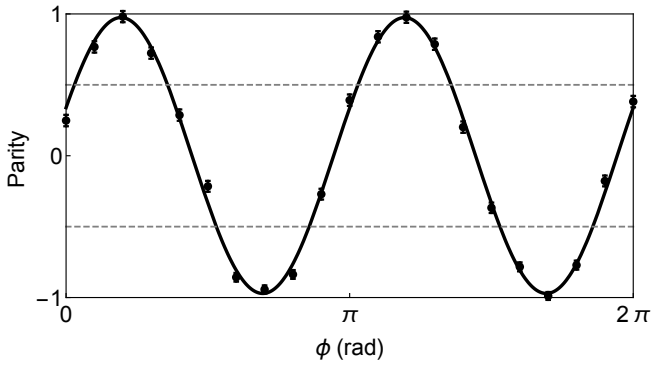

(b)

Figure 2.27: (a) The time evolution of the populations for different input states following equation 2.72. Red - $P(|0'\rangle\,|0'\rangle)$, blue - $P(|D\rangle\,|D'\rangle)$, black - $P(|0'\rangle\,|D\rangle) + P(|D\rangle\,|0\rangle)$. Gate duration corresponds to 2.7 ms. (b) Plot of parity $\Pi = P(|0'\rangle\,|0'\rangle) + P(|D\rangle\,|D\rangle) - P(|0'\rangle\,|D\rangle) - P(|D\rangle\,|0'\rangle)$, where a $\pi/2$ pulse is applied to each ion after the gate time τ with a phase ϕ. Adapted from [39].

2.12 Fault-tolerant two qubit gates

Despite the tremendous progress in ion trapping technologies, the fidelities of the discussed above quantum operations still have room for improvement with the ultimate goal to reach fault-tolerant operation. Furthermore, in order to address the scalability criteria, these gates need to be implemented on a microfabricated surface ion trap, which requires balancing of competing parameters such as secular frequencies and the anomalous heating rate. Therefore a detailed analysis of various parameters determining the final gate fidelity using a magnetic field gradient was carried out by Dr. David Murgia [67]. The obtained parameters are expected to improve the gate fidelity to a value of >99%. This section gives a brief description of these parameters and the experimental requirements.

2.12.1 Gate error infidelities

The fidelity of a two-qubit gate is determined by the stability and robustness of the experimental system and the fundamental limitations of the ion trap system. The former can be controlled externally with active feedback systems, therefore it is assumed that the contributions can be minimised to an insignificant level. The main three sources of error that contribute to the gate infidelity are identified as the heating of the motional mode, off-resonant coupling to the carrier transition, and decoherence of the dressed-state qubit. The estimates for these terms were calculated for the axial stretch mode of motion and the dressed state qubit comprised of states $|0'\rangle$ and $|D\rangle$. Summing all the error terms and subtracting from the value of 1, provides the measure for the total infidelity.

The error due to heating of the axial stretch mode is given by [112]

$$E_{heat} = \frac{5}{8} - \frac{1}{2}\exp\left(-\frac{-2\frac{\mathrm{d}\overline{n}}{\mathrm{d}t}\tau}{4}\right) - \frac{1}{8}\exp\left(-\frac{-8\frac{\mathrm{d}\overline{n}}{\mathrm{d}t}\tau}{4}\right), \tag{2.74}$$

where the term $\frac{\mathrm{d}\overline{n}}{\mathrm{d}t}$ is the motional heating rate and τ is the duration of the gate operation. In order to keep this error small, the product of both terms must be minimised.

The off-resonant coupling to the carrier transition is a consequence of the motional sidebands being separated from the carrier by the frequency of the axial modes, which is on the order of a few hundred kilohertz. As indicated in fig. 2.24, a non zero detuning from the resonant case will drive the carrier and cause decoherence in the system. The contribution to the gate error is given by [69]

$$E_{orc} = 4\left(\frac{\Omega_{RF}}{\nu + \delta}\right)^2, \tag{2.75}$$

where ν is the secular frequency and δ is the detuning. In order to keep the coupling small, the optimisation of the ratio corresponds to driving the RF transitions with a reduced Rabi frequency, which implies longer gate time τ. This is in competition with the heating rate in equation 2.74, which complicates the task of optimisation. However, pulse shaping techniques can be used for the gate fields, which minimise the off-resonant coupling significantly [39].

The final error term is the decoherence of the dressed state qubit, which requires the having the coherence time of the qubit (t_{coh}) being significantly longer than the gate time

τ. The estimation of these parameters was carried out in [69], which results in the equation

$$E_{coh} = 0.7222 \left[1 - \exp\left(-\frac{0.46\pi\tau}{t_{coh}}\right)\right]. \tag{2.76}$$

The equations for all the error terms indicate overlapping parameters, with the main factor being the gate time τ. In order to minimise the duration of the gate, the trapped ion heating rate must be reduced, while providing a large Lamb-Dicke parameter and Rabi frequencies.

2.12.2 Ion heating rate optimisation for surface ion traps

The key parameter limiting the fidelity of the quantum operations, is the trapped ion heating rate described in section 2.3.1. The heating rate can be minimised using various in-situ cleaning methods, however with unpredictable success. Instead, a guaranteed improvement of the heating rates can be achieved by cooling of the trap electrodes. In the work of [67], the heating rate was estimated to be minimised by a factor of 10 by operating the ion trap module at temperatures of 70 K to 100 K. To reach these temperatures a cooling system is required to keep the heating rate as small as possible. Implementing such cooling will therefore be a focus in this thesis.

2.12.3 Magnetic field gradient optimisation

The balancing of multiple different parameters can be quite complex, however one of the key parameters determining the dynamics of the entanglement gate, is the strength of the magnetic field gradient. The magnitude of the gradient controls the effective Lamb-Dicke parameter in equation 2.55, which determines the strength of internal-motional state coupling. Ideally, the effective Lamb-Dicke parameter is increased to values at least the same order as in the case where optical radiation is used. The design and incorporation of a static magnetic field gradient into a surface ion trap is described in the later chapters.

2.12.4 Secular frequency optimisation

The error terms in the previous section indicated that a large secular frequency will minimise the off-resonant coupling and heating, however at the same time compromising the effective Lamb-Dicke parameter, which increase the gate duration τ. Therefore, it is expected that the optimisation of the secular frequency will be an iterative process. To have a wide range of available secular frequencies, the ion trap system must be able to achieve axial secular frequencies of $\approx$1 MHz. This parameter is controlled by the trap geometry

an applied voltage as indicated in equation 2.4. The most optimum frequency will be determined once the heating rate is known.

2.12.5 Motional and Rabi frequency stabilisation

So far the gate errors did not account for the general drift of various experimental parameters such as secular frequencies of the ion motion, the frequency and intensity of the preparation and detection laser, and microwave and RF power. All of these systems are susceptible to the fluctuations in the surrounding environment, whose effect can be minimised with passive and active stabilisation systems. In order to keep the contribution to the gate error small, the stabilisation of the microwave and RF parameters must achieve stability of 10 ppb. The active stabilisation of the laser parameters is detailed in chapter 3.

2.13 Conclusion

This chapter described the requirements for trapping Yb ions on a microfabricated surface ion trap and using them as qubits to implement high fidelity multi-qubit gate operations. The qubit states are addressed using RF radiation, which requires a large magnetic field gradient in order to obtain a sizeable Lamb-Dicke parameter responsible for the spin-motion coupling strength. In addition to this, the use of a novel qubit system is described, which is significantly more robust to ambient magnetic field fluctuations. In order to achieve fault-tolerant multi-qubit gates, several different parameters require improving. With these requirements in mind, the following chapters detail the experimental systems designed, assembled and used for this task.

Chapter 3

Versatile laser locking setup for Yb and Ba ions

3.1 Introduction

As described in chapter 2, Doppler cooling and qubit state preparation and detection relies on the use of lasers. To perform a long term experiment the laser frequency needs to be stable within an order of magnitude lower than the linewidth of the addressed transition, which in the case of the $^2S_{1/2} \leftrightarrow {}^2P_{1/2}$ an Yb^+ ion is 19.6 MHz [95]. This minimises the detection error when reading out the qubit state between 'bright' and 'dark'. Owing to the fluctuating environment, free running lasers are not well suited for this task, therefore feedback systems are used to correct the frequency of the laser compared to a stable reference [113, 114]. The choice of a stable reference determines the complexity and the final achievable stability and robustness of the laser control system. This chapter covers the basics of active feedback and the stable references that are used in the research group with a discussion regarding the electronic feedback systems.

3.2 Introduction to stabilisation

The methods and techniques used in laser stabilisation systems were established in the field of control theory [115], with the primary aim of optimising the behaviour of a system. The general techniques and methods applied in control theory can also be implemented in other parameter control schemes. Throughout this thesis, the electronic systems developed for laser frequency stabilisation were also applied to stabilise the temperature of sensitive devices, minimise power and voltage fluctuations applied to an ion trap and other precision

demanding tasks.

3.2.1 Block diagram basics

Any device of interest can be represented as a black box, with inputs and outputs and its operation in theory can be simplified to an equation. To circumvent any confusion, a graphical picture is often used in control theory to describe a complicated system - this method is known as the block diagram [116] representation. An example of one such system can be seen in fig. 3.1. The physical origins of x, y and G need not be well defined, but for simplicity they will describe the electronic signals and circuits. These

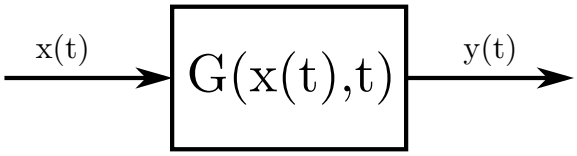

Figure 3.1: An example of a graphical representation of a device with input *x(t)*, the operation of the device *G(x(t),t)* and the output *y(t)*.

blocks will be used later in the chapter to easily visualise electronic feedback systems. Multi-instrument systems can then be described by linking up different blocks with lines denoting the direction of flow of the signals or information. The object of interest in these systems is then the final output, which can be disturbed by interference with other signals or the environment the setup is placed in.

3.2.2 Passive stabilisation

Block diagrams are generally used to describe active components of a system, sometimes neglecting the interaction with the environment. To counteract temperature drifts and acoustic perturbations, the most sensitive components can be isolated by placing them in an enclosure. The same enclosure can be evacuated to reduce the presence of convection or thermally isolated to reduce heat exchange. In this thesis, enclosures were used to isolate optical and electronic setups from external lighting, electromagnetic radiation and the general acoustic noise of the lab. However, when dealing with critical parameters such as laser frequency, the preferred method of stabilisation is by the use of active components which offer near-instantaneous monitoring of a parameter with the ability to correct for fast perturbations.

3.2.3 Active stabilisation

In describing an actively stabilised system, it is important to establish what stability is needed and the limitations of the instruments and control devices that are going to be used. Active stabilisation refers to monitoring the parameter of interest and correcting for any perturbation, shown in block diagram form in fig. 3.2. It is clear from the figure that

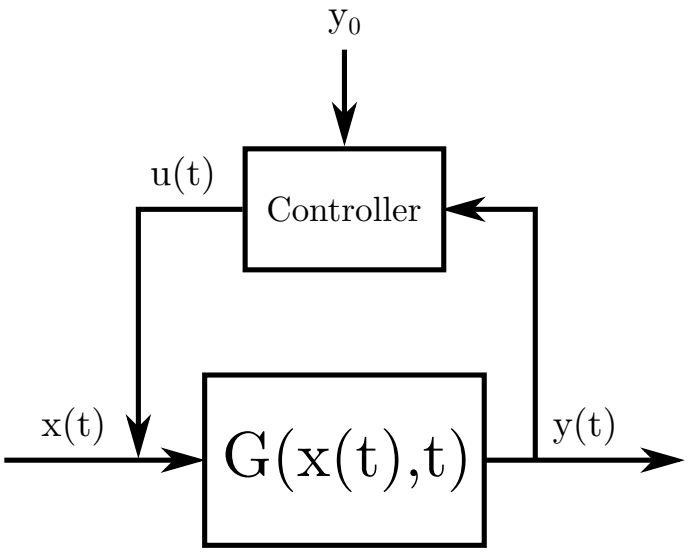

Figure 3.2: A simplified block diagram of a generic active stabilisation system.

the signal flows in a loop, consequently these systems may also be referred to as feedback loops. In this example, the controller functions as both the device which compares the output $y(t)$ to some desired output y_0, and processes an appropriate control signal $u(t)$, which is summed with the input $x(t)$. The function of comparing the output to the set point and generating the control signal are often significantly distinct and are represented by individual blocks, and will be described in the sections to follow.

3.2.4 Reference and error signal

In the previous section the desired output was called y_0, but it can also be known as a reference or set point. Comparing the parameter of interest with this reference will provide a measure of accuracy and stability, which is called the error signal $e(t)$. A correct error signal provides knowledge not only of how far off the controlled parameter is, but also the sign of the error indicates the direction of drift from the reference. An example of a general error signal is given in figure 3.3, with the main interest being the slope at the centre point. The requirements for an error signal are quite intuitive. In the presence of small perturbations, a larger gradient at the zero point will correspond to a bigger voltage swing, which is easier to compensate. Secondly, the extent of the linear region of the error

signal indicates the capture range of the control system - any kick to the system within this range can be corrected for by feedback.

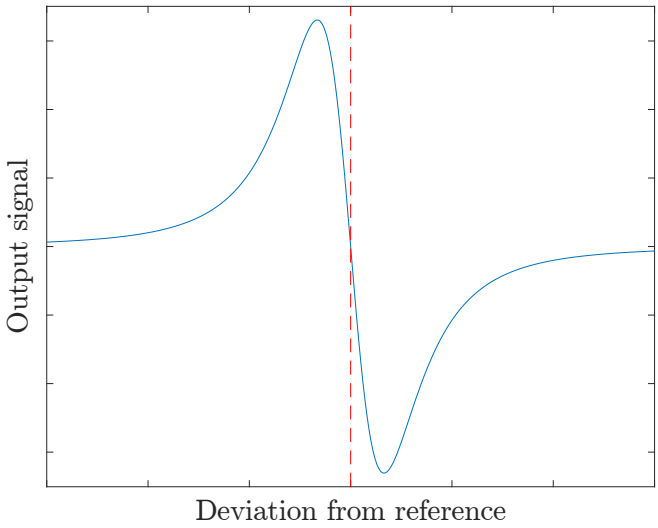

Figure 3.3: An example of an error signal, the red line denoting the zero deviation point. Any deviation from the reference will make the output signal increase, with the sign of the output signal indicating the direction of change. This can be used to correct for any drift or instantaneous jump of the output signal. Almost all error signals can be approximated to be a dispersion type signal, which for this particular example is a derivative of a Lorentzian function.

In addition to this, the more stable and less susceptible to noise it is, the more accurate control of a parameter. Later sections will discuss this particular point for laser frequency stabilisation with the detailed description of generating error signals from different references.

3.2.5 PID control

Once an error signal is obtained, the control of a parameter is implemented by inverting the error and manipulating it with a PID (proportional-integral-derivative) controller. The operation of PID controllers can be expressed using a block diagram as in figure 3.4. The purpose of the proportional controller is to correct the instantaneous offsets from the reference, whereas the integral and derivative arms process the past and future changes of the system, respectively. The amplitude of each contribution is defined by the three coefficients K_P, K_I and K_D. All of the systems used in the lab rely mostly on the proportional and integral arms of the controllers (PI controllers) for long term stability, with the derivative arm not included or set to zero. The derivative control function is primarily used for linewidth reduction, which in this case was not the main objective. The

reason for not including the derivative function is the fact that derivative control is prone to producing large voltage swings when the instrument experiences fast perturbations, which if not treated carefully can damage the device.

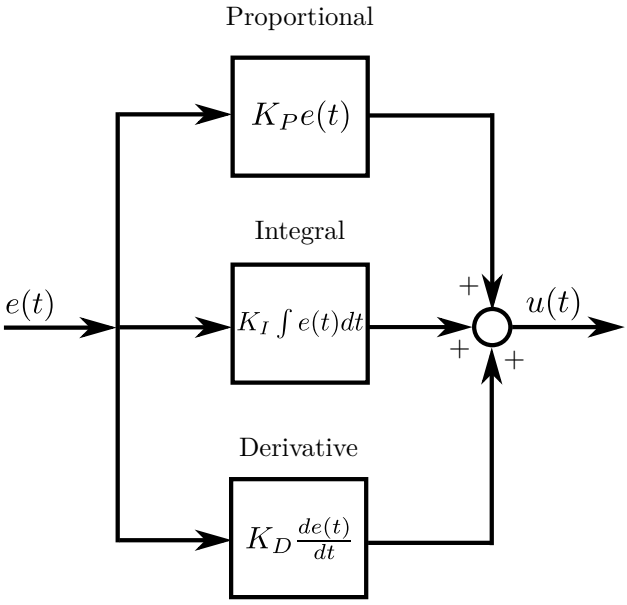

Figure 3.4: Block diagram detailing the operation of a PID controller. The coefficients K_P, K_I and K_D can be tuned to obtain an optimal control signal $u(t)$.

The physical implementation of a PID controller can be performed by using either analogue or digital electronic circuits. The choice of which is preferable depends on the required performance of the system, the degree of necessary customisability and the noise performance of the controller. During the work carried out, multiple different setups were used and their performance will be described in later sections.

3.2.6 Stability analysis and the Allan deviation

Once a device is stabilised, the performance of the controlling circuit is evaluated by collecting measurements over the course of multiple days. Instinctively, the figure of merit for a device would be the variance or the standard deviation ,σ_{S}, from the mean, but this single number gives little information. Over large averaging times most errors due to the fast noise get averaged out, leaving the error miniscule. Because of this, the Allan variance and deviation σ_{y}, routinely encountered in clock analysis, is used to describe their performance. When analysing the frequency of oscillations the standard measurement choice is the fractional frequency difference, which is the ratio of the absolute frequency fluctuations of the oscillator relative to the reference frequency. The calculation of the error can be simplified and described in a single equation, but for stability analysis a more

detailed description is given in [117]. The Allan Deviation has the advantage of looking into neighbour to neighbour differences on different timescales in an array of number of samples of the fractional frequency difference between two oscillators. To calculate the Allan Deviation $\sigma_{\mathrm{y}}(\tau)$ of a set of M number of samples of a measurement y with a sampling time of τ, the nearest neighbours (y_1 and y_2, y_2 and y_3, ...) are subtracted, squared and summed, as in equation 3.1.

$$\sigma_y(\tau) = \sqrt{\frac{1}{2(M-1)} \sum_{i=1}^{M-1} (y_{i+1} - y_i)^2}. \tag{3.1}$$

The obtained Allan deviation value is for a sampling time τ, in order to look into how the system behaves if sampled less frequently, the original array can be revised for longer sampling times. To do this, we take the original measurement of y and, in order to calculate the Allan Deviation for a sampling time of 2τ, average the value of y_1 and y_2 and assign it as the new y_1. Then we repeat this grouping and averaging for the rest of the array of samples, in the end obtaining a set of half the size of the original one with a sampling time of 2τ. The calculation is finished by using eq. 3.1 on the new set. The calculations for longer sample times follow the same procedure, with the general sampling time limit chosen to be $(M/3)\tau$, due to the fact that a revised array of three samples is the minimum acceptable number for representing a stability measurement.

The calculated Allan deviation data is typically plotted as a function of sampling time on a logarithmic scale. Fig. 3.5 shows an example of the Allan deviation containing distinct characteristics which can be used as a guide when optimising the stability of a controlled parameter. One of these is the presence of pronounced dips in the deviation whenever a harmonic oscillation of a particular frequency is present in the data, or an increased error for longer sampling times indicating a slow drift.

In order to calculate the Allan deviation of an optical frequency, the frequency fluctuations of a light beam must be converted to something which can be easily measured using modern electronics. For optical radiation, devices based on interferometry are used to obtain a signal proportional to the frequency difference from a reference. The different available references are detailed in the following section.

3.3 Optical references

The fast oscillations of optical radiation cannot be measured with modern day electronics, as such the laser light of interest needs to be processed with a frequency discriminator.

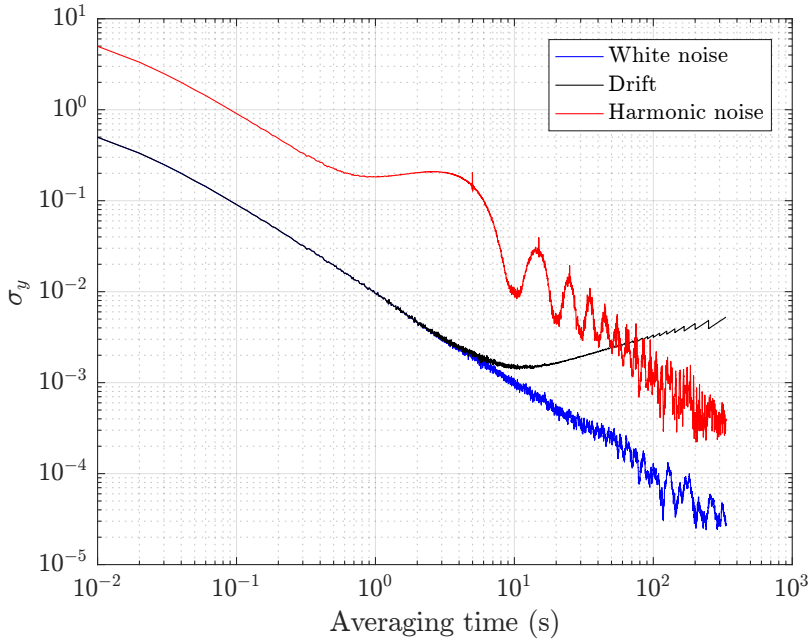

Figure 3.5: Example of an Allan deviation plot. The blue line corresponds to a measurement of a DC signal with white noise superposed on it, which is averaged out for longer times. This explains why the deviation gets smaller for long times. Introducing a drift to the signal produces a rising tail in the black line, which is the main target when optimising frequency drift. The red signals is an amplified white noise signal and summed with a low frequency sinusoidal signal. This results in multiple dips at the tail, where the averaging time corresponds to multiples of the period of the oscillation. The performance of a feedback system can be improved by plotting the Allan deviation and finding the type of noise that needs eliminating, ideally reaching the white noise profile.

The purpose of such a device is to permit and maintain a discrete oscillation frequency and dampen any other. Over the history of laser technology development, multiple different discriminators have been developed, each providing a distinct advantage. The unifying factor in all frequency references is the Lorentzian lineshape of a small width and ideally stable over long times. The choice of which to use depends on the requirements of the experiment, which might be the required accuracy, stability, robustness and in recent applications, the ability to be compact and portable. This section covers the four types and properties of available optical frequency references for Yb ion trap experiments, the optical resonator, spectroscopic references, highly stable laser and a wavemeter.

Optical resonators

The earliest adoption of a frequency discriminator [118] is the optical counterpart to an electronic resonator, a device whose resonance frequency is determined by its configuration. In the optical domain, resonance can be observed by making a beam of light traverse a

closed path imposed by highly reflective mirrors. The simplest implementation of an optical resonator is the Fabry-Perot cavity, which is a pair of parallel planar mirrors separated by a certain distance L (see fig. 3.6). To form any optical cavity, the mirrors do not need to be planar, and most real world optical resonators contain mirrors with a curvature of a certain radius. In the example, a monochromatic beam is reflected back and forward by highly reflecting mirrors, completing a round trip of distance $2L$. The propagating beam of frequency $\nu = \omega/2\pi$ can be described by the wave function $Ae^{i(kz-\omega t)}$, where A is the amplitude of the wave, $k = 2\pi\nu/c$ is the wavenumber with c corresponding to the speed of light in the medium. Every $2L$ distance travelled, the beam returns to its starting point, where the beam will have a phase shift in the exponential component compared to the initial wave. The phase shift of a single round trip is $\varphi = 2kL = 4\pi\nu L/c$, from which it is clear that in the case of the phase shift being equal to $2\pi n$ for n number of round trips, the multiple waves will add up in phase. The accumulation of these reflected waves will increase the amplitude of the oscillation within the resonator. Equating the phase shift to multiples of 2π, the resonant frequency can be calculated as

$$\nu_n = n\frac{c}{2L}. \tag{3.2}$$

The resonant frequencies are separated by a frequency difference of

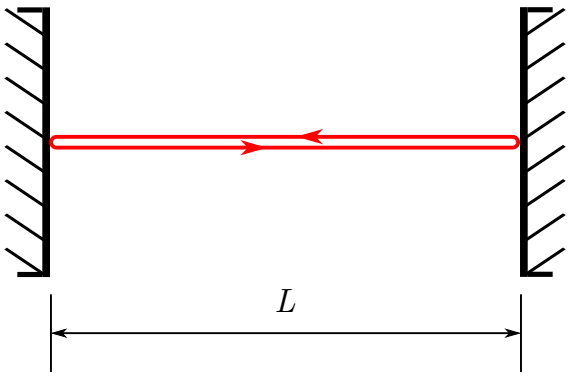

Figure 3.6: An example of a Fabry-Perot resonator formed with a pair of mirrors separated by a distance of L. A beam of light within the resonator will traverse back and forth between the mirrors and will interfere with itself. For a fixed L, the interference will be either constructive or destructive depending on the frequency of the beam. The constructive interference frequency is given by equation 3.2.

$$\nu_F = \frac{c}{2L} \tag{3.3}$$

which is called the free spectral range. This selectivity of frequencies is the basis of optical resonators as references and etalons. The on-resonance beam within the cavity can also be called a cavity or resonator mode, with the condition that every round trip the wave function of the beam recreates itself. The modes separated by the free spectral range are called longitudinal modes of the cavity.

As in electronic circuits, the damping of the oscillations introduces additional phase shifts and attenuation in the signal. For the Fabry-Perot cavity, this is caused by having slightly absorptive mirrors. Assuming both mirrors have the same reflectivity of r, the round trip introduces a multiplicative factor of $re^{-i\varphi}$ in the reflected wave. Summing up these reflected waves results in a geometric series where each element is reduced successively by the non-ideal reflection. The field intensity in the cavity is then given by [119]:

$$I = \frac{A^2/(1-r^2)}{1 + (2\mathcal{F}/\pi)^2 \sin^2(\pi\nu/\nu_f)} \tag{3.4}$$

with the factor $\mathcal{F}$ called finesse, given by

$$\mathcal{F} = \frac{\pi\sqrt{r}}{1-r}. \tag{3.5}$$

The finesse of a Fabry-Perot cavity is used to describe the quality of the resonator. A quality factor Q can be used to describe optical cavities, but it has a dependence on the frequency of the photons, achieving large values for microwaves and therefore the finesse is typically used. Having non-ideal mirrors allows the built up beam to escape, which can then be measured using a photodetector. By sweeping the frequency of the beam, it is possible to observe resonance at the frequencies given by eq. 3.2. The effect of the finesse then can be seen in fig. 3.7. The linewidth δ of these resonances can be calculated from eq. 3.4 by finding the frequencies at which the intensity is halved from the maximum (FWHM) and subtracting them, which gives the relation

$$\delta\nu \approx \frac{\nu_F}{\mathcal{F}}. \tag{3.6}$$

Equations 3.3, 3.5 and 3.6 describe the performance of an optical cavity as a frequency discriminator. From these parameters it is clear that the main interest in designing an optical resonator is to increase the mirror reflectivity, which permit resonant frequencies with lower linewidths. A narrower linewidth resonator provides the ability to reduce the linewidth of the input laser by using the cavity as an optical filter.

In designing real optical resonators, planar mirrors are rarely used, due to the required

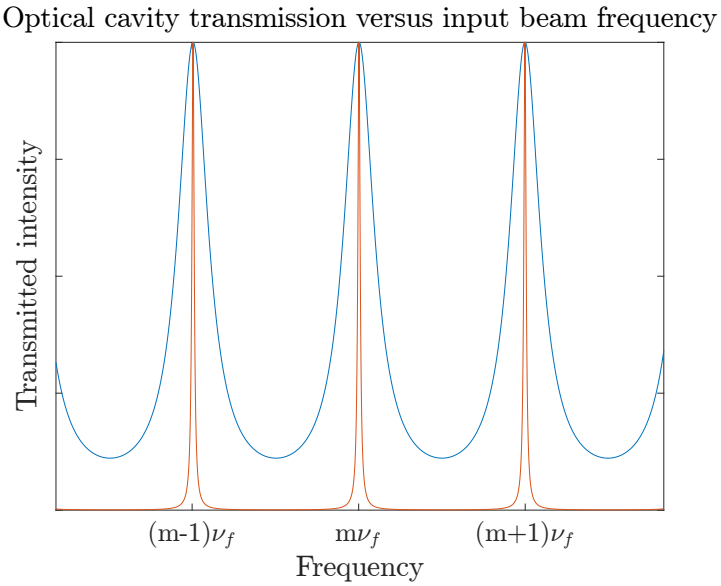

Figure 3.7: The transmission of the input beam when the frequency is swept for different values of finesse (blue - 4, red - 60). The relative height of the peaks is not drawn to scale due to the lower finesse not allowing to build up as much power within the cavity.

precision of aligning the input beam and having the mirrors parallel to each other. The requirements are relaxed by using concave mirrors as shown in fig. 3.8, where the second mirror has a focusing effect on the beam, guiding it on to the optical axis. Even if the beam enters the cavity off-axis, the concave mirror directs the beam towards the centre, in such a way that the beam can return to the initial point to complete a full round trip.

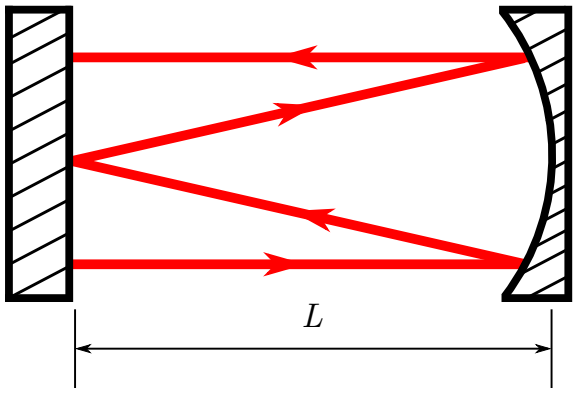

Figure 3.8: An optical cavity with a planar and concave mirror of radius $R > L$.

By monitoring the beam leaking out of the cavity, frequency fluctuations of the input beam result in a change in intensity, which is the basis of laser frequency stabilisation with optical resonators. Using a photodetector the intensity is converted to a voltage, which can be fed into a PID controller. By using the halfway point of one of the peaks, the fluctuations from this point will have a negative or positive sign, depending on the

direction of the drift. This method of stabilisation is known as the side-of-fringe lock and is the easiest implementation of a laser frequency lock [120]. The drawback of using the side-of-fringe method is the measurement of the DC intensity of the beam, which is susceptible to intensity fluctuations of the input beam. Furthermore, most electronic circuits exhibit flicker noise, which has a frequency dependence of $1/f$ [121], leading to a reduced signal to noise ratio.

Alternatively, there are other methods of generating an error signal from an optical resonator. By introducing a small amplitude sinusoidal modulation on the frequency of the laser, the peak intensity undergoes small oscillations of the same frequency but different phase, depending on which side of the peak the laser frequency is set to. This change of phase can be converted to a voltage by mixing the photodiode signal with the modulation signal to obtain an error signal [83]. For relatively slow modulation (< 1 MHz), a lock-in amplifier is used to process the photodiode signal. The added benefit of using a modulation is the increase of the signal to noise ratio due to only extracting the error signal from a single frequency signal instead of looking at the full spectrum of the output signal of the photodiode. Although the modulation technique provides a significant improvement, the bandwidth is fundamentally limited by relying on the leakage beam, which takes time to build up a detectable amount of power.

A solution to this is to monitor the reflected input beam, where on resonance the photodetector would see a reduction in intensity. The reflected input beam can be picked off by using a polarising beam splitter or introducing a glass plate at an angle leading up to the cavity. The reflected light in general will contain the promptly reflected and leakage beams. The scheme in this case is known as the Pound-Drever-Hall method (PDH) [122]. The modulation frequency in the PDH method is larger than the linewidth of the modulated laser (typically > 1 MHz), in which case the spectrum of the laser beam contains additional sidebands separated from the carrier by the modulation frequency, see fig. 3.9. When the carrier is on resonance it vanishes, whereas the off-resonant sidebands do not. The leakage beam is the phase inverted carrier which is then mixed with the reflected sidebands to produce a beat signal at the modulation frequency. This beat signal will be in phase or out of phase with the modulating signal depending on which side of the resonance peak the laser frequency sits. By converting this phase difference to a voltage, an error signal can be generated for laser frequency stabilisation. An example of such an error signal can be seen in fig. 3.10.

The light beam was considered to be a simple ray of light, however laser beams have

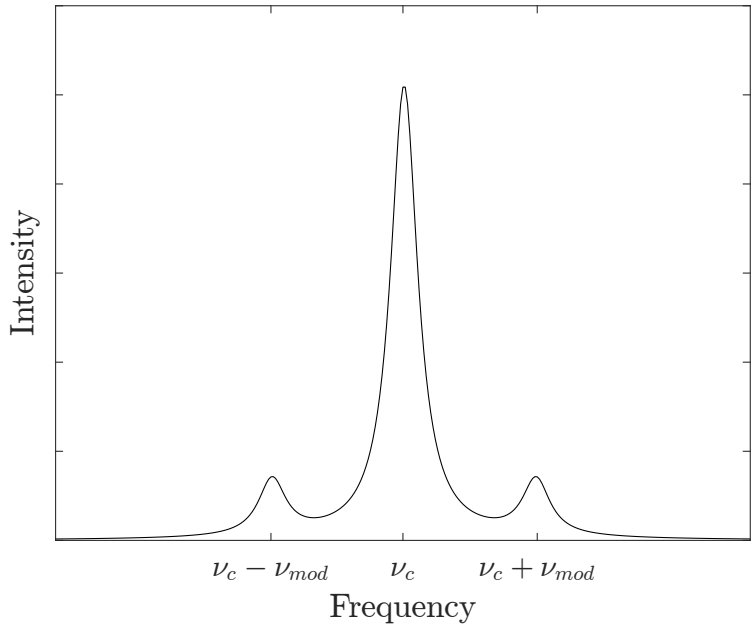

Figure 3.9: The spectrum of a laser of carrier frequency ν_c modulated with a frequency of ν_{mod}.

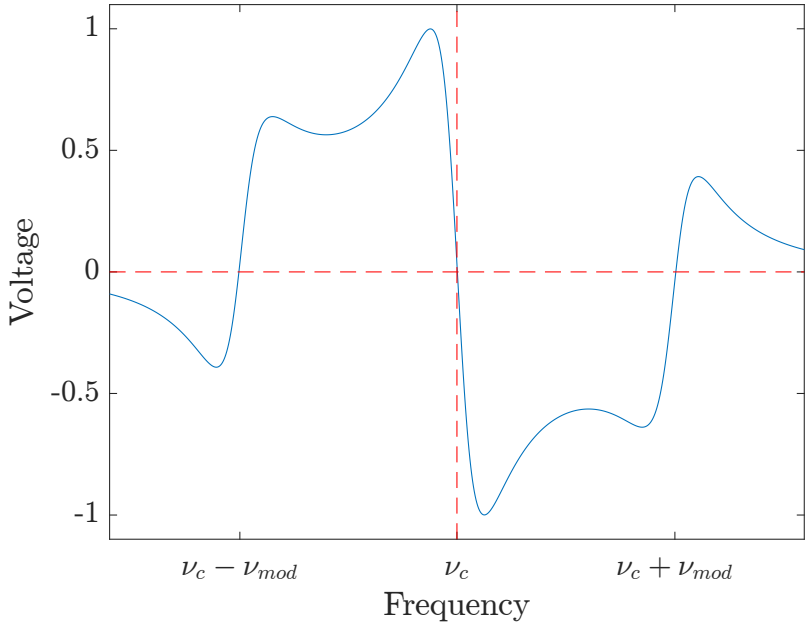

Figure 3.10: The error signal obtained using the Pound-Drever-Hall scheme. Note that the gradient of the signal at the centre point (ν_c) has an opposite sign compared to the sidebands.

a Gaussian intensity distribution which has implications on the performance of optical resonators. The wave front of a Gaussian beam has a curvature instead of the ideal case of

behaving as a planar wave with each wave front having a flat intensity distribution. When launching the beam into the cavity, if the curvature of the wave front is not matched to the curvature of the mirror used, there will be additional modes present in the cavity spectrum, called the transverse cavity modes or Hermite-Gaussian modes [119]. The presence of these modes is reduced by using optical elements such as telescopes to tailor the beam profile and curvature to match with the cavity permitted modes. As these modes tend to build up less energy within the cavity compared to the fundamental, they are not used in laser stabilisation.

Despite the optical cavity being a simple concept, the implementation is still a challenge in engineering. This is due to stringent constraints on the cavity length, which for a cavity length of 10 cm stabilising a 739 nm wavelength to a long term stability of 1 MHz corresponds to length stability of less than 25 nm. Therefore most optical cavities rely on using robust exotic materials to set the cavity length. At the same time, it is advantageous to have the ability to change the cavity length, such that when the laser frequency is set the cavity is tuned into resonance. The balance of these two requirements is not an easy task, with significant time devoted to isolating the cavity from the noisy environment. Nonetheless, the optical cavity is the most common method to stabilise a laser frequency due to its simple design and the ability to be used for any wavelength within the visible and infrared range. Therefore, they were frequently used in the work described in this thesis. For wavelengths bellow 400 nm, the versatility of the cavity is limited by the mirror substrate and coating, which are highly absorptive for UV wavelengths and thus do not obtain high values of finesse. However, most UV light lasers rely on frequency doubling from a red laser, which can be used to for stabilisation instead.

Spectroscopic references

In atomic, molecular and optical physics research, the use of ECDL lasers is widespread, as they offer highly stable, widely tunable and narrow linewidth sources of coherent light [123]. The latter property has greatly alleviated the requirements in probing optical transitions in atoms or molecules producing a spectrum for a particular element. The same techniques that are used to gain insight into the spectrum of a sample can be exploited in laser stabilisation, by probing a gas or vapour with a narrow linewidth laser [124]. A typical spectroscopy setup will be based on the basic schematic of fig. 3.11. Since the main wavelength of interest is the 369 nm Doppler cooling transition, metal-vapour discharge lamps could be used to extract absorption lines [125, 126]. In these devices Yb

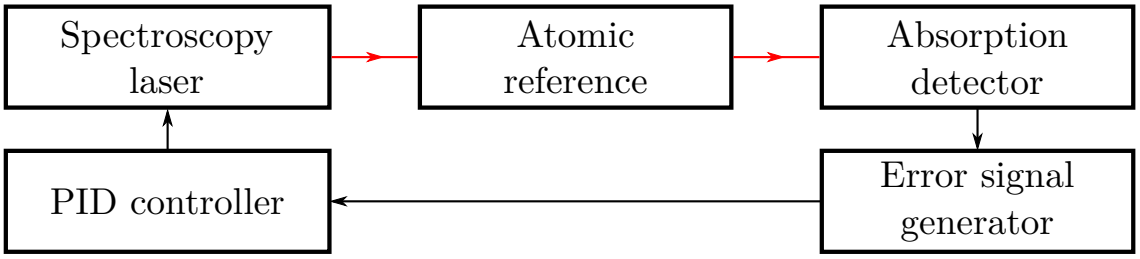

Figure 3.11: A block diagram for a spectroscopic stabilisation scheme.

ions are produced by bombarding a sample of Yb with a plasma. It would seem that this would be the best method of obtaining a stable reference, however the discharge lamps have significant cost, are prone to being sensitive to magnetic field fluctuations and have unpredictable lifetimes. Therefore most spectroscopic stabilisation setups use well established vapour cells frequently encountered in cold atom experiments, including I, Rb, K, Cs and Na, with transition linewidths on the scale of a few megahertz. The drawback of using these transitions is that they are in the visible range, far away from the UV area of interest. As a result, these systems rely on having a laser of the correct wavelength and incorporating optical cavities to mediate the stability of a reference to a separate laser.

There are two methods of generating the error signal for the spectroscopy laser (laser addressing the atomic transition), one relies on selectively exciting the zero-velocity atoms while the other is based on balancing polarisation dependent photon absorption.

The first method is called saturated absorption spectroscopy [127, 128, 129] whose example implementation can be seen in fig. 3.12. The thermal motion of the atoms inside the vapour cell, which has a Boltzmann distribution, can significantly broaden the absorption spectrum of gases. In typical cases this corresponds to increasing the width of the transition to $\approx$0.5 GHz. To reduce this effect, it is possible to excite atoms which do not have a velocity component in the laser beams reference frame, which results in lineshapes which are not Doppler broadened. This is achieved by using two counter-propagating beams, called the pump and the probe. The purpose of the higher power pump beam is to significantly depopulate the atoms from their ground state to one of the metastable hyperfine transition states, while the probe is used to sample how many atoms are still present in the ground state. Therefore only the probe absorption is monitored. By having the beams counter-propagate, there is a Doppler-shift in the reference frame of the atoms in the vapour cell, such that when the frequency of the laser is detuned from

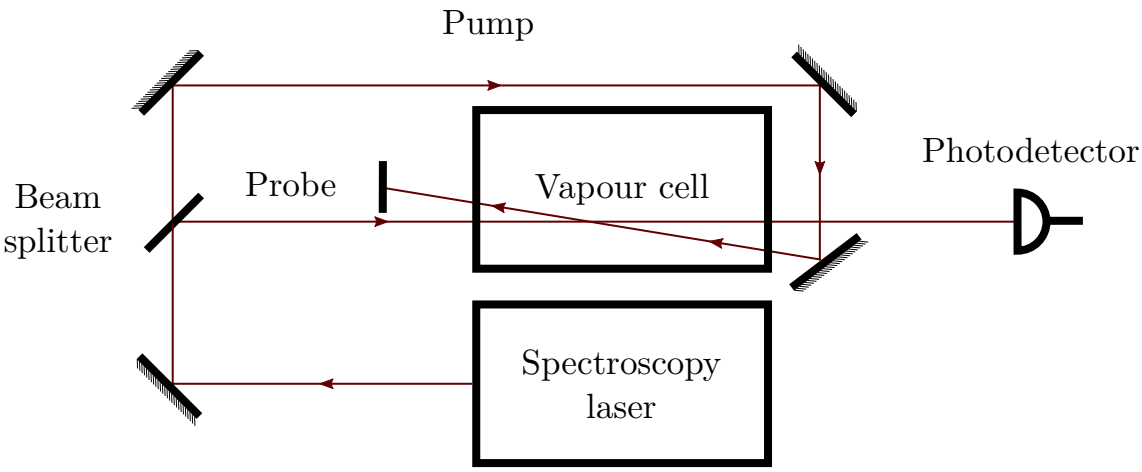

Figure 3.12: The optical assembly for performing Doppler-free saturation absorption spectroscopy. The laser beam is split unevenly into the pump and probe components, which are overlapped inside the vapour cell. A photodetector is used to measure absorption of the probe beam photons, which manifests as a decrease in the measured intensity.

resonance, the pump will excite atoms with a velocity of $-v$, while the probe will sample atoms of $+v$. Since both beams address different velocity atoms in the gas, the probe will indicate absorption by showing a decrease in intensity. If the laser was tuned closer to resonance, the probe starts showing and increase in intensity, which can only mean that there are less atoms in the ground state to absorb the probe photons. This corresponds to the pump exciting the same velocity atoms as the probe, which can only result if there is no Doppler shift. The spectrum of the vapour then contains the superimposed resonant excitations. In the case of generating an error signal from saturation absorption spectroscopy, a modulation and demodulation scheme is required to obtain the error signal, which increases the footprint of the electronic setup. Despite this, the error signal obtained from a modulated absorption spectroscopy scheme has the largest achievable gradient out of the two spectroscopic schemes, which is desirable when trying to achieve the most accurate laser frequency.

The second scheme commonly encountered is the Dichroic-Atomic-Vapour Laser Lock scheme (DAVLL) [130, 131]. An example of this type of setup can be seen in fig. 3.13. The setup relies on the use of an offset magnetic field, B, lifting the degeneracy of the magnetically sensitive Zeeman states (fig. 3.14a) by a frequency splitting given by $\delta_Z = \mu \Delta m_f B$, where μ is the magnetic dipole moment and the Δm_f is the difference in the projected angular momentum of the electron relative to the quantization axis. Governed by selection rules [127], $m_f = +1$ and $m_f = -1$ can only be populated with the circular σ^+ and σ^- polarisation respectively. By setting the interrogation beam to have a linear π polarisation, which is an equal superposition of σ^+ and σ^- , and sending the beam

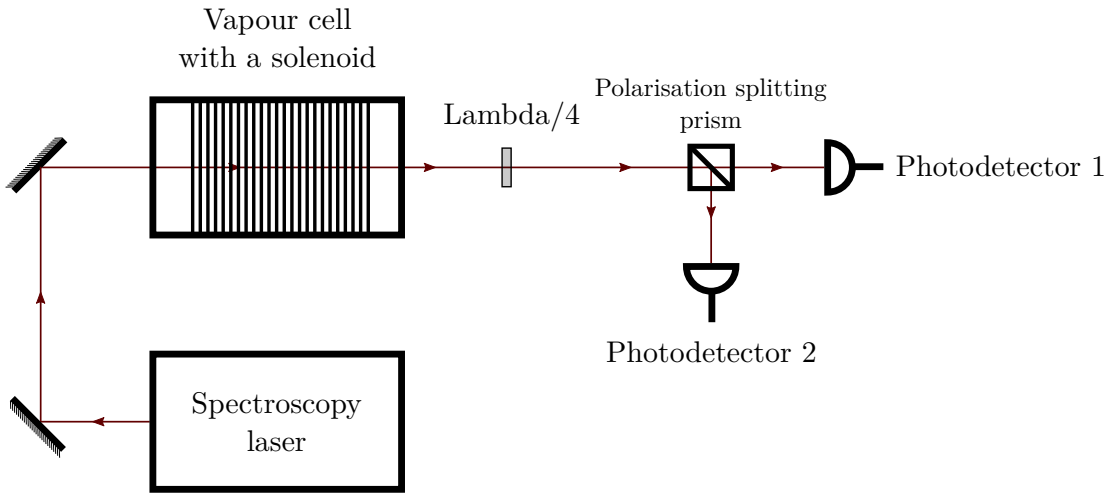

Figure 3.13: An example of a DAVLL optical setup. The solenoid is used to generate an offset magnetic field to split the Zeeman states.

through the cell, the measurement of the different polarisations will indicate unequal absorption. Subtracting the measured intensities an error signal can be obtained, see fig. 3.14b, with the zero point corresponding to having both polarisations being equally absorbed. Although this technique is simple to set up and does not require modulation to obtain a good error signal, it suffers from fluctuations in the offset magnetic field and input beam polarisation. However, the method has seen significant improvements and can achieve the same linewidth and stability as the saturation absorption spectroscopy scheme [132, 133].

Both methods allow to stabilise the spectroscopy laser to the atomic transition of interest. However, often the spectroscopy laser and the laser to be stabilised have a difference in wavelength of several nanometres. To transfer this stability the separate laser (secondary) therefore requires the use of an intermediate reference for both lasers. In most cases this is an optical cavity with a variable length. The tuning of the cavity length is achieved by placing one mirror on a piezo-transducer on one end of the cavity, which allows to scan the cavity length with an externally controlled voltage. Overlapping and launching the spectroscopy and the secondary laser beams into an optical cavity will produce resonant peaks for both lasers when the cavity length is swept. There are two types of transfer cavity schemes, scanning and dual-resonance, which allow to distinguish the different laser beams and stabilise one to another.

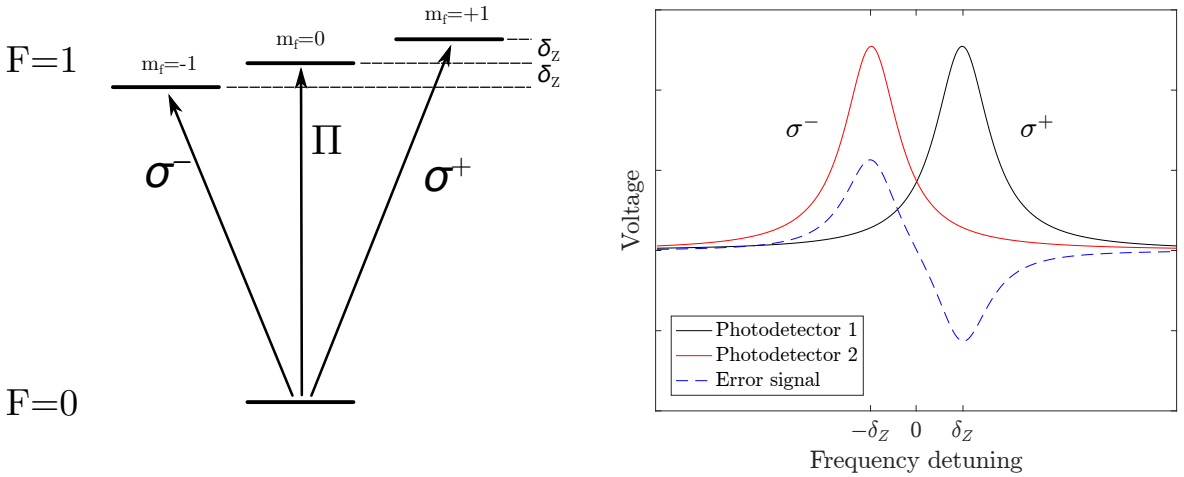

(a) (b)

Figure 3.14: (a) The energy level diagram, with the m_f states shifted by the Zeeman effect. (b) The output signals of photodetectors measuring absorption of the two orthogonal polarisations. By subtracting these signals a zero-crossing error signal is obtained.

Transfer cavity

In the scanning scheme the cavity piezo is swept with a triangular ramp signal over one free spectral range. Measurement of the time separation between peaks then provides an error signal for the secondary laser. This technique is versatile due to the fact that it can be scaled up to multiple lasers for a single cavity, with the only requirement being the fast processing of the cavity spectrum. These systems are quite prevalent in atomic physics experiments and the need for fast processing is greatly alleviated with simple programming devices [134, 135, 136]. However, the detection speed of the different peaks is limited by the speed at which the cavity can be swept.

A more simple and higher bandwidth approach is the use of a dual-resonance cavity. First a cavity length is found where both of the beams are resonant with the cavity. The cavity length is then stabilised with respect to the spectroscopy laser [137, 138]. The different laser beams are separated at the output by either using optical filters or assigning different polarisations and splitting them on a polarising beam splitter cube.

The added transfer cavity makes the optical setup larger, requires more instruments to process the error signal and the added layer of cavity stabilisation complicates the overall experimental setup. This is particularly detrimental to systems that are supposed to be compact and require minimal user maintenance. However, due to the inherent stability of an atomic references, they are still widely used in ion trap experiments.

The use of a spectroscopic scheme with a transfer cavity allows to stabilise a laser which

has a wavelength much different than the one from the spectroscopy laser. However, if the frequency difference between these two lasers spans only several gigahertz, it is possible to directly measure this offset with the use of a laser beating scheme.

Laser frequency offset lock

The scheme of stabilising a laser system by measuring the beat frequency is known as offset frequency locking [139, 140], with the groundwork developed in optical heterodyne detection [141]. A beat signal is produced by a superposition of two waves of different frequencies. Two lasers being a source of coherent monochromatic light, can produce a beat signal which can be measured using a photodetector. However, due to the limitations of modern electronics, the detection bandwidth for the visible spectrum covers at best several tens of gigahertz. Nonetheless, in the case of using separate lasers with frequency differences of several gigahertz, laser beating offers an elegant solution for monitoring the frequency of one laser relative to another.

A photodiode outputs a voltage proportional to the intensity of a light source. The intensity of a monochromatic laser beam is proportional to $|\vec{E}|^2$, where $\vec{E} = A\cos(2\pi ft)\vec{x}$ is the electric field component of the travelling wave and A and f being the amplitude and frequency of the electromagnetic oscillation respectively. Since the response time of a photodetector is much longer than the incident oscillation, the signal is averaged to obtain a voltage proportional to $\frac{1}{2}A^2$. By mode matching two laser beams onto a photodiode, the measured intensity can be expressed as

$$I = |\vec{E}_1 + \vec{E}_2|^2 = (\vec{E}_1 + \vec{E}_2).(\vec{E}_1 + \vec{E}_2)$$

$$I = |\vec{E}_1|^2 + |\vec{E}_2|^2 + 2A_1A_2\cos(2\pi f_1 t)\cos(2\pi f_2 t)\vec{x}_1.\vec{x}_2.$$

The first two terms in the last equation give a DC voltage on the photodiode signal, which can be ignored, while the last term gives an AC signal. If the oscillations are orthogonal between both fields, this will become zero, and the intensity will be the sum of the individual contributions. By using the trigonometric identity $\cos(x)\cos(y) = \frac{1}{2}(\cos(x+y) + \cos(x-y))$ and assuming equal polarisations, the last term can be written as

$$A_1A_2[\cos(2\pi(f_1 + f_2)t) + \cos(2\pi(f_1 - f_2)t)].$$

As the first term oscillates much faster than the bandwidth of a detector, the second term contributes as the only observable AC signal, with a frequency equal to the difference of

the two electromagnetic fields. Measurement of this signal not only gives the frequency difference, but it also allows to analyse the noise profile of the lasers used.

In this description, only the frequencies of the lasers were considered, but in reality the photodetectors measure the phase difference of the electromagnetic fields, rather than frequency. This fact is exploited in phase locking two lasers as used in the work shown in [139]. The simplified picture of laser beating overlooks one last factor determining the amplitude of the frequency difference signal, which is the mode-matching of the two beams. As all laser beams can be approximated by a Gaussian profile, the difference in the beam profiles, curvature and divergence will significantly reduce the attainable signal. For this reason beams must be carefully aligned and their Gaussian profiles matched. An example of the setup can be seen in fig. 3.15. The master laser refers to a pre-stabilised laser, whereas the slave is the laser to be stabilised. Not included in the optical path are polarisation waveplates, which are used to obtain the same polarisation for the two independent beams.

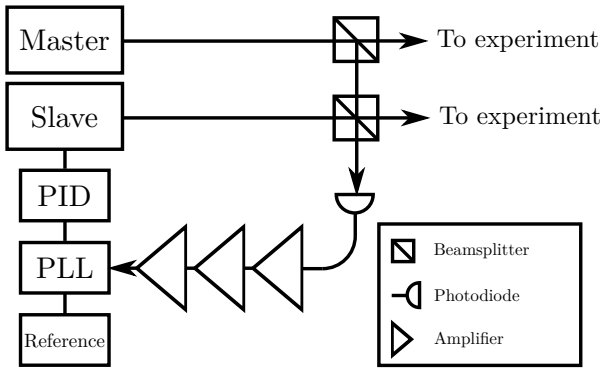

Figure 3.15: The block diagram of a frequency offset lock. The PLL (phase lock loop) outputs a voltage proportional to the difference of the beat and the required offset (reference) frequency.

The most obvious guess for a method of converting the detected frequency difference to a voltage would be to use a mixer to obtain an error signal. The limitation of using such a basic system is the requirement of a large bandwidth reference oscillator to be able apply offsets of several GHz, which can be costly. Therefore a PLL is used, whose ability to use inbuilt frequency multipliers make it possible to obtain an error signal for a wide range of frequencies. The process of converting an RF signal to a voltage is well known in frequency synthesis, namely in designing and building feedback circuitry for voltage controlled oscillators (VCO). The building blocks of a PLL are given in fig 3.16.

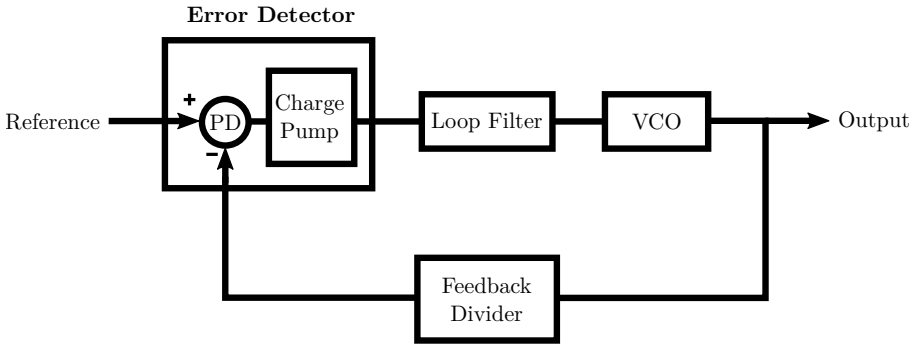

Figure 3.16: Diagram of a PLL. The loop starts by splitting a portion of the VCO output signal and dividing the frequency of the signal with a feedback divider. The resultant signal is compared to a reference oscillator with a phase detector (PD). The phase detector produces pulse waveform which is then converted to current pulses of different polarity. These are then filtered and summed by the loop filter to produce an error signal to control the VCO frequency.

As the name implies, a PLL is traditionally used to stabilise the phase difference between a well established reference signal and the output of a VCO. The VCO frequency does not need to be close to the reference signal, in fact, by using frequency dividers in the PLL, the VCO signal can be converted to a lower frequency signal, to be able to be compared to the reference. Both reference and the divided VCO signals are fed to a phase-frequency detector (PD), which produces a digital signal output with the duty cycle determined by the phase difference. The digital signal controls the charge pump, to produce pulses in currents, whose direction depends on the sign of the phase difference. To control the VCO signal, the pulses are converted to a voltage using a loop filter, which performs as an integrator. The output signal of the loop filter steers the VCO to produce a frequency signal which is in phase with the reference. For laser frequency stabilisation the VCO output signal is replaced by the beat frequency which is determined by the slave laser, allowing one to produce an error signal to keep the beat frequency phase stable with a reference.

One of the biggest advantages of using laser beating is the small footprint of the whole system - in fact the system can fit in a portable case by feeding both beams into the same optical fibre. This not only guarantees good alignment stability, but it achieves good mode matching.

Wavemeter

A standard tool in most experimental labs, a wavemeter provides the possibility of measuring the frequency down to several MHz [142]. The principal behind the operation of a wavemeter is performing light analysis using a Fizeau interferometer [143]. The light patterns formed on a camera inside the wavemeter are compared to a stable reference laser such as a HeNe, which is the actual reference of the wavemeter setup. The images themselves are typically fringe patterns that are used in calculating the wavelength, which then can be output as a digital signal to be read by another device. The error signal from the wavemeter is simply the difference in frequency from a set point value selected by the user, which makes the capture range of a wavemeter extremely large, although the gradient quite small. Wavemeters are known to have a non-negligible drift over timescales of several hours, which requires occasional recalibration with an external source. However, the main drawback of using a wavemeter is the time it takes to perform the image analysis, which greatly reduces the bandwidth of the feedback process to a typical value of 100 Hz [142]. Nevertheless, wavemeters are well suited for stabilising the slow drift of non-critical lasers since they are simple to implement into an experimental control system.

3.4 PID control systems

Once an error signal is obtained it has to be processed by a PID control circuit and fed to the laser. Since the early days of laser locking, analogue operational amplifiers were the driving force of PID laser stabilisation systems, partly due to their large bandwidth, stability and accuracy. But with the development of digital electronics, different platforms, such as microcontrollers, central processing units (CPU) and field programmable gate arrays (FPGA) became easily available. This section covers the PID schemes frequently encountered in laser frequency stabilisation.

3.4.1 Operational amplifiers

The operational amplifier (op-amp) is one of the first workhorses in integrated circuit manufacturing, with applications spanning areas of scientific, medical and industrial devices. In experimental physics, the mass production of op-amps has provided many solutions to the issues encountered in metrology, signal processing and of course control engineering. A PID controller can be simply implemented by using resistors, inductors and capacitors with an op-amp in a negative feedback configuration. An example of a PID schematic can

be seen in fig. 3.17.

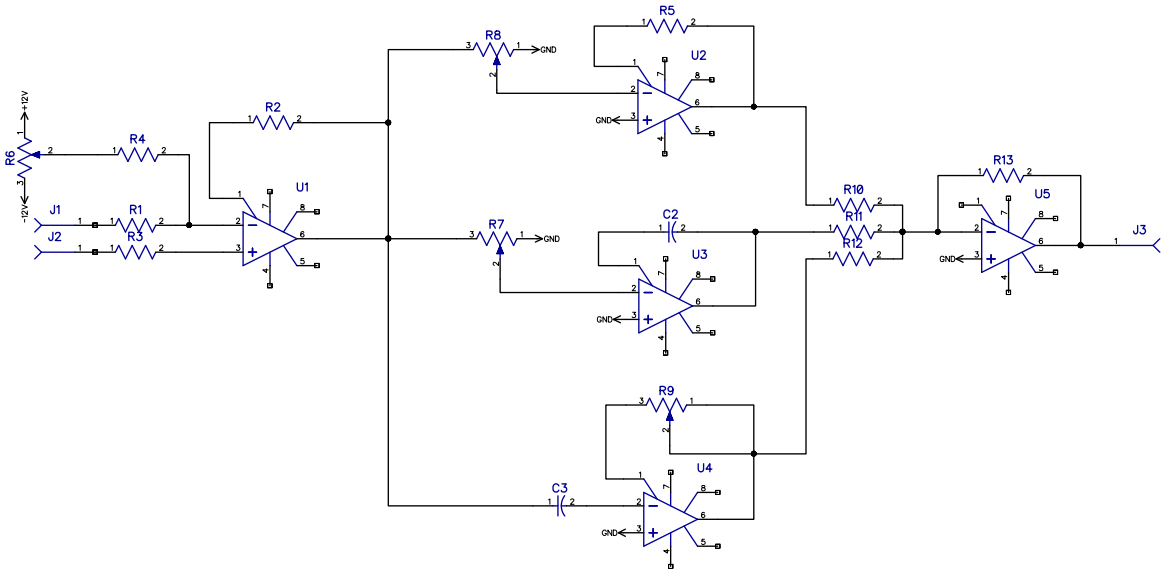

Figure 3.17: Schematic of a PID controller. The first op-amp U1 serves as a summing amplifier to introduce or remove any offsets (using R6) in the error signal (input J1 or J2, depending on required polarity), then it is split into three paths each leading to an op-amp responsible for proportional multiplication (U2), integration (U3) and differentiation (U4) functions. The last stage of the controller is another summing amplifier to add the individual components together to obtain the output signal (J3). Typically, the PID circuit has adjustable value components such as potentiometers to set the optimum gain for each op-amp in the circuit.

The example PID scheme contains potentiometers to tune the gain parameters of the op-amp, which can be a highly complex operation. Nonetheless it is important to quantify the performance of the control scheme and if possible understand the limitations of these systems. A good guide for optimising feedback for laser stabilisation can be found in [144]. To start with, one of the main concerns in designing a PID controller for a device is the bandwidth of operation, which determines on what time scales the controller can compensate for perturbations adequately. General purpose op-amps have already a reasonable bandwidth of at least 1 MHz, which tends to be larger than the bandwidth of the laser controller. This is only true for unity gain, which in general will not be the case as most error signals need some level of amplification. The main criteria for op-amps is then the gain-bandwidth product which determines the achievable bandwidth of an op-amp versus gain. A large bandwidth PID controller can correct for a wider noise spectrum, therefore to achieve large gain and bandwidth, the gain-bandwidth product needs to be as large as possible. In addition the frequency response of an op-amp, the precision needs consideration too. The error signal can be compromised by

choosing poor precision op-amps, which have a larger noise floor level or a lower accuracy, leading to sub-optimal performance of the whole system. To avoid this, higher quality instrumentation op-amps are used for measuring the error signal accurately [145]. The same low noise amplifiers are used in a buffer amplifier configuration at the output of the PID controller, to avoid any possible impedance mismatch which would cause some small reflections distorting the control signal. As for the op-amps for controlling the PID parameters, most of the concentration is paid to the integrator op-amp, largely because the sub-optimal performance of this component results in unpredictable behaviour of the whole control circuit. The op-amp integrator in the given example (fig. 3.17) can be described using the time constant factor $1/R7C2$, which has units of time and describes the timescale at which the integrator will have the largest effect on the error signal. By choosing a large value such as 10 seconds, the integrator will have little effect on perturbation frequencies of kHz, relying on the compensation to be performed with the proportional component, but for slow oscillations the integrator will take over and steer the system to the set point. Even though, the optimisation of the PID circuit is an iterative process, there are general rules when setting the initial parameters of the controller. One of them is setting the proportional amplifier gain to be adjustable in the range of 0.1 to 2, which was accomplished by having a $R8 = 10\,\mathrm{k\Omega}$ potentiometer with a fixed $R5 = 20\,\mathrm{k\Omega}$ fixed resistor. As for the integrator, the typical integration time $1/R7C2$ was set to $\approx 0.3\,\mathrm{s}$ with components $R7 = 10\,\mathrm{k\Omega}$ and $C2 = 33\,\mu\mathrm{F}$.

The use of op-amps in modern laser control systems is still prevalent, largely due to the low noise levels and the high bandwidth feedback. Furthermore, the circuitry is simple and robust, making them excellent 'set and forget' systems. Despite this, these circuits sometimes are non-intuitive and optimisation of parameters is referred to as being a 'black art' of laser locking, which can be a repetitive and time-consuming process.

3.4.2 Digital electronics systems

The development of digital electronics has greatly influenced the progress of control engineering, culminating in a field of its own of digital control. But analogue signal processing still remains a challenge, partly due to the requirement of converting an analogue voltage signal to a digital array which then has to be processed and converted back to be usable. Both processes are handled by ADC (analogue to digital converter) and DAC (digital to analogue converter) integrated circuits, which introduce lower limits for precision and speed of the conversion. Nonetheless, these devices have seen many improvements and

currently are in a position to implement a moderate bandwidth feedback system.

All digital systems rely on a programming language to control the hardware, which can complicate the implementation of a laser locking system. Some programming languages are more involved and less intuitive than others and less user friendly. However, converting all of the operation to a readable text file, digital systems outperform analogue electronics in the case of making modifications on the fly and testing them immediately. This also simplifies the implementation of complicated functions such as scanning the laser's frequency until it is within the capture range of the error signal, building filters and conditional loops which greatly increases the robustness of the overall system. In fact, the whole process of generating an error signal can be left to the control circuitry, only requiring the input of the photodiode signal[1]. An added benefit of digital hardware is the small footprint of these circuits, with complete circuits requiring at most $20\,\mathrm{cm} \times 20\,\mathrm{cm}$ of space. Such compactness allows the system to be scaled up much easier to increase the number of input and outputs.

There are several hardware options when implementing a digital control system. The main differences being the bandwidth which determines the speed of the calculations and cost. At the lower end of the range, microcontroller platforms such as the Arduino, Microchip SAM and PCU families offer the cheapest and most basic building blocks for constructing bespoke embedded digital hardware. The bandwidth of these systems is typically limited by the relatively slow internal oscillator (1 MHz to 8 MHz), but they can be easily combined with analogue components [146]. The main disadvantage of microcontrollers is the unintuitive programming syntax, making the code difficult to read or modify. A step up in the speed would be the use of a CPU to perform fast calculations. One of the easiest implementations of this is the use of analogue input/output boards[2] in conjunction with a software based PID running on a PC, which offers simple programming with a reasonable bandwidth of $\approx$1 kHz. The drawback of this system is the added cost of a PC which in general does not run consistently and is susceptible to drops in performance. A solution to this would be to develop the feedback circuitry on a small-scale CPU system[3], in the process compromising speed and simplicity. The main significant limitation for these systems is the successive processing of code and lacking fundamental timestamping, which introduces a limitation on the number of calculations the system can perform before introducing significant time delays. This also limits the amount of independent input and

[1] Toptica Photonics AG DigiLock
[2] National Instruments PCI series boards
[3] Raspberry PI

output channels, which have to be sampled one after another. Ideally, these operations would be processed independently in parallel, a feature addressed by field programmable gate arrays (FPGA).

An FPGA is a collection of digital logic gates which can be combined in many different ways to perform highly user specific operations. The programming languages are slightly more complex, owing to the ability of operating the platform on the hardware level. With the increasing interest in FPGAs, most programming languages such as C++, Python, LabVIEW and MATLAB have adopted FPGAs and offer the ability to convert an easy to understand script to a platform specific code. These advancements have made FPGAs the preferred choice in instrument control in the fields of atomic, electronic and optical physics, largely due to the high speed operations and inherent parallelism. In fact, there is a growing interest to implement analogue signal processing using FPGAs, an area that has been successfully addressed by an FPGA based platform, RedPitaya, which offers the basic developer tools to build any signal processing system to be used in the lab.

3.5 Laser locking setups for Yb and Ba ions

Ion trap experiments heavily rely on the frequency stability of the lasers used to photo-ionise atoms [147], efficiently Doppler cool the ion motion [148] and perform high-fidelity ion qubit preparation and readout operations [40, 149, 150]. Despite advancements in laser technology, without an active feedback system the laser frequency fluctuates unpredictably, which results in systematic errors. However, there are multiple different stabilisation systems, described in the previous sections, which provide a means of keeping the lasers frequency to a well defined value. To start with, one needs to choose a stable reference. The choice of reference determines the complexity and stability of the overall system, which is largely composed out of optical and electronic devices. Therefore, the method of stabilisation requires careful consideration, particularly when working with many lasers of different wavelengths. Currently, there are 12 laser systems in use in the lab that require accurate frequency control, each serving it's purpose for a total of six ion trap experiments and requiring different levels of stability as shown in table 3.1.

Table 3.1 indicates that the most critical lasers for Yb^+ experiments are the doubling 739 nm systems, all used for Doppler cooling the trapped ion and performing qubit state detection. The same scale of stability is required for the Ba^+ Doppler cooling laser at 493 nm, due to having a natural linewidth of 15.6 MHz, and the repumper 650 nm due to the strong decay channel from the state $6P_{\frac{1}{2}}$ into $5D_{\frac{3}{2}}$ with a natural linewidth 5.3 MHz

Table 3.1: Laser purpose and stability requirement table

Laser	Purpose	Required stability
Toptica 369 nm doubling system[4]	Yb^+ Doppler cooling, preparation and fluorescence detection	<1 MHz/hour
M2 Ti:sapphire doubling 369 nm system[5]	Yb^+ Doppler cooling and fluorescence detection	< 1 MHz/hour
399 nm ECDL[6]	Yb photo-ionisation	≈ 10 MHz/min
935 nm ECDL[7]	Yb^+ repumper	≈ 50 MHz/hour
413 nm ECDL[8]	Ba photo-ionisation	< 1 MHz/hour
493 nm ECDL[9]	Ba^+ Doppler cooling	< 1 MHz/hour
650 nm ECDL[10]	Ba^+ repumper	< 1 MHz/hour

[151]. In the mid-range of the required stability are the Yb^+ 935 nm repumper lasers and the photo-ionisation lasers for both species. The Yb^+ repumping transitions are power broadened to several GHz to excite the Yb^+ ion out of the $^2D_{3/2}$ manifold, as described in chapter 2. Therefore a less stringent ≈50 MHz stability is required. The same is true for the photo-ionisation lasers which are only used to load the ion trap. However, to ensure isotope selectivity for both species, modest stability and accuracy is required to keep the laser frequency to within an isotope shift of 300 MHz. The same holds for the Yb^+ 638 nm repumper, which is only used occasionally to depopulate the ion from the $2F_{7/2}$ state.

To address all of the listed requirements, various locking setups have been designed and constructed with the method and optical reference for each setup listed in table 3.2 with the layout of the setup shown in fig. 3.18. A brief summary will be given first. An in depth description can be found in the subsections below.

One of the M2 lasers was set up to use a Rb saturation spectroscopy scheme to achieve the required stability. It relies on using a transfer cavity in a dual-resonance configuration, described in 3.3 to transfer the stability of the spectroscopy 780 nm laser to the 739 nm laser light. The double resonance case is preferred simply because of the basic requirements for stabilising the cavity instead of developing highly complex electronic systems for the continuous scanning cavity scheme. The preference over the DAVLL method is due to the requirement of polarisation stability and susceptibility to magnetic field drift. The system performs adequately, but was not chosen to be replicated in other experimental systems.

[4] Toptica Photonics AG TA-SHG36
[5] 2x M Squared Lasers SolsTiS ECD-X
[6] 2x homebuilt Sanyo DL-4146-301S and 1x Toptica Photonics AG DL pro HP
[7] 2x homebuilt Roithner RLT940-100GS and 1x Toptica Photonics AG DL100
[8] Homebuilt Sanyo DL-6148-030
[9] Moglabs CEF extended cateye diode laser
[10] Toptica Photonics AG DL 100
[11] Moglabs ECD004

Table 3.2: Each laser was stabilised by a method that suits the frequency requirements for an ion trap experiment.

Laser	Method of stabilisation and optical reference
Toptica 369 nm doubling system	Laser beat lock
M2 Ti:sapphire doubling 369 nm system	Low drift cavity
M2 Ti:sapphire doubling 369 nm system	Rb saturation absorption spectroscopy with a transfer cavity
3x 399 nm ECDL	Wavemeter
3x 935 nm ECDL	Wavemeter
413 nm ECDL	Low-drift cavity
493 nm ECDL	Low drift cavity
650 nm ECDL	Low drift cavity

This is mostly due to the requirements for additional lock-in amplifiers and PID circuits which unnecessarily complicate the setup.

To provide means of stabilising multiple critical lasers to the same reference, a passive low-drift four optical cavity setup was designed and assembled. The four cavities are constructed out of a single glass block, with each cavity length set individually with the use of piezos. The wavelengths that were chosen to be used with the cavity include the whole suite of lasers for Ba^+ ion experiments (413 nm, 493 nm and 650 nm) and the 739 nm laser light, which is frequency doubled to generate the required 369 nm light. This light can be used to stabilise the remaining 369 nm systems as outlined below. The cavity is measured to have a modest finesse of 243, which results in a cavity mode having a linewidth of 6.2 MHz.

Since all of the lasers frequencies are monitored using a commercial wavemeter[12] with a precision of $\approx$10 MHz, it is possible to use an active feedback system to correct for frequency drift. This is done by using a program written in LabVIEW. The wavemeter is prone to drift, however it was found to be sufficiently low for the 399 nm and 935 nm stability requirements. The day to day use proved to be accurate to keep a single pair 399 nm and 935 nm lasers as stable as specified in table 3.1.

One of the aims of the locking setups described in this chapter, is to simplify the user interface from laser stabilisation systems, which means having more robust and automated control electronics. A further requirement is the bandwidth of these systems needs to be large enough such that if needed, the PDH locking method could be implemented, as described in section 3.3. Due these requirements, an FPGA system was chosen, owing to

[12]High Finesse

its versatility, speed and ease to interface when processing the error signal and optimising the PID parameters. One of the earliest implementations of such a system consisted of a National Instruments module[13]. The performance of the system was satisfactory and greatly alleviated the user interface by the use of National Instrument LabVIEW software, which was inbuilt into the control module of an ion trap experiment. However, the performance of these modules is limited to the less demanding wavemeter stabilisation scheme. This is due to the excess high frequency noise and limited bandwidth on the analogue output channels. Instead of using these systems, the electronics feedback system is constructed out of commercial laser FPGA controllersToptica Photonics DigiLock and homebuilt platforms[14].

The following sections give an in-depth description of the implemented locking schemes with outlook for further improvement.

[13]National Instruments PCIe-7842R
[14]RedPitaya

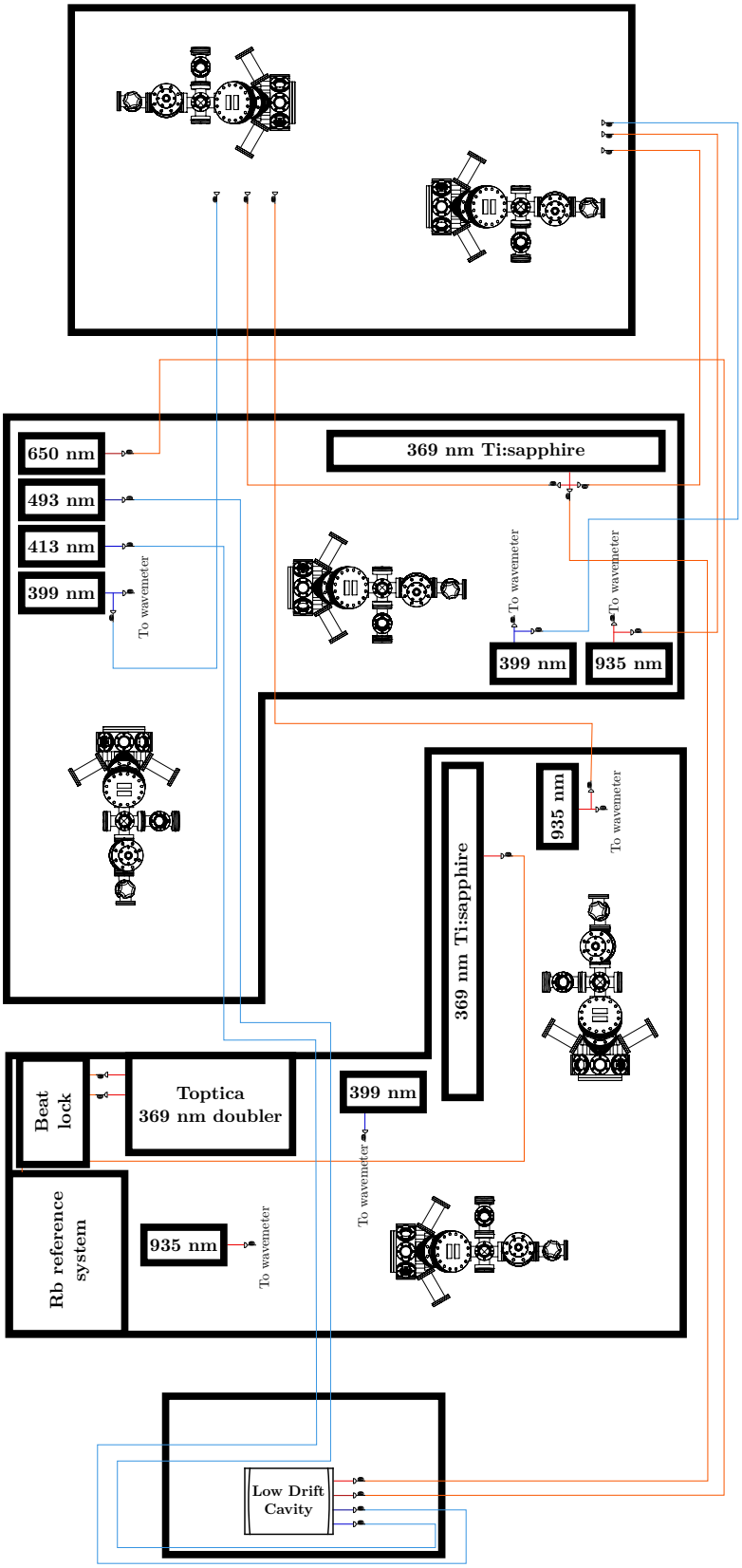

Figure 3.18: The layout of the various locking setups, which provides laser frequency stabilisation to six experimental systems placed on three optical tables. Single mode fibres are used for beam profile cleaning and transporting the light between tables.

3.5.1 Rb reference

As mentioned previously, the spectroscopic reference, used for stabilisation of the 369 nm laser, is based on the saturated absorption spectroscopy of the hyperfine transitions in ^{87}Rb, the choice determined by the cheap and readily available vapour cells[15] and laser diodes at the 780 nm wavelength. The full optical layout of this scheme can be seen in fig. 3.19.

The 780 nm lasers used for Rb spectroscopy were based on a Littrow extended cavity diode design [152], whose wavelength can be tuned by rotating the diffraction grating with a piezo transducer controlled by a voltage. The system was modified from an earlier implementation by previous group members[16]. The main changes include fibre-coupling the 780 nm laser output beam and splitting the pump and probe beams with a partially reflecting mirror instead of a polarising beam splitter. The main motivation for fibre-coupling was mostly due to the poor output stability and beam profile quality of the initial 780 nm laser system. Using a single mode polarisation maintaining fibre helped to reduce the alignment to tweaking the fibre coupling, which is an easier process. It also meant using waveplates to correctly set up the input beam polarisation for fibre coupling, otherwise the output beam polarisation would drift periodically. The polarisation drift would change the pump and probe powers causing the observed signal to fluctuate in amplitude, which is why the polarising beam splitter was removed.

The early iteration of the optical and electronic system contained homebuilt ECDL laser and electrical circuits.The latest iteration of the spectroscopy scheme uses a commercially available 780 nm laser[17] with an inbuilt stabilisation control scheme within the controller unit. It greatly alleviated the daily experiments as the system proved to be more intuitive and easy to use compared to the early iteration. All of the data collected was obtained using this commercial laser system. Although the commercial system does simplify some steps of the laser frequency stabilisation scheme, the whole scheme still relies on the early iteration of the optical setup that I have developed.

The probe and pump beams were split to have a power ratio of 9:1, making sure that the probe beam does not saturate the photodetector. Another beam can be seen in fig. 3.19 going through the cell in the same direction as the probe. This is to remove the Doppler broadened spectrum via the balanced photodetector, which simply subtracts the signal of one photodiode from another. This is not necessary to obtain a good error signal,

[15] Thorlabs GC25075-Rb
[16] Dr. Robin Sterling and Dr. Kim Lake
[17] Moglabs Cateye CEF

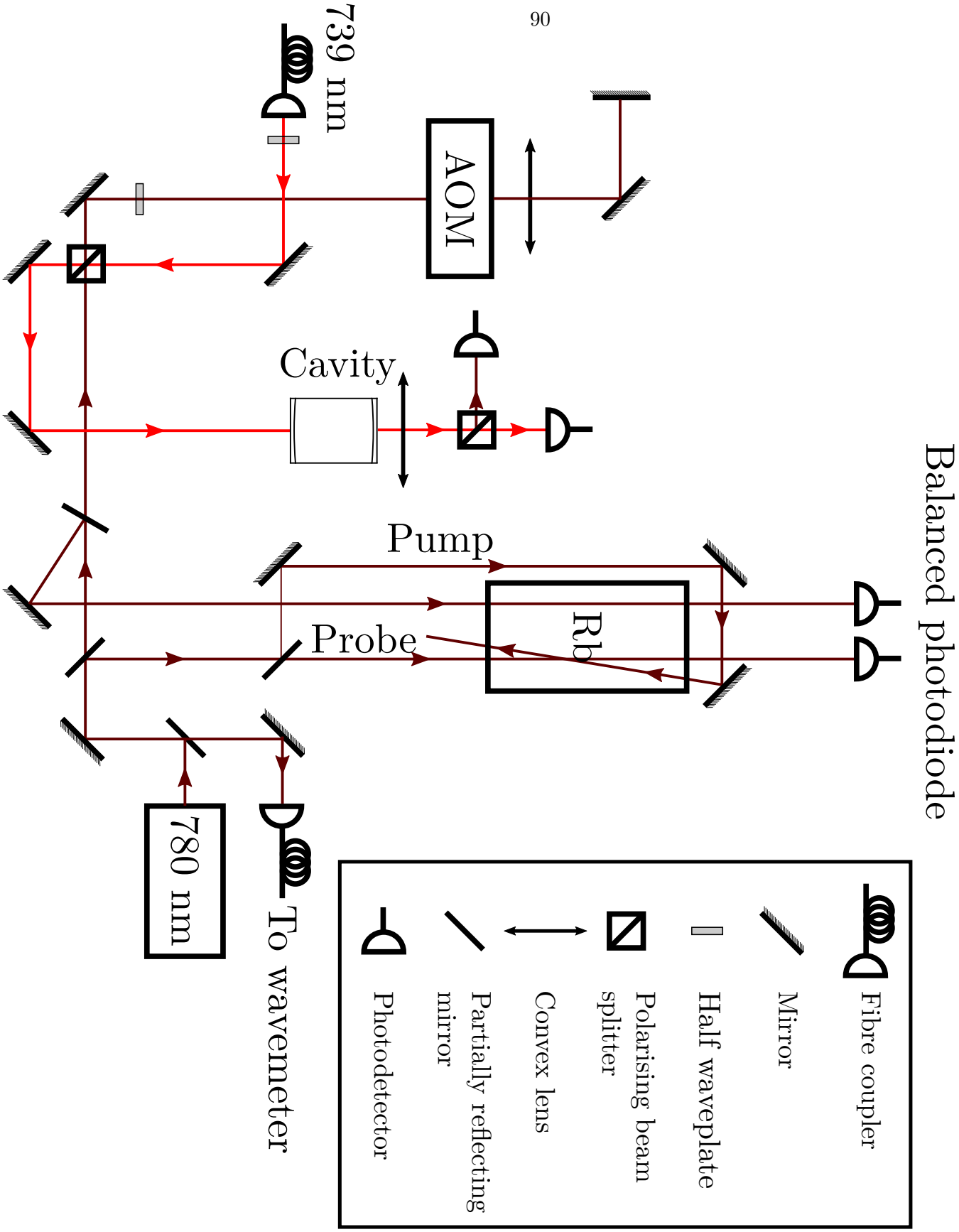

Figure 3.19: The optical layout of the Doppler-free Rb saturation spectroscopy system with the transfer cavity allowing transfer of the 780 nm laser stability onto the 739 nm laser. Both lasers use single-mode fibres for beam profile clean-up.

but it proves useful when optimising the overlap of the pump and the probe. The overlap of the pump and probe is generally quite small and does not need to extend the whole way through the Rb cell, with even the smallest amount allowing observation of the hyperfine transitions of ^{87}Rb (see fig. 3.20a).

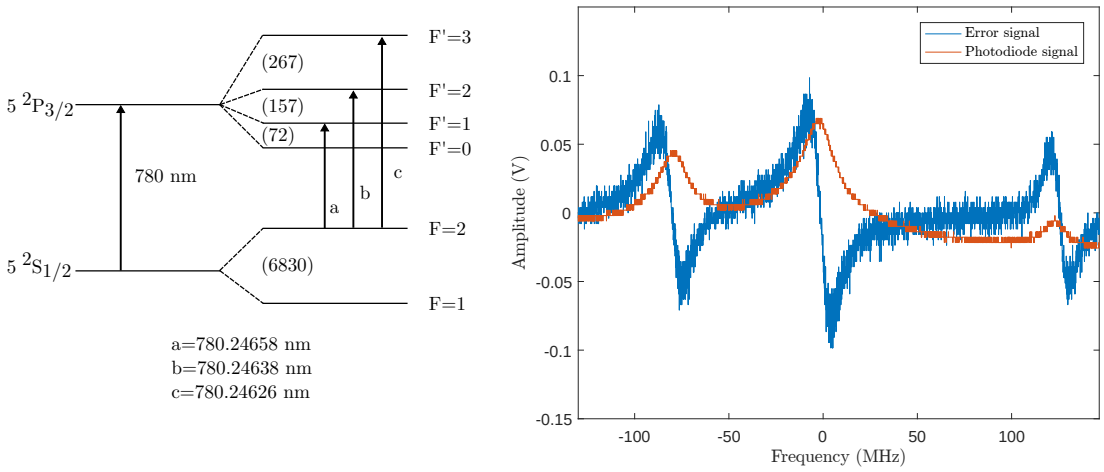

(a) (b)

Figure 3.20: (a) ^{87}Rb energy level diagram. The main reference peaks used in laser stabilisation are the hyperfine transitions *a*, *b*, *c*. The numbers in brackets refer to the energy splitting in MHz. (b)^{87}Rb spectrum photodiode signal and error signal.

An example spectroscopy signal can be seen in fig.3.20b as the red trace measured on an oscilloscope. The peaks in the graph do not necessarily correspond to the Doppler-free hyperfine transitions, as there is a possibility for non-zero velocity atoms to be excited into these states by setting the frequency midway between two transitions. This results in additional peaks of the spectrum, called crossover transitions [127]. Crossover transitions occur for multi-level energy states, whose separation is less than the Doppler broadening. For ^{87}Rb, the broadening spans ≈500 MHz, which covers the *a*, *b* and *c* transitions (fig. 3.20a) used for stabilisation. Crossover transitions are avoided when stabilising the laser, since they correspond to exciting non-zero velocity atoms. To generate the blue trace error signal as seen in the example, the 780 nm laser diode is modulated with a 0.32 V amplitude 100 kHz frequency sinusoidal signal and subsequently demodulated with a lock-in amplifier[18]. To be able to demodulate the photodiode signal properly, the bandwidth of the photodiode must extend to the modulation frequency. This can be checked by looking for a sinusoidal 'fuzz' superimposed on the spectrum signal. The signal is demodulated with a lock-in amplifier of the commercial laser controller, which also includes the proportional and integral PI controller circuitry. The Allan deviation for the 780 nm laser is given in fig

[18]Scitec Instruments 410

3.21. The same data can be used when comparing how the stability changes in the later stages of the system. It is clear that for time scales of over 10 s, the laser is stable within 100 kHz, which sets the lower limit of the frequency fluctuations of the 739 nm system. Because of this, the optimisation of the whole chain was started with the Rb spectroscopy setup. The stability of the laser was inferred by measuring the stabilised laser's probe

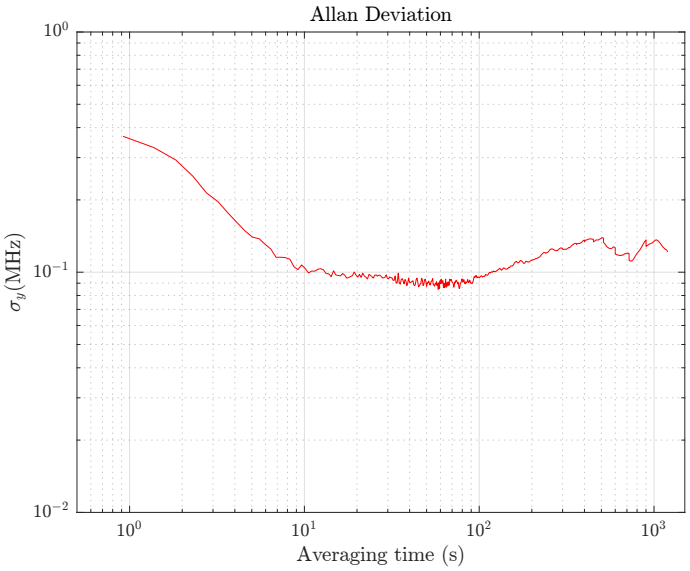

Figure 3.21: The stability of the 780 nm laser was measured using a photodetector, with the voltage variations converted to frequency using the gradient of the transition.

beam photodiode signal. The Allan deviation is mainly limited by the measurement accuracy of 3 MHz, however the stability of <1 MHz is achieved for averaging times over 1000 seconds. The two contributions to this error are the photodiode accuracy and the noise floor of the error signal. In order to quantify any drift due to the laser, a separate photodetector was used to measure the beam intensity right at the output of the single mode fibre. This was done to see if there are any intensity fluctuations which correlate to frequency drift of the 780 nm laser frequency drift. In addition to this, a polarising beam splitter was put in front of the photodetector to measure the intensity changes caused by polarisation drift. Both cases showed negligible change in the beam intensity, pointing to other sources of error for the 780 nm laser drift. A potential source are the magnetic field fluctuations or the pointing stability of the laser beam, which was assumed to be negligible. Using the hyperfine energy levels introduces potential errors due to magnetic field drift, which changes the frequency shift of the different Zeeman states. This effect can be seen by placing a strong permanent magnet next to the vapour cell, which indicates a drop in peak intensity and an increased linewidth of the transition. Therefore, in

order to further reduce laser frequency drift, metallic shielding can be used to minimise the amplitude of the fluctuations. However, as the performance was deemed adequate for daily experiments, no precautions were taken to shield the Rb vapour cell with μ-metal [153] or any highly inductive material.

Once the 780 nm laser is stabilised, the next step is using a transfer optical cavity, which transfers the stability to the 739 nm laser, as described in 3.3. In this case, the dual-resonance setup is used, due to the simplicity of generating an error signal for the secondary laser. Both 780 nm and 739 nm laser beams are overlapped on a PBS and launched into the cavity, after which they are separated by another PBS. A lens is used to focus the beams onto individual homebuilt photodiodes. The cavity has one mirror mounted on a piezo transducer[19], which allows us to find the mirror spacing where both of the lasers are resonant with the cavity. The length is found by setting the 739 nm and 780 nm laser onto the required frequencies and scanning the cavity length until both photodiodes indicate transmission. By stabilising the transducer to the 780 nm laser, the cavity becomes a reference to the secondary laser. Being an active reference, this cavity does not need to be machined with high precision or made out of exotic materials. In fact it is sufficient to shield the cavity using a medium-density fibreboard (MDF) box to reduce acoustic perturbations. The remaining frequency fluctuations should in theory be reduced by the transducer, which has a bandwidth limitation of 1 kHz in order to avoid crossing the self-resonance frequency of 75 kHz. To be able to tune the frequency of the locked laser, the 780 nm laser beam is double-passed through an AOM, which allows a tuning range of $\approx$50 MHz on the stabilised laser by changing the RF drive frequency of the AOM. The change in the AOM drive frequency shifts the 780 nm laser frequency and with it, the cavity length. The tuning of the cavity length with the AOM controls the 739 nm laser frequency while still having the whole system locked. The 739 nm laser has a piezo assembly containing two piezo stacks, one responsible for slow and the other for fast feedback. The fast piezo was modulated with the same signal as the spectroscopy laser, which allows us to use a similar modulation scheme. Instead of using another lock-in amplifier, the error signal was obtained and manipulated with a commercial laser feedback module[20], which also incorporated the PID controller.

To assess the stability of the 369 nm locked laser, the reference oscillator was chosen to be the Doppler cooling transition in a trapped $^{171}Yb^{+}$ ion. The ion scatters photons at the rate defined by the transition linewidth, if the laser is set to halfway up the transition, any

[19] Piezomechanik HPSt 150/14-10/12
[20] Toptica Photonics DigiLock

frequency fluctuation will result in a change of the fluorescence rate. Knowing that the linewidth of the transition is ≈20 MHz and the given minimum and maximum count rates, the gradient of the lineshape can be used to calculate the absolute frequency fluctuations from the halfway point. Although the transition is sensitive to magnetic field fluctuations, it serves as a good performance test in the case of a real experiment. The scattered photons were collected by a photomultiplier module and integrated to produce a proportional voltage signal. As the main interest is the long term performance, only timescales of above 5 s are considered. The results are presented and compared to the spectroscopy 780 nm laser in fig.3.22. The 369 nm indicates an Allan deviation of 50 kHz for averaging

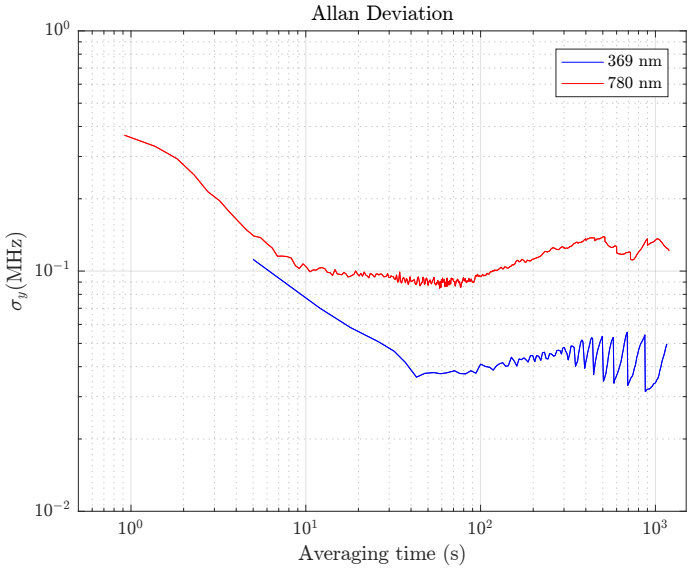

Figure 3.22: Comparison of the Allan deviations for the spectroscopy 780 nm and the Doppler cooling 369 nm laser frequencies.

time of 100 s and longer. Although the doubling of the 739 nm laser also doubles the extent of the fluctuations on the 369 nm laser light, the measured Allan deviation for the UV beam shows a significantly lower deviation when compared to the spectroscopy laser. This can be explained by the difference in the measurement accuracy of the two lasers. The spectroscopy laser frequency measurement cannot compare to the precision of measuring fluorescence counts using a highly sensitive phtotomultiplier on a single trapped ion isolated from the environment.

Despite the adequate results, a spectroscopy system requires maintenance of both the laser and the transfer cavity. Optimising each component can be arduous and time consuming, therefore the system was decided to not be replicated. Furthermore, stabilisation of many different wavelengths requires multiple cavities. Instead, a passive optical cavity

was opted for, owing to the simplicity of the scheme.

3.5.2 Low-drift cavity

The main properties of an optical cavity were described to be the free-spectral range ν_F, finesse $\mathcal{F}$ and the cavity linewidth $\delta\nu$. The free spectral range is determined by the length of the cavity and can be chosen to have any preferred value. Ideally, the free spectral range would be chosen to be as small as possible, in order to have multiple closely spaced lock points. This would mean having cavities several metres long, which introduces complications when isolating the system from the environment and more pronounced acoustic noise. Therefore, most cavities are chosen to have free spectral ranges of 1 GHz to 2 GHz.

On the other hand, the finesse $\mathcal{F}$ and the cavity linewidth $\delta\nu$ are governed my the quality of the mirrors. By using modest reflectivity above 0.997, it is relatively straightforward to assemble an optical cavity with finesse of 200 and linewidth of 5 MHz, which is more than enough for a transition linewidth of 20 MHz. Despite the advantages of using optical cavities, the engineering of these systems still remains a challenge, largely due to requirements to isolate the system as much as possible from the fluctuating environment. To improve the long term stability of the cavity, a vacuum system was built to isolate a low-drift cavity from thermal fluctuations due to convection. The main objective when designing the system is to achieve an optical cavity, which drift only 1 MHz in 24 hours, with the capability to individually stabilise four lasers with wavelengths of 413 nm, 493 nm, 650 nm and 739 nm. The design is based on systems used in Mainz and Innsbruck [154, 155].

The ULE cavity block

To be able to stabilise multiple lasers with a single passive system, the cavities were manufactured from a block (see fig 3.23a) of Corning ULE Premium grade glass[21]. The block dimensions are 65 mm × 65 mm × 100 mm, which gives a free spectral range of 1.5 GHz. The ULE glass has a coefficient of thermal expansion of $30 \times 10^{-9}\,\mathrm{K}^{-1}$ [156], which means that increasing the temperature by 1 °C will make it expand by 3 nm. For a laser frequency of 340 THz, this would correspond to a frequency change of 1 MHz. Considering the typical temperature stability of the lab, the performance is sufficient to stabilise any laser used to interrogate the ion. However, the overall stability of the cavity is also determined by the expansion of the mirror assembly, a process which is not easy to predict. Nonetheless, the expansion can be assumed to be dominated by the largest object, which is the mirror spacer.

[21] Docter Optics

To form a semi-hemispherical cavity, a planar and concave mirror assembly was used as in the example of fig. 3.8 in section 3.3. The curvature of the concave mirror was chosen to be $R = 250\,\text{mm}$, which results in the beam being focused at a focal point of $f = \frac{1}{2}R = 125\,\text{mm}$ from the mirror [119]. The mirror substrate was made out of 12.7 mm diameter fused silica cylinder with a thickness of 6.35 mm, which was coated[22] with a dielectric coating to achieve a reflectivity of 0.995 for the four specified wavelengths. The outside of the mirrors was coated with an antireflective coating to achieve a reflectivity of less than 0.0075. This was done to minimise any loses and interfering reflections when launching the beam into the cavity. With these specifications, the cavity finesse was estimated to be ≈ 626 with a linewidth of 2.4 MHz.

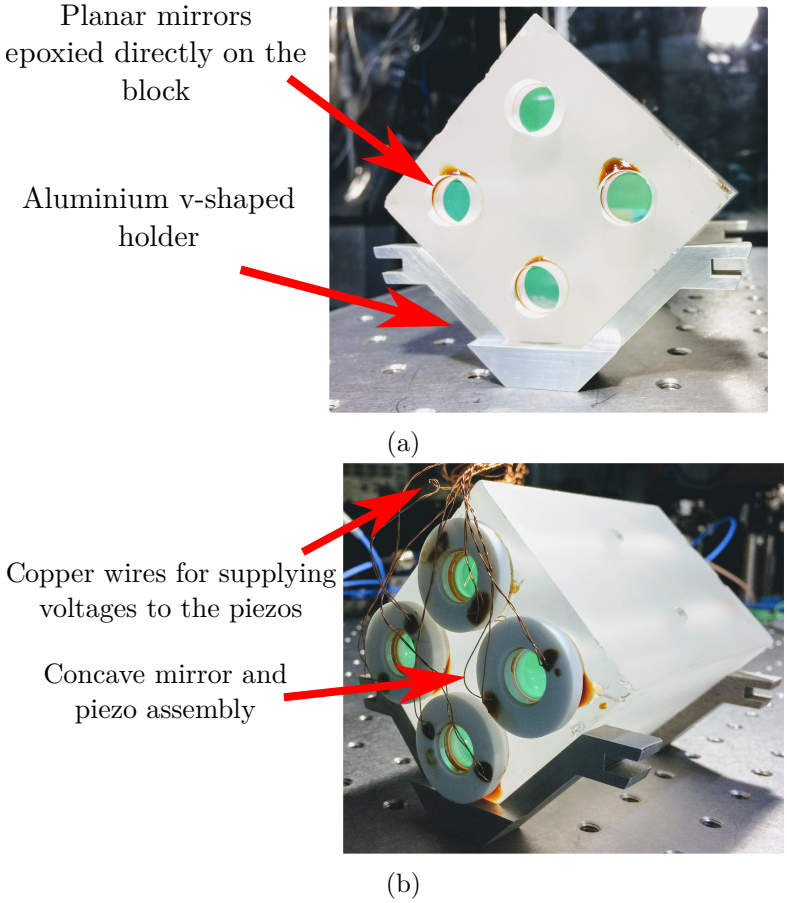

Figure 3.23: Picture of the front and back of the block with holes on the side for evacuating air using a pump. a) The front of the cavity has four planar mirrors epoxied directly on the block. By launching the beam into the cavity through this end, the alignment procedure can be simplified by overlapping the incident beam with the reflection from the mirror. b) Back of the block showing the second set of mirrors with a 250 mm radius of curvature.

One set of mirrors was epoxied[23] directly on the block, while the remaining half were

[22] Optida
[23] EPO-TEK 353ND

mounted concentrically on piezo transducers[24] via a ceramic Macor piece as seen in fig 3.24a. The electrical contacts between the piezo rings and the voltage feedthrough pins were made using thin copper wire and silver epoxy[25]. The choice of mounting the mirrors on two concentric transducers gives the advantage of cancelling their thermal drift by making the piezos counter-expand, such that the net displacement of the mirror is minimised, see fig. 3.24b. Epoxy was used to assemble the mirror holder and piezo assemblies, with great care taken not to introduce off-axis misalignment of the mirrors and not placing any epoxy in-between any of the parts. In the case of the resonant frequency not matching the required laser wavelength, the cavity length needs to be changed to the next resonance, which is separated by the free spectral range ν_F. Knowing the piezo expansion from the specification data-sheet, the required voltage was calculated to be 500 V. The piezo control voltages were generated with a high-voltage multi-channel DC system[26] with the particular aim of having a ripple voltage noise of $<$10 mV, which corresponds to frequency fluctuations of $\approx$1 kHz. The drift of the output voltage was measured and deemed suitable for a drift of 100 kHz over a day.

[24] Ferroperm PZ26
[25] EPO-TEK H21D
[26] ISEG IBS 80 30

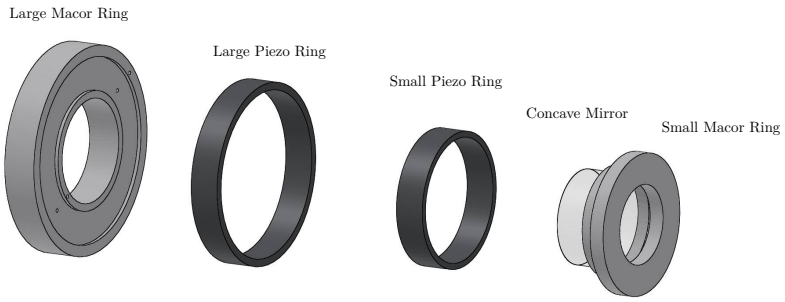

(a)

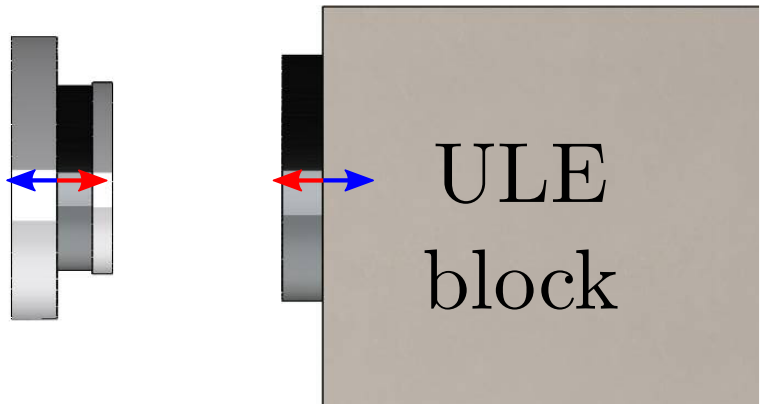

(b)

Figure 3.24: a) Exploded view of the mirror assembly. Small drops of epoxy were used for connecting the individual parts, with copper wires being soldered to the sides of the piezo rings. b) It is possible to passively minimise the cavity length drift by using two piezos, which expand or contract in opposite directions. The red arrows indicate the direction of expansion when heated and blue when cooled.

Vacuum system

The fully assembled setup can be seen in fig 3.25. The vacuum system is primarily composed of a DN100CF reducing tee[27] with custom AR (anti-reflection) coated windows[28], to prevent the build up of parasitic etalons due to imperfect transmission through the window. The same effect can be achieved by using a slightly tilted window [155].

[27] MDC Vacuum E-CRT100-40
[28] MDC Vacuum VPZ100QBBAR

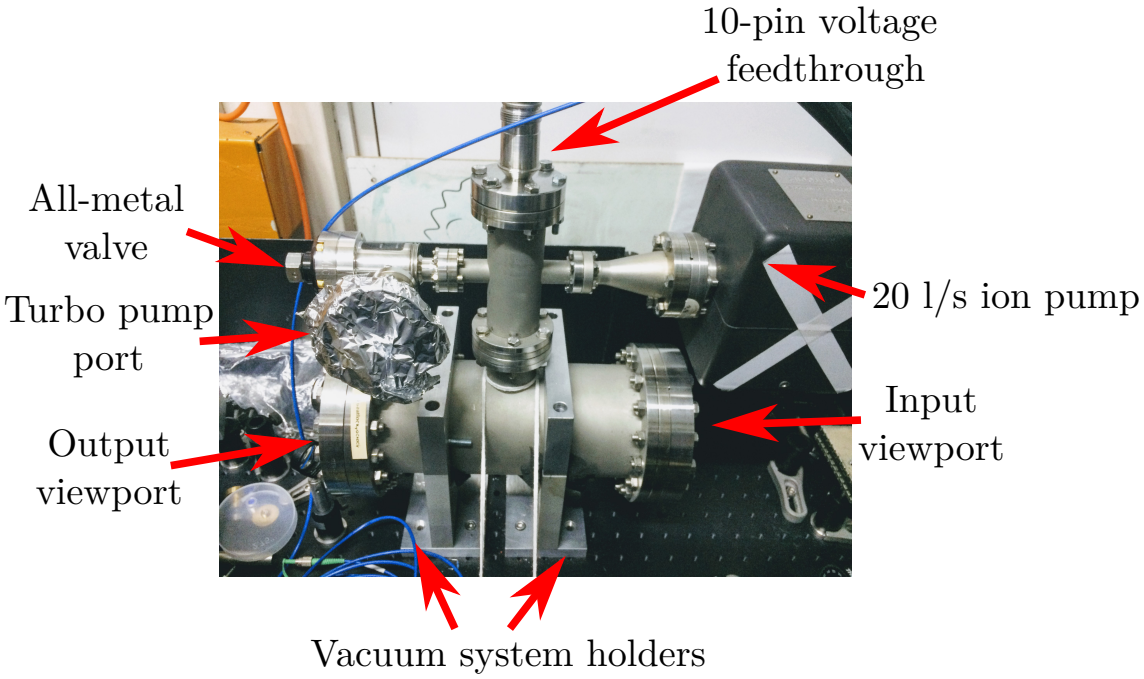

Figure 3.25: The assembled vacuum system. The optical breadboard sits on a standard desk with 5 cm of padding.

To restrict thermal flow between the vacuum system and the glass block, the cavity assembly is held by two small footprint aluminium v-shape brackets seen in fig 3.23a. To reduce thermal fluctuations due to convection, the system needs to be evacuated and maintained at a pressure of 10^{-6} mbar. This can be done by initially using a turbo pump and subsequently an ion pump. To reduce the background pressure due to absorbed water and gases within the vacuum system wall, the system is baked at 90° C after which the turbo pump is valved off[29] and disconnected from the system. The ion pump and valve are mounted on a cross-piece and permanently attached to the main vacuum system. A ten pin electrical feedthrough[30] is used for supplying DC voltages to control the cavity length via piezoelectric transducers. The initial design of the vacuum system included an in-vacuum Peltier element for temperature control of the block, but this was later removed for better vacuum performance. The idea to use the in-vacuum Peltier was motivated by work done on similar systems, where the coefficient of thermal expansion for ULE glass was reported to have a temperature dependence [157, 158], with an effectively zero point sitting in the range from −4° C to 20° C. The exact value depends on the manufactured batch and the machining properties of the block. The temperature of the block was assumed to be at room temperature (23 °C). In future experiments, the system will contain an insulating box with a heating stage for temperature control.

[29] MDC Vacuum MAV-075-V
[30] MDC Vacuum IFA10-C40

Cavity operation

The cavity was operated using one of the Ti:sapphire lasers by picking off a portion of the 739 nm light and launching it into the cavity. The alignment is performed by scanning the laser's frequency by several GHz and observing the intensity of the transmitted light at the output end of the cavity.

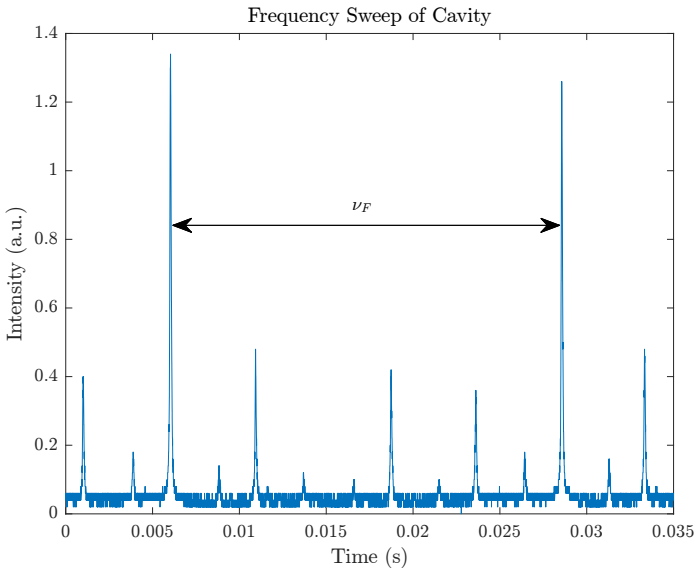

Figure 3.26: Frequency sweep over a free spectral range of the assembled cavity measured with a photodiode at the output. The larger peaks correspond to the fundamental longitudinal frequency modes with the adjacent smaller peaks belonging to the transverse modes, which are spaced unevenly.

During initial setup, a camera was used to confirm that the mode in use is the TEM00 transverse mode and was then replaced with a photodiode, which proved to be good enough for day to day use as the alignment did not change significantly. The use of this mode simplifies the locking procedure, since it produces the strongest error signal as illustrated in fig 3.26. Since the free spectral range is ≈1.5 GHz, the calculated finesse for the 739 nm wavelength is 243, which gives a linewidth of 6.2 MHz for the fundamental longitudinal mode.

By applying voltages to the piezo transducers, the resonant frequency of the cavity can be tuned, but as the settling time of the piezo transducers can be quite long, both piezoelectric rings have to be used such that their drift cancels out. To do this, the smaller diameter piezo ring has a voltage applied that is ten times less than the larger ring. During use of the cavity it was noticed that leaving the piezo transducers floating in voltage caused significant drift over time, therefore all of the channels on the DC supply were operated at non-zero values. As the 739 nm laser was already frequency modulated with a small

amplitude voltage via a fast piezoelectric transducer within the laser, it was possible to use a lock-in amplifier to generate an error signal from one of the available resonant frequencies. The PID controller was implemented using an FPGA platform[31]. The stability of the cavity was assessed using a wavemeter . The performance of the low drift cavity shows adequate performance, comparable to that of 780 nm Rb referenced laser, but having the advantage of easy frequency tunability. The system could be improved by placing the cavity vacuum system under a better controlled environment with temperature control and reduced acoustic interference. Despite the low-drift cavity showing better stability

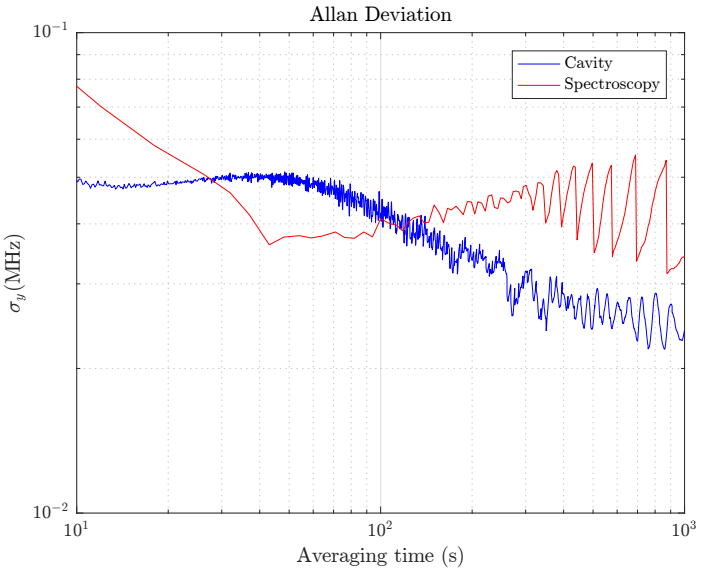

Figure 3.27: Comparison of the Allan deviation of a 739 nm laser stabilised to the low drift optical cavity and the 369 nm fluorescence data from the spectroscopy lock described in 3.5.1. The 739 nm laser shows better stability for averaging times longer than 100 s.

compared to the spectroscopy method, it does not achieve the stability requirements set out in the beginning of this section. To achieve the required stability, the system will be improved by isolating the optical setup and adding temperature stabilisation of the vacuum system. Furthermore, the reduction of the background pressure inside the vacuum system has indicated a significant improvement, which will be investigated by baking out the system.

3.5.3 Laser frequency offset lock

The need to address both $^{171}Yb^+$ and $^{174}Yb^+$ isotopes requires lasers at different wavelengths, as the additional neutrons in the nucleus shift the energy levels of the valence

[31] Toptica DigiLock

electron. The shift of interest is in the Doppler cooling transition by 2 GHz, which is too large to be efficiently shifted by an AOM, without introducing significant power losses. It is desirable to be able to transfer the stability of a laser dedicated to $^{171}Yb^{+}$ to a laser used for $^{174}Yb^{+}$ experiments. Instead of using a transfer cavity, a more compact solutions is to use the laser beat scheme described in section 3.3.

The beat frequency of two lasers can be detected by overlapping the two independent beams onto a photodiode. The combination of two oscillating fields will produce the sum and difference frequency components of the two beams. The overlap of the two beams is achieved by using a 50:50 beam-splitter, with one output of the splitter used for checking the overlap while the other is measured by a fast photodetector as shown in fig. 3.28.

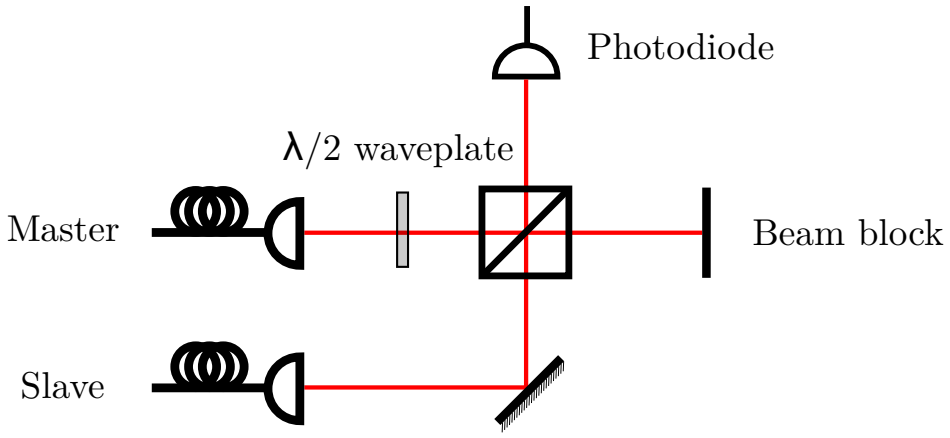

Figure 3.28: The optical setup for measuring a beat signal between the master and slave laser. The beam block also serves as an indicator for checking beam overlap.

The limit of the detectable frequency difference is determined by the photodetector, whose bandwidth can be approximated by $f_{BW} = \frac{1}{2\pi R_{load} C}$. The goal of increasing the bandwidth reduces to achieving the lowest possible resistance and capacitance of the circuit. For detecting frequency offsets in the GHz range, a Si photodiode[32] is biased with 15 V to reduce the capacitance of the semiconductor junction and terminated onto a 50 Ω bias tee[33], which allows to combine and separate the DC bias and the beat signal on the output port of the bias tee.

As all of the 369 nm lasers are frequency doubled, there is a significant amount of light available at the 739 nm wavelength. The two 739 nm beams are picked off with a sampler and fibre-coupled into single-mode polarisation maintaining fibres[34]. Using the same type

[32] Hamamatsu S9055-01
[33] Mini-Circuits ZX85-12G-S+
[34] Thorlabs PM780-HP

of fibres and couplers alleviated the mode-matching onto the photodiode as both beams were the same mode from the fibres and the collimated beam diameter was almost identical (≈1.5 mm). One of the beams had a $\lambda/2$ waveplate such that any polarisation mismatch could be corrected. The overlap was achieved using 500 µW of output beam power from the fibres. Even with the simplification of using single mode fibres, the signal from the photodiode needs to be amplified by 54 dB using three successive 750 MHz bandwidth RF amplifiers[35] to a −3 dBm level for further processing. A sample of a 63 MHz beat signal can be seen in fig. 3.29. The bandwidth of the amplifier would suggest that the

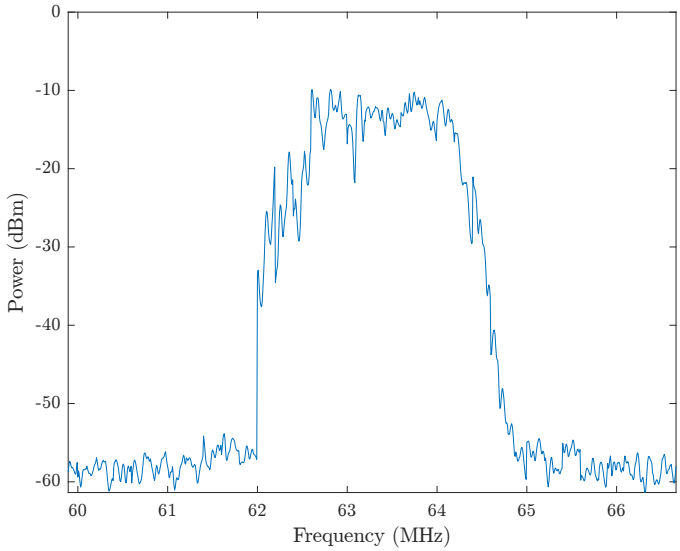

Figure 3.29: Spectrum of a beat signal measured on a spectrum analyser. The width of the peak is ≈3 MHz set by the linewidths of the 739 nm lasers and the amplifier noise.

limit of the offset frequency is 750 MHz, but measuring the signal on a spectrum analyser revealed a limit of ≈2 GHz, where the beat frequency was increased until the power level was measured to be below the −3 dB level. Keeping in mind the main light of interest is 369 nm, the maximum offset is then 4 GHz, which is more than enough to span the isotope shift. To convert the frequency difference into a control signal, this beat signal is mixed with a reference frequency to obtain the error signal using a PLL[36] (phase lock loop). A phase lock loop is primarily used to tune the frequency of a voltage controlled oscillator (VCO), but in the case of laser stabilisation the VCO output is replaced with the beat signal and the loop filter encompasses the PID circuitry. The final implementation of the PLL circuit can be seen in fig 3.30.

[35] Mini-Circuits ZFL-750+
[36] Analog Devices EVAL-ADF4007EBZ1 evaluation board

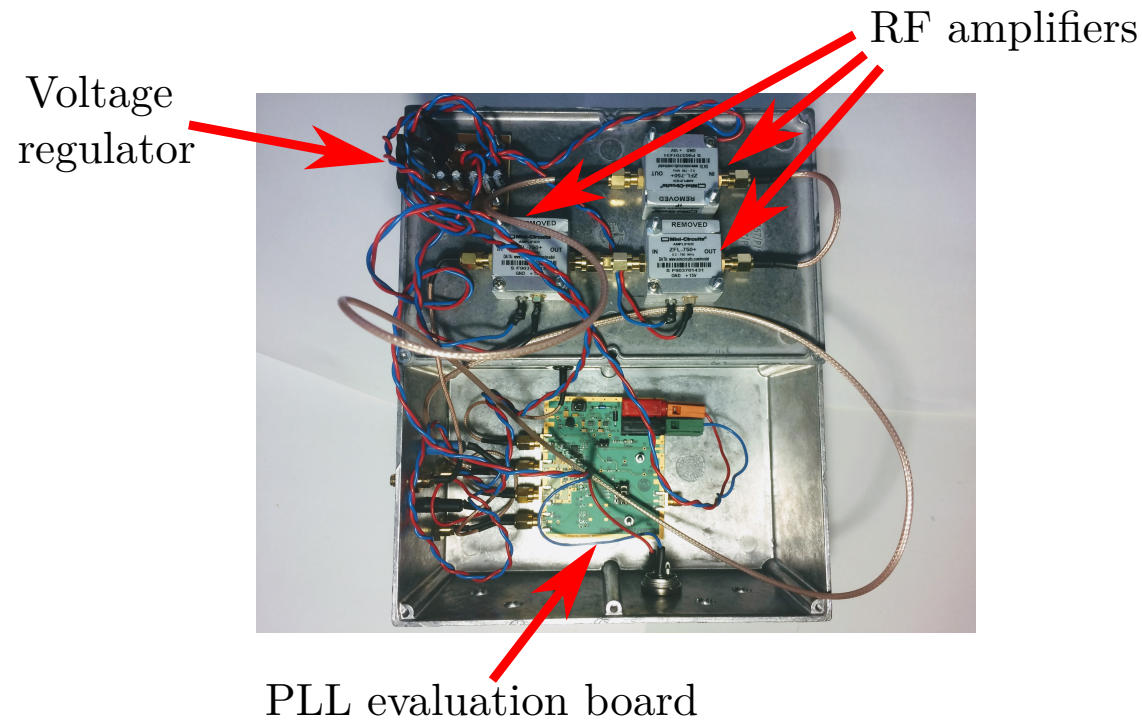

Figure 3.30: The electronics system for amplifying the beat signal and processing for laser stabilisation. A 15 V voltage regulator provides power to the RF amplifiers, PLL board (lower half) and the bias voltage for the photodiode.

In this particular scheme, there are two references that need to be considered, the master laser and the reference RF source. As most modern signal generators have a frequency stability of 1 ppb, the RF source is not assumed to be the significant limitation of the system. The master laser used was one of the doubling lasers, which was pre-stabilised with the Rb reference. The lowest achievable offset was limited to 40 MHz as the combination of the drop in the amplifier gain did not allow a sufficient amplitude signal for the PLL. The Allan deviation of a beat signal between two lasers is given in fig 3.31. The data indicates a stability of 100 Hz for averaging times of 1000 seconds, limited by the reference radio-frequency stability.

Although the system built in the lab was only tested with 739 nm beam, the use of 369 nm is still possible with the requirement of using more power for the UV beam, due to the sensitivity of the Si photodiodes being lower for wavelengths $<$400 nm.

3.6 Conclusion

This chapter described the fundamental principles of active feedback systems and stability analysis used in laser control systems. Different optical references and feedback systems are presented and discussed for use in trapped ion experiments. Following this, a ver-

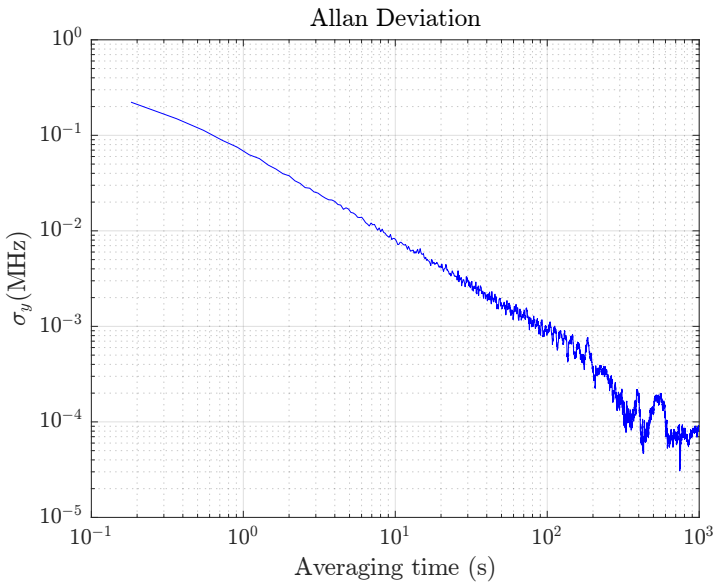

Figure 3.31: The Allan deviation of a 739 nm laser locked with an offset of 408 MHz from another 739 nm system, which is stabilised using the Rb spectroscopy scheme. As expected, the profile has the same features as a white noise signal as described in section 3.2.6 with no visible drift. This is due to the stable radio-frequency reference signal.

satile stabilisation system was designed for the laboratory and implemented to provide six experimental ion trap systems with frequency stabilised lasers for manipulating Yb^+ and Ba^+ ions. Finally, the individual components of the control schemes were described and their performance evaluated. The obtained Allan deviation data confirms that the system performs as intended, with further improvements possible, which have also been highlighted.

Chapter 4

Experimental system for implementing high-fidelity two-qubit gates

4.1 Introduction

Trapping and manipulating ions requires sophisticated devices and instruments. The aim of engineering an experimental setup is to build a system capable of having long trapping lifetimes, low noise electronic signal delivery systems and sufficient shielding from external environment fluctuations. Owing to the reduced ion-electrode distance in a microfabricated surface trap, these requirements constitute a challenge for building a scalable processor using trapped ion qubits. In order to couple the internal and motional states, a precisely aligned magnetic field gradient is required at the vicinity of the trapped ion, which requires precision ion positioning. Furthermore, the reduced ion height increases the anomalous heating rate due to surface imperfections, which results in larger infidelities in two-qubit gates. To address these challenges, two experimental systems were designed and assembled for the purpose of having a large magnetic field gradient on a surface ion trap with the goal of minimising gate infidelities described in chapter 2.

This chapter covers the assembly of an experimental setup consisting of a surface trap with permanent magnets housed within a vacuum system capable of reaching UHV (ultra high vacuum) and the ability to cool the ion trap temperature down to 70 K. A description of the ion trap mounting structure is presented with particular attention given to the in-vacuum PCB assembly used for electronic signal delivery. In addition to the vacuum system, the external RF and microwave emitters are discussed in detail. Most

of the work was carried out by previous PhD students[1] and more detail can be found in their theses. My contribution to this work includes the development of surface ion trap treating procedures, trap electrode electric potential simulation for trapping ions within a magnetic field gradient and the assembly, and operation of the experimental system.

4.2 Microfabricated ion traps for high fidelity gates

As detailed in chapter 2, to be able to impart a significant spin dependent momentum kick on an ion using microwaves, a magnetic field gradient must be generated within the trap potential. This can be achieved by placing either current carrying wires or permanent magnets in close proximity to the ion trap. The strength of the gradient determines the effective Lamb-Dicke parameter and can thus affect the speed of the entangling gate. For typical few centimetre scale ion traps, the simulated field gradient can be up to 150 T/m [39].

Following the example of atom traps [159], it is possible to generate the magnetic fields using current-carrying wires. However, the current required to generate a gradient of the same order of magnitude leads to dissipating a large amount of heat into the trap substrate. Despite this, methods of generating gradients with current-carrying wires is still being investigated and promises to provide the ability to control the strength of the magnetic field [160]. This method is the core constituent of generating gradients in a large scale quantum computing architecture [45]. In the meantime, a pair of permanent magnets is used instead to generate a large gradient with a nil at the trapped ion position.

The main limitation of the achievable gate fidelity was assumed to be the anomalous heating rate and the secular frequencies of a trapped ion [67]. These two effects are governed by the ion-electrode distance, which is commonly referred to as the ion height. The optimum ion height was estimated to be in the range of 150 µm to 165 µm, which in conjunction with a simulated magnetic field gradient of 140 T/m was projected to give a gate fidelity within the range of 99.9%.

The optimised electrode geometry for a surface trap with a 165 µm ion height can be seen in fig. 4.1.

[1] Dr David Murgia and Dr Eamon Standing

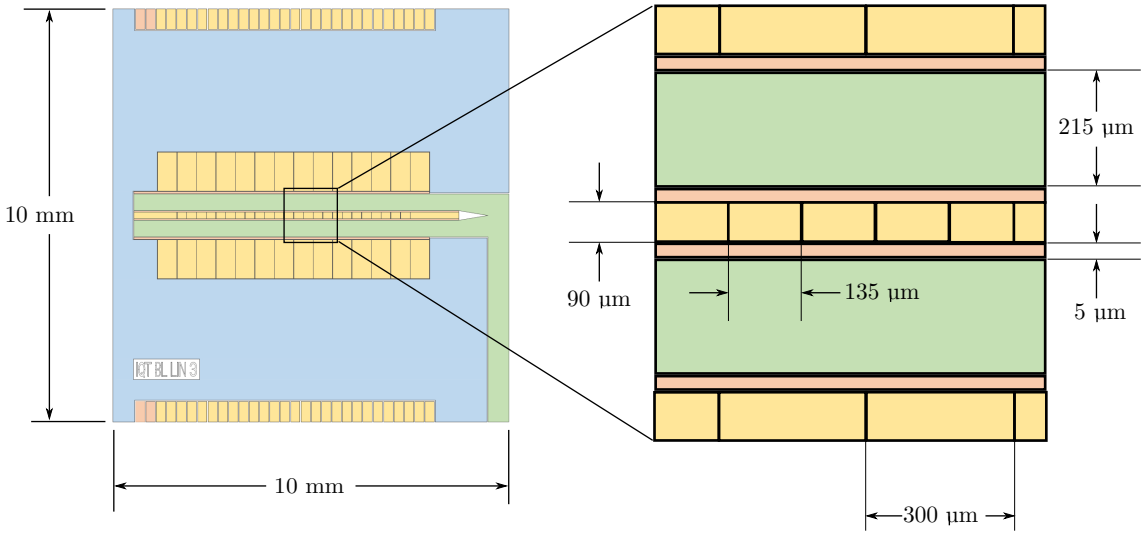

Figure 4.1: The layout of the 165 µm ion height linear trap. The electrodes are grouped in the following colours, green - RF drive, yellow - DC for axial confinement, red - DC principal axis rotation electrodes. The blue structure is the ground plane for both DC and RF signals. The bond-pads for the DC electrodes are placed at the top and bottom of the trap structure. Adapted from [67].

The trap contains segmented DC electrodes situated in between the RF rails, which optimises the ion's trapping potential for processes such as ion shuttling, separation and recombination. However, such structures require connections to their respective bond-pads that cannot fit on to the top conductive surface. Therefore, the bond-pad connections are provided by electrically conductive wires within the trap substrate and vertical interconnect access (VIA) providing the connection between the buried wires and the electrode surface. A short summary will be given here, with the fabrication methods and techniques detailed in the thesis of Dr. Bjoern Lekitsch [82]. These procedures are vital in describing the problems encountered with the fabricated traps and the methods developed to treat them.

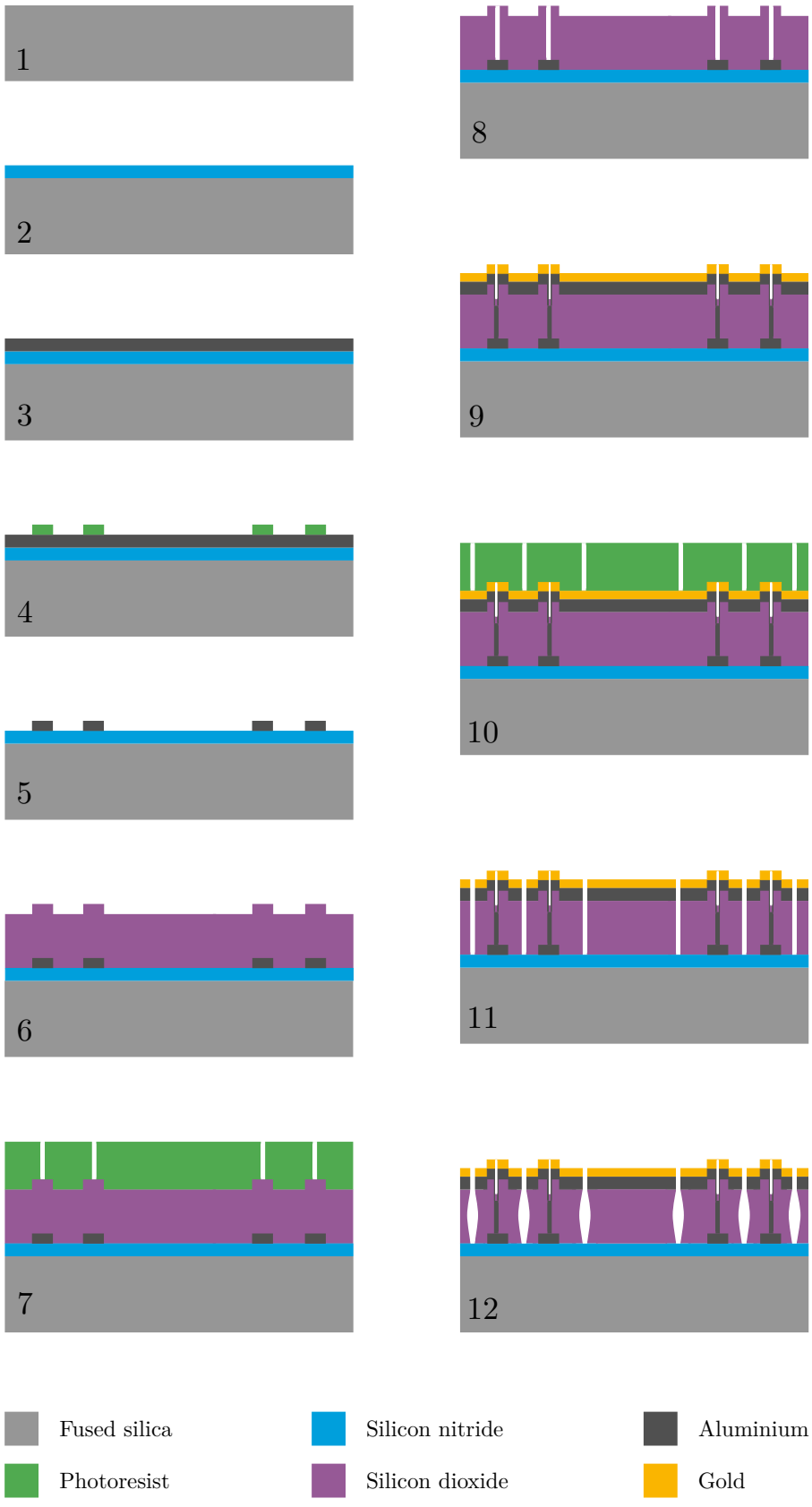

Figure 4.2: The stages of the fabrication process, adapted from [67] with the steps described in the main text. The traps were fabricated on fused silica, with the conductive layers formed with aluminium. These layers are insulated using a thick layer of silicon dioxide. The layer of silicon nitride is deposited to make the traps resilient to bulk voltage breakdown.

Microfabrication relies on photolithography to imprint a desired design onto a surface with the use of a mask and photoresist, where the photoresist is a material sensitive to light, which can be grouped by type into positive and negative. When positive photoresist is exposed to light, it becomes soluble and can be removed with solvents, whereas any shadowed areas will remain. The same is true for negative photoresist, but the unexposed material is soluble instead. The purpose of the mask is then to form shadows with the right pattern, which is transferred to the photoresist by light exposure. To deposit an even layer, the substrate is spun at a high rate as the photoresist is dripped onto it. By using multiple stages of photoresist and mask exposure, it is possible to build up multi-layer traps with designs similar to the one in fig. 4.1.

The fabrication follows steps detailed in fig. 4.2. The trap was fabricated on a 650 µm thickness fused silica wafer (1), which was cleaned using fuming nitric acid and microwave plasma followed by first sputter depositing a 200 nm thick silicon nitride insulator layer (2) and another round of cleaning with argon plasma. Due to superior insulator properties when compared to the standard silicon dioxide, the silicon nitride layer was found to significantly increase the breakdown voltage of the trap [83]. The plasma cleaning process removes any organic contaminants that might accidentally deposit on the surface and form unwanted patterns or cause chemical reactions during exposure to chemicals. The next step of fabrication is forming the buried wire structure, which is carried out by laying down a 450 nm thick aluminium layer (3) and positive photoresist. By itself, aluminium does not have good adhesion to insulators, which was improved by depositing 20 nm thick titanium layers before and after the aluminium, not shown in the figure. The buried aluminium wire pattern is formed by using a 1 µm thick layer of positive photoresist and placing the mask on top, after which it is exposed to UV light. After removing the exposed photoresist with solvent lift-off (4), the unnecessary aluminium is then wet etched to reveal the buried wire layout (5). The wires are isolated by depositing a 3 µm insulating layer of silicon dioxide (6) using plasma-enhanced chemical vapour deposition (PECVD). To form the VIA connection, a 5 µm layer of negative photoresist is applied and is UV exposed to form the conducting channel for the bottom aluminium layer (7). To go through the silicon dioxide layer a dry etch is used, after which an oxygen plasma asher is used for cleaning up the photoresist (8). The aluminium VIA and the top conducting layer are formed in one single sputtering process, obtaining a 1 µm thick layer of aluminium, above the silicon dioxide. Not shown again, are the 50 nm titanium adhesion layers, sandwiching the aluminium. The top layer is finished off with a 250 nm sputter deposited gold (9) to

form a protective barrier from oxidation and chemical reactions.

To form the top electrode structure, positive photoresist is deposited to form a 5 µm thick layer followed by the placement of the electrode layer mask, which is then exposed to UV to imprint the required design (10). An inductively-coupled plasma (ICP) etch is needed to go through all of the deposited layers of gold, aluminium and silicon dioxide. The remaining photoresist is cleaned off with fuming nitric acid and oxygen plasma (11). Finally, a wet etch with hydrofluoric acid is used to form undercuts into the silicon dioxide layer (12). The formation of undercuts isolates the individual electrodes, preventing current from flowing through the silicon dioxide, which can damage the trap [161]. The additional benefit of using the undercut is the better shielding from the dielectric substrate, which can charge up and influence the trapping field seen by the ion.

The fabricated wafer is then diced into individual squares of 12 × 12 mm using a diamond scriber, which contains the trap structure and a small edge of fused silica which can be used to safely handle the chip without touching the electrode geometry. The finalised chip can be seen in fig. 4.3. The thickness of the trap was measured to be 0.69 mm, a parameter which is vital for precisely aligning the trap to the permanent magnets.

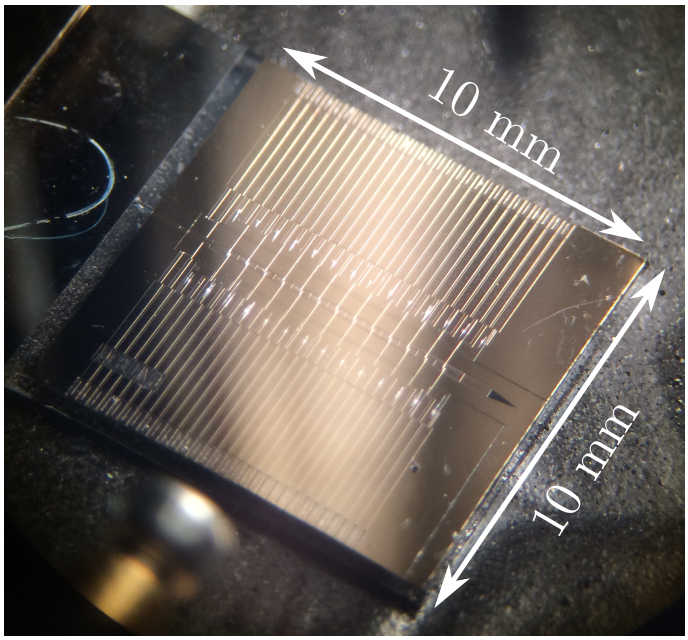

Figure 4.3: The finished microfabricated ion trap.

Although the fabrication process can be itemised in easy steps, the whole procedure is sensitive to the performance of tools used for depositing material and cleaning. Unfortunately, the received traps were covered in contaminants, had shorted electrodes and the inner segmented electrodes had non-negligible resistances to their bond pads. In order to solve these issues, an extensive procedure was developed, which I describe in the following

section.

4.2.1 Trap treatment

To verify the performance of the trap, rigorous tests were required to search for debris in between the electrodes, and for any other contamination. The most simple method is by using a microscope to image the trap and a multimeter for checking the electrical connections. Electrical testing of microfabricated traps can be quite delicate due to the size of the electrodes, therefore a micrometre precision system built by Dr. David Murgia [67] was used to check the connectivity of the trap electrodes, seen in fig. 4.4. The testing stage consists of two thin needles mounted on high accuracy positioners. The sample is held down by suction cup tape, which does not contain any adhesives that remain on the back of the chip. The needles are connected to a multimeter, which can be used to measure resistances between neighbouring electrodes or the bond pad to electrode connection. Using this measurement stage, the traps were found to have several shorted electrodes, with neighbour to neighbour resistances of 500 Ω. Further analysing the trap surface revealed a multitude of issues with the traps. The solutions to these problems included the removal of leftover photoresist and etching of a gold layer.

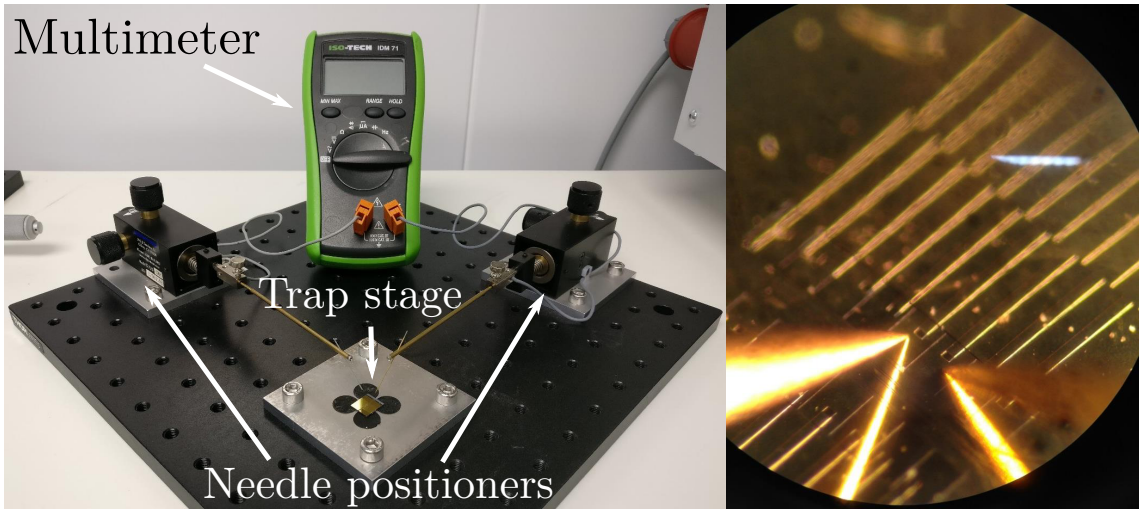

Figure 4.4: Left - the electrical connection testing stage. Right - microscope image of the needle making contact with an electrode.

4.2.2 Photoresist removal

Testing the electrical properties of the sample trap electrodes revealed multiple shorted electrodes, which could not be seen by using an optical microscope. A scanning electron microscope (SEM) imaging system, capable of resolving features the size of less than 1

µm, was used to inspect traps for contamination. The images, seen in figures 4.5a and 4.5b revealed poor quality gaps with thin layers overhanging above them. In addition, the trap surface was dotted with spots, which could not be removed using acetone or isopropyl alcohol ultrasonic baths. However, these images did not provide the underlying explanation for why only some electrodes were shorted and others were not, but treating these issues served as a starting point to the process of improving the fabrication of the trap.

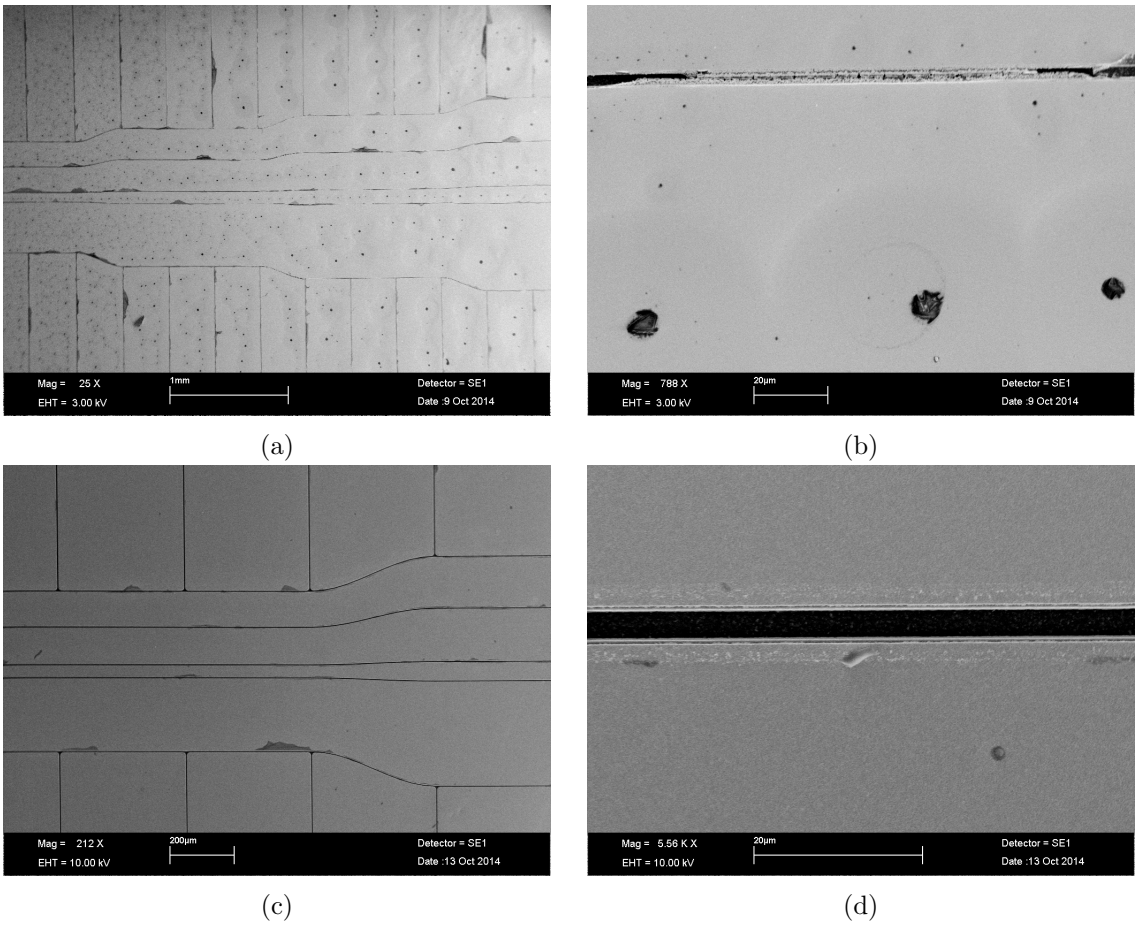

Figure 4.5: Trap SEM images before ((a) and (b)), and after chemical treatment ((c) and (d)).

The first guess for the origin of these deposits was the final photoresist layer, which was cleaned with fuming nitric acid and oxygen plasma. The failure of these processes might have left residual photoresist, which pointed to the possibility of removing these structures using a photoresist stripper solvent. To test this, a positive photoresist stripper[2] was selected for its low etching rates for metals (3 - 100 Å per minute for titanium and aluminium, no effect on gold).

The process of exposing the traps to photoresist stripper was optimised by varying

[2]MicroChemicals TechniStrip P1316

the exposure time, the temperature of the stripper and applying additional sonic bath treatments. The best results were obtained by heating a beaker of the stripper to 80°C and submerging a sample trap for ten minutes followed by a rinse with acetone and isopropyl alcohol to remove any residual stripper stuck on the trap. During the exposure the trap would be occasionally swivelled to remove the possible flakes of the photoresist, ending with a ten second ultrasonic bath. Figures 4.5c and 4.5d show the resulting effects of photoresist removal from a sample trap. The chemical treatment removed the overhanging flaps and the spots, which confirmed the assumption of the origin of these contaminants.

The presence of positive photoresist remnants can be explained by the fact that during fabrication it was deposited and then exposed to elevated temperatures to make it more robust for the later stages, a process known as photoresist hard bake. This however, makes it resilient to solvent lift-off or etching [162]. Considering that ICP etches can reach high temperatures, it is a likely candidate for causing the contamination of the gaps. The photoresist removal procedure was applied to different traps with a high success rate, with the next issue being the shorting of electrodes.

4.2.3 Gold etching

In an ideal ion trap, the RF electrodes are completely isolated from the rest of the trap electrodes, with resistances measured to be above 1 MΩ. The first complication encountered was the ≈100 Ω connection between the RF electrode and the trap ground layer. It was considered that these shorts could be removed by applying a 6 A constant current to burn them off, but it was discovered that they were more severe than initially thought. From the fabrication point of view, the RF electrodes can be shorted only during the deposition of the final layer of aluminium, titanium and gold. Furthermore, presence of photoresist in the electrode gaps implies that the ICP etch might not have performed as expected, leaving the gaps littered with metal particles.

SEM imaging failed to show any obvious shorts, however assuming a sheet of gold is deposited in the electrode gap, which has a width of ≈5 µm and length of ≈5 mm, fore a resistance of 100 Ω the thickness of such a layer is less 1 nm, which could not be imaged using the available equipment. To check this assumption, it was decided to remove thin layers of the metals used in fabrication,to see if shorts were also removed. The first material to be etched was gold using a commercially available etchant[3] based on an iodine solution.

[3] MicroChemicals TechniEtch ACI2

The gold etching rate was specified to be 40 nm per minute, which is relatively fast considering the top layer has a 250 nm thickness. Therefore, the etchant was diluted with deionised water to have a ratio of 1:5. With the slower etching rate, a sample trap would be exposed for different periods of time and electrically tested afterwards. It was found that the procedure was successful, confirming the assumption of metal being deposited or not etched away during fabrication. The optimum procedure, which does not remove all of the gold, included a ten second exposure to the gold etchant and a deionised water clean to remove any residue. This would then be followed by testing the connections on the needle stage. If the connection was still there, the exposure to gold etchant would be repeated. On average the traps required between one and two minutes of gold etching to completely remove the shorts. Although, there was no method of measuring the thickness of the layer removed by the etch, the trap colour changed from gold to slightly silver, which suggested that a significant layer was removed. The diluted etch rate is estimated to be 6.7 nm per minute, which allows to calculate the thickness of the shorting layer can to be 7 nm to 13 nm.

The procedure was successful on most traps, but there were a few samples which would remain shorted even when the whole gold layer was removed. It is possible that these traps could have aluminium or titanium deposits, which cannot be removed with the gold etchant. A different etchant could have been used for these metals, but the method was not investigated since these traps would only have aluminium electrodes which can oxidise and absorb unwanted gases.

4.2.4 Buried wire connections

One of the last issues with the traps was the buried wire resistances, which were measured to be in the range of 1 kΩ to 100 kΩ. Inspecting the trap with a microscope, showed large gaps in the buried wire-to-electrode connection. The presence of resistance in the DC electrode path can have an unwanted influence on the trapping potential. This is explained by a simple schematic seen in fig. 4.6. The inner DC electrode can be modelled to have a capacitance set by the dimensions of the electrode and a resistance due to the buried wire. Both of these are displayed as lumped elements driven by an AC source, which is the RF drive signal that couples to the DC electrode. One side of the capacitor corresponds to the RF electrode, whereas the other half is the DC electrode. For the DC electrode not to couple to the RF drive, the voltage between the capacitor and the resistor has to be zero. The voltage is set by the ratio of the impedances, which in the

ideal case is dominated by the capacitor, given by $X_c = 1/(\omega C1)$, where ω is the angular frequency of the driving source [145]. To prevent the DC electrode oscillating with the RF signal, the impedance of the buried wire must be much less than the impedance of the capacitor formed at the DC and RF electrode. An inner electrode with dimensions of 145 µm × 90 µm has a capacitance of ≈3.3 fF calculated from [163], which in order to have an impedance ratio of 1000:1 for an angular frequency of $\omega = 2\pi \times 25\,\mathrm{MHz}$, the resistance of the buried wire has to be below ≈1 kΩ. Due to the rotation electrode extending through the full length of the RF electrode, the capacitance of these features is increased by an order of magnitude, therefore a buried wire resistance of less than 100 Ω is desirable.

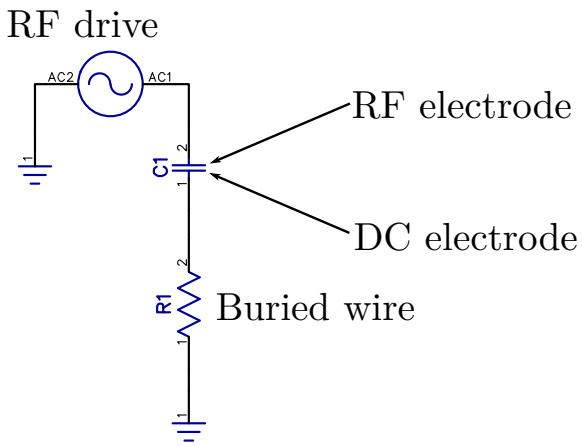

Figure 4.6: The lumped element circuit describing the effect of an electrode with a resistance to ground caused by the buried wire. One of the capacitor plates represents the DC electrode, while the other is the RF.

Reconnecting the buried wires to the electrodes was achieved by using the needle testing stage and dragging one needle over the gap while applying a lot of pressure on it. This caused the gold layer to slightly break up and be redeposited in the gap to make a connection. Although it would seem that these connections would be temporary, it was found that these new connections were resilient enough to be washed with solvents or any other handling procedure and still remain unaffected. The finished procedure resulted in inner DC resistances being reduced to 50 Ω to 500 Ω.

All of the encountered problems with this run of microfabricated traps were solved using easy to obtain tools and chemicals, while saving the time and effort of fabricating new samples in a cleanroom, which can be costly. Furthermore, the microfabrication

procedure was modified to account for these issues in the future. It was decided to proceed with these traps while new traps were fabricated.

4.3 Permanent magnets for the generation of a large static magnetic field gradient

To scheme for using long wavelength radiation to manipulate the motional state of the trapped ^{171}Yb ion relies on using magnetic field sensitive states with a static magnetic field gradient. Ideally the gradient has a 'nil' point where the absolute field is effectively zero and increases in magnitude along one of the chosen axes. A set of two magnets positioned with their poles opposite to each other produces a nil at a certain distance above the magnet surface, as indicated in fig. 4.7, which is also referred to as the magnetic nil height. In this configuration the magnets are attracting each other, therefore a magnet spacer is required, which sets the distance between the two magnets. For more details, the thesis of Dr Eamon Standing provides an in depth analysis of the scheme [164].

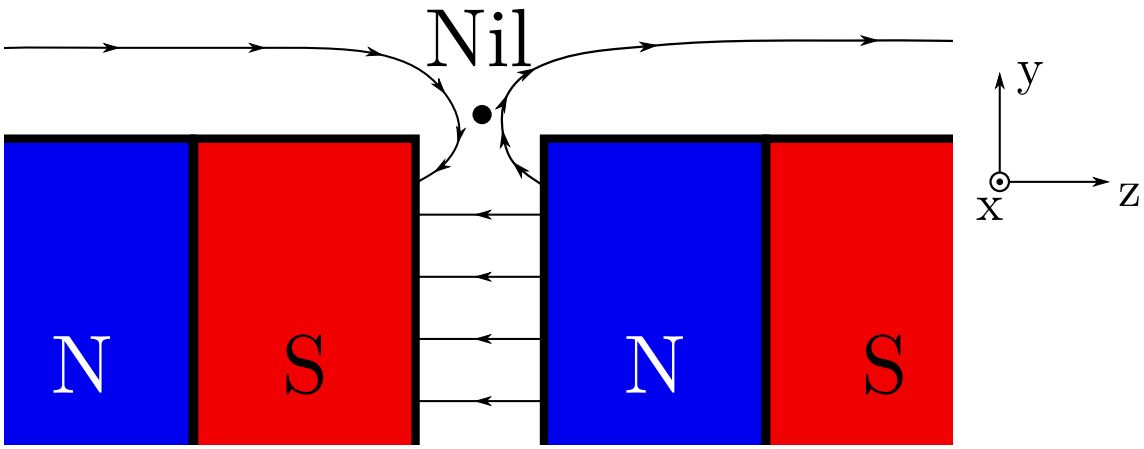

Figure 4.7: Illustration of the case where the magnets are held separated by a certain distance while facing each other with opposite poles. At the 'nil' point the magnetic field lines from each magnet cancel. Going away from the 'nil' along the z-axis, the field component B_y increases in magnitude, which is the required magnetic field gradient. The same is true along the y axis, which has a strong gradient for the B_z component.

The given illustration provides gradients along two axes, y and z, for the components B_z and B_y respectively. The alignment of the gradient relative to the principal axes of motion of the ion will determine which type of motional modes can be used: axial or radial. In this work, the gradient was chosen to be used with the axial motional modes (along z), which requires the magnets to be positioned as shown in fig. 4.8. The choice was motivated by the results obtained in [39], where the entangling gate utilised the

axial motional modes. The magnets are placed in a non-magnetic spacer, which sets their separation. The ion trap is then aligned relative to the magnets and lowered into contact. To fix the chip position, epoxy is applied on the side of the chip substrate. To avoid large magnetic field offsets, the critical parameter in placing the ion trap above a pair of permanent magnets is the relative distance between the RF and magnetic field minima. The trap RF nil is set by the position and width of the electrodes, therefore only the magnetic nil can be adjusted. This is done by changing the spacing between the magnets, as shown in fig. 4.9, where the magnetic nil position and gradient is plotted against the magnet separation. The strength of the gradient is determined by the remnant magnetic field of the samarium cobalt (SmCo) magnet pair, which in this case was 1.08 T with dimensions of 3.5 mm × 7.5 mm × 10 mm. The magnet design and simulations were carried out by Dr Eamon Standing using COMSOL Multiphysics simulation package, with a detailed description found in [164]. In this section only a summary of the results is given.

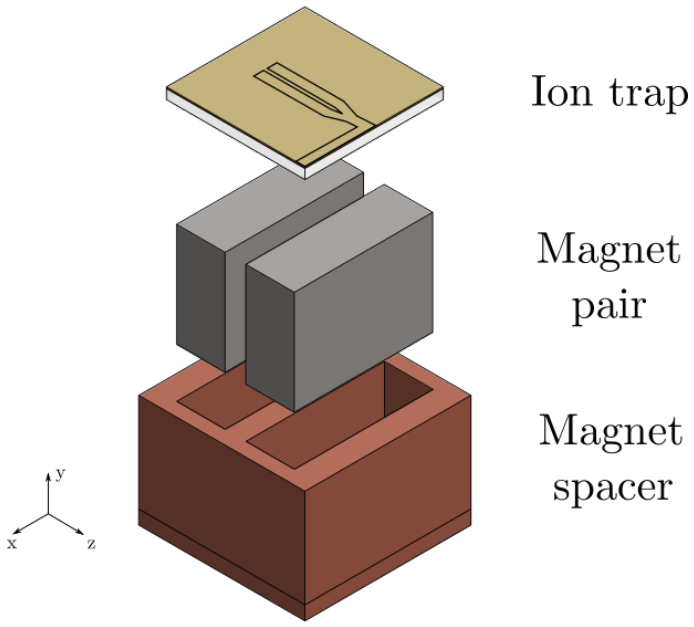

Figure 4.8: The trap placement to obtain an axial magnetic field gradient in the z direction.

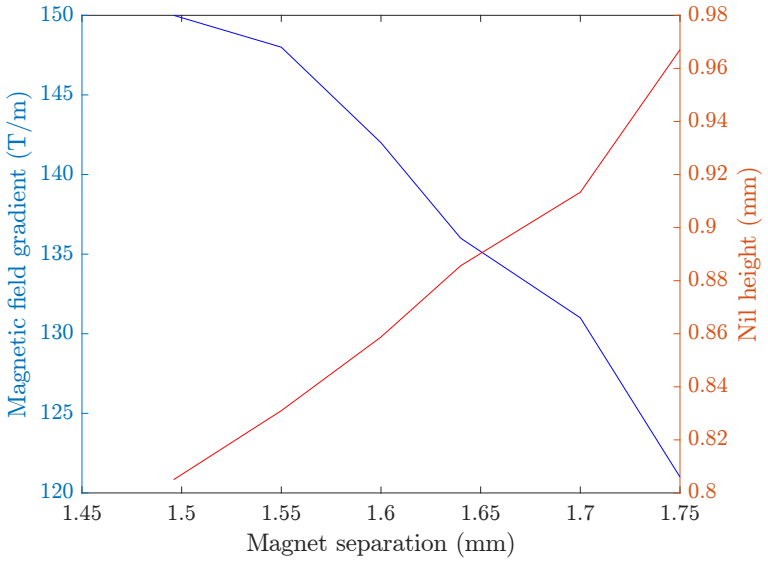

Figure 4.9: Plot of the magnetic nil height (red) and the gradient strength at the nil (blue) against the magnet separation, data collected by simulation.

The presence of a strong magnetic field gradient can introduce large field offsets due to large displacements from the magnetic field nil. Therefore, great care must be taken when setting the permanent magnet separation and aligning the trap structure relative to the magnets. The required magnetic nil height has to be equal to the sum of the trap thickness and the ion height, set by the RF nil position. In this case, the required nil height was calculated to be 0.855 mm, which for the chosen magnets require a separation of 1.56 mm. Simulating the magnetic fields at the ion trapping position, resulted in obtaining a 140 T/m gradient for the B_y component of the magnetic field, shown in fig. 4.10.

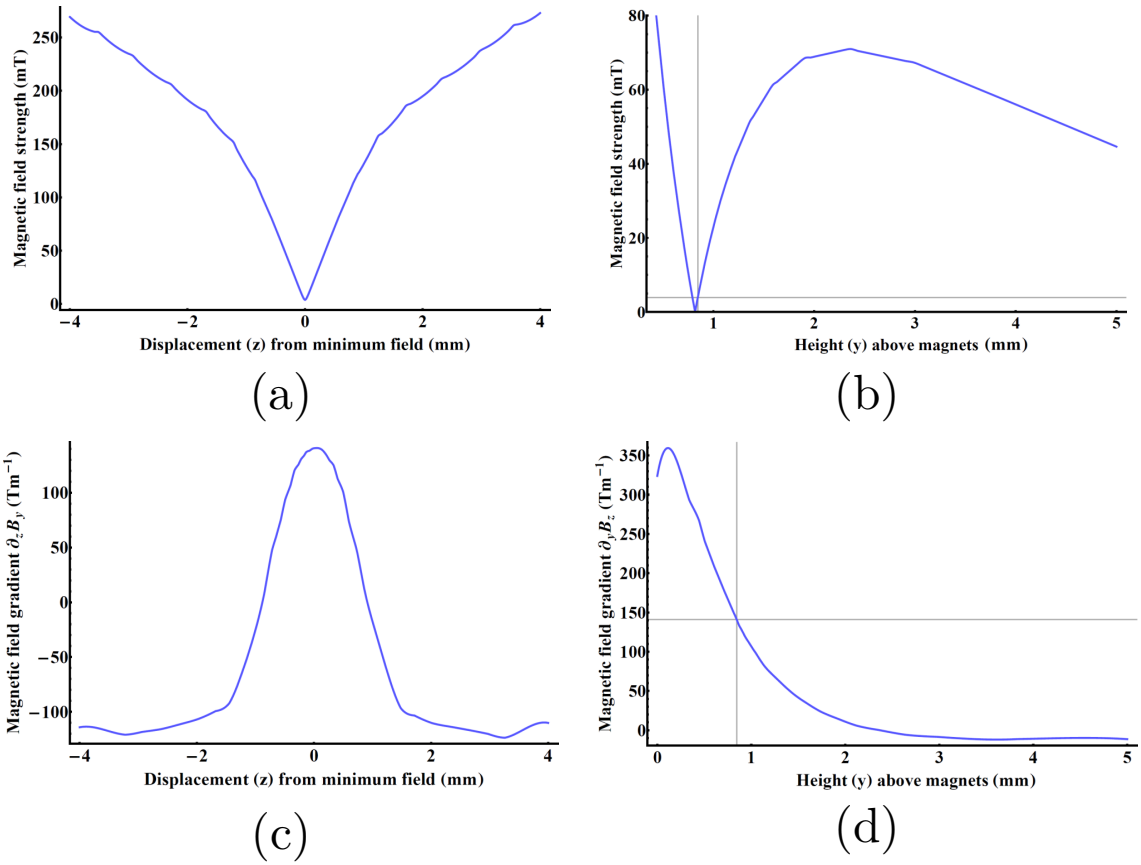

Figure 4.10: Plot of the magnetic field simulations along the different axes. (a) Plot of the absolute magnetic field strength which indicates a minimum at $z = 0$, (b) indicates the magnetic nil height of 0.855 mm above the magnet surface. The simulations show that there are two axes along which strong gradients are produced, (c) an axial magnetic field gradient of ≈140 T/m along z and (d) another one along y also with a gradient of ≈140 T/m. The remaining axis x has a negligible gradient. Adapted from [67].

The simulation results are used to find the required alignment precision in order to estimate the required precision when aligning the magnetic and RF nil positions. Misalignments along the y and z-axes will produce large magnetic field offsets determined by the misalignment factor of ≈1.4 G/µm. In order to keep the magnetic field below the 20 G limit given in chapter 2, the trap RF nil is required to be positioned within ≈14 µm of the magnetic nil. The required precision is minimised further by placing compensation coils and permanent magnets around the ion trap, as described in section 4.8, which can minimise the magnetic field by 60 G. This limit imposes the bound on the alignment accuracy of ≈40 µm for both the y and z axes. The y axis alignment is set by the magnet separation distance, thickness of the trap substrate and any unpredictable gaps between the magnet and substrate surfaces. Finding the gradient of the red line in fig. 4.9, an increase of magnet separation by 1 µm will change the magnetic nil height by ≈1.56 µm. To obtain an accurate magnet spacing, the magnet spacer is wire eroded out of copper

with dimensions given in fig. 4.11.

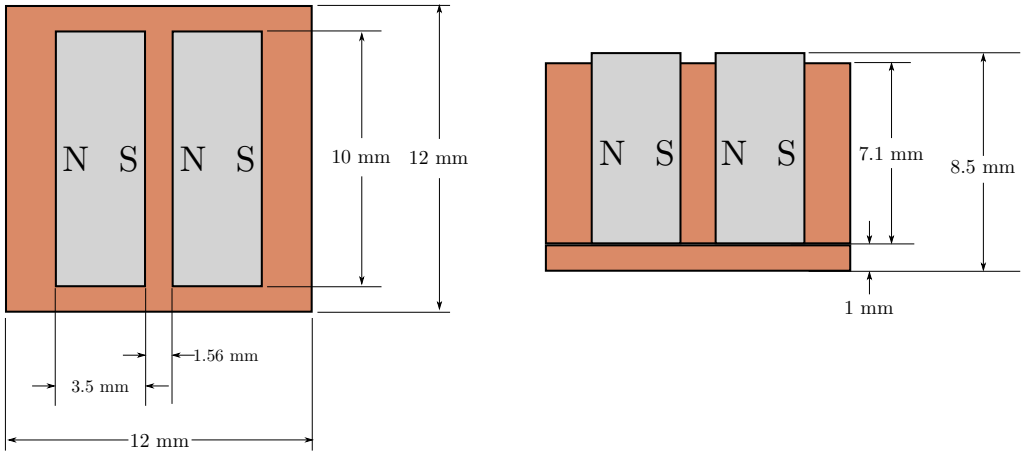

Figure 4.11: The top and cross-section of the permanent magnet spacer for generating a magnetic field gradient with a minimum at a distance of 0.855 µm.

The spacer material was chosen to be non-magnetic, which prevents it from being magnetised and distorting the field. The machined spacers required some filing to exactly match the designed dimensions, with errors minimised to less than 1 µm, confirmed by inspection with a microscope.

Once the magnets were placed in the spacer, the alignment of the trap relative to the magnets was achieved using a custom built alignment stage built by Dr. Eamon D. Standing, as seen in fig. 4.12. It contains a digital microscope for imaging the spacer and the trap, translation stages for all the axes, a heating stage and a trap holder which suspends the chip above the spacer with a suction pump. The heating stage is required to cure the epoxy for fixing down the trap to the spacer. As mentioned previously, the magnetic nil can only be misaligned by 40 µm along the z axis, set by the alignment accuracy of the stage. The whole assembly was tested and it was found to give an alignment accuracy of 1 µm. This was sufficiently accurate to place the trap on the magnets with little misalignment in the x and z-axes.

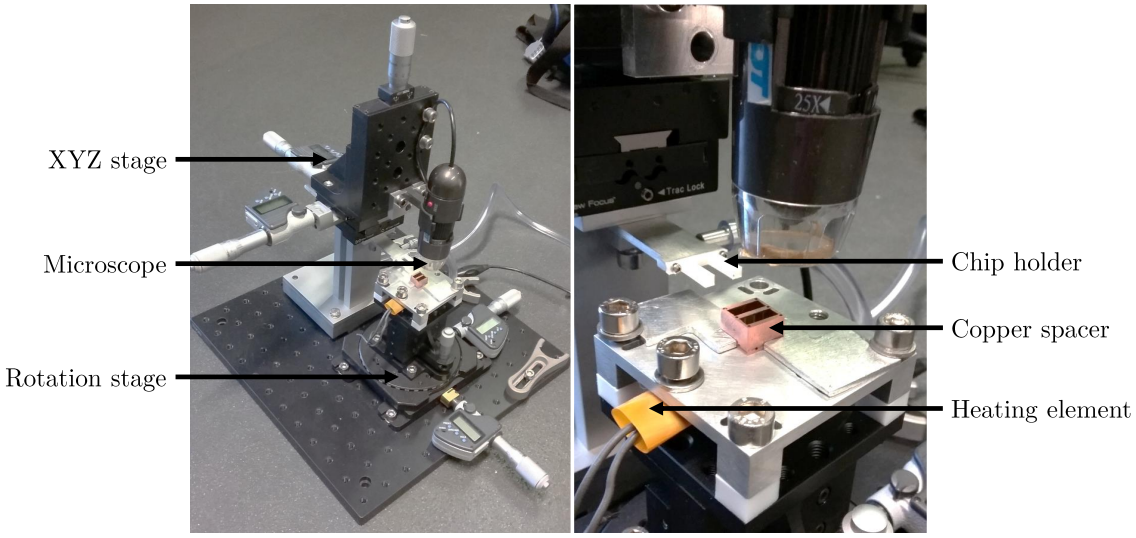

Figure 4.12: The trap alignment stage, image from [67].

The procedure of aligning the chip to the magnets starts by imaging the magnets and making sure that all translation stages are independent so that movement along the side of the spacer results in no additional movement in the perpendicular axis. The chip is then positioned above the magnet spacer using the holder and aligned relative to the magnets. The trap is lowered onto the spacer and epoxy[4] is carefully deposited on the corners of the trap, making sure that there is no epoxy in the gap between the trap and spacer. Finally, the heating stage is set to 100 °C and the epoxy is cured for one hour. During the curing process it is possible for the assembly to slightly move, therefore the trap was carefully monitored for any movement. The whole assembly was then remeasured and simulated to find any possible magnetic field offsets, which were found to be 17 G for B_y and B_z components, and 20 G for B_z with the a gradient of 140 T/m.

Although the magnetic field simulations suggested a strong gradient, it was decided to investigate the possibility of measuring the radial gradient of B_z with a magnetic field probe attached to a motorised placement stage to map out the field. The placement stage was limited to step sizes of 100 µm and the sensitivity of the probe (50 mV/T). In these tests only the magnet spacer with magnets was used, in order to avoid damaging the trap itself. The measured gradient was 20% smaller than expected (seen in fig. 4.13), but within the margin of error of the simulation, which confirmed the validity of the model. With this in mind, the trap assembly was placed in a modular trap mounting system within a vacuum chamber.

[4]EPO-TEK H21D

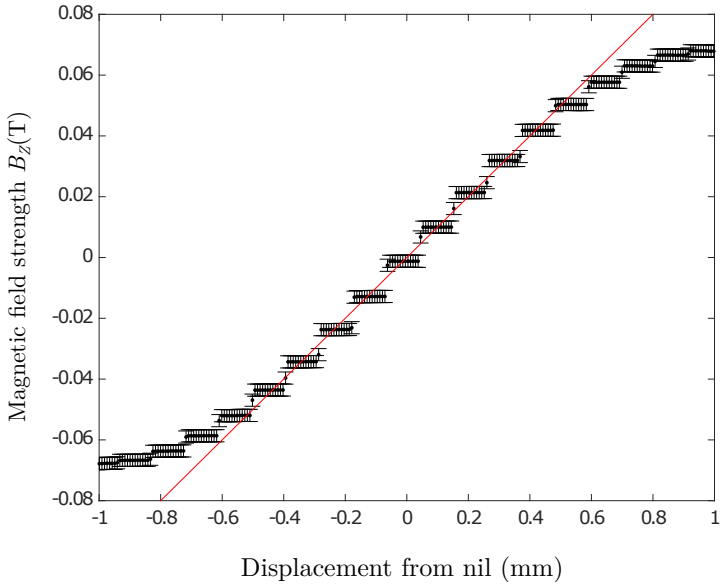

Figure 4.13: Dashed lines show the measured values of the magnetic field while moving the sensor along the trap z axis. The linear fit corresponds to a gradient of 100 T/m. Adapted from [164].

4.4 In-vacuum PCB and mounting structure

Microfabricated traps allow for precise control over individual ions. This comes with requirements of a large number of control signals used to manipulate the quantum state of the ion. With this increased capability, it has become a challenge to mount these traps inside a vacuum system and be able to perform quick maintenance. To address these concerns, a modular PCB-based mounting structure was designed for use on current and future experiments[5]. The new capabilities include hundred individual channels for DC signals, four high current channels and four 50 Ω matched channels for high frequency signals.

4.4.1 DC routing and filtering

The full assembly can be divided into two parts, which are referred to as the front and back PCBs. These are made from copper coated Rogers RO4350B substrates with an ENEPIG gold finish. The purpose of dividing their functions is to make the front PCB removable in case of the ion trap failing to operate as intended, while leaving the back PCB untouched, so that it can remain in the vacuum system for re-use. For this to be possible, a connection between the PCBs is made via spring-loaded (pogo) pins[6] which

[5]Designed by Dr. David Murgia and Dr. Bjorn Lekitsch.
[6]Mill Max 0852-0-15-20-83-14-11-0

come into contact by applying sufficient pressure. Both PCB components are described in the following sections.

Front PCB

The front PCB contains the surface trap with the attached magnet spacer, show in fig. 4.14a. The magnet spacer is epoxied onto a copper platform, as shown in fig. 4.14b. The purpose of the platform is twofold, one is to ensure a good thermal bridge between the ion trap and a heat exchanger (which is covered in a later section 4.7), the other is to provide a stable mount for the front PCB by having four connecting bolts, a set of two for the platform-front PCB connection and another set for the front PCB-heat exchanger contact point (see fig. 4.14a). The platform also sets the correct trap position above the front PCB, which guarantees unobstructed laser access to the ion.

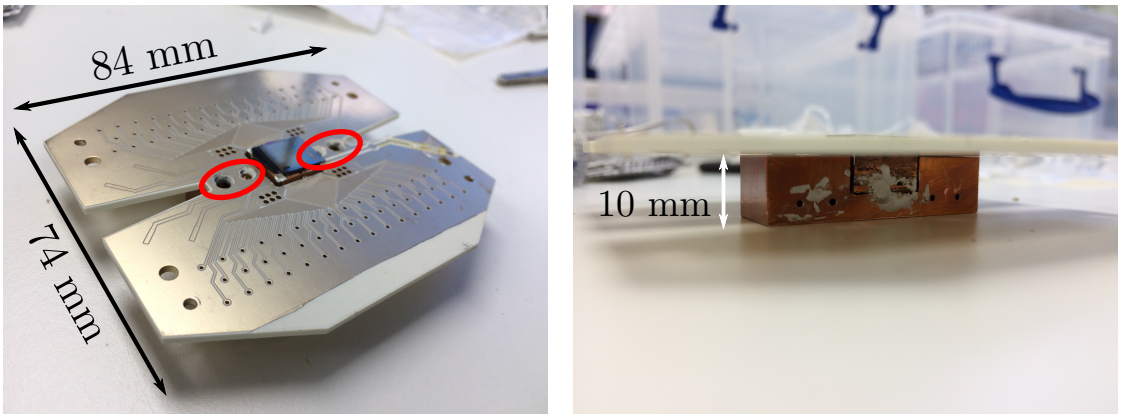

(a) (b)

Figure 4.14: (a) The front PCB with the trap assembly mounted using a set of tapped holes highlighted in red circles. (b) On the other side of the PCB, the ion trap and spacer assembly is epoxied onto a oxygen-free copper platform for setting the correct distance between the ion trap and PCB surfaces for unobstructed laser access.

In addition to providing access to DC electrodes, the front PCB contains four 50 Ω tracks for microwave frequencies, one track for the radio-frequency voltage path and four high current bondpads, seen in fig. 4.15.

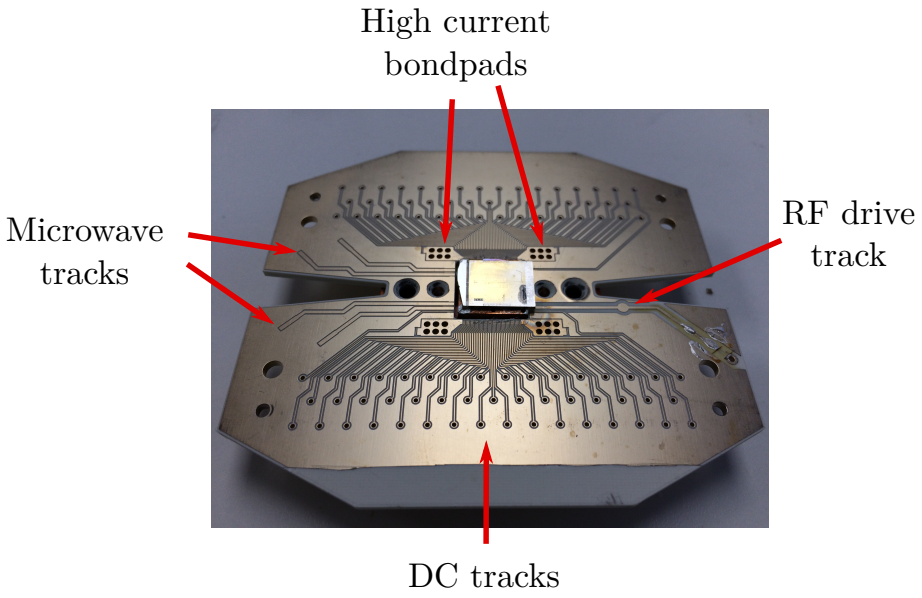

Figure 4.15: The track layout of the front PCB. The RF drive and microwave tracks are 50 Ω impedance matched and therefore require surface mount coaxial connectors to be used. In the case where the ion trap has current carrying wires to generate the magnetic field gradient, the front PCB has four high current bondpads, which can be used for contact.

The trap electrodes are then wire-bonded onto the front PCB bond pads with 25 µm diameter aluminium wire, in some cases double-bonding a single electrode. This makes it possible to monitor the applied voltage and reduces the risk of having a disconnected electrode due to a broken wirebond. The wire-bonded tracks break out into individual pins and connect to the VIAs which pass through the PCB substrate, where on the backside they correspond to individual circular pads. These in turn make contact with the spring loaded connectors of the back PCB.

Back PCB

The DC electrodes of the ion trap capacitively couple to the applied RF signal, which distorts the trapping potential. To avoid this, the DC electrodes must have a ground connection for oscillating voltages, which can be implemented with the use of a low pass filter. The filtering in this experimental setup is performed with the back PCB, which connects to the front PCB via spring-loaded connectors.

The spring-loaded connectors are soldered[7] onto the back PCB (see fig. 4.16) with the additional 1 kΩ resistors[8] and 620 pF capacitors[9] for filtering. The resistor and capacitor values were chosen to obtain a first order filter with a cut-off frequency of ≈260 kHz. The

[7] Multicore 96SCLF320AGS88 with use of Chemtronics Flux-Off Aqueous, process described in [165]
[8] KOA Speer RK73N2ATTD102M
[9] Presidio Components VP0505NP0621K150V4M1R6

cut-off frequency was chosen to provide a good ground for the trap radio-frequency filter, with the ability to perform high speed ion shuttling operations using the DC electrodes. The other side of the back PCB contains the 25-way DSUB connectors, which interface to four male cable connectors[10] containing pins[11] crimped onto a 25 wire ribbon cable[12]. The other end of the ribbon cable connects to a DSUB feedthrough[13] via two DSUB connectors[14].

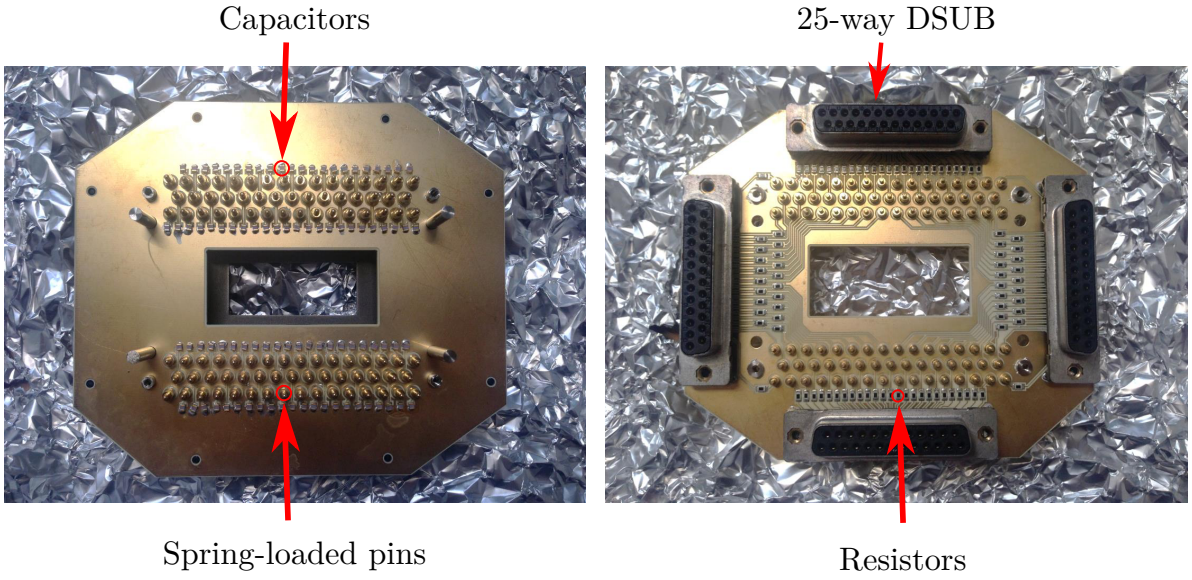

Figure 4.16: Both sides of the back PCB. The part contains the low-pass filter used for providing the DC electrodes a ground for RF signals, which otherwise can distort the trapping potential. The low-pass filter is formed by connecting the DC electrode to a resistor in series and a capacitor in parallel, with a cut-off frequency of 260 kHz.

The pressure applied between the front PCB and the connector was set using threaded inserts on the back PCB, which were epoxied into the circular holes in the four outer corners. The front PCB was then guided onto the back PCB while M3 socket screws were tightened into the inserts until sufficient contact was made, as shown in fig. 4.17.

[10] Allectra 211-MS25-PK-S
[11] Allectra 212-PINM-25
[12] Allectra 311-KAP-RIB25-1000
[13] Allectra 210-D50-C100-2
[14] Allectra 211-FS50-PK

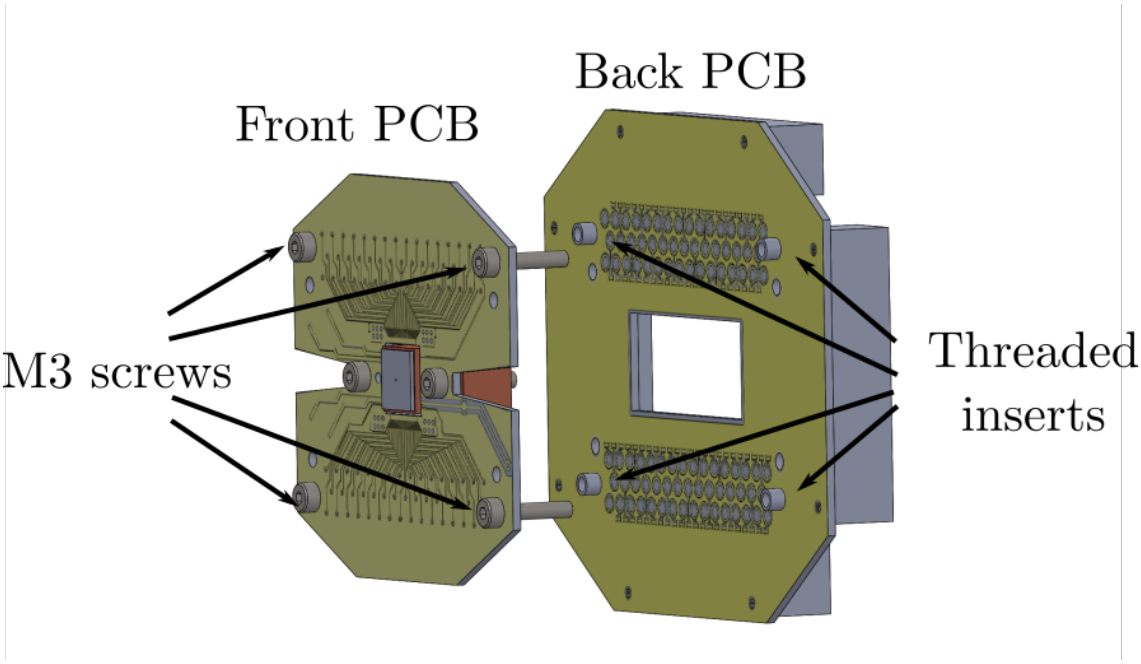

Figure 4.17: Exploded view of the PCB assembly. To apply sufficient pressure to the front PCB, the four M3 screws are tightened into the threaded inserts of the back PCB. The inserts are epoxied directly on the back PCB.

Once the ion trap assembly is positioned correctly in the vacuum chamber, the front PCB tracks are checked and mapped out onto the DSUB feedthrough. Although the DC signal path from the trap electrode to the DSUB connector contains in-vacuum filtering, there is still a possibility of injecting noise through the DC voltage source. To counteract this, an external low-pass filter box is mounted on the feedthrough, with a cut-off frequency of 32 Hz, which heavily attenuates high frequency signals that might be present. This completes the path for DC voltages from the outside source to the ion trap electrodes. The RF trapping signal requires impedance matching and larger voltages, therefore a more refined separate signal path is required, which is covered in the next section.

4.5 Trapping RF voltage delivery

To be able to confine ions above the trap surface, DC and RF voltages are used to generate a quadratic potential. The amplitudes of the applied DC and RF voltages define the a and q parameters described in chapter 2, for which the stability map shown in fig. 2.2 of section 2.2.1, indicates the required voltages to obtain a closed trapped ion trajectory. The stability indicates the relation $a < q$, which corresponds to applying significantly larger RF amplitude signals when compared to the DC values. The absolute value for the required voltages is determined by the requirement to reach a trap depth of at least

0.1 eV, given by eq. 2.7, which is sufficient to trap high energy atoms leaving the oven. To achieve this for $^{174}Yb^{+}$ a typical trap will have several hundred volts applied to the RF electrodes at frequencies of 10 MHz to 30 MHz.

Using the in-vacuum modular system, the ion trap RF drive is delivered via an SMA-SMP coax cable and an SMP connector[15] epoxied onto the front PCB and wire-bonded to the trap RF electrodes. The requirements for a high fidelity two qubit gate point to large axial secular frequencies (> 200 kHz), which implies radial secular frequencies on the order of several megahertz. This corresponds to applying 200 V amplitude at $\approx$20 MHz, which was calculated using the software provided in [166]. To generate a large enough voltage and not dissipate too much power onto the trap, a high Q system is required to provide a transformation from a 50 Ω feed line to the impedance of the trap itself, which is in the range of 100-1000 Ω. The transformation is provided with a quarter-wave helical resonator [99], which can be decomposed into an antenna and a pickup coil, both in close proximity with a shielding can enclosing them. All of the components are made out of copper to achieve a low resistance, which would otherwise degrade the Q of the system. The output of the resonator is connected to an electrical feedthrough, which is connected to an in-vacuum cable leading to the trap electrodes. Previously a high RF power two-pin feedthrough was used to deliver the RF drive signal to the trap, however it was limited to applying frequencies of $\approx$20 MHz set by the feedthrough capacitance of 20 pF. In order to be able to apply higher frequency signals, the two-pin feedthrough was replaced by a double-sided SMA coaxial feedthrough[16]. This requires having a 50 Ω coaxial cable with SMA connectors on both ends, linking the output of the resonator to the feedthrough. This introduces an impedance mismatch between the resonator output and the impedance of the line, however by keeping the 50 Ω line below 20 cm, the jump in impedance has little effect on the voltage applied to the trap [167].

An example of one of these resonators is given in fig. 4.18, with the design guidelines for the dimensions of the coils and shielding enclosure provided by [67],[99].

[15] Rosenberg 19S101-40ML5
[16] Allectra 242-SMAD50-C40

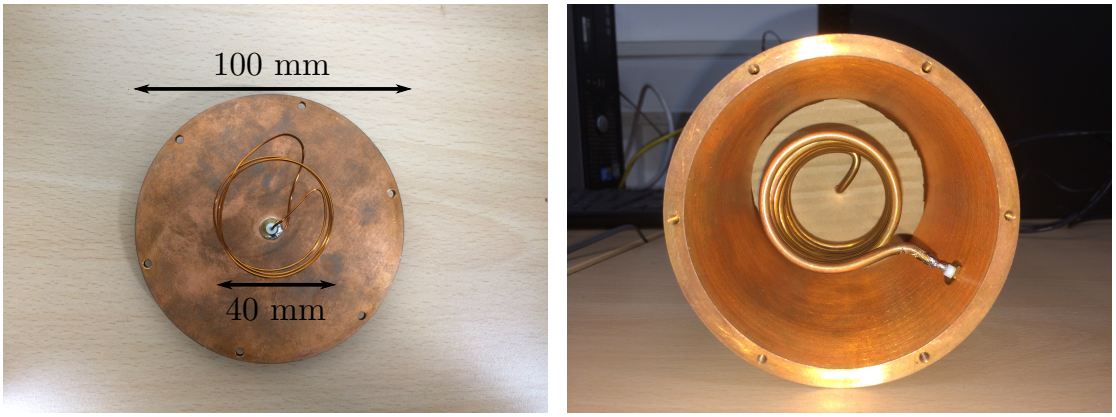

(a) (b)

Figure 4.18: (a) The antenna coil of a helical resonator is wound to have three turns using thin copper wire. The signal is fed in on the other side via an SMA connector. (b) The pickup coil is 50 mm in diameter made out of 3.8 mm diameter copper wire wound to have seven turns with a pitch of 10 mm. The coil was mounted in a cylindrical copper shield. One end of the coil is grounded to the shield, while the other has an SMA connector for output. The resonator is completed by inserting the antenna coil into the shield and fixing it in position with screws through tapped holes. The total height of the assembled resonator is 14 cm.

Early experiments used an RF setup that can be simplified to a schematic given in fig. 4.19. Not included in the picture is a RF directional power meter. Knowing the input power P fed into the resonator, the root mean square (RMS) voltage applied to the ion trap can be shown to be given by [99],

$$V_{RMS} = (L/C)^{1/4}\sqrt{PQ}. \tag{4.1}$$

The resonance frequency and the Q value are given by:

$$f_0 = \frac{1}{2\pi\sqrt{LC}} \tag{4.2}$$

$$Q = \frac{1}{R}\sqrt{\frac{L}{C}} \tag{4.3}$$

where L is the mutual inductance of the two coils, C is the capacitance of the attached load and any parasitic contributions and R is the total resistance. The mutual inductance is determined by the length and shape of the coils and the distance between them. Since the pickup coil is too rigid to be easily shaped by hand, only the antenna is tuned to obtain the required frequency. The main advantage of helical resonators is the large Q value, which determines the voltage gain when transforming from a 50 Ω source to the trap impedance.

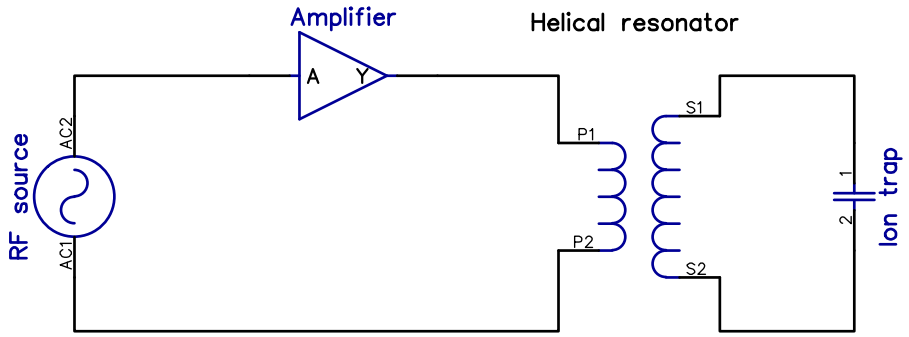

Figure 4.19: Simplified schematic of a RF drive system for applying large voltages to an ion trap. The 50 Ω RF source provides an output in the range −70 dBm to 20 dBm, which is amplified by a 43 dB amplifier to obtain required power. The step up in voltage is provided by the helical resonator, which is represented as two inductors, one being the antenna and the other the pick up coil. The amplified signal is then fed into the resonator leading to the trap through a high-voltage connector flange.

Once complete, the resonator is tested using a vector network analyser (VNA) to extract reflection parameters. This means measuring the reflected power and comparing it to the input. Instead of using a real trap, a 20 pF capacitor mounted on a SMA connector is used. The goal of optimising the resonator is to increase the Q value and tune the resonant frequency f_0. An example of a typical resonance dip can be seen in fig. 4.20. From this curve the Q value is calculated by finding the frequencies (f_+ and f_-) at which the reflected signal halves in power (-3 dB point) and finding the ratio $Q = \frac{f_0}{f_+ - f_-}$.

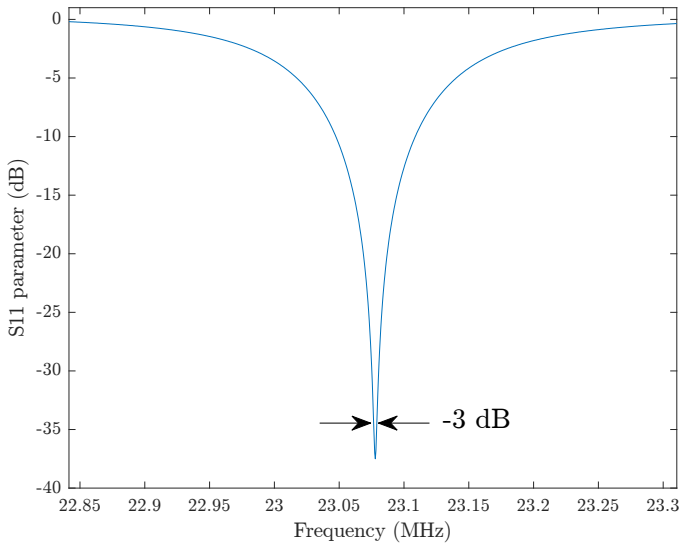

Figure 4.20: The resonance curve of a helical resonator connected to a 20 pF capacitor. The resonance frequency was found at 23.08 MHz. The S11 parameter is defined as the ratio between the reflected and applied signal voltage.

In the given example of fig. 4.20, the resonator was connected to a capacitor using a short coaxial cable. The resonators used with real traps would be tuned until a Q-value of ≈300, which from previous experiments results in a power of less than 0.3 W applied to the ion trap to obtain voltage amplitude of 100 V.

The exact applied voltage can also be calculated from the measured secular frequencies of a trapped ion. However, not knowing the accurate value of the applied voltage before trapping introduces the risk of accidentally breaking down the trap, or unoptimised trapping parameters, therefore the resonator system was upgraded to include a capacitive probe based on the design given in [168]. The schematic of the system is pictured in 4.21.

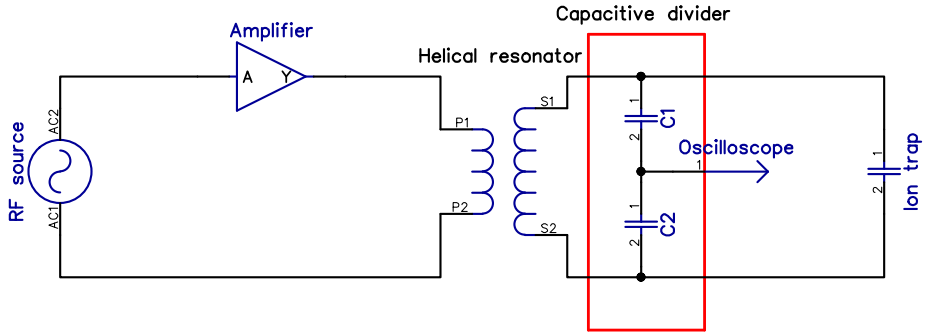

Figure 4.21: Schematic of an RF system with the ability to monitor the applied voltage with the use of a capacitive divider.

The capacitive probe works similarly to a simple resistive divider, but the division ratio is given by the ratio of impedances of $X_1 = \frac{1}{\omega C_1}$ and $X_2 = \frac{1}{\omega C_2}$. The probe has a series capacitance of ≈0.2 pF, dominated by $C1$. This is to avoid introducing any additional capacitance which could significantly load the resonator and shift the resonance frequency. To avoid any unnecessary impedances and to be able to handle large voltages, high performance capacitors[17] were used when building the divider. The divider is made on a PCB board and is mounted just outside the resonator as close as possible to the trap (see fig. 4.22). The performance of the divider is tested by using a dummy load instead of the trap, during which the division ratio and the frequency dependence is established. By keeping the RF path through the vacuum system short and assuming negligible inductance, the trap voltage can be calculated by multiplying the voltage on the oscilloscope by the division ratio. It is noteworthy to mention, that despite the same components being used to make multiple dividers, they would vary in their division ratio in the range of 380 to 580. It was assumed these changes were due to the manufacturing imperfections of the PCB board.

[17] Vishay Quad HIFREQ range

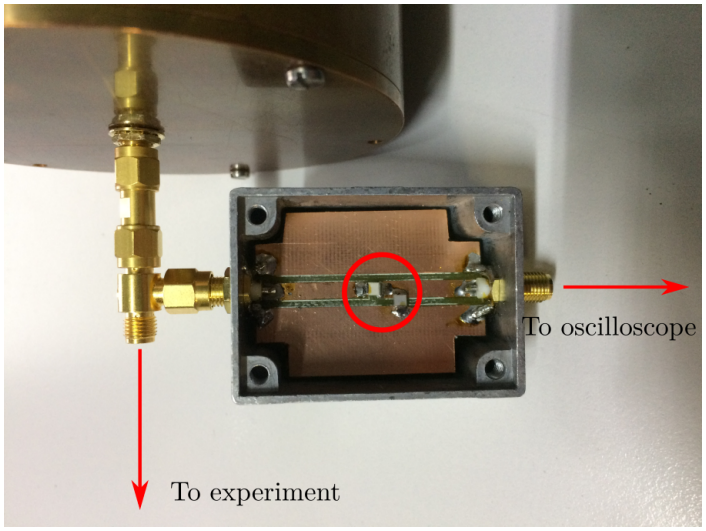

Figure 4.22: The capacitive divider PCB attached to the resonator via an SMA tee-piece. The circled area indicates the capacitive divider formed by the capacitors $C1$ and $C2$.

The ability to measure the applied voltage was used not only to obtain the necessary trap depth, but also to develop a feedback system to correct for any fluctuations within the RF delivery circuitry. This is described in chapter 5 of this thesis.

4.6 Metallic vapour source

The basic aim of any experimental ion trap system is to reliably and repeatedly trap ions. This requires a well characterised source of neutral atoms and the ability to ionise the required isotope. A vast majority of experimental ion trap setups use photoionisation for exciting the valence electron of a neutral atom into the continuum, selectively obtaining the right isotope ion from an atomic beam, which is described in chapter 2. The source of neutral atoms is the vapour of a heated lump of metal, obtained by heating it to temperatures of 300 to 700 °C, depending on the atomic species. It is also possible to guide cold atoms into the ion trap from an external magneto-optical trap as it has been demonstrated in [169]. Although the latter method provides a cleaner trap loading procedure, the former method is preferred due to its simplicity. In order to heat the sample to these temperatures, either resistive heating or laser ablation can be used [170]. In this thesis the first method is used to obtain a source of neutral atoms. To reach the high temperatures, the metal sample is placed in an atomic oven. This consists of a small cylindrical container, through which an electrical current can be passed. The oven has enough resistance to be able to heat up significantly and is isolated so as not to dissipate heat to the surrounding components.

To be able to use an atomic oven with a surface ion trap, the atomic source must not deposit atoms on the trap surface. This has been observed to lead to shorting of the electrodes. To minimise the likelihood of damage to the trap, an atomic oven mounting system was developed specifically for traps using Yb^+ ions. The design of the oven was based on the previous iterations within the group, with the added capability of mounting more than two ovens.

The ovens were made out of 1.5 mm outer diameter and 1.2 mm inner diameter stainless steel tube[18] of 16 mm length with one end spot-welded onto a small square of constantan and silver-coated copper wire[19] insulated with Kapton, while the other open end provided access to the oven to be filled with pieces of Yb. The purpose of using constantan was to introduce the right amount of resistance ($\approx 0.25\,\Omega$) and ensure that it would be the only heated point when passing a current. The temperature of the oven must reach 400 °C to start emitting a significant amount of vapour from the metal sample. To pass a current through the oven, the copper wire is connected to a high power current feedthrough via a barrel connector. The current path is closed by clamping the open tube end into a bracket pictured in fig. 4.23.

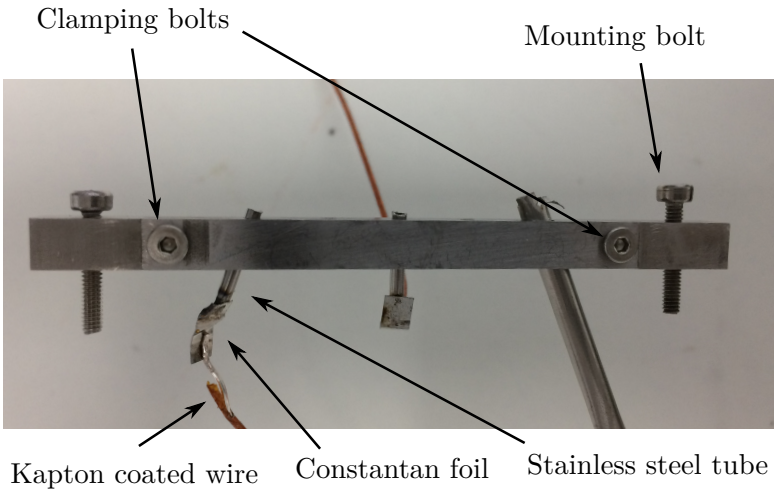

Figure 4.23: The two part bracket mounts five atomic ovens with a 20° angle between them. This is done to have all of the ovens point in the direction of the trap centre. The clamping bolts are tightened to squeeze all the ovens evenly. The mounting bolts are used in mounting the assembly into the vacuum system.

The bracket holds five ovens directed at the trap centre. Three of them contain naturally occurring Yb, the fourth is enriched with ^{171}Yb, and the fifth is commercial Ba oven[20]. In order to reduce heat transfer between individual ovens, the bracket pinches the

[18] Stainless Tube and Needle Co. 17G Thin Wall 304/316
[19] LewVac KAPW1X061
[20] AlfaVakuo

individual ovens, which minimises the contact area. The bracket is mounted on a stainless steel plate of 1.5 mm thickness, which is screwed into a groove grabber[21] positioned on one of the rims inside the vacuum system. The fully mounted oven setup can be seen in fig. 4.24.

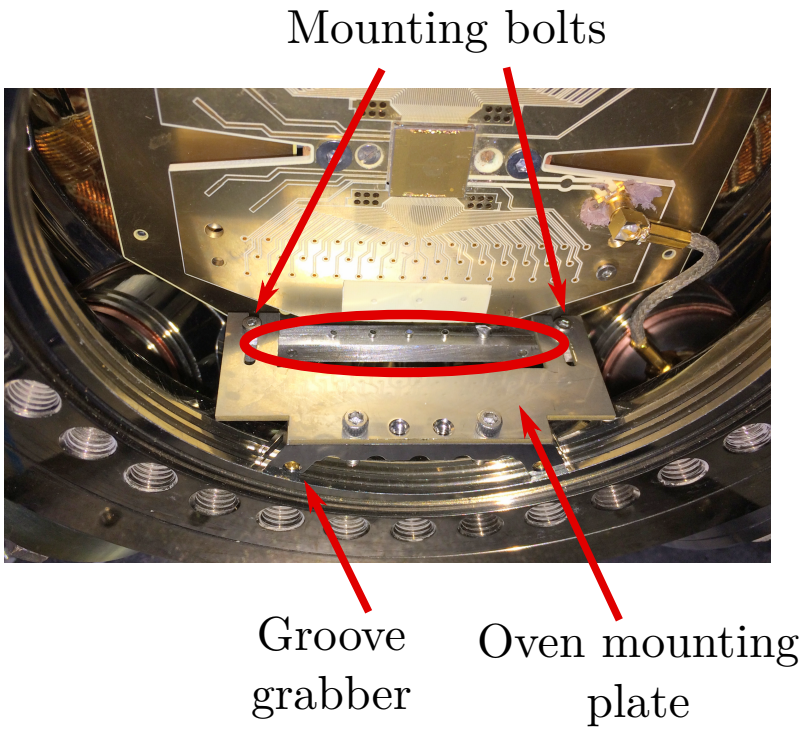

Figure 4.24: The oven assembly mounted on the stainless steel plate attached to a groove grabber.

Using a thermal oven introduces the complication of the clouds of neutral atoms sticking to conducting surfaces. To minimise this effect, the ovens are aligned to skim the surface of the ion trap, which reduces the amount of Yb atoms deposited onto the surface, which can short the electrode structure, cause additional ion heating and result in varying stray electric fields. The process of alignment requires observation of the ovens by eye from above the vacuum chamber, looking across the trap surface in the direction towards the oven aperture. It is then a case of making sure that the ovens are barely visible when simply looking at the ovens from above.

The use of a Ba oven introduced the requirement of sealing up the vacuum system in a short time, due to barium having a short oxidation time, which leaves the metal with a highly inert white layer. This oxide layer has a melting temperature of several thousand degrees. An alternative solution is a commercial oven, which was used in this case. Here, barium is sealed in a stainless steel tube with a layer of indium separating

[21] Kimball Physics MCF600-GrvGrb-C01

it from atmosphere. When heating up the indium to 160 °C, the seal evaporates and leaves the barium unaffected. However, it was found that the indium has a high chance of bubbling and coating the trap electrodes. To avoid this, after the barium oven was mounted the indium seal would be snipped off while having a constant stream of nitrogen flowing over the oven to reduce interaction with oxygen. The system is then quickly sealed and pumped down.

To characterise the performance of the ovens, they were mounted in a mock experimental setup and tested for fluorescence using a 399 nm photoionisation laser light, and a digital camera. Initially it was found that a 6 A current for three minutes was needed to start observing fluorescence, but later this was reduced to 4.3 A, see fig. 4.25. Observing fluorescence using a barium oven is not straightforward as it requires separate lasers to obtain a closed cycle transition to scatter photons. This was not available at the time, therefore the oven was not tested using the fluorescence method.

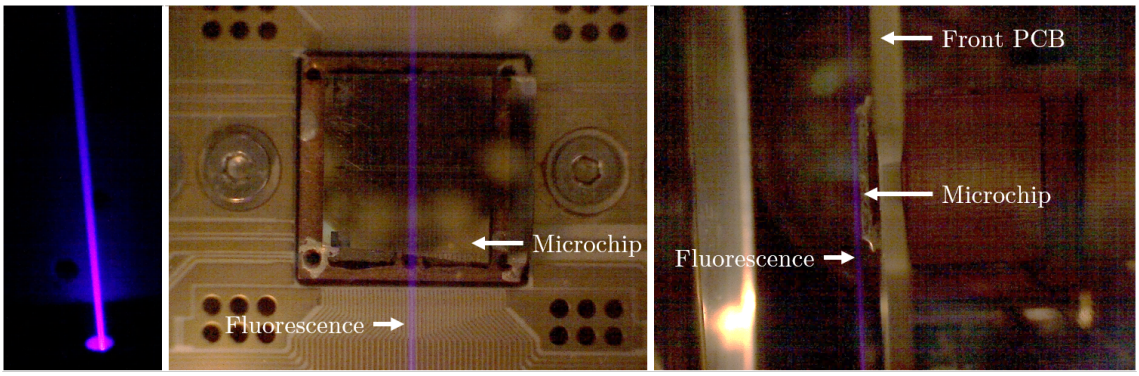

Figure 4.25: Oven fluorescence using the 399 nm laser. Adapted from [67].

The possible explanation for the requirement of a larger initial current is the presence of oxides and absorbed water within the stainless steel tube, which require a high temperature to burn off in order for the Yb vapour to escape. Moving the laser closer to the trap surface showed a significant decrease in atom fluorescence, which confirmed the correct alignment of the oven.

4.7 Cooling system

Ion heating rate measurements suggest that the surface quality of an ion trap electrode becomes significant for ion-electrode distances of <150 µm, as at these scales surface roughness and contaminants introduce unwanted electrical noise [171, 172], which have a non-negligible effect on the trapping field. These effects eventually will manifest in an increased heating rate of the trapped ion, in turn diminishing the fidelity of multi-qubit

gate operations. To improve trap performance, there are a multitude of methods for improving surface ion trap quality - cleaning the surface with ion bombardment outside or inside the vacuum system [173, 174] or laser cleaning the ion trap electrodes [78]. Although these methods have proved to be successful, they do not appear to be consistent. A more straightforward method is to reduce the trap temperature by several hundred Kelvin, at which point the thermal motion of the atoms composing the surface is reduced. This leads to a lower Johnson noise level [145] and in turn decreases thermal losses in electronic signal propagation. In addition to the reduction of electric noise, the background pressure of the vacuum system is reduced by several orders of magnitude, due to the reduced temperature of the background gases within the vacuum system. This reduces the likelihood of losing the trapped ions through collisions. With these advantages in mind, a cooling system was built for the vacuum system, to cool down the ion trap to a temperature to 70 K projected to give an improvement of the heating rate by an order of magnitude [175].

The design includes an input and output connection for circulating the coolant of choice, with a pressure of < 1 bar. The heat exchanger between the chip and the coolant is pictured in fig. 4.26. A modified heat exchanger design could allow for pressures of > 20 bar. This will be described in chapter 5.

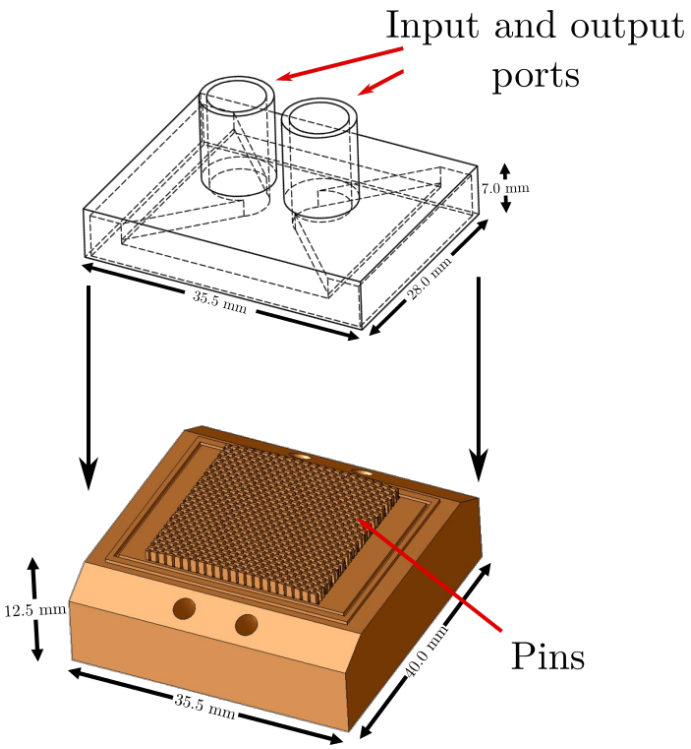

Figure 4.26: Drawing of the heat exchanger. The top stainless steel part provides the input and output port for coolant, which can be pushed through using a cryogenic pump. The copper heatsink and the stainless steel part are brazed together to form a leak tight connection. The purpose of the pins is to increase the surface area for the coolant to exchange heat with. Image from [67].

Initially, the system was designed to provide a cooling power of 20 W to remove heat generated by current carrying wires, running at 20 A to generate a magnetic field gradient. Since the system eventually utilised permanent magnets to generate the static magnetic field gradient, the heat exchanger is dedicated to cooling the trap temperature to reduce trapped ion heating rates. To reach the required temperature of 70 K, liquid nitrogen is supplied to the heat exchanger, which was based on the design in [176]. The steady state temperature of the cooled ion trap is determined by the rate of liquid flow and the heat load of the the ion trap module and any heat flowing in through the ambient environment. Estimates of these parameters is given in chapter 5.

The heat exchanger contains fins which introduce a large resistance to the flow of the coolant, and in turn the coolant starts absorbing more heat from the heat exchanger. The heat exchanger was made out of oxygen free copper for increased thermal conductivity and UHV compatibility, with flexible stainless steel tubing brazed onto the backplate. The end of the tubing has VCR connections which directly mount onto two custom liquid nitrogen feedthroughs.

The presence of a flowing coolant can introduce low amplitude vibrations in the vacuum

system components, which can cause adverse effects. In order to avoid this, the mounting structure of the cooling system must not have resonant vibrational frequencies that coincide with the secular frequencies of the trapped ion (≈200 kHz). This was achieved by mounting the heat exchanger with the use of titanium struts and brackets pictured in fig. 4.27, which are stiff enough to minimise low vibration perturbations. The whole assembly is held in place by a pair of groove grabbers mounted on the back port of the hemisphere.

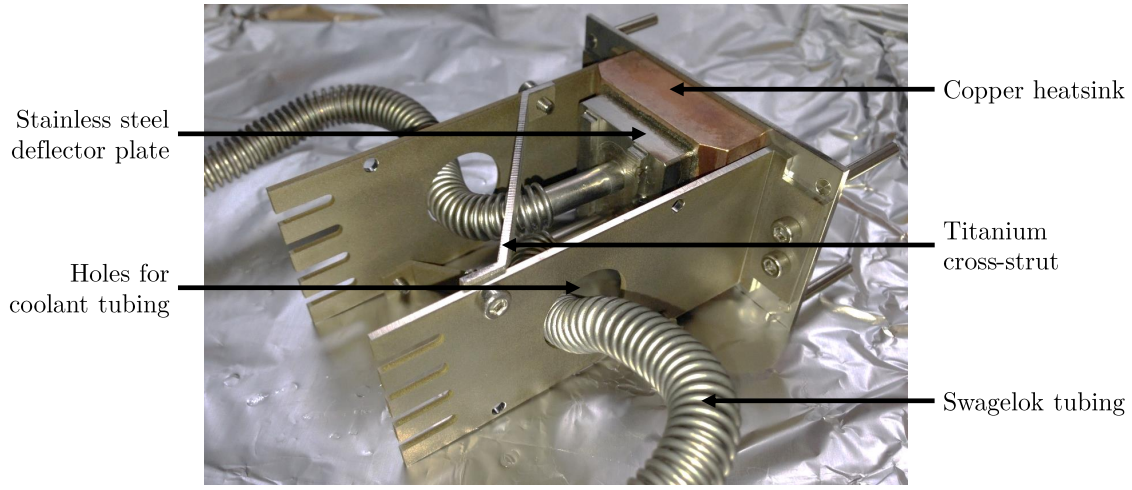

Figure 4.27: Heat exchanger mounting structure with titanium struts.

4.8 External magnetic field compensation coils

The use of permanent magnets under the trap carries the risk of introducing an unknown magnetic field offset at the trapping position. This complicates ion trapping and manipulation, due to non-negligible shifts in the $^2S_{1/2}$ manifold taking the ion out of the Doppler cooling cycle. To zero any unwanted fields, external electromagnetic coils and permanent magnets were placed on the outside surface of the vacuum system hemisphere. This field compensation system was designed and simulated by Dr Eamon Standing and is detailed in [164].

To be able to compensate in all axes, the design includes two pairs of electromagnetic coils and a set of high strength permanent magnets pictured in fig. 4.28.

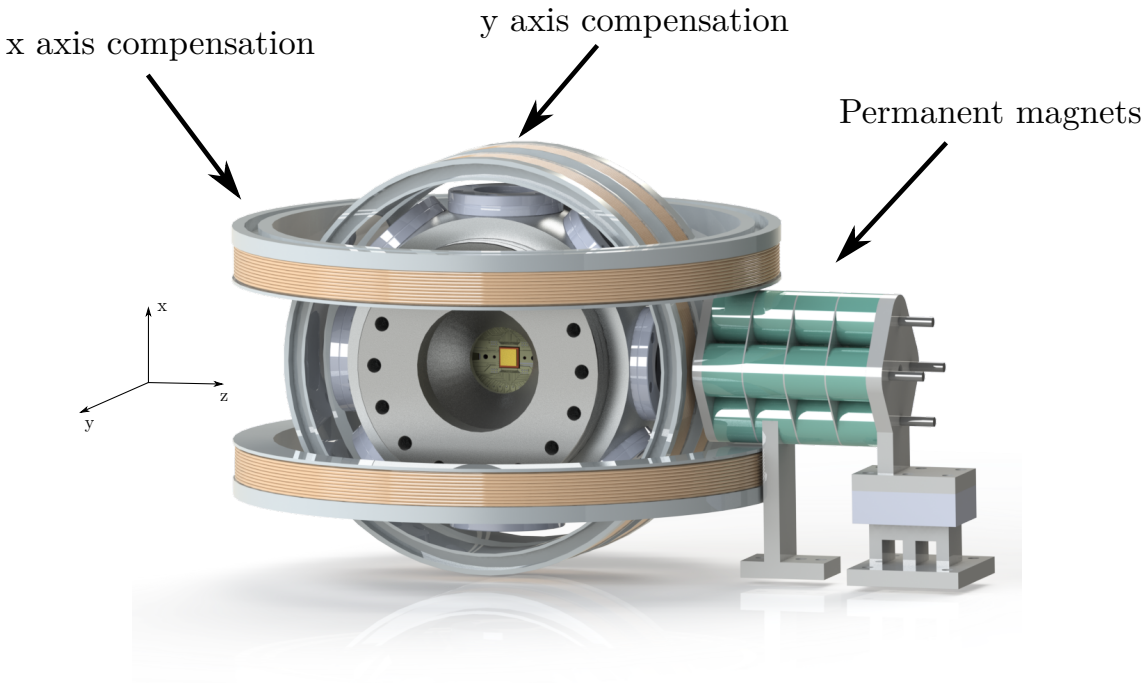

Figure 4.28: The external magnetic field compensation setup.

The x- and y- axes were compensated with coils wound using 1.8 mm diameter copper wire, counting 65 turns for the y-axis and 120 for the x-axis. The x-axis compensation coil pair was wound around a cylindrical frame with a diameter of 250 mm and a height of 33 mm. The y-axis frame was 330 mm in diameter with a slightly larger height of 36 mm. The spacing between the coils was 2.2 cm for y compensation and 9.5 cm for the y axis pair. The use of pairs of electromagnetic coils allows us to have a uniform magnetic field over the extent of the ion motion of $\approx$0.4 µm which can be easily adjusted by tuning the applied current. The largest field that could be compensated with the coils was found to be 60 G, which corresponds to applying an 8 A current, producing a significant amount of heating. For heat management purposes, the winding mounts have grooves which can be lined with tubing for water cooling. The coils were held in place with posts mounted onto the optical table.

Due to the size of a third coil pair being too large for the experimental setup, the remaining z-axis was decided to be compensated with external permanent magnets mounted on an easily adjustable stage. To generate a 140 G magnetic field at the ion trapping position, a total of 16 permanent magnets were mounted on the stage. The individual cylindrical magnet was 25 mm in length and 32 mm in diameter and has a remnant magnetic field strength of 1.4 T. The stacks of magnets are held by aluminium supports, which are

screwed down to the optical table. To be able to make adjustments to the applied field, the supports can be mounted on a micrometer precision translation stage. By moving the magnets towards and away from the hemisphere, the field can be adjusted to the required level.

4.9 RF and microwave emitters

Section 2.9 of chapter 2 described the Yb ion qubits used in performing single and multi qubit operations, all of which require RF and microwave radiation. In order to carry out these coherent operations, the applied radiation has to posses narrow linewidth and the correct polarisation defined by the quantization axis. Furthermore, the generated fields must have a large Rabi frequency, to keep the manipulation time as short as possible to minimise errors due to the heating rate of the trapped ion. Fortunately, the field of RF and microwave engineering of sources has been established for a long time, resulting in cheap and readily available devices. The only requirement is then designing the emitters which emit the required fields for ion addressing. In this experimental setup, the radiation propagates into the vacuum system through the imaging viewport. This is in the direct field of view of the stainless steel mesh mounted on the viewport to shield the trap from the static charge on the dielectric window. This mesh attenuates the oscillating fields required for addressing the ion. A solution to this challenge is to use a mesh containing a cut-out hole of 2 cm diameter, pictured in fig. 4.29.

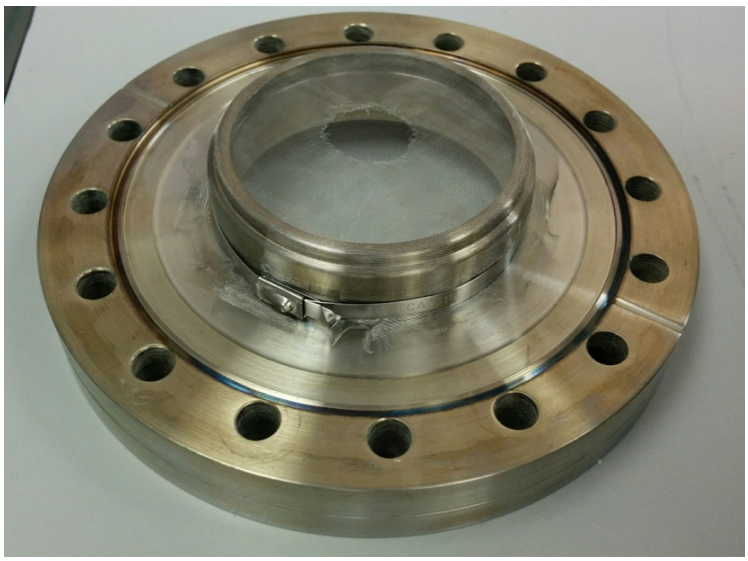

Figure 4.29: Picture of the imaging viewport with a stainless steel mesh for static voltage shielding.

To understand the distribution of the radiated field within the vacuum system, an

analysis was carried out. This section describes the RF and microwave radiation emitters developed and used in this particular experimental setup.

4.9.1 RF and microwave addressing

The bare state qubits detailed in chapter 2 require microwave fields to drive the transitions $|0\rangle \leftrightarrow |+1, 0', 1\rangle$ with a frequency of ≈12.64 GHz. In the dressed state scheme, the microwave fields are used to dress the magnetic field sensitive states to obtain the qubit system defined by the states $|0'\rangle$ and $|D\rangle = \frac{1}{\sqrt{2}}(|+1\rangle - |-1\rangle)$, which is manipulated using RF pulses of frequency given by the Zeeman shifted frequency calculated as $\omega_+ = \frac{\mu_B B}{\hbar}$. Typical RF frequencies are in the range of 10 MHz to 20 MHz.

To address the ions individually with multiple frequencies at the same time with phase and frequency controlled signals, the emitter has to have no sharp resonances at the required frequencies, where the phase undergoes inversion. To address these requirements, an antenna coil was wound from 3.35 mm wire to have 3 turns with a diameter of 50 mm. The coil was soldered to a BNC connection and mounted on a post, which is positioned next to the window as shown in fig. 4.30.

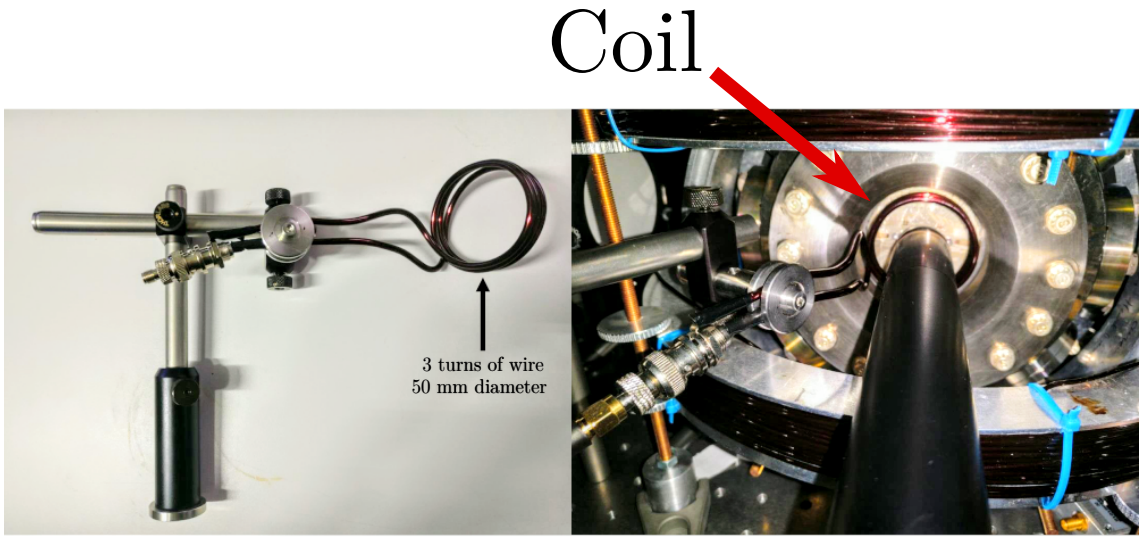

Figure 4.30: Picture of the RF coil (left) and when placed in front of the imaging viewport. Taken from [67].

The RF frequency was supplied by a custom made direct digital synthesis (DDS) box made by Dr. David Murgia [67], which was amplified with a high power 40 dB RF amplifier[22]. The amplifier is robust enough to handle large power reflections even when completely impedance mismatched between the output of the amplifier and the coil.

[22] Mini-Circuits LZY-22+

To deliver microwave radiation to the trapped ion, a commercially available microwave horn[23] was placed close to the viewport, next to the imaging tube and the RF coil. The horn emits radiation with a linear polarisation, therefore it was mounted on a rotational stage which made it possible to tune the polarisation seen by the trapped ion. The source of the microwave frequency was a vector signal generator[24] (VSG) with a 43 dB amplifier[25].

To evaluate if both RF and microwave radiation penetrates far enough into the system, electromagnetic field simulations were carried out by Eamon Standing using EMPro[26]. The magnetic field strength data is shown in fig. 4.31 for an input power of 1 W.

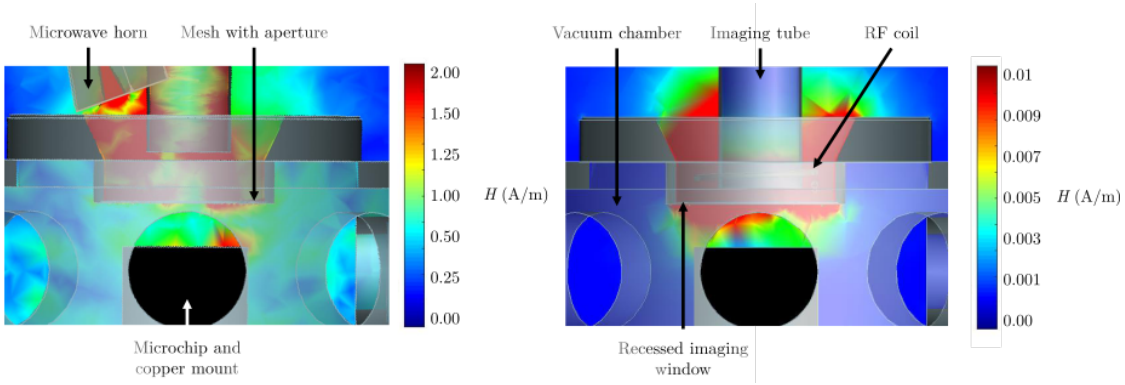

Figure 4.31: Field intensity simulations for a microwave horn (left) and a RF coil (right). In the left hand image, the intensity at the trap is given to be ≈1 A/m , while on the right was 0.005 A/m.

Although both microwave and radio-frequency fields are attenuated by a factor of two when compared to results without the mesh, this is sufficient to meet the requirements of the experiment, giving Rabi frequencies of $\Omega_{MW} \approx 2\pi \times 110\,\text{kHz}$ and $\Omega_{RF} \approx 2\pi \times 2\,\text{kHz}$. Although the RF field is significantly weaker when compared to the microwave case, typically the RF signal is amplified to power values of ≈40 W. The microwave and RF frequency shows an improvement by an order of magnitude compared to [39] and can be further increased with the use of a higher gain amplifier. Several high power microwave systems are described in the following chapter 5.

4.10 Trap operation

Once the vacuum system was assembled, the baking procedure was carried out for two weeks to reach a pressure as low as 10^{-11} mbar using a combination of ion and titanium sublimation pumps. Following this procedure, the experimental system was placed on an

[23] Flann Microwave 18240-10
[24] Keysight E8267D
[25] Microwave Amps AM25-12-13-30-33
[26] Keysight Electromagnetic Professional Software

optical table for further testing and experiments. The procedure of trapping ions on a microfabricated chip requires a careful interplay of multiple different electronic and optical systems described in the previous sections. The following paragraphs detail the operation of the ion trap system.

4.10.1 Trapping voltages

The first test to be carried out on the experimental system was the measurement of the trap capacitance and the characteristics of the RF electrodes. Having the trap exposed to elevated temperatures for several weeks can cause some loose wire-bonds to break, which will affect the capacitance of the RF path from the ion trap to the feedthrough. The measured capacitance of the trap was 17 pF, the same value as before the bake. With this in mind, the RF drive system was connected to the vacuum system feedthrough and the imaging was aligned to image the RF and DC electrodes.

To fully confine an ion in all directions, DC voltages are used to form a quadratic potential well in the axial direction, with the minimum positioned at the anticipated magnetic field nil.

DC electrodes are also used to introduce a small angle of rotation about the trap axis by applying voltage to the rotation electrodes, which extend along the RF electrode. In all of the trapping instances, a single rotation electrode was used to introduce an angle of 10° to the principal axis by applying ≈ 1 V. On the other hand, the axial confinement voltages were changed over time to optimise the trapped ion lifetime. The voltages were provided by an analogue output card[27] controlled using LabVIEW, which were fed into the system via the external filter box. The stability of the output card was measured to be 0.001 $\mathrm{V\,h^{-1}}$, which is sufficient for the foreseeable experiments. The output range of the card was limited to ± 10 V, which is adequate for achieving secular frequencies up to 200 kHz using the outer DC electrodes pictured in fig. 4.32.

[27] ADLINK PCI-6208V-GL

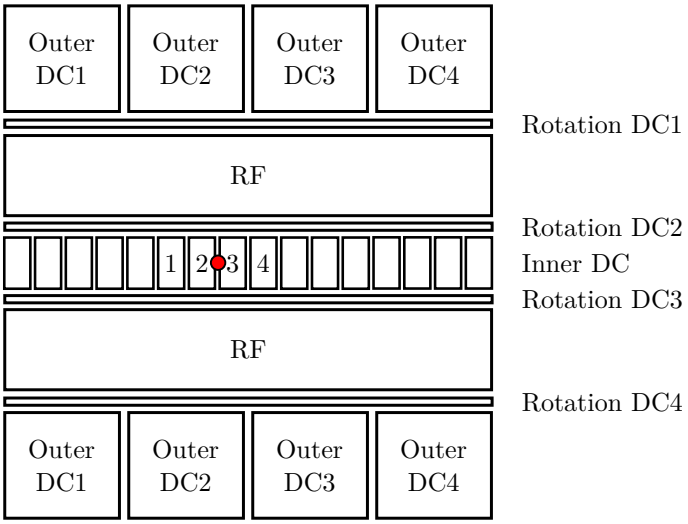

Figure 4.32: The electrode layout of the ion trap chip with the magnetic field minimum marked red.

4.10.2 Trapping $^{174}Yb^{+}$

In order to establish optimum trapping parameters for this particular trap, it was decided to trap the $^{174}Yb^{+}$ isotope first, owing to a simpler cooling cycle scheme compared to $^{171}Yb^{+}$ and the relative insensitivity to magnetic fields. The laser beams are aligned onto the RF trapping nil and imaged on the CCD camera, as seen in fig. 4.33.

The laser beam powers were set to enter the vacuum system with the following values: 369 nm - 100 µW, 399 nm - 100 µW and 935 nm - 2.3 mW. All of these values power broaden the transition linewidths, which alleviated the requirements for setting the laser wavelengths. Using the wavelengths detailed in [177, 64], a trapping run consists of turning on the current supply for the oven to provide 4.3 A for 3 minutes. At the end of the run, the RF voltage is reduced to zero to remove any accidentally trapped dark ions and the oven supply turned off to cool down the atomic oven. Initially, many trapping cycles were required, but later the experimental setup was optimised to trap at the end of a single trapping run. This was due to making incremental changes to the DC voltages and the laser wavelengths, while observing how it would affect the trapping times.

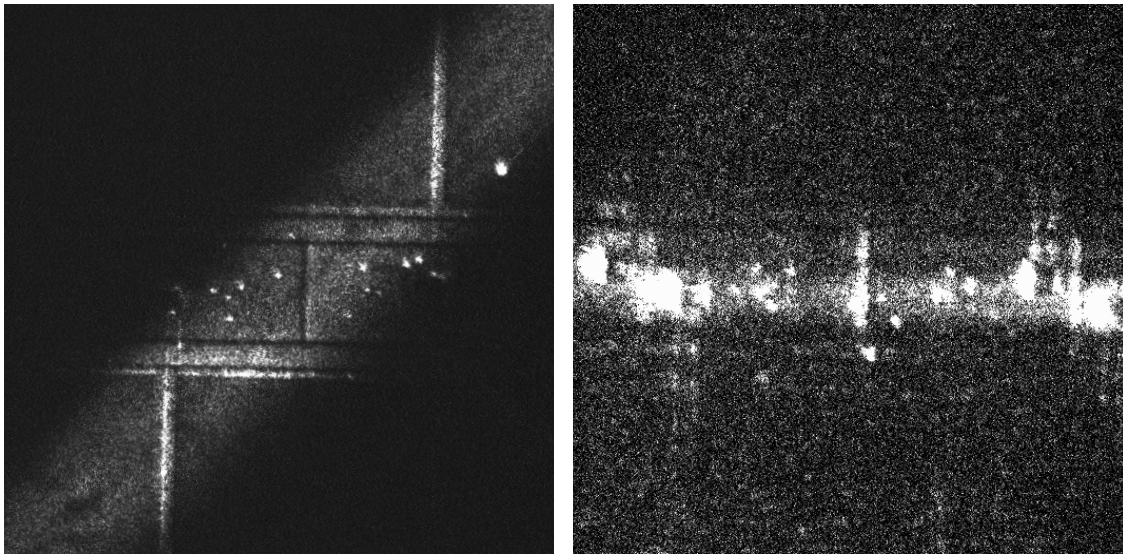

(a) (b)

Figure 4.33: (a) The 369 nm beam skims the surface of the trap at a 45° angle to the RF electrodes, with the other beams positioned to propagate parallel to the RF electrodes (b).

The trapped ion should appear to be circularly symmetric, which means that the ion is positioned at the nil of the potential well. Any misalignment between the DC and RF nil may result in unwanted micromotion of a trapped ion. Micromotion manifests itself as additional tails or fuzzing in the CCD image of the ion, as pictured in fig. 4.34a.

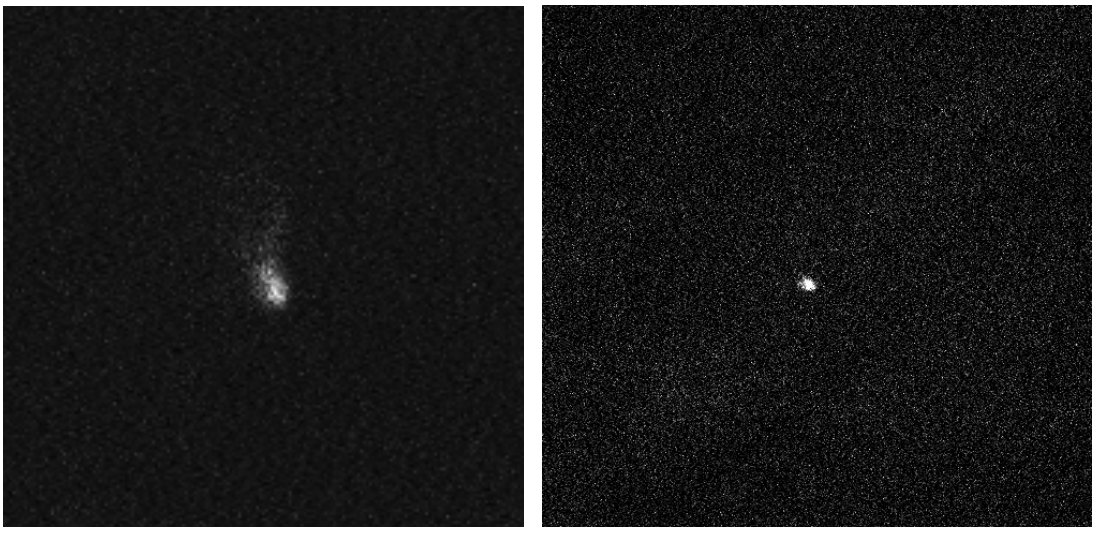

(a) (b)

Figure 4.34: CCD images of an ion without (a) and with (b) micromotion compensation.

To compensate micromotion, the RF voltage is reduced and the ion is observed for any shift in position. The DC voltage on the appropriate electrodes is then changed to compensate the shift. This process is then repeated until the RF voltage no longer affects

the position of the ion. The image of an ion trapped in an optimised well can be seen in fig. 4.34b.

To characterise the trapped ion, secular frequencies of the ion motion were measured using the 'tickling' method. The amplitude of the ion's oscillation frequency can be increased by applying a sinusoidally varying voltage. If set to the secular frequency, the amplitude of the motion increases, which stretches out the ion in the corresponding direction. In this setup, the voltage was applied using the RF addressing coil, which generated a large enough electric field at the ion position. The frequencies were measured to be $\omega_x = 2\pi \times 190(2)$kHz, $\omega_y = 2\pi \times 1.038(2)$MHz and $\omega_z = 2\pi \times 1.053(2)$MHz. Solving to find the applied RF voltage, the measured radial secular frequencies correspond to a voltage amplitude of 217 V and a trap depth of 0.083 eV. Since the simulations of other traps used in the laboratory gave accurate results, it was assumed that the capacitive divider was responsible for the error. To account for this in the voltage applied to the chip, the capacitive divider ratio was recalculated to be 603.

Despite the success of trapping the ions reliably, the ion trap showed signs of decay. The main issue was the unexpected presence of glow which developed over time, resulting in short ion lifetimes and unreliable trapping. The glow was proportional to the applied voltage and would be localised in the gaps of the inner segmented DC and rotational electrodes with the RF electrodes, as shown in fig. 4.35. A similar observation is reported in [178], where the glow was caused by sharp electrode edges, but it does not explain the development of such features over time, when originally there was no glow observed.

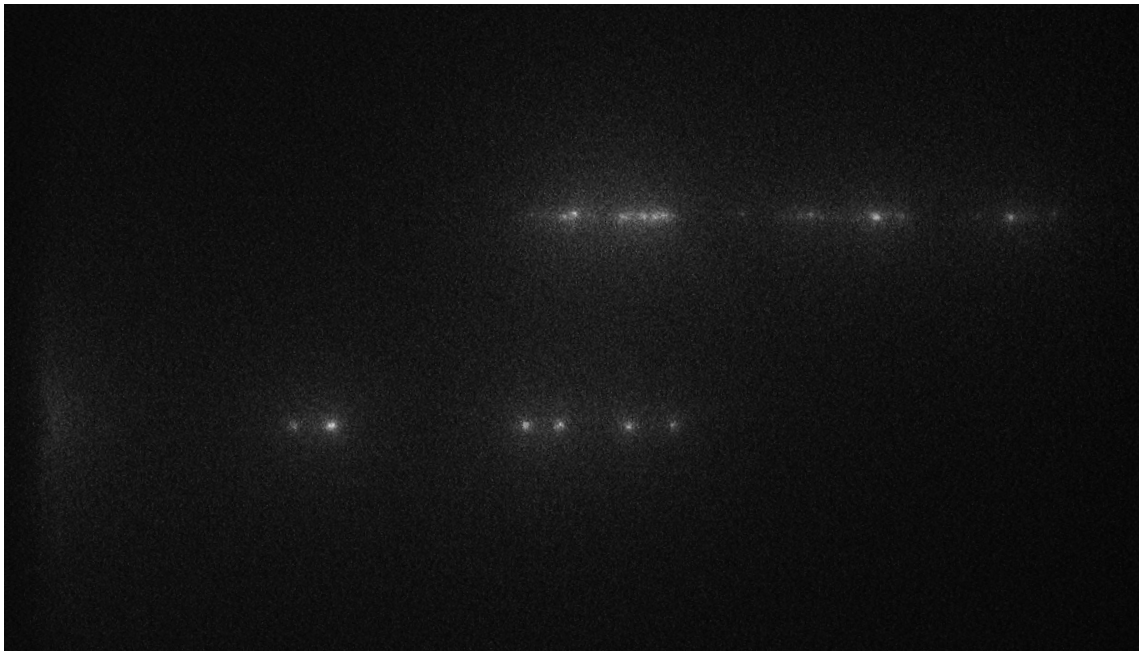

Figure 4.35: Glow in the gaps between the RF and DC electrodes extending throughout the trap.

In order to halt the damage to the trap, the RF voltage applied to the trap was reduced to 100 V, where no glow would be seen. This meant operating with a trap depth of 0.05 eV. Even with the reduced trap depth, it was possible to trap reliably with ion lifetimes exceeding 30 minutes. The optimum DC voltages are pictured in fig. 4.36.

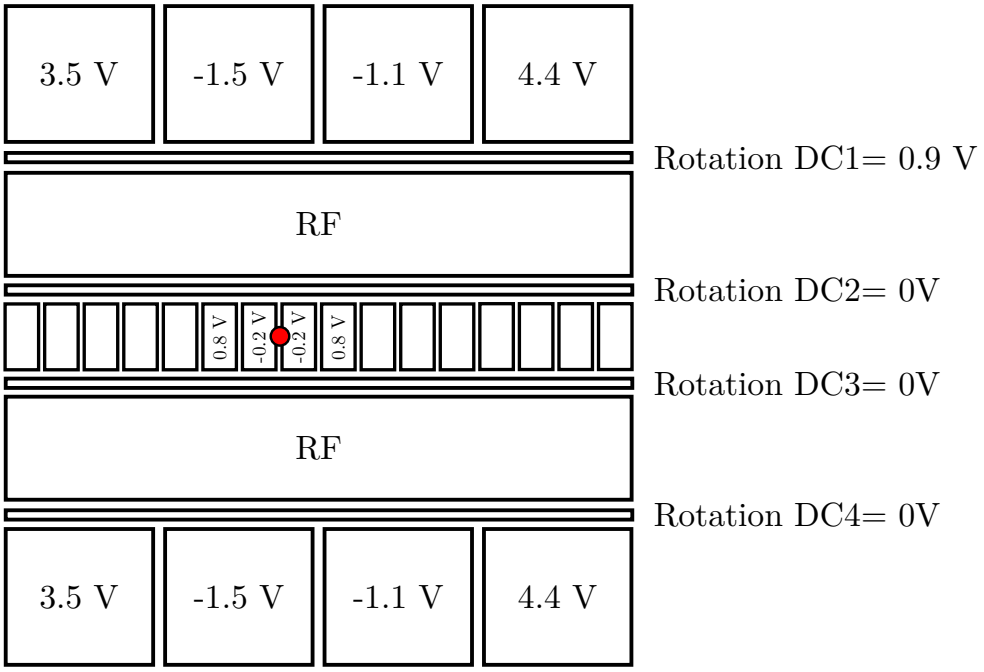

Figure 4.36: Optimum trapping voltages for the halved amplitude RF voltage.

The use of inner DC segmented electrodes was motivated by the ion failing to crystallise

using only outer DC electrodes. The secular frequencies for these reduced voltages were measured to be $\omega_x = 2\pi \times 184$kHz and $\omega_y = 2\pi \times 0.637$MHz and $\omega_z = 2\pi \times 0.643$MHz. Following multiple successful trapping runs and good trapped ion lifetimes, the trap was deemed optimised for attempting to trap the ^{171}Yb isotope.

4.10.3 Trapping $^{171}Yb^{+}$

The odd isotope, ^{171}Yb, possesses a complex energy level scheme due to the added hyperfine energy levels. This not only results in a frequency shift to the lasers used in the photoionisation and Doppler cooling, but it also makes the cooling cycle less efficient due to the ion decaying into the off-resonant hyperfine states. Furthermore to excite the ions into the $^2P_{1/2}, F = 1$ states, the 369 nm beam must be set to have all of the possible polarisations. Such a step between the parameters can be troublesome, therefore as a first step towards trapping the new isotope, the trap would be loaded with a couple of ^{174}Yb ions (pictured in fig. 4.37a), while the 399 nm laser would be set to ionise ^{171}Yb. The natural ovens contain 14% of ^{171}Yb, therefore the presence of a dark ion in the chain would indicate that ^{171}Yb isotopes may have been ionised and sympathetically cooled by the surrounding ions as seen in fig. 4.37b.

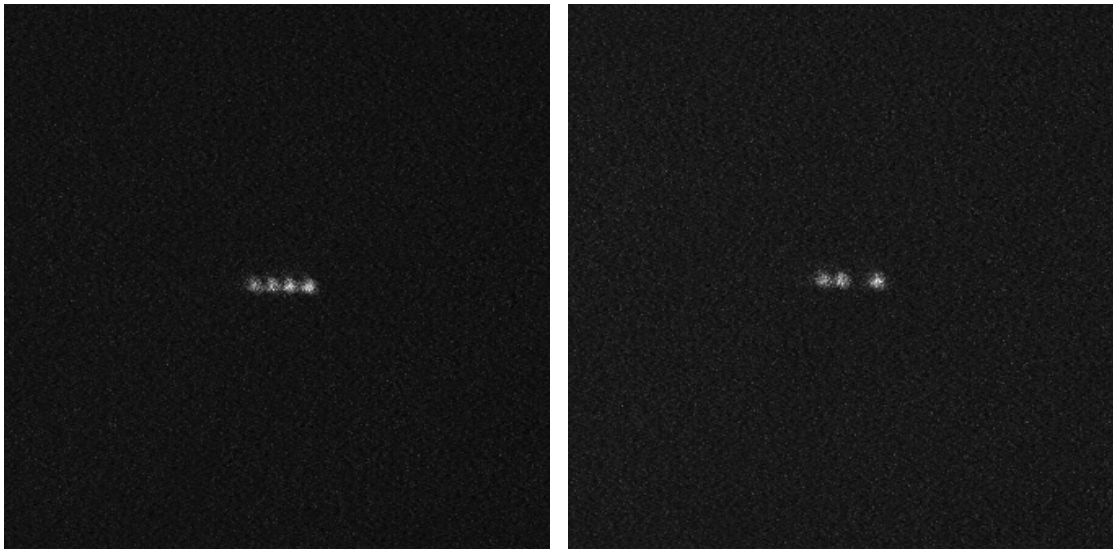

(a) (b)

Figure 4.37: (a) Linear chain of trapped $^{174}Yb^{+}$. (b) Running the atomic ovens and setting the photoionisation laser to the $^{171}Yb^{+}$ wavelength produces dark ions within the chain.

The procedure of trapping dark isotopes greatly reduces the uncertainty of the required magnetic field dependent 399 nm wavelength. In this case it was found to be close to the expected value specified in [177]. The observation of dark ions motivated the switch to

the ^{171}Yb laser setup and the use of microwave radiation for depopulating the trapped ion from the $F = 0$ state by exciting to the $F = 1$ state. The horn was directed at the ion trap with an angle in every trap axis to produce a non-singular microwave polarisation. An image of two trapped ^{171}Yb ions is shown in fig. 4.38.

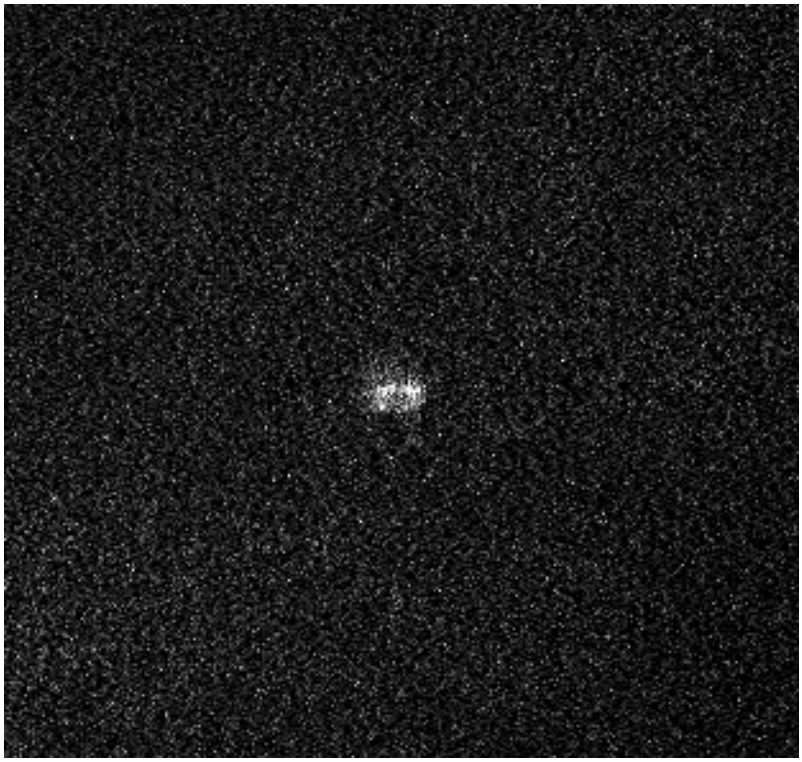

Figure 4.38: CCD image of a pair of ^{171}Yb ions.

One of the first objectives when trapping the ^{171}Yb isotope is the measurement of the magnetic field gradient. This can be performed by measuring the change in ion fluorescence when the microwave frequency is scanned. Any deviation from the zero field will shift the magnetic field sensitive m_f states in frequency. Fixing the 369 nm laser frequency and scanning the microwave field frequency will excite the ion into the split m_f states, which will manifest in increased fluorescence. To find the gradient of the field, a pair of ions can be used to find the difference of the size of the shift, which is then used to calculate the difference in the magnetic field seen by the ions. Although it is a crude method, the measurement of the gradient confirms the accuracy of the magnetic field simulations. Unfortunately, the gradient was not measured properly.

Although the experimental system was able to trap several ^{171}Yb ions, the trap unexpectedly underwent voltage breakdown, which resulted in a RF electrode capacitance of 17 nF. A value as high as this implies that the electrodes shorted to the nearest DC electrodes, therefore the trap was taken out for inspection of the glow damage.

4.11 Conclusion

This chapter described the design and assembly of an experimental system to perform high-fidelity microwave driven two-qubit gates with magnetic field gradients. This entailed the construction of a versatile in-vacuum trap mounting system and the development of optical and electronic systems for trapping and manipulating ^{174}Yb and ^{171}Yb ions. This work served as a starting point for a new and improved experimental system, described in the following chapter.

Chapter 5

System improvements for fault-tolerant microwave two-qubit gate fidelity

5.1 Introduction

During the operation of the experimental setup described in the previous chapter a number of areas for improvement have been highlighted. This chapter covers the assembly of an experimental setup, which addresses those areas, consisting of a singe-layer surface trap with permanent magnets housed within a vacuum system containing a high pressure helium cooling system and an in-vacuum microwave and radio-frequency emitter. The improvements outside the vacuum system include a trap voltage stabilisation setup and microwave radiation power stabilisation.

5.2 The ion trap and magnet assembly

The issues encountered with the surface traps described in chapter 4, were believed to be a result of errors in the microfabrication process. The inclusion of complex electrode features, which are a highly sensitive to faults in the fabrication procedure, was deemed to have a large risk of failure. Therefore, to avoid these problems in the new system, the trap electrode architecture was simplified to a single conductive layer. This greatly reduces the number of fabrication steps needed to produce a new set of traps and therefore reduces the likelihood of errors.

Despite not obtaining a measurement of the magnetic field gradient, the method of

generating the gradient using permanent SmCo magnets was deemed suitable for the second experimental setup. This was supported by the successful trapping of $^{171}Yb^{+}$ isotope, which indicates that the magnetic field offset is small enough for stable trapping. However, considering that the system will be operated with a cooling system, the thermal contraction of the magnets and the spacer can damage the ion trap or cause unwanted changes in the magnetic properties. The possible effects were investigated and a new magnet spacer was machined to prevent them.

5.2.1 Single-layer trap

Similarly to the ion trap system described in chapter 4, the trap geometry must enable the ion to be confined with secular frequencies of $\omega_z = \omega_y \approx 2\pi \times 2\,\text{MHz}$ radially and $\omega_x \approx 2\pi \times 1\,\text{MHz}$ axially at an ion height of 150 µm to be able to implement a high-fidelity two qubit gate. Therefore, the electrode layout was kept similar to the one in chapter 4 , but with a single centre electrode instead of the segmented DC electrodes. In order to have more control electrodes, the outer DC electrode width was decreased to 71 µm so that there are now 27 pairs of electrodes for axial confinement. The trap geometry is shown in fig. 5.1. It has two RF electrodes of equal width with four rotation electrodes placed adjacent to them. The RF input at the bottom right of the chip was designed to have a bend, with a ground plane symmetrically placed on both sides of the track. This was implemented following extensive simulations by Weikang Fan and Anton Grounds on the propagation of the RF signal through the trap, which suggests that sharp corners and lack of a surrounding ground plane introduces high voltage zones, which are prone to arcing. The gaps were chosen to be 5 µm wide, which provided significant shielding from the dielectric substrate. The design also contains contact pads for a diode temperature sensor (top left corner), which is planned to be used for monitoring the trap temperature, but was not implemented in this setup.

The trap design incorporates a gold electrode structure fabricated on a 650 µm thick sapphire wafer, a material well know for its excellent radio-frequency properties [179]. The fabrication process follows steps pictured in fig 5.2 performed by Weikang Fan, who is a PhD student in the group:

1. Clean 650 µm wafer with oxygen plasma.
2. Metal sputter deposit Cr/Al/Cr adhesion layer with thickness of 0.25 µm.
3. Metal sputter deposit Cr/Pt/Au 0.15 µm seed layer for electroplating.

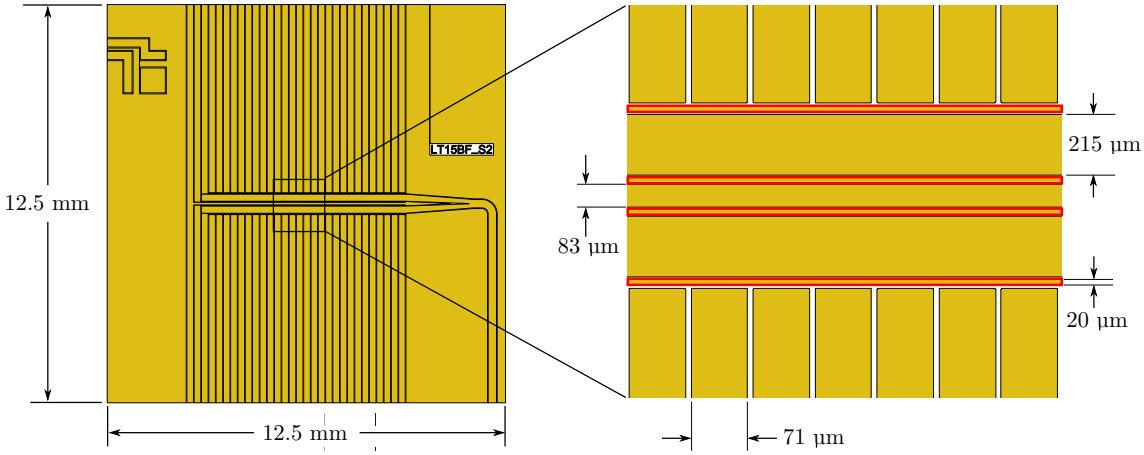

Figure 5.1: The electrode layout for the single-layer trap design with a pad for a thermal sensor at the top left corner. The RF electrodes are of equal width, with the 20 µm rotation electrodes highlighted in red.

4. Spin-coat 5 µm of negative photoresist and expose to UV light to develop the gap structure.

5. Electroplate 5 µm of gold.

6. Deep reactive-ion etch (DRIE) of the seed layer and adhesion layers.

7. Oxygen and argon plasma cleaning and acetone bath for removal of photoresist.

The new fabrication method had quick turn-around times which meant that modifications could be implemented quickly if necessary. The choice of electro-plating the gold layer was motivated to avoid the problems encountered with the old fabrication run, specifically the redeposit of gold into the gaps between electrodes and the ability to provide thick layers. A thick layer of gold provides a good conductive channel for the RF drive signal. Although electroplating does not achieve the same smoothness as gold sputtering, the process can be optimised to reduce electric field noise caused by patch potentials [75]. The picture of the trap is given in fig. 5.3a, where the electroplating gives a highly smooth surface with feature sizes less than 1 µm, see fig. 5.3b.

The final thickness of the completed trap was measured to be ≈655 um, which needs to be accounted for when designing a magnet spacer to set the correct magnetic nil height above the magnet pair.

5.2.2 Magnet spacer

The magnetic field gradient was generated using the same magnets as used in the previous system. However, owing to the single layer design, a surface trap with an ion height of 150

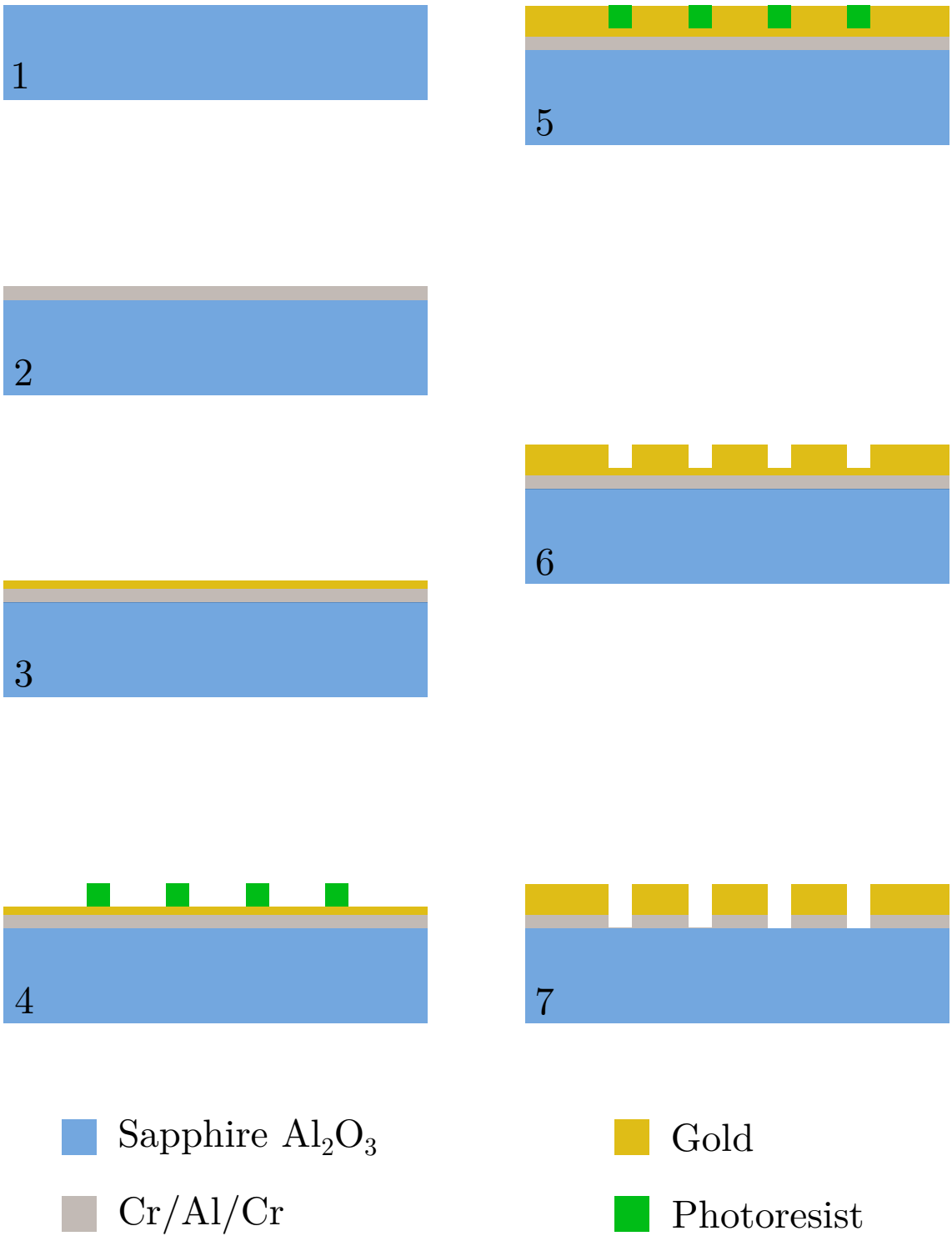

Figure 5.2: Fabrication procedure for single-layer ion traps on a 650 µm sapphire substrate with a conducting gold layer of a thickness of ≈5 µm. The fabrication steps correspond to the steps described in the main text. By itself, gold does not adhere to sapphire well, therefore an adhesive element such as chromium is used to provide a good contact for both materials [73]. Aluminium is used as a diffusion barrier to stop the gold to migrate through the adhesion layers. The chromium-aluminium layers were sputter deposited, while the gold was electroplated with an in-house electroplating bath.

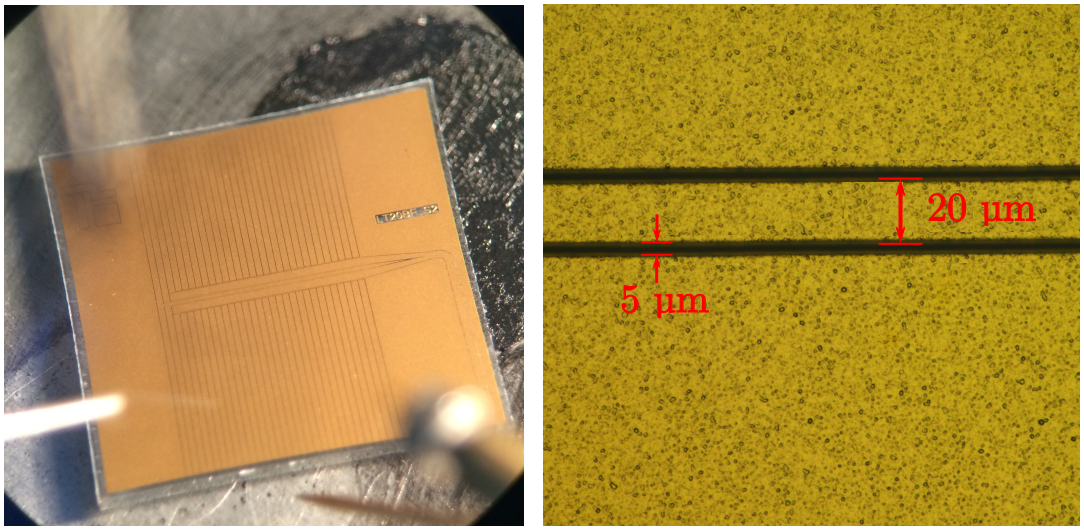

(a) (b)

Figure 5.3: (a) The fabricated ion trap imaged with a microscope. (b) Zoomed in picture of the trap rotation electrodes and the gaps. The electroplated gold layer contains grain sizes of <0.5 µm.

µm meant generating an axial magnetic field gradient with a nil 805 µm above the surface of the magnets, which is 50 µm closer when compared to the previous system. It was shown in chapter 4, that in order to lower the magnetic nil height, the magnet separation needs to be reduced. For the chosen trap, this corresponds to having the two magnets separated by 1.496 mm, which is estimated to produce a gradient of 150 T/m. The contour plot of the magnetic field strength is given in fig. 5.4. The simulations result in a magnetic field

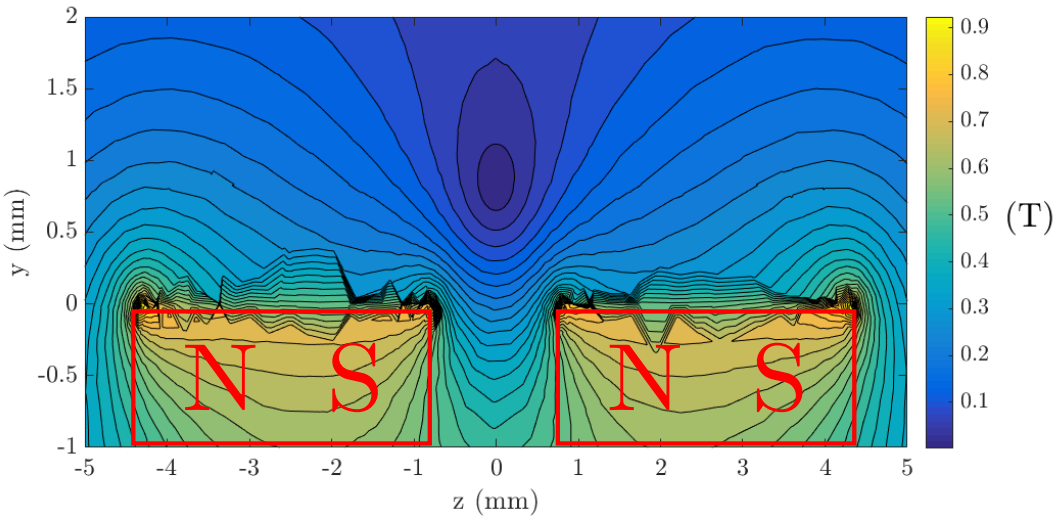

Figure 5.4: Contour plot of the absolute magnetic field (T). The magnet surface lies along the y=0 axis.

nil at the required height, with an error of a 2 G offset. The plot of the magnetic field along different axes is given in fig. 5.5.

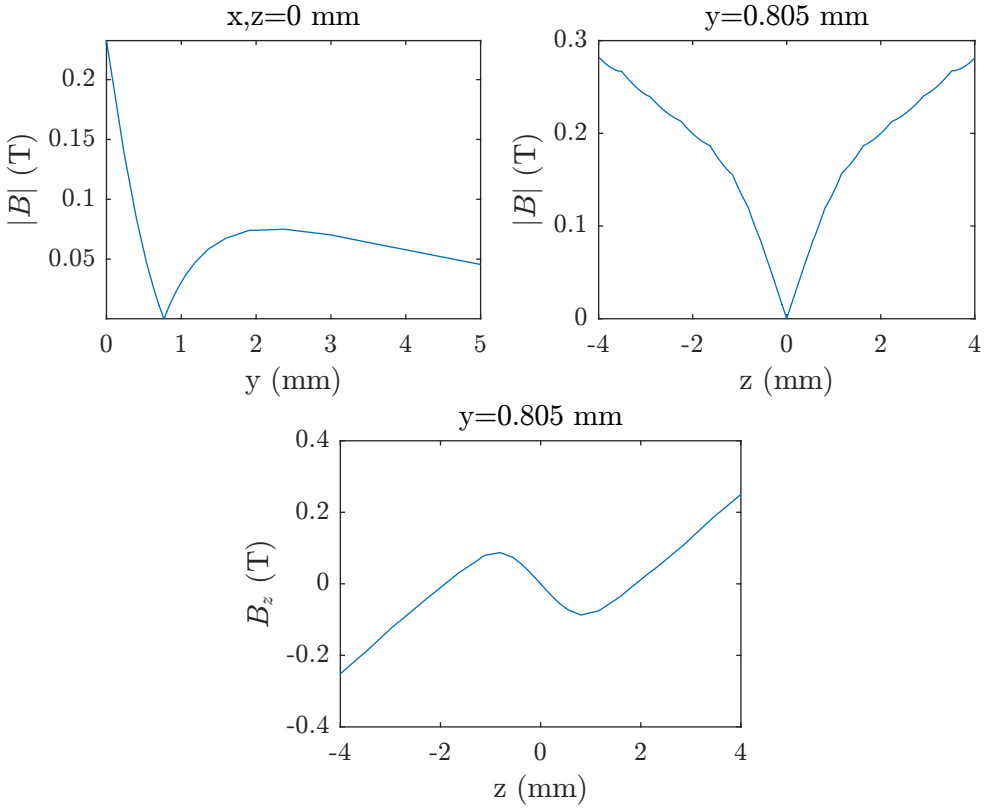

Figure 5.5: The magnetic field simulation results for an axial magnetic field gradient for a magnet separation of 1.496 mm with the B-field nil located at 0.805 mm height above the surface (top left) of the magnets. Simulations also confirm that the gradients strongest component is B_z (bottom) with a value of 150 T/m.

The contraction of different materials and the magnetic properties require consideration when reducing the ion trap temperature to 70 K. It has been shown in the work of [180] that the magnetic properties of SmCo improve when cooled down to 77 K, by becoming more resistant to demagnetisation. Therefore, it was assumed that the magnetic field gradient should not undergo any decrease when operating the cooling system. However, the biggest concern was the contraction and movement of the ion trap assembly, caused by the different thermal expansion coefficients, α, of the magnet pair, the spacer and the ion trap substrate, including the epoxy used to fix them together.

The contraction of the spacer can be large when materials such as copper are used ($\alpha_{Cu} = 16 \times 10^{-6}$ m/mK) [181]. Having the ion trap fixed with epoxy to the spacer, results in build up of stress within the sapphire substrate ($\alpha_S = 5 \times 10^{-6}$ m/mK) [182] due to the copper pulling on four corners of the chip, which can produce cracks. Ideally, the amount of contraction of these two components is equal, resulting in minimal stress through the material. On the other hand, having a good thermal conductivity will allow

the temperature of the trap to be reduced to the lowest possible value set by the cooling power of the exchanger. Therefore, tungsten was chosen to be the material of choice due to it's excellent thermal conductivity and thermal expansion coefficient of $\alpha_W = 4.5 \times 10^{-6}\,\mathrm{m/mK}$ [183] matching that of sapphire.

Despite the advantages that tungsten has over other materials such as copper and titanium, machining the spacer proved to be a challenge. This is due to tungsten being one of the strongest metals, making it resilient to drilling and filling. The only known method of achieving the required precision was wire-eroding, with machining accuracies specified down to 0.5 µm. To check the precision of the available wire-eroding machine, several tungsten pieces were made and measured using a highly accurate microscope. The measurements revealed errors up to 100 µm from the expected value, which were found to be inherent to machining tungsten. This was confirmed by producing the same pieces using titanium and achieving an accuracy of 5 µm, which then could be easily filed down to reach the required value. The results from these tests suggested that using tungsten would not guarantee the correct magnet separation, therefore a design incorporating a titanium plate separating these magnets is used instead, see fig. 5.6, with an expansion coefficient of $\alpha_{Ti} = 8.9 \times 10^{-6}\,\mathrm{m/mK}$. Calculating the change in thickness of the plate when cooled to 70 K gives a result of $<$1 µm, which has no noticeable effect on the position of the magnetic nil.

By using a plate of correct thickness, the tungsten component of the spacer assembly only needs to provide housing for the magnets and a cooling path through contact with the trap. Since the trap does not make contact with the titanium plate, its contraction when cooled should not exert any pressure on the substrate. The dimensions of the assembled magnet spacer can be seen in fig. 5.7. The titanium plate was set to have a thickness of 1.406 mm, which is 90 µm thinner compared to the simulation value. This was designed to compensate for surface roughness of $\approx$45 µm, which prevented the magnets from forming a perfect surface to surface connection with the plate. The assembled magnet spacer was remeasured and the true magnet spacing was found to be 1.526 mm, which results in the increase of the magnetic nil height by 30 µm, which corresponds to a 30 G offset field. Although this would mean that the magnetic nil is misaligned from the trapping position, in the simulations, it was assumed that there are no gaps between the surface of the substrate and the magnets, which was found to not be true. In most cases, a gap of $\approx$30 µm thickness was measured between two surfaces. Therefore the assembled magnet spacer was deemed suitable for matching the ion height with the magnetic field nil.

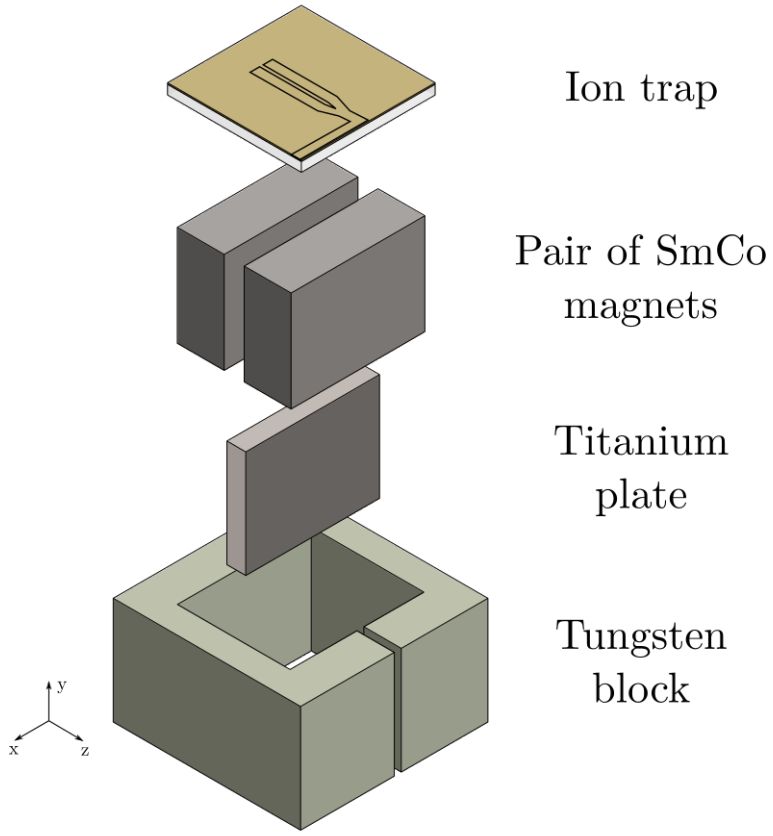

Figure 5.6: Exploded view of a magnet spacer assembly using a titanium plate to set the magnet-magnet spacing.

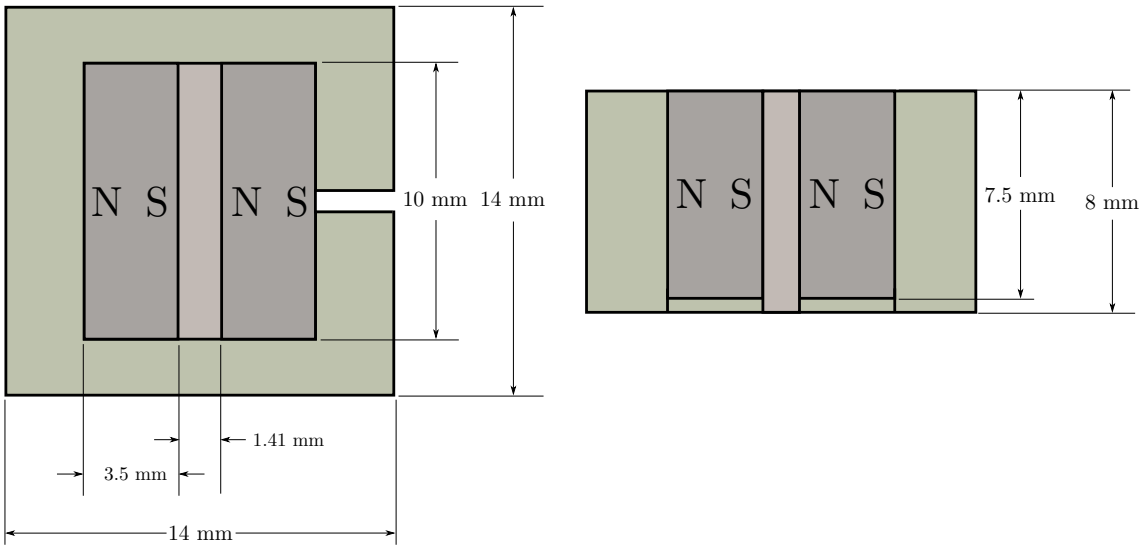

Figure 5.7: The final dimensions of the tungsten and titanium magnet spacer for (a) top down and (b) side slice views.

The process of trap alignment to the spacer was improved on the previous iteration

with the use of a commercial die bonder[1] pictured in fig. 5.8 with the alignment steps developed by Adam Lawrence. The die bonder consists of a platform where the tungsten

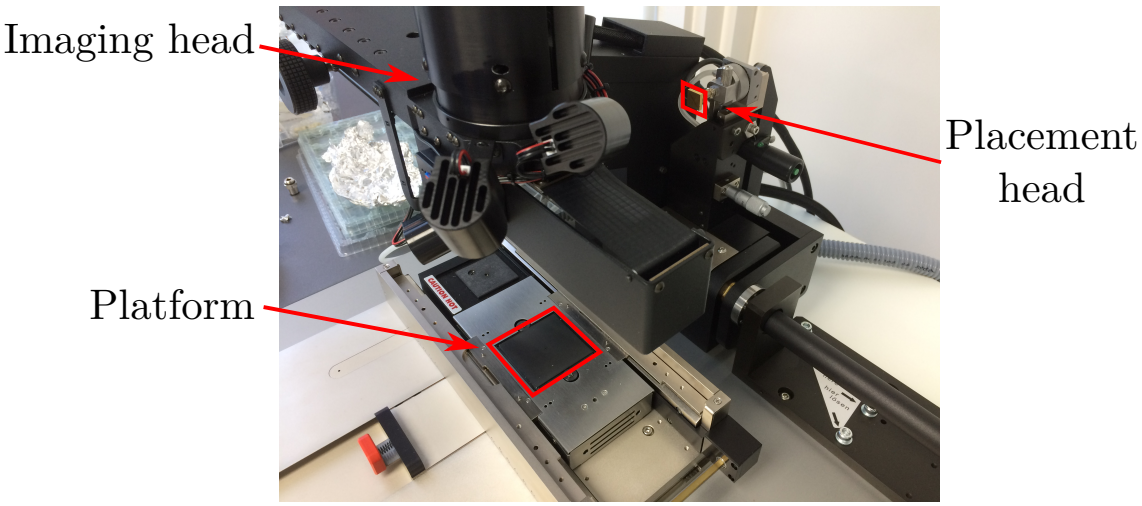

Figure 5.8: The commercial die-bonder used for trap-magnet alignment.

spacer assembly is held using suction, while the ion trap is picked up with the placement head. Both of the components are imaged simultaneously by combining the images with a beam splitter onto a digital camera. Once the reference points on the trap are mapped out on the spacer, the procedure is simply lowering the positioning head with a high precision lever, which guarantees less than 5 µm movement. The trap is lowered until a specific amount of force is exerted on the lever, which can be set by the user. In this position, the epoxy[2] is deposited at the four corners of the trap and the heating stage is turned on to cure the epoxy at 100 °C for an hour. The choice of using different epoxy for fixing the trap in position was motivated by several instances of the silver epoxy leaving deposits on the trap surface when cooled down to 10 K temperature. The finished trap assembly was inspected for misalignment, in case there was any unwanted translation and rotation. The measurements were carried out using an optical microscope[3], which gave an alignment accuracy of 2 µm for the x and z axes.

The finalised ion trap and magnet assembly is shown in fig. 5.9. Following this, the procedure of placing the ion trap in the system follows the steps outlined in the previous chapter.

[1] Finetech FINEPLACER pico ma
[2] EPO-TEK H67-MP
[3] Nikon microscope capable of ×1500 magnification

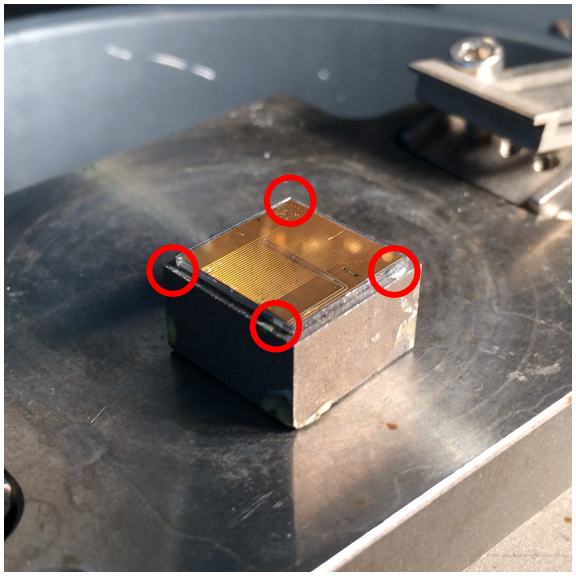

Figure 5.9: Picture of the ion trap aligned and epoxied on the magnet spacer. The epoxy points are highlighted with red circles.

5.3 Cooling system

In recent years it has become clear that in order to perform high fidelity operations with trapped ions using surface traps, it can be helpful to reduce the temperature of the system. Such conditions contribute to the reduction of the trapped ion anomalous heating rate [80], reduction in dielectric losses in relevant substrates [184] and reduced resistance of electronic circuits [185], which reduces power dissipation due to resistive heating. During the development of the vacuum system, a closed cycle 20 bar pressure cold helium circulation system was built for a separate experimental system, which will be part of the larger scale device [45]. The circulation system was designed to provide four vacuum systems with the ability to cool down the ion trap assembly to temperatures of 70 K to 100 K. For this purpose a heat exchanger was designed by Foni Raphael Lebrun-Ricalens [186], which is fitted inside the vacuum system using a low-vibration mount, both described in this section.

5.3.1 Cold helium source

The closed cycle system is based on a commercial Gifford-McMahon (GM) cooler[4] [187], with the coolant distributed by insulated stainless steel piping lined throughout the lab with a centrifugal pump. The diagram of the full cooling cycle can be seen in fig. 5.10. In a circulation system, the cooling power is largely determined by the flow rate of the

[4]Sumitomo Heavy Industries CH-110GM

coolant, where the maximum cooling power is given by [186],

$$\phi = C_V \Delta T \frac{\mathrm{d}V}{\mathrm{d}t}, \tag{5.1}$$

where C_V is the volumetric heat capacity of the coolant, ΔT is the temperature difference between the flowing in and flowing out coolant and $\frac{\mathrm{d}V}{\mathrm{d}t}$ is the volumetric flow rate. Taking

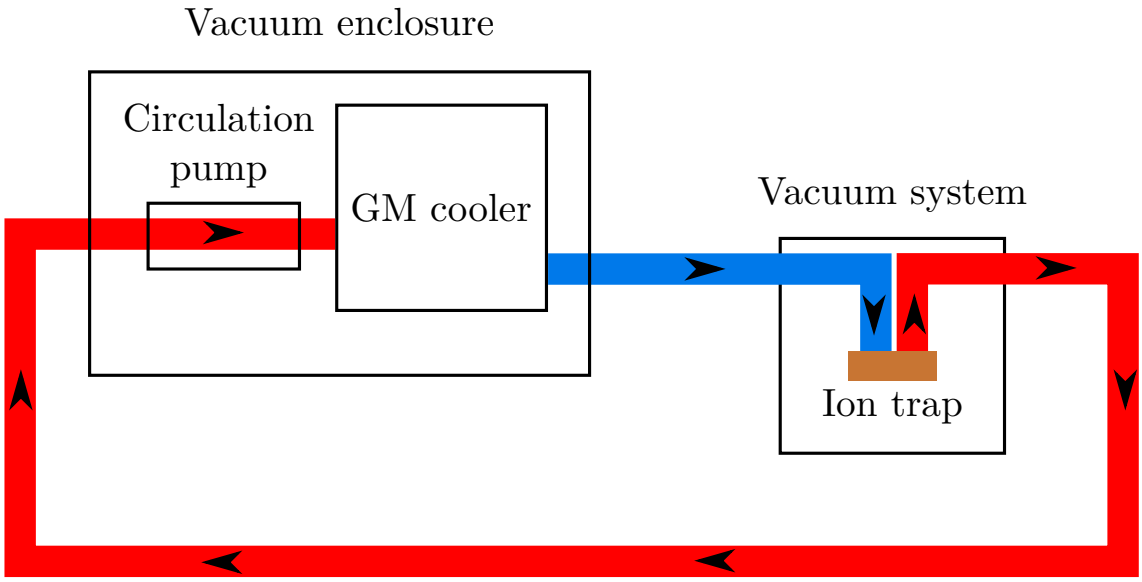

Figure 5.10: Diagram of the closed cycle helium cooling system connected to an ion trap vacuum system. The supply and return lines are contained within a single piece of piping.

account of the static losses due to the flow of the helium, the GM cooler system provides a total cooling power of 135 W when operating the coolant at 77 K with a flow rate of 2.1 $\mathrm{m^3\,h^{-1}}$, which is distributed to a total of four experimental setups. The ion trap system described in this thesis was allocated 15 W, which sets the limit for cooling power losses to achieve steady state operation. The flow rate was set by the centrifugal pump[5] mounted inside the GM cooler enclosure, but to have individual control of the coolant flow rate, each ion trap system has variable valves. The maximum flow rate for these systems is expected to be 0.25 $\mathrm{m^3\,h^{-1}}$.

The pump pushes the gas through using a differential pressure of 1 bar through the supply line, which leads to the heat exchanger, where the coolant absorbs the heat and flows out and into the return line. The return line is fed back into the recycling cooler, where the warm helium gas is refrigerated again. The pressure of the whole line is kept at 20 bar. The use of long supply and return lines can introduce cooling power losses due to conduction with air. This effect is minimised by placing both supply and return lines in a metal tube which is evacuated to 10^{-6} mbar to reduce heat loss through conduction with

[5] Cryozone Noordenwind Cryofan

air, with both lines insulated using stainless steel braiding and several layers of mylar, which is an excellent thermal insulator.

The GM cooler used for the refrigeration can generate a significant amount of vibration, however by placing the experimental system far away from the source, the stainless steel lines and flexible connectors attenuate the vibration amplitude. Nevertheless, the flow of a high pressure gas through the heat exchanger can result in a significant amount of vibration, which can severely disturb the ion trap system. This and the requirement of optimum heat transfer is mostly determined by the heat exchanger, which makes contact with the ion trap.

5.3.2 Heat exchanger

The design of the heat exchanger follows the calculations performed in [186] for optimised heat transfer with particular attention given to vibration performance. The rate of heat exchange is proportional to the surface area of the cooled object. On the other hand, the coolant should not undergo a significant pressure drop between the input and output ports, which can lead to turbulent helium flow and large forces exerted on the structure. To balance both effects, a spiral channel design for the heat exchanger was used, seen in fig. 5.11, which increases the contact area and only produces a pressure drop of $<100\,\mathrm{Pa}$ for a flow rate of $0.25\,\mathrm{m}^3/\mathrm{h}$. The helium gas enters the structure through the centre and is

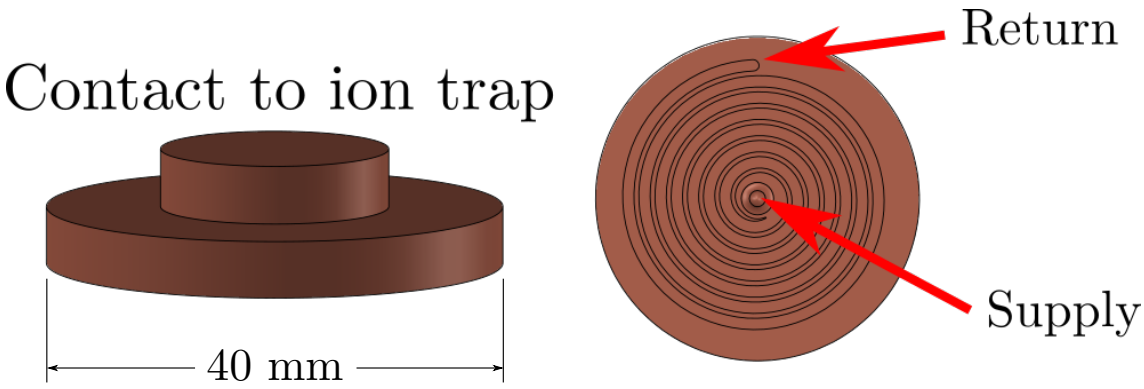

Figure 5.11: The spiral design of the heat exchanger is formed by a 30.4 mm spiral with a track width of 2 mm consisting of 7.5 turns.

pushed through the spiral until it reaches the output port. To make sure the coolant only follows the path of the spiral, the housing of the heat exchanger is brazed with the copper part to make a surface-to-surface connection. The housing was machined from stainless steel, which can withstand the 20 bar pressure and has a low thermal conductivity. The full assembly can be seen in fig. 5.12. The return path of the warm helium is formed by a stainless steel assembly comprising out of two parts. The first part contains a small

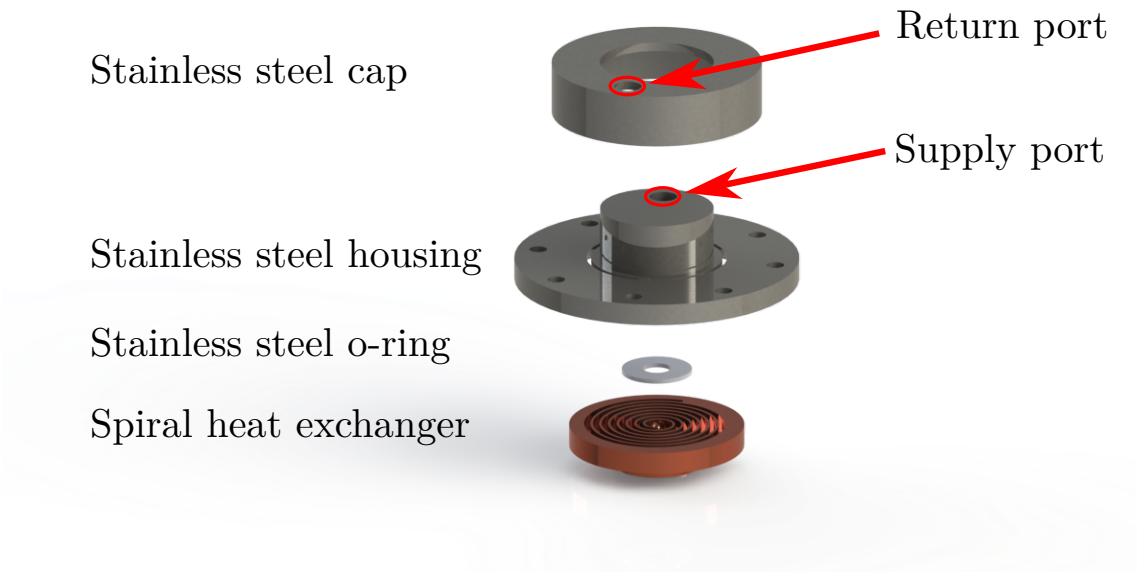

Figure 5.12: Exploded view of the whole heat exchanger. Stainless steel connections were welded, whereas the copper to stainless steel joint was brazed on.

clearance through which the warm helium is pushed upward into an enclosure formed by the stainless steel cap seen in fig. 5.13. The stainless-steel o-ring forms a circular hole, which guarantees that helium enters the heat exchanger only through the centre.

The helium supply and return lines are fed into the vacuum system with the use of two right angle feedthroughs with stainless steel 1/4 inch VCR connections. The feedthroughs contain a wall, which separates the UHV environment of the experimental system and the vacuum jacket of the helium lines. The helium lines are connected to the heat exchanger with the use of a 1/4 inch copper tube and a Swagelok to VCR adapter, with the other end of the copper tube directly brazed onto the stainless steel housing. The in-vacuum helium lines had to be flexible enough to be able to seal the VCR connections and be hidden within the vacuum system for reaching ultra high vacuum. Therefore copper was chosen as the material of choice. However, copper can significantly contract when cooled, resulting in applying large shearing forces on the connectors and the braze joints. A loop was formed with the tube, such that the tubing could expand and contract without pulling on any of the connections. The complete assembly can be seen in fig. 5.14.

5.3.3 Heat exchanger mounting system

Mounting the heat exchanger into the vacuum system required careful consideration, as not only is it heavier and larger than the previous design, it also required better thermal and

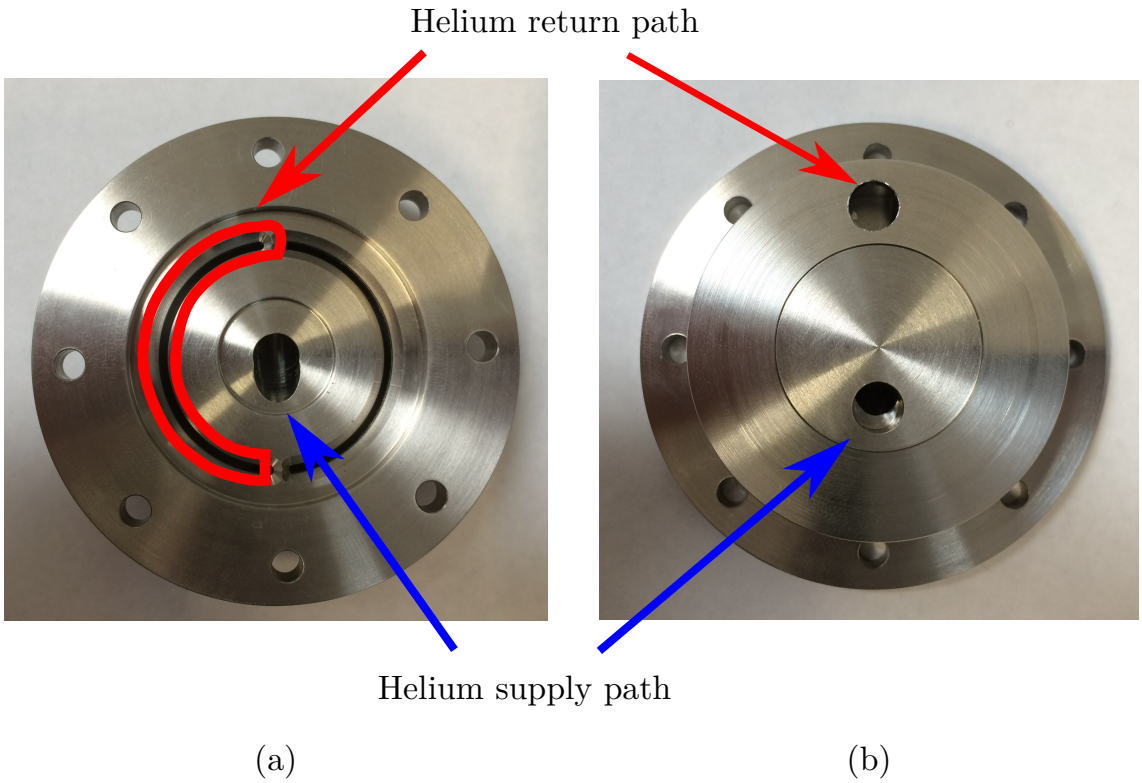

Figure 5.13: The top (a) and bottom (b) view of the stainless steel components for completing the helium path. Cold helium enters the through ports highlighted in blue, centred with the copper heat exchanger in fig. 5.11. The warm helium leaves the heat exchanger through the semi-circle port in (a) and out through the circular opening in (b), which is connected to a tube leading out of the vacuum system. The 4 mm clearance holes positioned in a circular pattern are used for attaching the components of the mounting system described in the next section.

vibrational insulation for the high pressure cooling cycle. Two designs for the mounting structure were chosen to be machined, one with all components made out of metal and the other having components with a low thermal conductivity. The first design of the structure can be seen in fig. 5.15. The heat exchanger is mounted using the DN63CF port at the back of the hemisphere with the use of two groove-grabbers and titanium plates, which were based on the design of the previous low-pressure cooling system, but with shorter reach from the flange into the vacuum system. This was done to accommodate a titanium disk, which provided four contact points for the heat exchanger. The disk contains a rectangular hole, which was made to reduce the weight of the system and provide another route for the copper tubing. The four contact points between the heat exchanger and the disk are bridged with titanium brackets, one end with an M4 tapped hole with the other having a u-shape cut out. The u-shape cut out side is positioned on one of the 4 mm diameter clearance holes on the stainless steel housing assembly in fig. 5.13. An M4 bolt is fed through the u-shape cut out to provide a connection between the stainless

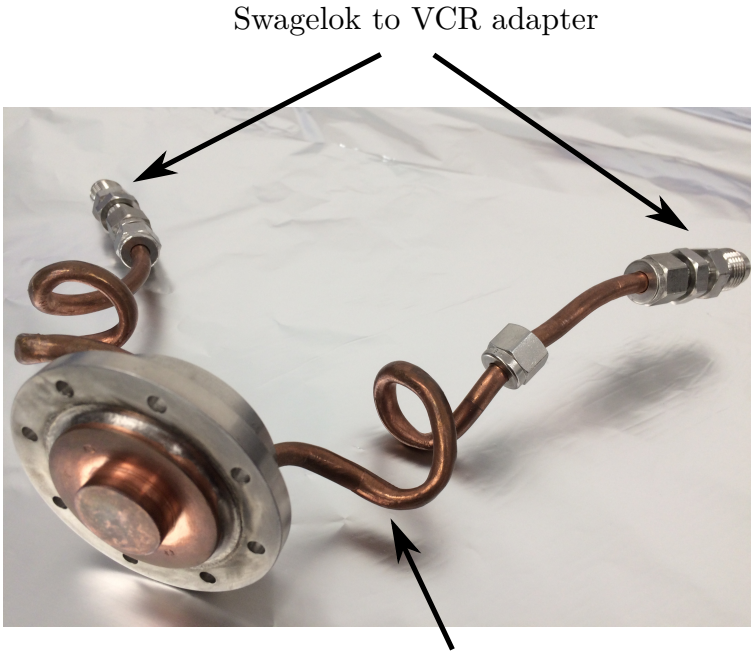

Figure 5.14: The fully assembled cooling system with helium feed lines consisting of 1/4 inch copper tubing.

steel plate and the heat exchanger. The other end of the titanium bracket makes contact with the titanium disk, provides a solid base to the four brackets to dampen vibrations in all directions. The final component of the mounting system is the stainless steel plate, which contains several M4 tapped holes for attaching the heat exchanger and M3 holes for aligning the in-vacuum PCBs. Once the cooling system was mounted, the distance from the heat exchanger to the in-vacuum PCB assembly was set by a copper block with M3 bolts going into the front PCB.

The supply and return lines that connect to the vacuum system are positioned directly above the optical table with the use of stainless steel tubing and DN63KF flanges. The external view of the cooling system feedthroughs can be seen in fig. 5.16.

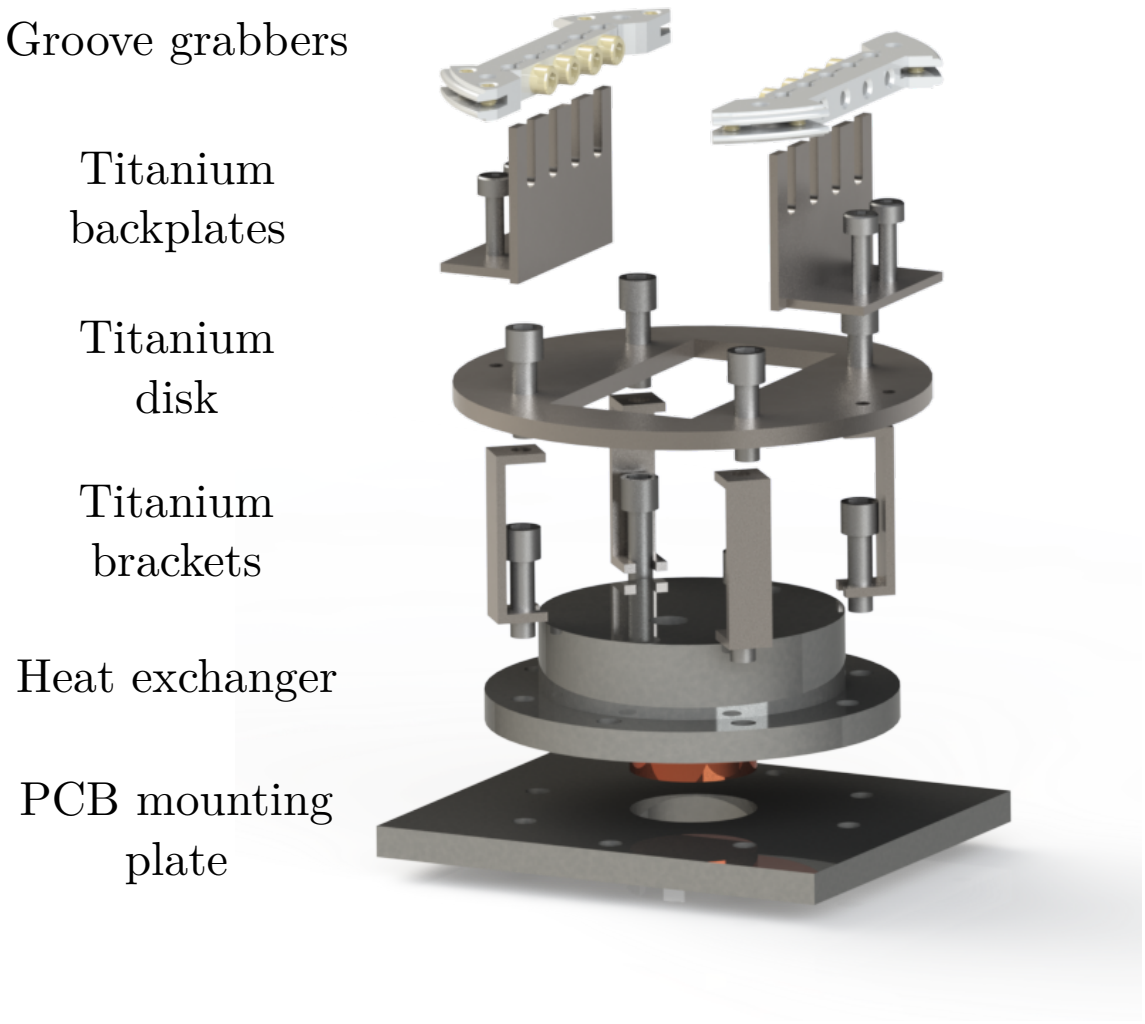

Figure 5.15: The complete mounting structure of the cooling system. Not pictured are the helium feed lines.

5.3.4 Cooling system evaluation

Heat transfer characteristics

The cooling power supplied to the ion trap module by the GM cooler is 15 W. The lowest possible temperature of the heat exchanger and the ion trap is determined by the balance of the cooling power and the heat flowing into the whole experimental assembly. In order to calculate the final temperature, these heating mechanisms must be estimated and if possible their effect minimised.

The fundamental limit to the minimum temperature an object can achieve is the blackbody radiation of the surrounding objects [188]. The cooled ion trap assembly will emit and absorb radiation at a rate proportional to the temperature difference between it and the walls of the vacuum system. The net absorbed power of a cooled object of

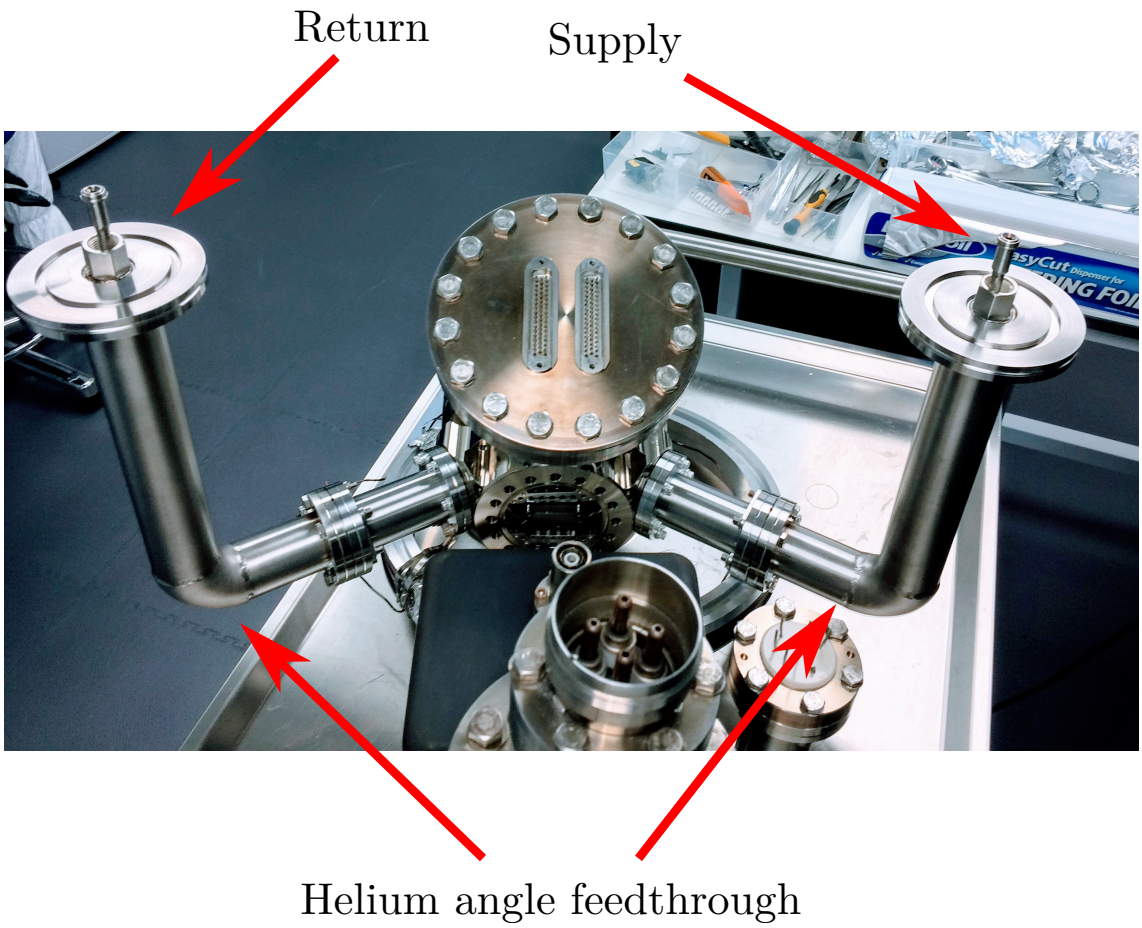

Figure 5.16: View of the vacuum system with the cooling system connected on the back DN63CF flange. The additional DN40CF nipples are used to set the correct position of the supply and return flanges on the vacuum system.

temperature T with a surface area A placed in environment of temperature T_0 is given by the Stefan-Boltzmann law [188]:

$$P_{net} = \varepsilon\sigma A({T_0}^4 - T^4), \tag{5.2}$$

where σ is the Stefan-Boltzmann constant and emissivity ε defines how absorptive the object is on a scale of 0 to 1, which is determined by how much of the ambient radiation is reflected off the surface. Not included in this equation, but used in the estimates is the view factor, which captures the fact that the emitted radiation is emitted with spherical symmetry which means that the angle of the absorbing surface will determine the total amount. Some of the radiation will be absorbed by the other surfaces of the PCB assembly or the mounting structure. In the calculations, this is approximated by a multiplicative factor set to 0.5. From the equation it is apparent that to reduce the amount of absorbed heat, the cooled object needs to have a small surface area and/or have a highly reflective

coating. Therefore, the copper heat exchangers have an electroplated gold layer, which achieves values of ε=0.025 [189], compared to unpolished and oxidised copper emissivity of ε=0.78 [189]. For this reason, the whole mounting structure was manufactured to have a smooth surface finish for the stainless steel and titanium components, while the copper parts were polished before putting the system in place. The ion trap and in-vacuum PCB assembly was estimated to have an average emissivity of ε=0.3 [189] due to the gold coating of the conductive layers. The stainless steel and titanium parts were assumed to have an emissivity of ε=0.4. In the calculations of the absorbed power by the full assembly, the average emissivity was assumed to be 0.5, to provide an overestimate for the amount of power absorbed.

The second most important mechanism determining the amount of heat flowing into the system, is the presence of conduction from the contact with the vacuum chamber. This includes the titanium backplates mounted with the use of groove grabbers at the back of the hemisphere, and the connections between the PCB and the wires leading to the DSUB and coaxial connectors on the vacuum system for DC voltage control and trapping radio-frequency fields. The power conducted between an object with a cross sectional area A with one end at temperature T and the other at T' can be approximated using [190]:

$$P_C = kA\frac{T - T'}{L}, \tag{5.3}$$

where k is the thermal conductivity of the material the rod is made out of. The equation was used to calculate the heating introduced by the 100-wire ribbon cables, which have a 0.35 mm diameter and the in-vacuum coaxial RF cable, which has a diameter of 0.5 mm. Connecting the mounting structure to the vacuum system introduces a heat load which can be approximated by the same equation. The contact area is given by the stainless steel groove grabber interface with the vacuum system, which has a total value of $4 \times 10^{-5}\,\mathrm{m}^2$. A steady state temperature difference of 20 K between the titanium backplates and the groove grabbers were used.

The numerical estimates for all these losses and additional heating are shown in table 5.1. The applied microwave radiation is typically 2 W, which is reduced by reflections off the trap and vacuum system walls.

Using Solidworks Simulation Package[6], the heat exchanger with the detailed parameters results in a steady-state temperature of 79 K, illustrated by the temperature map in fig. 5.17. This temperature was deemed sufficient for significantly reducing the trapped

[6]Dassault Systems Solidworks

Table 5.1: Origins and estimates of unwanted heating mechanisms.

Cause	Estimated amount (W)
Blackbody radiation	7
Radio-frequency trapping fields (Power dissipation)	0.6
Microwave and radio-frequency addressing radiation	1
100 wire DC ribbon cables	1.6
RF coaxial cable contact	0.55
Mounting structure-to-vacuum system contact	2.4
	Total = 12.15

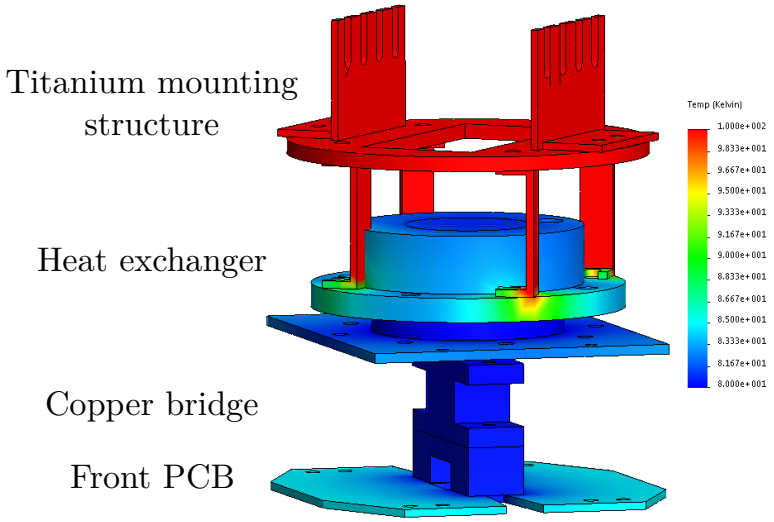

Figure 5.17: Temperature map of the heat exchanger mounting system and the front PCB. Not all components were included in the drawing, however their contributions were added to the simulation in the form of sources of heating on surfaces which they make contact with. The copper bridge is used to make contact with the ion trap platform.

ion heating rate as described in [79]. Although most of the entries in the table cannot be reduced, it is possible to improve the heat losses due to the mounting structure by using thermally resistive plastics such as PEEK [191], but potentially increasing the sensitivity to vibrations. A PEEK based system has also been designed (see below) which has been used for comparison.

Vibration amplitude

The integrity of the mounting structure determines the amount of movement experienced by the ion trap system. The amount of vibration that can be tolerated is determined by the wavelength of the radiation used to manipulate the trapped ion motion and the secular frequencies. Using the magnetic field gradient scheme, the 12.64 GHz field for manipulating the qubit has the shortest wavelength (24 mm). To analyse the performance

of the mounting system, simulations were carried out using the Solidworks Simulation Package to quantify the amplitude of the vibrations.

Ideally, the vibrations should not excite any of the resonant frequencies of the mounting structure, which will have the largest amplitude response. The scale of this response is governed by the size and material of the mounting structure. In the simulations used to estimate the response of the mounting structure, the heat exchanger is perturbed by a 0.01 bar pressure, with a white noise frequency spectrum for the range 0 kHz to 1000 kHz. The results of the simulation are given in figure fig. 5.18, where the displacement amplitude is plotted against the frequency of the vibration. The lowest resonance frequency of the assembly is 290 Hz, with an amplitude of 13 µm. This indicates that perturbations due to helium flow will not excite the high amplitude oscillation at secular frequencies, which are typically >100 kHz. Simulations of the turbulent flow inside the heat exchanger indicate, that the vibration spectrum starts only at frequencies of ≈1 kHz, which is expected not to cause any vibration to the mounting structure.

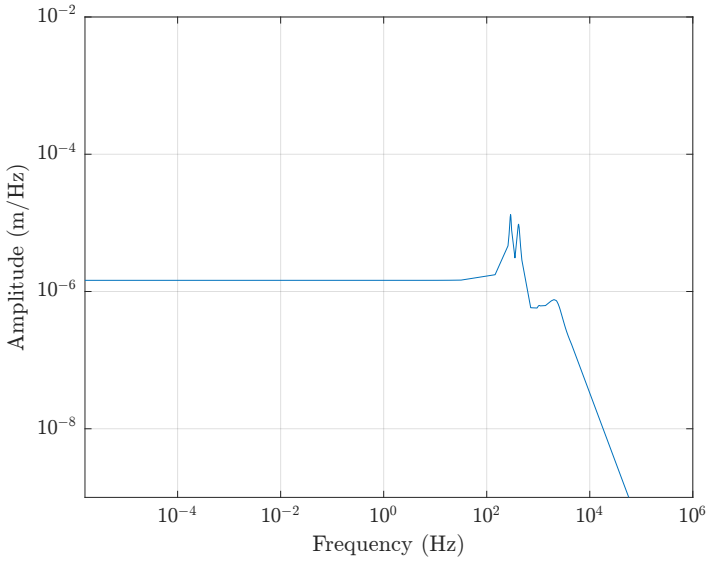

Figure 5.18: Response graph of the mounting structure measured at the heat exchanger. The peaks at ≈290 Hz correspond to resonant frequencies, where the amplitude of the oscillation is on the scale of several micrometres.

As the graph indicates, the heat exchanger can undergo vibrations of several micrometres, which is much lower than the estimated limit. Therefore, the system is expected to not interfere with the qubit system being used quantum gate experiments.

5.3.5 Modified heat exchanger design

Although the heat exchanger was successfully tested to withstand large pressures and temperatures of 70 K using liquid nitrogen, during the procedure several drawbacks of the mounting system were identified. The main issue is the copper tubing, which proved to be difficult to compress or shape while the heat exchanger was inside the vacuum system. Forceful handling of the tubes left some pinch points, which do not completely block the flow of helium, nevertheless affects it and causes a reduction of cooling power. Furthermore, using copper tubes carries the risk of significant contraction when cooled, which introduces loose connections on the Swagelok connectors and the braze points. To remove any possible risk that results from using copper, the next iteration of the heat exchanger was designed to have stainless steel tubing. The design of the system can be seen in fig. 5.19.

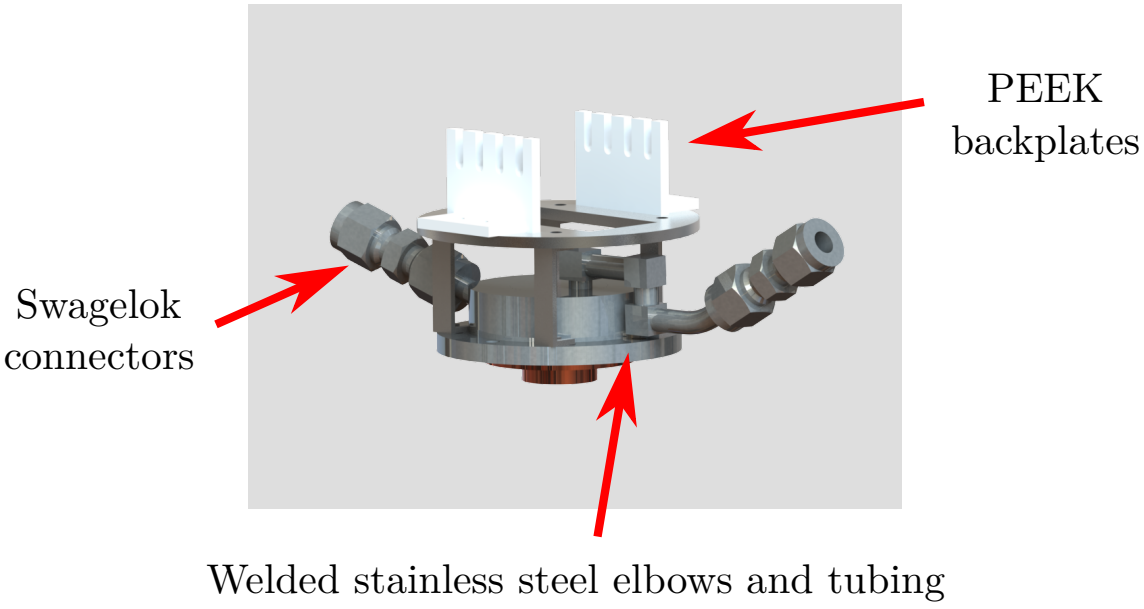

Figure 5.19: Drawing of the heat exchanger with the copper helium lines replaced with stainless steel elbows and tubing, and Swagelok connectors. The low thermal conductivity PEEK backplates are used to reduce the heat load from contact with the vacuum system.

The main improvement from the previous version is the use of fully stainless steel tubing for connecting to helium supply and return lines, which avoids the complications of contracting copper tubing. This however does require a different method of closing the system. A solution to this is to use flexible bellows pictured in fig. 5.20, which can be compressed to reveal the Swagelok connections and then extended and fixed into the vacuum system.

The bellow length can be varied by ≈25 mm, but results in having no support for the right angle feedthroughs. Therefore, stainless steel brackets were designed to connect the

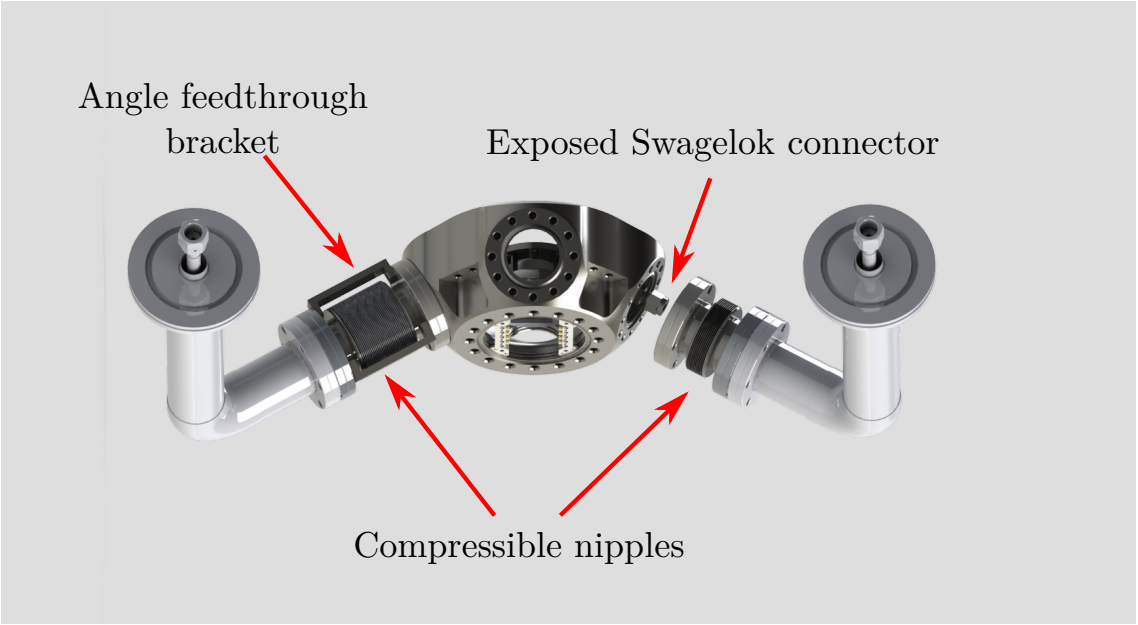

Figure 5.20: Illustration of the mounting system for the new cooler. The compressible nipples have a stroke length of ≈25 mm, which is enough to expose the tubing connectors and tighten them. Once the helium supply and return lines are sealed, the nipples are extended up to the hemisphere and tightened with screws. The angle feedthrough brackets are used to provide a method of fixing the angle feedthroughs relative to the chamber.

DN40CF flange of the feedthrough to the flange of the vacuum system. These brackets are the larger versions to the titanium brackets pictured in 5.14.

The updated mounting system has PEEK backplates instead of titanium to reduce the heat load even more, but with the added uncertainty of mechanical stability. The response to vibration comparison between the different material backplates is given in fig. 5.21. The simulations suggest that the vibration amplitude will increase by a factor of two, with resonant excitations resulting in amplitudes of 10 µm. Despite the obtained results, it is difficult to know the actual amount of vibration present in the cooling system without testing it. It was decided to machine the PEEK backplates and once one of the system was tested, decide if the change of material is worth the reduction in mechanical stability.

Finally, to further reduce the heating due to blackbody radiation, some of the components will be plated with a layer of gold to reduce their emissivity. This could potentially reduce the heating power by half, which is expected to improve the performance of the overall circulation system.

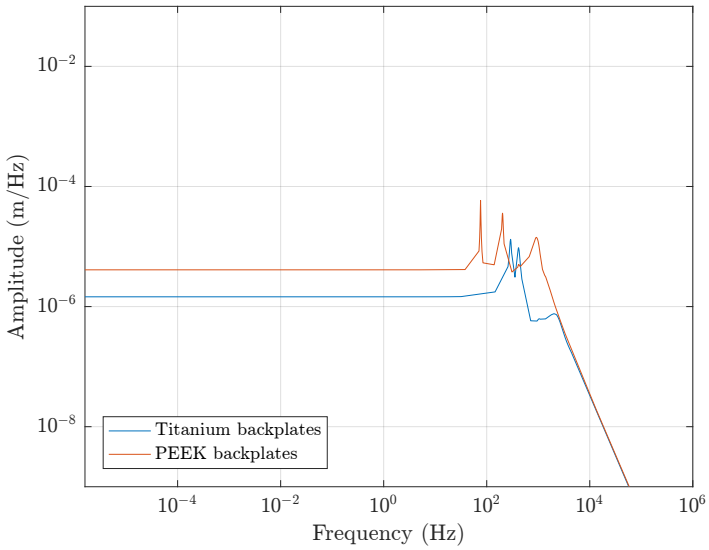

Figure 5.21: Comparison of the response for different material backplates - PEEK and titanium. The PEEK backplates increase the amplitude of the vibration and has lower resonant frequencies due to having a reduced stiffness when compared to titanium.

5.4 In-vacuum microwave and RF emitters

In chapter 4, simulations of the microwave and radio-frequency fields propagating through the imaging window revealed large power attenuation. This is due to a stainless steel mesh being placed on the window to shield the ion from static charges. This means the interaction strength between the magnetic dipole and the field is greatly reduced, resulting in Rabi oscillation frequencies of $\Omega_\pi = 2\pi \times 9.94\,\text{kHz}$ for an input power of 1 W. This frequency can be increased by using a higher gain amplifier, but at the cost of acquiring expensive equipment for handling large microwave powers. The details of a system capable of delivering up to 80 W of power is described in section 5.5. Nonetheless, increasing the power by a factor of a 100 corresponds to an increase in the field strength by 10, which is not efficient considering the requirements. Furthermore, in-vacuum emitters may play a significant role in a large scale quantum computing architecture such as in [45]. This does of course relinquishes the ability to manipulate their position and orientation. This section describes the design assembly of an in-vacuum microwave emitter system.

5.4.1 In-vacuum emitters

The requirements for a microwave antenna includes the ability to generate all of the required polarisations to address the Zeeman shifted energy levels in the $^2S_{1/2}$ manifold. This means having appreciable magnetic field amplitude components (B_x, B_y and B_z) to

obtain the linear and circular polarisations, which can be calculated using [192]:

$$B_- e^{-i\phi_-} = \frac{1}{2}(B_x e^{-i\phi_x} + iB_y e^{-i\phi_y}) \tag{5.4}$$

$$B_\pi e^{-i\phi_\pi} = B_z e^{-i\phi_z} \tag{5.5}$$

$$B_+ e^{-i\phi_+} = \frac{1}{2}(B_x e^{-i\phi_x} - iB_y e^{-i\phi_y}), \tag{5.6}$$

where ϕ_-, ϕ_π and ϕ_+ are the phases of these components. From the equations it is clear that only two components of the B field are required to address the all of the levels, either the pair B_z and B_x or B_z and B_y. Any emitter placed inside a vacuum system, must be either set to the correct polarisation manually or have the option of controlling the polarisation outside the vacuum system.

A possible solution was pointed out in the work of [192], where a circular waveguide was built, optimised to deliver 12.6 GHz radiation to the ion. The polarisation control was implemented with the use of two monopoles, orientated perpendicular to each other within the waveguide. Each monopole produces different polarisation oscillations, whose phase and power can be controlled externally to obtain any superposition. Even though the in-vacuum waveguide increased the Rabi frequency, the size of the device prevented the same implementation to be used in the vacuum systems described in this thesis. Furthermore, the recessed window situated 1 cm from the ion trap, would block a significant amount of radiation reaching the ion.

An innovative solution was proposed by group member Anton Grounds, where two wires of 25 µm diameter are placed in close proximity to the ion (see fig. 5.22), similar to a balanced two-wire transmission line [193]. To optimise the transmission of this system, the wires would need to be accurately spaced to obtain the correct impedance of free space $\approx$376 Ω. This requires a wire-to-wire distance of $\approx$300 µm, with an accuracy of 100 µm. As in the case of the circular waveguide, the individual control of the wires guarantees polarisation control. Even though, the system can be assembled directly on the ion trap structure with the use of wirebonds as the transmission lines, it would be delicate to any perturbation during the baking of the vacuum system and any other movement. To obtain a more robust solution, a design using in-vacuum microwave coaxial wires was developed instead, which can be used for both microwave and radio-frequency addressing of the ion.

The shape of the magnetic field lines around a wire conducting a DC electrical current can be described by the well known ‘right hand rule’, which gives a circularly symmetric field around the wire. For oscillating currents, the same is true, but with the additional

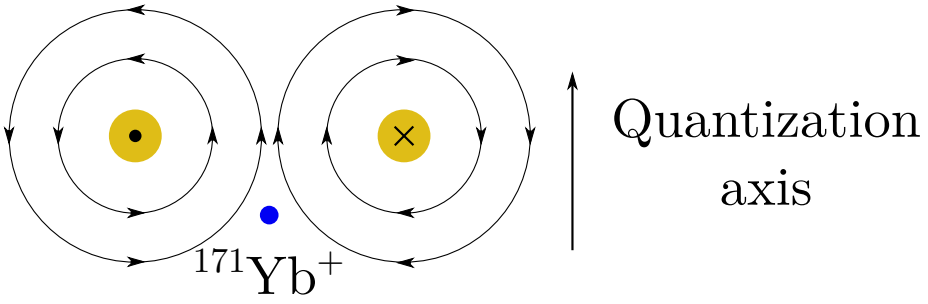

Figure 5.22: Illustration of the two wire balanced line scheme for an ion trap with the quantization axis normal to the plane. Two wires in close proximity to each other and the ion will generate a magnetic field whose polarisation is dependent on the phase between them. Wire dimension and distances are not to scale.

effect of the impedance of the line determining the propagation of the current. To be able to expose the trapped ion to the intense magnetic fields, the outer conductor of the the two coax wires needs to be removed, which introduces an impedance jump along the wire, going from a 50 Ω line to an impedance set by the surrounding conductors, which can be in the range of 100 Ω to 500 Ω [193]. To obtain a reliable picture of the field distribution, simulations were carried out using EMPro software package and the bemsolver package [166] .

5.4.2 Magnetic and Electric field simulations

One of the main purposes of carrying out the simulation is to find out if the magnetic field strength close to the conductor provides an improvement and if so, what polarisation will the field have and will the electric component distort the trapping field, rendering the trap useless. The wire diameter used in the simulation is determined by the available in-vacuum coaxial wires[7], which have an inner conductor of diameter 0.94 mm and outer conductor of 3.6 mm.

To determine if the trap fields are distorted by having two additional grounded wire conductors, the bemsolver software was used to find the optimum distance where there is negligible effect on the electric field nil. The simulations showed, that in order to have no significant effect on the position of the nil, the inner conductor to trap distance needs to be at least 10 times larger than the ion height. Therefore, for an ion height of 150 µm the minimum distance is ≈1.5 mm. Simulations for the centre-to-centre separation between the two wires pointed to the optimum distance of 4 mm, where the distance is large enough to provide good imaging access at the same time being in close proximity to the ion. With

[7] Allectra 380-SMA18G-MM-400

these parameters in mind, the field simulations were carried out using EMPro.

To confirm that the field polarisation is the one expected from basic electromagnetic theory, the vector field was calculated first. The simulation was set up to have two coax wires with a 4 mm length of exposed conductor above a conducting gold layer, see fig. 5.23. The input and output ports for both of the wires were set to have a 50 Ω impedance, with the input power of each wire set to 0.126 W. Having an output port for the microwave wires allows the system to be fully described with the help of the S-parameters [193].

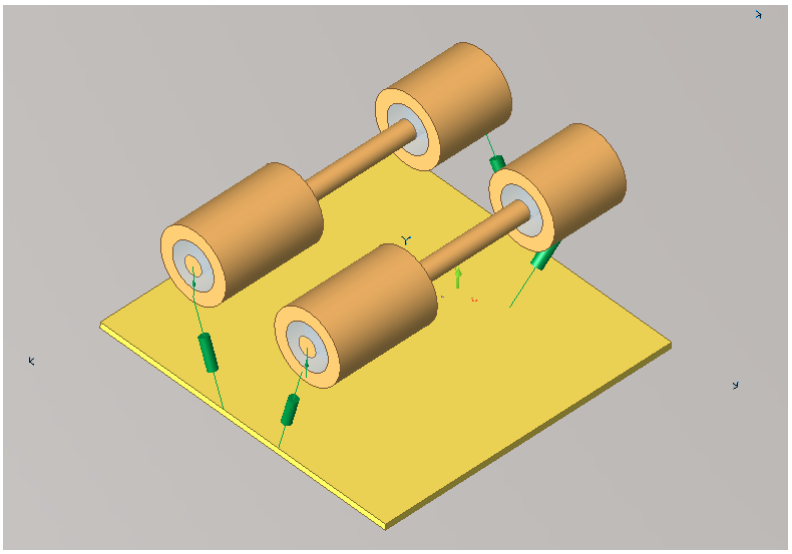

Figure 5.23: The drawing of the simulated two-wire setup. The actual setup contains longer sections of the full coax cable, but it is assumed that the losses within the cable are negligible.

The vector field at a plane dissecting the two wires can be seen in fig.5.24 for the case of in phase (5.24a) and out of phase (5.24b) fields. From the figures it is clear that the basic assumptions made for the DC wire case hold true for microwave oscillations.

Even though the simulations of the electric potential indicate that the presence of the grounded conductors will not have any influence on the trapping field, the presence of an oscillating current can produce a large enough electric field to influence the trapping potential. To analyse this, the electric potential of the two wires was calculated and illustrated in fig. 5.25. The voltage amplitude of these oscillations relative to the trapping potential serves as an indicator of how much the ion will be perturbed by the wires. The electric potential was simulated for different wire-to-wire and wire-to-chip surfaces and the results analysed to find which set minimises the electric field strength at the ion trapping position. The results in fig. 5.25 are for two wires separated by 6 mm, fixed 5 mm above the surface of the trap. Applying the a signal of power 0.126 W per wire, the resultant oscillating electric field magnitude at the ion is ≈50 V/m. An electric field of such scale

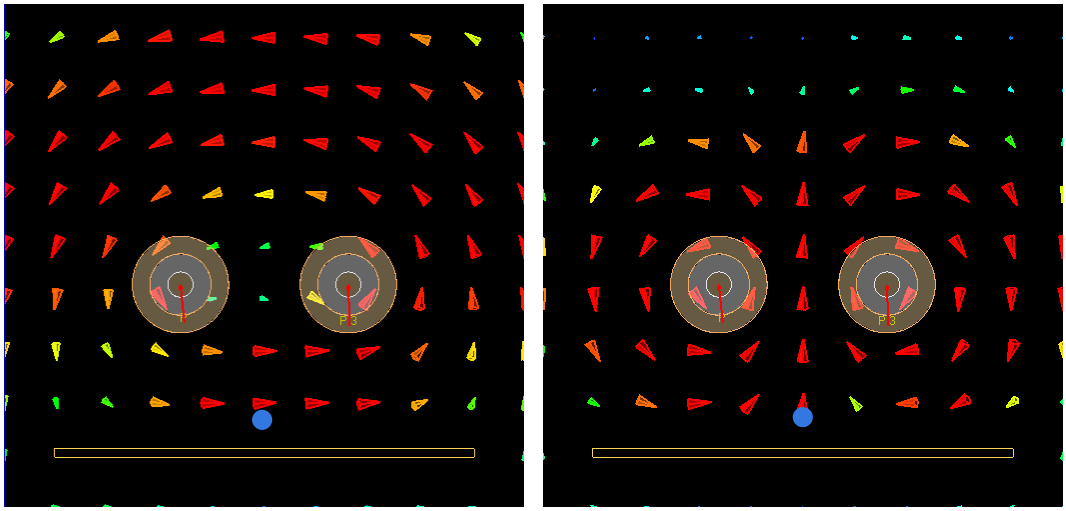

(a) (b)

Figure 5.24: (a) The in phase signals introduce a polarisation which oscillates parallel to the surface along the horizontal axis. (b) By setting the wires to have opposite phase, the magnetic field oscillates along the vertical axis. By setting the phase between these two situations, the polarisation can be set to have any value. The ion position is marked by the blue circle.

is expected to have no significant effect on the ion motion.

The magnetic field magnitude H is plotted in fig.5.26. Both radio-frequency and microwave fields have a significant magnetic component of $5\,\mathrm{A/m}$ and $0.76\,\mathrm{A/m}$. The simulation indicates values significantly larger compared to a standard microwave horn in producing a field of $0.18\,\mathrm{A/m}$ running at $2\,\mathrm{W}$. The resulting microwave Rabi frequency using the two wire scheme was calculated to be $\Omega \approx 2\pi \times 85\,\mathrm{kHz}$.

The exposed wire introduces a change in the impedance of the coaxial wire, which results in reflections back into the input and reduced power transmission along the line. By simulating the reflection parameters of the system, the obtained results serve as benchmarks which can be used later when evaluating the performance of the actual system. The simulation results and the measured parameters are compared in the next section.

The electric and magnetic field simulations confirmed the assumptions made about having two conducting wires placed close to the trap. The arrangement of two parallel wires produces a large magnetic field intensity at the trapping position, with a potential increase of the Rabi frequency by an order of magnitude. In addition to this, the polarisation of the resulting field can be tuned with the use of a phase shifter outside the vacuum system.

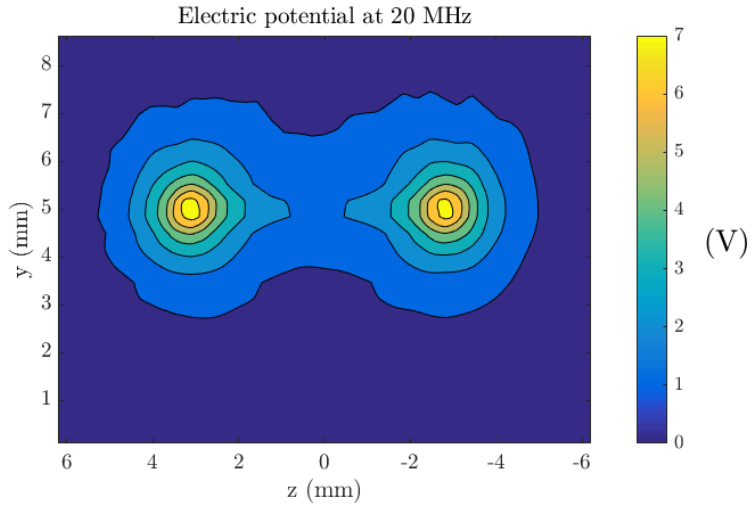

(a)

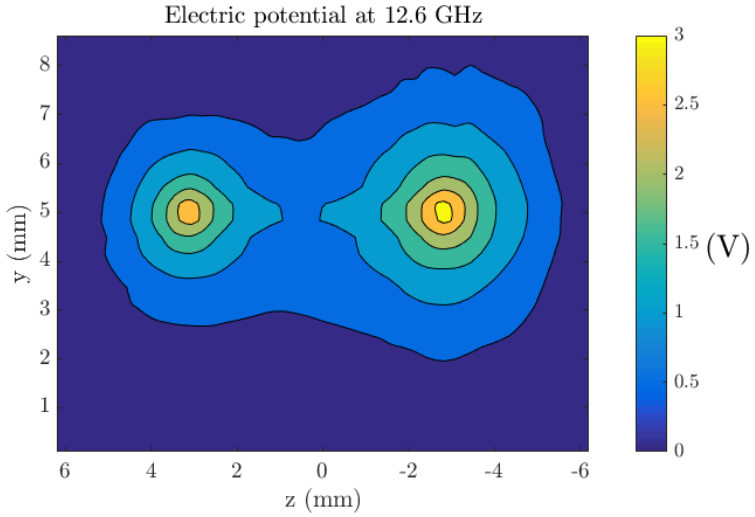

(b)

Figure 5.25: Contour plot of the electric field potential for both radio-frequency (a) and microwave (b) signals. Not pictured in the figure is the conducting trap layer situated at y=0 mm. Comparing the maximum potentials, the radio-frequency potential on the surface of the wires is twice as large as the microwave case. This is likely due to the reflection from the impedance jump of the cable, which will be described later in this section.

5.4.3 In-vacuum microwave wire mounting

The UHV compatible coaxial wire is commercially[8] available cut to a specified length of 40 cm. To provide input and output outside the vacuum system, a four SMA connector flange[9] is attached to the vacuum system hemisphere. The flange is optimised for microwave frequencies, resulting in low insertion loss and attenuation for the 12.6 GHz frequency. Since the wires are semi-rigid, they can be fixed in position at points away

[8] Allectra 380-SMA18G-MM-400
[9] Allectra 242-SMAD18G-C40-4

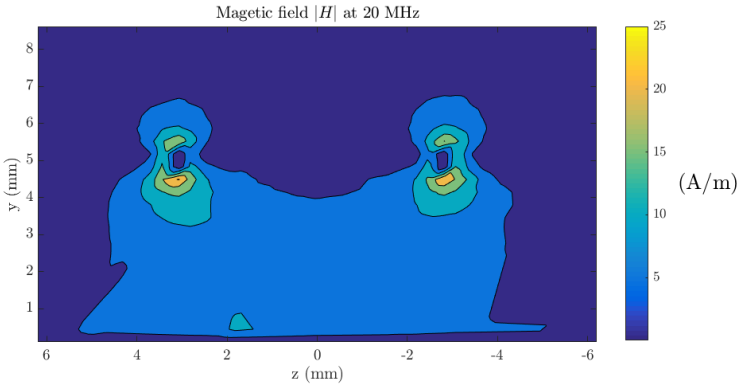

(a)

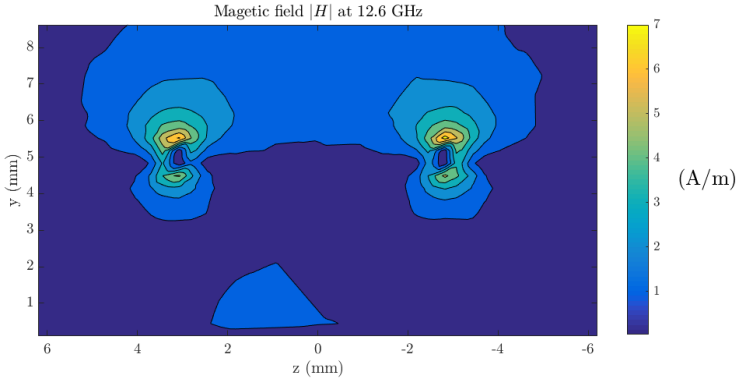

(b)

Figure 5.26: Contour plot of the magnetic field strength H for RF (a) and microwaves (b). At the expected ion position the field strength of the radio-frequency field is equal to 5 A/m and for microwaves it is 0.76 A/m.

from the trap. Therefore mounting brackets were designed to fit on the top and bottom of the in-vacuum front PCB. The brackets were designed for setting the correct separation and distance above the trap structure pictured in fig. 5.27a. Each bracket is attached to the PCB with a M2 screw and nut. The wires are then laid down into the grooves and fixed with a thin metal plate with the use of another pair of M2 screws.

The finished assembly of wires mounted in the vacuum system can be seen in fig. 5.27b. To check the performance of the wires, the system was tested with the VNA to obtain the reflection parameters.

The measured parameters were obtained by performing a frequency sweep over the typically used radio frequency range of 1 MHz to 1000 MHz and a microwave range of 12.4 GHz to 12.7 GHz. Of interest is to see how the reflection parameters compare between simulation and the actual assembly. The radio-frequency data is plotted in fig. 5.28, where the simulations match the measurement quite accurately, but the microwave frequency (fig. 5.29) simulations estimated a significantly larger reflection coefficient. Despite the fact that almost half of the microwave power is reflected, the distance from the source to the

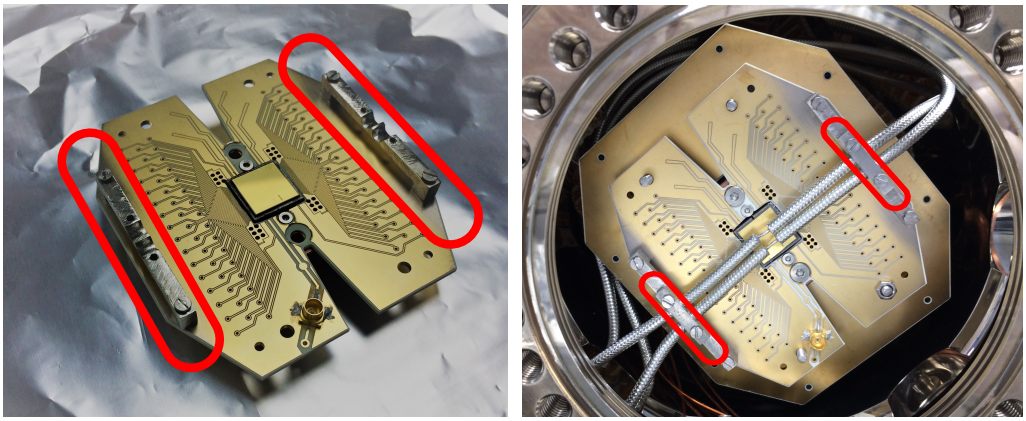

(a) (b)

Figure 5.27: a) The microwave wire mounting brackets (circled in red) are placed at the top and bottom of the front PCB, with the wires tightened to the groove with the use of a plate which can be screwed in with two M2 screws, which are highlighted in (b).

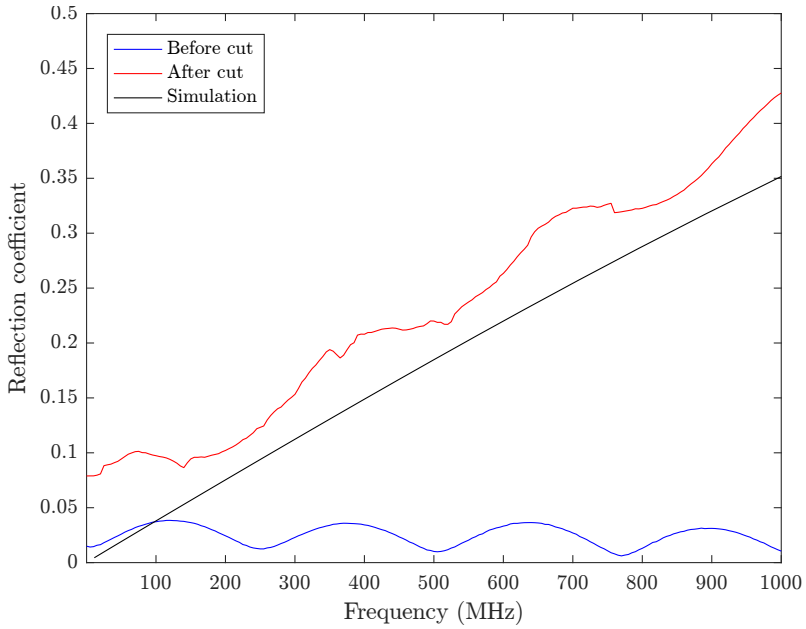

Figure 5.28: The reflection coefficient plotted for the cases of the wire before and after being stripped, while the black line is the simulation data. In the region of 1 MHz to 100 MHz, the reflection coefficient remains small (≈ 0.1).

ion is greatly reduced, which is the main factor responsible for the improvement of the field intensity by an order of magnitude.

5.5 High power microwave setup

Although the in-vacuum coaxial wires were estimated to improve the Rabi frequency, the placement of the cables in close proximity to an ion trap can lead to unexpected damage to the trap. Furthermore, in the case where the wires are damaged during baking, an

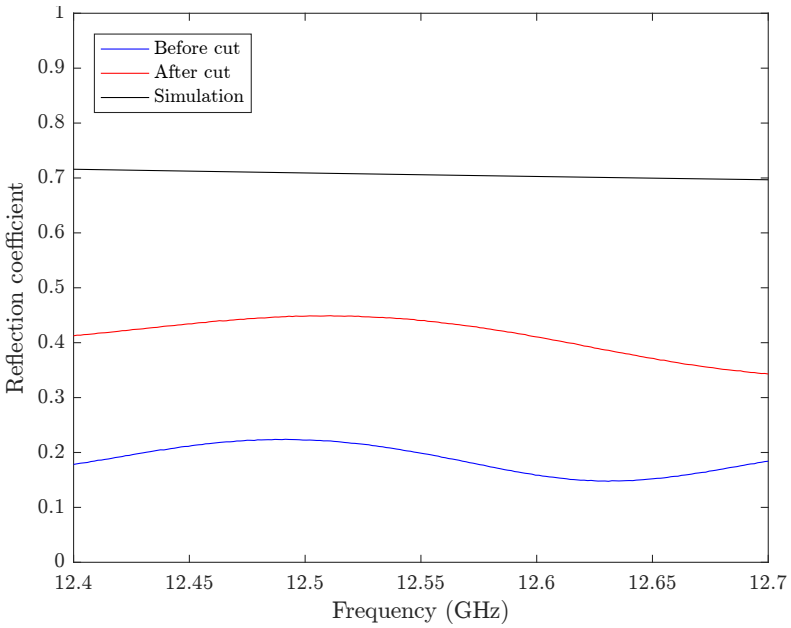

Figure 5.29: The microwave reflection coefficient plotted versus frequency. The difference between each line is more pronounced when compared to the radio-frequency plot. The reflection coefficient remains under 0.5 for the frequency of 12.64 GHz.

external microwave system could be used instead. In addition to this, in the case of using non-linear ion traps, such as an x-junction, does not easily allow to incorporate in-vacuum cables. This lead to the development of two high power systems, capable of delivering 20 W and 80 W of microwave power. Amplifiers used for generating such powers are generally custom built for the right frequency, with the gain profile bandwidth spanning several 100 MHz. The central frequency for both amplifiers corresponds to the 12.64 GHz clock transition $|0\rangle \leftrightarrow |0'\rangle$ of the ${}^2S_{1/2}$ manifold. The initial design of the scheme was developed by Anton Grounds and Nikolaus Lorenz.

The first system schematic can be seen in fig. 5.30. The lower power system was

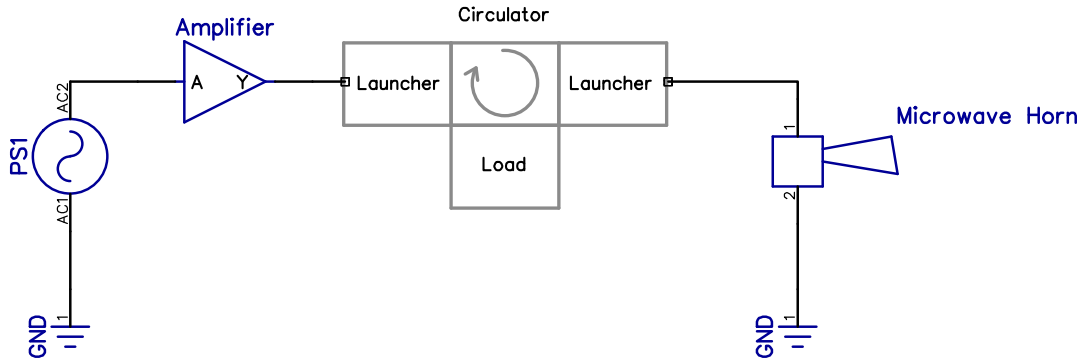

Figure 5.30: Schematic of the 20 W microwave system. The circulator directs any reflection into the load, preventing feedback into the amplifier.

designed for the purpose of retrofitting the microwave setups currently in use in the laboratory with a higher power amplifier[10], to bring up the output power from 2 W to 20 W. The amplifier output is fed from an N-type connector via a high power coaxial cable[11] to a circulator. The three-port circulator serves as a directional isolator, meaning that energy is transferred from port 1 to port 2, port 2 to port 3 and port 3 to port 1 [194]. Any reflection from the impedance mismatch at the circulator output must follow the same direction of flow. In the case shown in fig. 5.30, having a load attached to the bottom port will prevent reflected power from the horn flowing into the amplifier.

To increase the power further, the obvious solution would be to add another amplifier in series to increase the overall gain of the system. However, such configurations can result in an increase of noise and unwanted frequency mixing [195], therefore it is better to split the microwave signal into two paths, where they are amplified to 40 W individually and then recombined in phase. The schematic of the setup is shown in fig. 5.31. The microwave source signal is split into two parts of equal power, one of which goes through a variable attenuator, whereas the other passes a phase shifter. The attenuator is used to control the final output power, while the phase shifter is used to match the phases of the two split signals at recombination. The individual arms of the system are then amplified[12] the same way as in the schematic of fig. 5.30 to prevent reflections back into the amplifiers. Both signals are combined with the use of a hybrid tee[13], which is a four-port device, with two outputs. When the two input signals are perfectly in phase, all of the power leaves the tee-piece through the right hand side, whereas any out of phase components are launched into the left hand port. By measuring the amount of power at the left hand side of the tee, the phase of one of the input signals is adjusted to maximise the power going to the horn.

Increasing the power to more than 40 W carries the risk of large amount of heating in the coaxial cables, which will eventually degrade the system over time. Therefore, a microwave waveguide needs to be used to contain the electromagnetic oscillations within its walls and efficiently transfer the radiation over large distances. Finally, the full combined power of the amplifiers is radiated using a standard horn[14].

[10] Microwave amps AM51-12.6S-43-43
[11] Gigatronix Ku-flex402
[12] Microwave amps AM49-12.6S-46-46
[13] Aaren Technology AT36WMT-62-UBR-4P
[14] Flann Microwave 18240-10

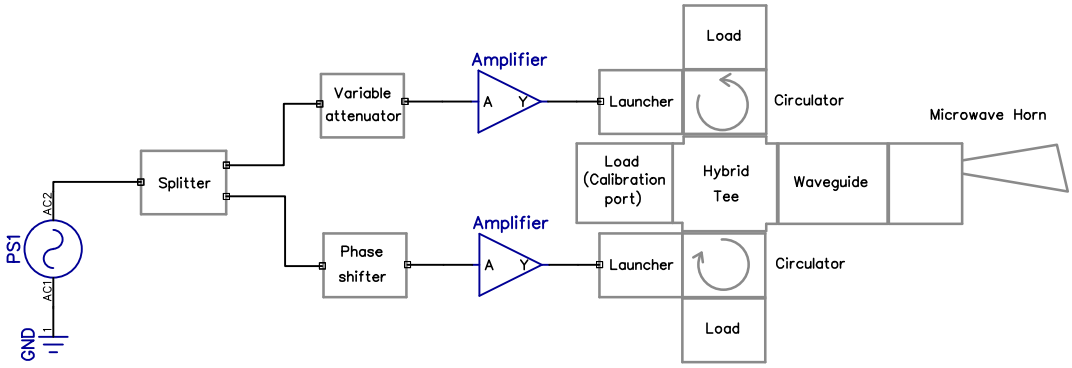

Figure 5.31: Schematic of the 80 W microwave power system.

5.6 Power stabilisation

When calculating the fidelities of a two qubit gate, it is often assumed the parameters, such as the secular frequency and the applied radiation power, remain fixed during the process. Despite the inherent stability of modern electronic devices, the environment of the experiment can change over time, which unpredictably shifts the frequency and power of the radio-frequency or microwave source. To reduce the influence of the environment onto the experimental setup, active feedback system similar to systems described in(locking section) were designed and implemented for stabilising the long term drift of the trapping RF voltage and the microwave dressing field intensity. The work was carried out with the help of undergraduate student Dominic Cooper.

5.6.1 Trap voltage stabilisation

The voltage of the RF drive used for trapping the ion determines the depth and the sharpness of the quadratic potential well, which in turn sets the motional frequencies of the trapped ion. The radial secular frequencies $\omega_{x,y}$ of a trapped ion of mass m and charge e for a ion-electrode distance of r_0 are given by [62]

$$\omega_{x,y} = \frac{e\eta_{RF}V_0}{\sqrt{2}m\Omega_D r_0^2}, \tag{5.7}$$

where V_0 and Ω_D are the amplitude and frequency of the RF drive. The η_{RF} factor is set by the geometry of the trap structure, which is in the range of 0 to 1. The term V_0/Ω_D is governed by the RF drive system, thus can be easily controlled. The frequency of the RF drive signal is generally stable and does not require active stabilisation. Therefore, the voltage stabilisation was the primary focus of improving the system robustness.

As mentioned in chapter 4, the RF trapping voltage path includes a capacitive divider, which splits off 1% of power going to the trap and measures the applied voltage divided by the splitting ratio. Although there can be some discrepancy between the measurement point and the actual voltage of the trap, this pick-off signal can be analysed and stabilised to a reference. This is achieved by converting the RF signal to a DC voltage with a rectifier circuit as in [168] and comparing to a voltage reference IC component. Alternatively a commercial power sensor can be used.

The schematic of the feedback system can be seen in fig. 5.32, in which a power sensor[15] samples the signal and sends the value to a LabVIEW script, where it is compared to a user selected set point. The obtained error signal is then fed through a software based PID controller and is output at one of the analogue outputs of the National Instruments FPGA, achieving a bandwidth of approximately 40 kHz, limited by the power sensor. The control signal is then amplified with the use of an op-amp to the required voltage level and used on a voltage variable attenuator[16], which controls the input power going into the amplifier. In this configuration, the feedback circuitry can correct for drift in the amplifier

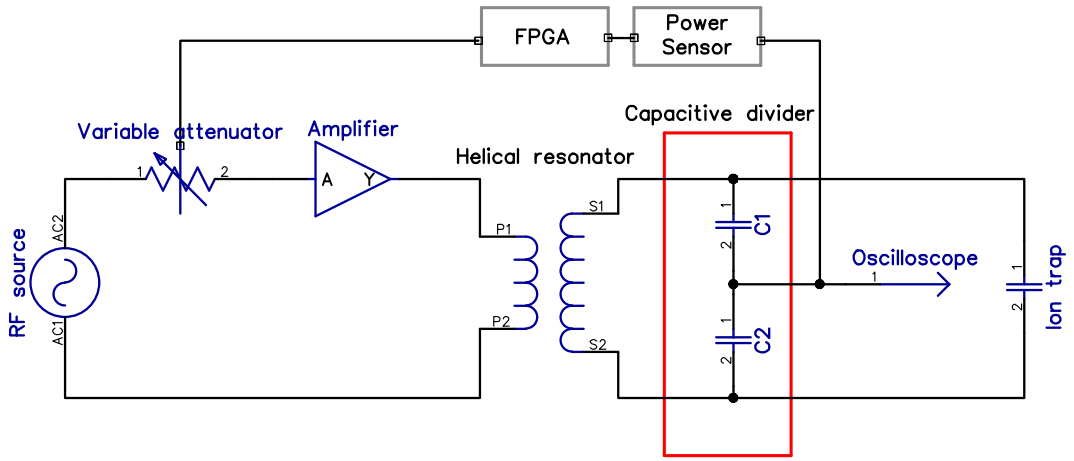

Figure 5.32: Schematic layout of the RF power stabilisation scheme. The FPGA provides the software PID controller and analogue voltage output channel for controlling the attenuator.

gain and the helical resonator. The cause of this drift is largely attributed to the thermal drift of the environment, which can be difficult to detect and cannot be predicted. As a further improvement to performance of the amplifier, an enclosure was used to minimise fluctuations of the amplifier gain, caused by air convection.

[15] Rohde & Schwartz NRP-Z221
[16] Mini-Circuits ZX73-2500+

To assess the stability of the applied trapping voltage, the capacitive divider output was measured for an hour with and without the feedback circuitry. The power spectral density of both signals is plotted in fig. 5.33. Comparison of both plots indicate a significant

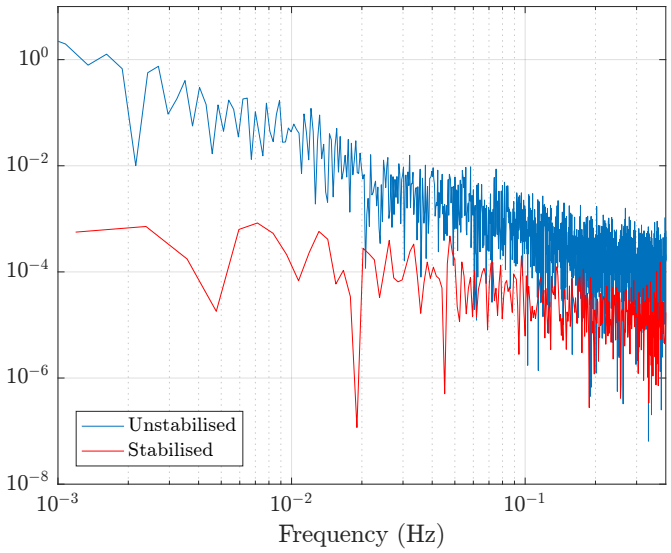

Figure 5.33: Power spectral density of the unstabilised and stabilised RF setup. The sampling time was set to be 1.23 s as the main interest was the long term performance.

improvement on the stability when using active stabilisation. This is most pronounced on the slow drift (low frequency) component, which corresponds to timescales of a thousand seconds. Using these results and equation 5.7, the radial secular frequency drift is expected to be minimised by factor of ≈ 30. Allan deviation analysis indicates that the voltage frequency fluctuations are suppressed by a factor of 10 when compared to the free running case. The achieve stability can be further increased by using a larger bandwidth method of power sensing, such as the one used in [168].

5.6.2 RF and microwave radiation power stabilisation

The qubits presented in chapter 2 are manipulated using either RF or microwave radiation. Using the bare state qubit, the Rabi frequency is proportional to the applied microwave radiation to drive the transition $|0\rangle \leftrightarrow |-1\rangle$ or $|0\rangle \leftrightarrow |+1\rangle$. Similar to the effect of magnetic field noise on the qubit, fluctuations of the microwave power will introduce decoherence, though not of the same magnitude. In the case of the dressed state qubit formed with $|0'\rangle$ $(\leftrightarrow)$ $|D\rangle$, microwave fields are used for dressing the bare atomic states, while RF signals are used to manipulate the dressed state qubit. Since the $|D\rangle$ state is inherently robust

against microwave fluctuations, only the RF Rabi frequency requires control. The drift in all of these parameters introduces incorrect frequency detuning in the two qubit gate analysed in detail in [69]. To keep the infidelity bellow 0.1%, the Rabi frequencies of these transitions must be accurate to within 0.4%. To achieve this, active feedback systems were investigated.

In the previous section 5.6.1, the radio-frequency voltage applied to the trap could be measured using simple capacitive dividers and homebuilt electronic circuits. In the case of radiated RF and microwave signals, a diode power sensor[17] was chosen, which was used in conjunction with a directional 40 dB waveguide coupler. A waveguide was chosen, such that the coupler can withstand powers up to 80 W and be used in any setup. Similarly to a wavemeter lock described in chapter 3 the sensor is interfaced with experimental control software to calculate the deviation from the set power and, using an analogue output card, produce a control signal using a software-based PID controller. The output signal is fed into a voltage variable attenuator[18], which controls the power level at the input of the amplifier. The schematic of the electronic setup can be seen in fig. 5.34. The bandwidth of the control circuit was found to be mostly limited by the diode sensor, set by the sampling rate of 40 kHz. To quantify the performance of the control scheme, a test setup was built to check the stability of the 20 W system with and without active feedback. The results are shown in fig. 5.35, where the long term measurement data is plotted as a power spectral density. The plot indicates how much the power level varies at a particular frequency. Considering the sensitivity of the power sensor, the stabilised system is expected to be stabilised within -59 dBm.

Although the long term drift stabilisation system indicates a significant improvement, the setup does not fully capture the actual experimental system. During an experiment, the RF and microwave emission is turned on and off for short periods of time <10 ms, which means that a constantly running feedback system must be fast enough to respond to the change in the set point value and not introduce any noise in the process. A possible solution to this can be the use of a constant single off-resonant frequency which does not interact with the ion, but is present in the amplifier output and can be monitored using the diode sensor. A small portion of the output signal can be picked off and filtered to obtain the power reading of the off-resonant signal. During the experiment, additional frequencies are introduced for a short period of time, which can change the power level of the signal. Therefore the feedback circuitry needs to be able to switch between different setpoints

[17] Rohde & Schwartz NRP-Z221
[18] Hittite 12377-3 evaluation board

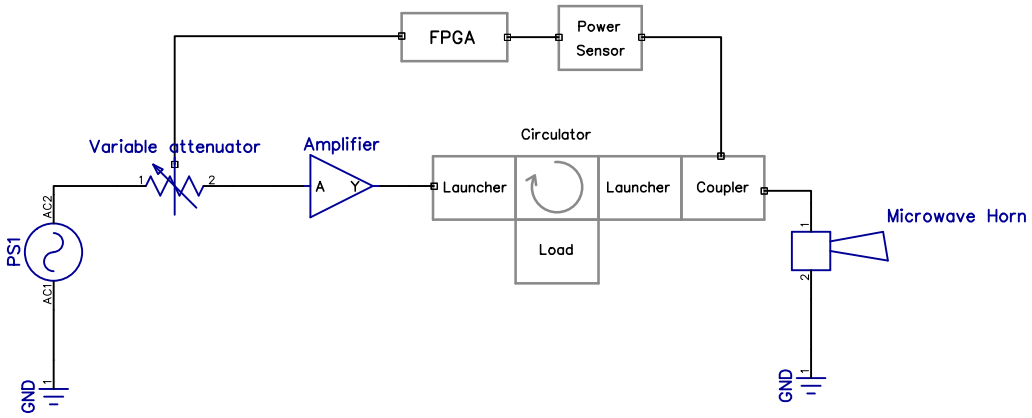

Figure 5.34: Schematic of the 20 W microwave system with an active stabilisation system.

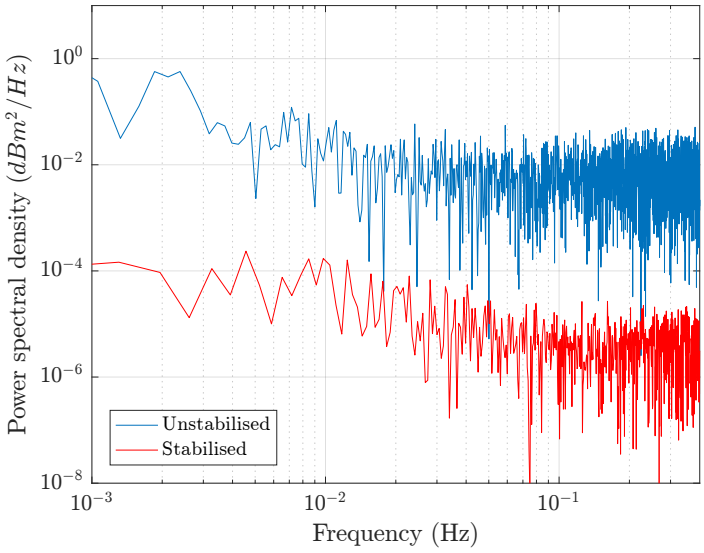

Figure 5.35: Power spectral density with and without an active feedback system.

in less than a millisecond and correct for any transient effects. A setup addressing these requirements is currently being set up.

5.7 Conclusion

This chapter contains a description of a second experimental setup designed to implement high-fidelity two-qubit gates. The improvements over the previous system include: simple and robust single layer microfabricated ion traps, a more accurate trap to magnet alignment procedure with the use of commercial diebonder, a custom cooling system and

in-vacuum radiation emitters. The system is expected to have a 150 T/m magnetic field gradient, which increases the effective Lamb-Dicke parameter to a value of ≈ 0.13. This is an improvement by a factor of 6.4 compared to the gradient used to implement the gate performed in [39]. With the increase of RF Rabi frequencies by an order of magnitude using either the in-vacuum wires or the high power amplifiers, the gate time for the Mølmer-Sørensen two qubit gate is expected to be reduced to $\tau = 0.27$ ms. This and operating the trap at a temperature of 79 K will minimise the effect of motional heating of the trapped ion. The gate infidelity of this effect is estimated to be $E_{heat} = 0.027\%$. Taking into account the off-resonant coupling and depolarisation errors given in [67], the infidelity can be minimised to $E_{total} = 0.3\%$. To minimise any remaining systematic errors, such as the drift of the ion secular frequency and power fluctuations of the RF and microwave fields, the chapter details the use of active feedback systems. The stabilised radial secular frequency indicates a stability of $\approx$500 Hz with room for further improvement. The initial test of stabilising the microwave power indicates excellent long term performance, with methods of incorporating the system into an experimental setup underway. With all of these improvements, the experimental system is deemed suitable for implementing a fault-tolerant on-chip two-qubit gate using a strong magnetic field gradient.

Chapter 6

Conclusion

6.1 Summary

The work presented in this thesis is a part of the effort in the Ion Quantum Technology group (IQT) to develop and construct scaleable quantum computing architectures. The purpose of this thesis was to demonstrate the scalability of manipulating trapped ions with long-wavelength radiation by performing a high-fidelity two-qubit entangling gate on a microfabricated surface ion trap. Two systems were used to this end, each described in their respective chapters.

To describe the operation of an ion trap system, background theory for ion trapping an manipulation was given, with a great attention dedicated for surface ion trap technology. Furthermore, the static magnetic field gradient scheme was described alongside with the microwave dressed state scheme used for preparing a highly robust qubit. Errors due to different experimental parameters are identified and methods of reducing them were introduced. With the obtained requirements, two experimental ion trap systems were designed to contain ion trap architectures for implementing high fidelity Molmer-Sorensen gates with infidelities below 0.3%.

Following this, a multi-setup laser frequency stabilisation system was designed to be implemented for multiple laser system control. This entailed the analysis of different optical references used in the active laser feedback systems and the consideration of the stability required for each of the lasers used for ionisation, Doppler cooling and repumping. Furthermore, different electronic control systems were presented and their capabilities considered. From these considerations, three optical setups were assembled. These include a Rb saturated absorption spectroscopy scheme, a low-drift cavity and a laser beat locking setups. The operation of these systems was analysed and have shown to meet most of the

desired stability requirements, with further improvement being carried out.

The next chapter described the assembly of the one of the vacuum systems used for demonstrating a high-fidelity two-qubit gate. The work included the preparation of the microfabricated surface traps, which were then aligned onto a permanent magnet pair to introduce a magnetic field gradient of 140 T/m. The experiment system was successful in trapping ions and was used to identify possible improvements for ion trapping and addressing.

The final chapter of the thesis details the improvements made on a second vacuum system, designed to minimise the two-qubit gate infidelities further. The improvements include the use of a simple single-layer design and optimise trap to magnet alignment. The experimental setup incorporates a new high-pressure cooling system and in-vacuum and external RF and microwave radiation emitters. The cooling system is expected to reduce the trapped ion heating rate by an order of magnitude, while simulations of the microwave emitters suggest Rabi frequencies on the order of $\Omega \approx 2\pi \times 100\,\mathrm{kHz}$. These two parameters are expected to significantly minimise the Mølmer-Sørensen gate infidelities. The systematic errors are accounted for by RF and microwave feedback systems used for stabilising the secular frequency of the ion motion and the emitted power of various radiation sources.

6.2 Outlook

The modifications to the vacuum system outlined in chapter 5 have been constructed and are in the process of being integrated into the chamber. Once the experimental system is ready, it will be used to trap ions, characterise the magnetic field gradient and carry out heating rate measurements. The system will then be used to perform single- and multi-qubit operations using the scheme described in chapter 2, with the end goal of demonstrating a fault-tolerant two-qubit Mølmer-Sørensen gate. The results of this work will contribute towards the research into scalable quantum computing architectures.

Bibliography

[1] C. Gobby, Z. Yuan, and A. Shields, "Quantum key distribution over 122 km of standard telecom fiber," *Applied Physics Letters*, vol. 84, no. 19, pp. 3762–3764, 2004.

[2] C. Neill, P. Roushan, K. Kechedzhi, S. Boixo, S. Isakov, V. Smelyanskiy, R. Barends, B. Burkett, Y. Chen, Z. Chen, *et al.*, "A blueprint for demonstrating quantum supremacy with superconducting qubits," *arXiv preprint arXiv:1709.06678*, 2017.

[3] N. M. Linke, D. Maslov, M. Roetteler, S. Debnath, C. Figgatt, K. A. Landsman, K. Wright, and C. Monroe, "Experimental comparison of two quantum computing architectures," *Proceedings of the National Academy of Sciences*, p. 201618020, 2017.

[4] D. Deutsch, "Quantum computational networks," in *Proceedings of the Royal Society of London A: Mathematical, Physical and Engineering Sciences*, vol. 425, pp. 73–90, The Royal Society, 1989.

[5] P. Shor, "Polynomial-time algorithms for prime factorization and discrete logarithms on a quantum computer, special issue on quantum computation of the siam journal on computing 26 (5)(1997) 1484–1509," *MATH MathSciNet*, 1997.

[6] L. K. Grover, "A fast quantum mechanical algorithm for database search," in *Proceedings of the twenty-eighth annual ACM symposium on Theory of computing*, pp. 212–219, ACM, 1996.

[7] D. P. DiVincenzo, "The physical implementation of quantum computation," *Fortschritte der Physik*, vol. 48, no. 9-11, pp. 771–783, 2000.

[8] E. Knill, "Physics: quantum computing," *Nature*, vol. 463, no. 7280, pp. 441–443, 2010.

[9] R. Barends, A. Shabani, L. Lamata, J. Kelly, A. Mezzacapo, U. Las Heras, R. Babbush, A. G. Fowler, B. Campbell, Y. Chen, *et al.*, "Digitized adiabatic quantum

computing with a superconducting circuit," *Nature*, vol. 534, no. 7606, pp. 222–226, 2016.

[10] A. D. Córcoles, E. Magesan, S. J. Srinivasan, A. W. Cross, M. Steffen, J. M. Gambetta, and J. M. Chow, "Demonstration of a quantum error detection code using a square lattice of four superconducting qubits," *Nature Communications*, vol. 6, 2015.

[11] L. Childress and R. Hanson, "Diamond nv centers for quantum computing and quantum networks," *MRS bulletin*, vol. 38, no. 2, pp. 134–138, 2013.

[12] D. Loss and D. P. DiVincenzo, "Quantum computation with quantum dots," *Phys. Rev. A*, vol. 57, no. 1, p. 120, 1998.

[13] J. I. Cirac and P. Zoller, "Quantum computations with cold trapped ions," *Phys. Rev. Lett.*, vol. 74, no. 20, p. 4091, 1995.

[14] D. Berkeland, J. Miller, J. C. Bergquist, W. M. Itano, and D. J. Wineland, "Laser-cooled mercury ion frequency standard," *Phys. Rev. Lett.*, vol. 80, no. 10, p. 2089, 1998.

[15] D. J. Wineland, R. E. Drullinger, and F. L. Walls, "Radiation-pressure cooling of bound resonant absorbers," *Phys. Rev. Lett.*, vol. 40, pp. 1639–1642, Jun 1978.

[16] D. J. Wineland, C. Monroe, W. M. Itano, D. Leibfried, B. E. King, and D. M. Meekhof, "Experimental issues in coherent quantum-state manipulation of trapped atomic ions," *Journal of Research of the National Institute of Standards and Technology*, vol. 103, no. 3, p. 259, 1998.

[17] R. Gerritsma, G. Kirchmair, F. Zähringer, E. Solano, R. Blatt, and C. Roos, "Quantum simulation of the dirac equation," *arXiv preprint arXiv:0909.0674*, 2009.

[18] K. Kim, M.-S. Chang, S. Korenblit, R. Islam, E. E. Edwards, J. K. Freericks, G.-D. Lin, L.-M. Duan, and C. Monroe, "Quantum simulation of frustrated ising spins with trapped ions," *Nature*, vol. 465, no. 7298, p. 590, 2010.

[19] F. Schmidt-Kaler, H. Haffner, M. Riebe, S. Guide, *et al.*, "Realization of the cirac-zoller controlled-not quantum gate," *Nature*, vol. 422, no. 6930, p. 408, 2003.

[20] K. Mølmer and A. Sørensen, "Multiparticle entanglement of hot trapped ions," *Phys. Rev. Lett.*, vol. 82, pp. 1835–1838, Mar 1999.

[21] C. A. Sackett, D. Kielpinski, B. E. King, C. Langer, *et al.*, "Experimental entanglement of four particles," *Nature*, vol. 404, no. 6775, p. 256, 2000.

[22] D. Leibfried, B. DeMarco, V. Meyer, D. Lucas, *et al.*, "Experimental demonstration of a robust, high-fidelity geometric two ion-qubit phase gate," *Nature*, vol. 422, no. 6930, p. 412, 2003.

[23] J. P. Gaebler, T. R. Tan, Y. Lin, Y. Wan, R. Bowler, A. C. Keith, S. Glancy, K. Coakley, E. Knill, D. Leibfried, and D. J. Wineland, "High-fidelity universal gate set for $^{9}Be^{+}$ ion qubits," *Phys. Rev. Lett.*, vol. 117, p. 060505, Aug 2016.

[24] C. J. Ballance, T. P. Harty, N. M. Linke, M. A. Sepiol, and D. M. Lucas, "High-fidelity quantum logic gates using trapped-ion hyperfine qubits," *Phys. Rev. Lett.*, vol. 117, p. 060504, Aug 2016.

[25] J. Benhelm, G. Kirchmair, C. F. Roos, and R. Blatt, "Towards fault-tolerant quantum computing with trapped ions," *Nat Phys*, vol. 4, pp. 463–466, Jun 2008.

[26] S. Debnath, N. Linke, C. Figgatt, K. Landsman, K. Wright, and C. Monroe, "Demonstration of a small programmable quantum computer with atomic qubits," *Nature*, vol. 536, no. 7614, pp. 63–66, 2016.

[27] B. P. Lanyon, M. Zwerger, P. Jurcevic, C. Hempel, W. Dür, H. J. Briegel, R. Blatt, and C. F. Roos, "Experimental violation of multipartite bell inequalities with trapped ions," *Phys. Rev. Lett.*, vol. 112, p. 100403, Mar 2014.

[28] D. Kielpinski, C. Monroe, and D. J. Wineland, "Architecture for a large-scale ion-trap quantum computer," *Nature*, vol. 417, no. 6890, p. 709, 2002.

[29] K. K. Mehta, C. D. Bruzewicz, R. McConnell, R. J. Ram, J. M. Sage, and J. Chiaverini, "Integrated optical addressing of an ion qubit," *Nature Nanotechnology*, vol. 11, pp. 1066 EP –, Aug 2016.

[30] A. G. Fowler, M. Mariantoni, J. M. Martinis, and A. N. Cleland, "Surface codes: Towards practical large-scale quantum computation," *Phys. Rev. A*, vol. 86, p. 032324, Sep 2012.

[31] K. R. Brown, J. Kim, and C. Monroe, "Co-designing a scalable quantum computer with trapped atomic ions," *Npj Quantum Information*, vol. 2, pp. 16034 EP –, Nov 2016. Review Article.

[32] C. J. Trout, M. Li, M. Gutierrez, Y. Wu, S.-T. Wang, L. Duan, and K. R. Brown, "Simulating the performance of a distance-3 surface code in a linear ion trap," *New Journal of Physics*, vol. 20, no. 4, p. 043038, 2018.

[33] F. Mintert and C. Wunderlich, "Ion-trap quantum logic using long-wavelength radiation," *Phys. Rev. Lett.*, vol. 87, p. 257904, Nov 2001.

[34] C. Ospelkaus, C. E. Langer, J. M. Amini, K. R. Brown, D. Leibfried, and D. J. Wineland, "Trapped-ion quantum logic gates based on oscillating magnetic fields," *Phys. Rev. Lett.*, vol. 101, no. 9, p. 090502, 2008.

[35] A. Khromova, C. Piltz, B. Scharfenberger, T. Gloger, M. Johanning, A. Varón, and C. Wunderlich, "Designer spin pseudomolecule implemented with trapped ions in a magnetic gradient," *Phys. Rev. Lett.*, vol. 108, no. 22, p. 220502, 2012.

[36] D. G. Leibfried, C. Ospelkaus, U. J. Warring, Y. Colombe, K. R. Brown, J. Amini, and D. J. Wineland, "Microwave quantum logic gates for trapped ions," *Nature*, vol. 476, 2011.

[37] N. Timoney, I. Baumgart, M. Johanning, A. F. Varon, M. B. Plenio, A. Retzker, and C. Wunderlich, "Quantum gates and memory using microwave-dressed states," *Nature*, vol. 476, pp. 185–188, Aug 2011.

[38] S. C. Webster, S. Weidt, K. Lake, J. J. McLoughlin, and W. K. Hensinger, "Simple manipulation of a microwave dressed-state ion qubit," *Phys. Rev. Lett.*, vol. 111, p. 140501, Oct 2013.

[39] S. Weidt, J. Randall, S. Webster, K. Lake, A. Webb, I. Cohen, T. Navickas, B. Lekitsch, A. Retzker, and W. Hensinger, "Trapped-ion quantum logic with global radiation fields," *Physical. Rev. Lett.*, vol. 117, no. 22, p. 220501, 2016.

[40] T. Harty, D. Allcock, C. J. Ballance, L. Guidoni, H. Janacek, N. Linke, D. Stacey, and D. Lucas, "High-fidelity preparation, gates, memory, and readout of a trapped-ion quantum bit," *Phys. Rev. Lett.*, vol. 113, no. 22, p. 220501, 2014.

[41] W. K. Hensinger, S. Olmschenk, D. Stick, D. Hucul, M. Yeo, M. Acton, L. Deslauriers, C. Monroe, and J. Rabchuk, "T-junction ion trap array for two-dimensional ion shuttling, storage, and manipulation," *Appl. Phys. Lett.*, vol. 88, 2006.

[42] S. Seidelin, J. Chiaverini, R. Reichle, J. J. Bollinger, D. Leibfried, J. Britton, J. H. Wesenberg, R. B. Blakestad, R. J. Epstein, D. B. Hume, W. M. Itano, J. D.

Jost, C. Langer, R. Ozeri, N. Shiga, and D. J. Wineland, "Microfabricated surface-electrode ion trap for scalable quantum information processing," *Phys. Rev. Lett.*, vol. 96, p. 253003, Jun 2006.

[43] C. D. Herold, S. D. Fallek, J. Merrill, A. M. Meier, K. R. Brown, C. Volin, and J. M. Amini, "Universal control of ion qubits in a scalable microfabricated planar trap," *New Journal of Physics*, vol. 18, no. 2, p. 023048, 2016.

[44] D. Hucul, I. V. Inlek, G. Vittorini, C. Crocker, S. Debnath, S. M. Clark, and C. Monroe, "Modular entanglement of atomic qubits using photons and phonons," *Nat Phys*, vol. 11, pp. 37–42, Jan 2015. Letter.

[45] B. Lekitsch, S. Weidt, A. G. Fowler, K. Mølmer, S. J. Devitt, C. Wunderlich, and W. K. Hensinger, "Blueprint for a microwave trapped ion quantum computer," *Science Advances*, vol. 3, no. 2, p. e1601540, 2017.

[46] D. J. Douglas, A. J. Frank, and D. Mao, "Linear ion traps in mass spectrometry," *Mass Spectrometry Reviews*, vol. 24, no. 1, pp. 1–29, 2005.

[47] S. Willitsch, M. T. Bell, A. D. Gingell, and T. P. Softley, "Chemical applications of laser- and sympathetically-cooled ions in ion traps," *Phys. Chem. Chem. Phys.*, vol. 10, pp. 7200–7210, 2008.

[48] N. Huntemann, C. Sanner, B. Lipphardt, C. Tamm, and E. Peik, "Single-ion atomic clock with 3×10^{-18} systematic uncertainty," *Phys. Rev. Lett.*, vol. 116, p. 063001, Feb 2016.

[49] T. Rosenband, D. B. Hume, P. O. Schmidt, C. W. Chou, A. Brusch, L. Lorini, W. H. Oskay, R. E. Drullinger, T. M. Fortier, J. E. Stalnaker, S. A. Diddams, W. C. Swann, N. R. Newbury, W. M. Itano, D. J. Wineland, and J. C. Bergquist, "Frequency ratio of al+ and hg+ single-ion optical clocks; metrology at the 17th decimal place," *Science*, vol. 319, no. 5871, pp. 1808–1812, 2008.

[50] P. O. Schmidt, T. Rosenband, C. Langer, W. M. Itano, J. C. Bergquist, and D. J. Wineland, "Spectroscopy using quantum logic," *Science*, vol. 309, no. 5735, pp. 749–752, 2005.

[51] P. Jurcevic, B. P. Lanyon, P. Hauke, C. Hempel, P. Zoller, R. Blatt, and C. F. Roos, "Quasiparticle engineering and entanglement propagation in a quantum many-body system," *Nature*, vol. 511, pp. 202–205, Jul 2014. Letter.

[52] J. Smith, A. Lee, P. Richerme, B. Neyenhuis, P. Hess, P. Hauke, M. Heyl, D. Huse, and C. Monroe, "Many-body localization in a quantum simulator with programmable random disorder," *Nature Physics*, vol. 12, no. 10, pp. 907–911, 2016.

[53] K. Toyoda, R. Hiji, A. Noguchi, and S. Urabe, "Hong-ou-mandel interference of two phonons in trapped ions," *Nature*, vol. 527, no. 7576, p. 74, 2015.

[54] H. G. Dehmelt, "Radiofrequency spectroscopy of stored ions i: Storage," *Advances in Atomic and Molecular Physics*, vol. 3, pp. 53–72, 1968.

[55] W. Paul and H. Steinwedel, "Ein neues massenspektrometer ohne magnetfeld," *Zeitschrift für Naturforschung A*, vol. 8, no. 7, pp. 448–450, 1953.

[56] D. L. Farnham, R. S. Van Dyck Jr, and P. B. Schwinberg, "Determination of the electron's atomic mass and the proton/electron mass ratio via penning trap mass spectroscopy," *Phys. Rev. Lett.*, vol. 75, no. 20, p. 3598, 1995.

[57] G. Schneider, A. Mooser, M. Bohman, N. Schön, J. Harrington, T. Higuchi, H. Nagahama, S. Sellner, C. Smorra, K. Blaum, Y. Matsuda, W. Quint, J. Walz, and S. Ulmer, "Double-trap measurement of the proton magnetic moment at 0.3 parts per billion precision," *Science*, vol. 358, no. 6366, pp. 1081–1084, 2017.

[58] K. Blaum, Y. N. Novikov, and G. Werth, "Penning traps as a versatile tool for precise experiments in fundamental physics," *Contemporary Physics*, vol. 51, no. 2, pp. 149–175, 2010.

[59] J. Pinder and J. Verdú, "A planar penning trap with tunable dimensionality of the trapping potential," *International Journal of Mass Spectrometry*, vol. 356, pp. 49 – 59, 2013.

[60] J. G. Bohnet, B. C. Sawyer, J. W. Britton, M. L. Wall, A. M. Rey, M. Foss-Feig, and J. J. Bollinger, "Quantum spin dynamics and entanglement generation with hundreds of trapped ions," *Science*, vol. 352, no. 6291, pp. 1297–1301, 2016.

[61] P. H. Dawson, *Quadrupole mass spectrometry and its applications*. Elsevier, 2013.

[62] W. Paul, "Electromagnetic traps for charged and neutral particles," *Rev. Mod. Phys.*, vol. 62, pp. 531–540, Jul 1990.

[63] P. K. Ghosh, *Ion traps*. 1995.

[64] J. McLoughlin, *Development and Implementation of an Yb^+ Ion Trap Experiment Towards Coherent Manipulation and Entanglement.* PhD thesis, University of Sussex, 2011.

[65] L. Ruby, "Applications of the mathieu equation," *American Journal of Physics*, vol. 64, no. 1, pp. 39–44, 1996.

[66] H. Haken, *Advanced synergetics: Instability hierarchies of self-organizing systems and devices*, vol. 20. Springer Science & Business Media, 2012.

[67] D. F. Murgia, *Microchip ion traps with high magnetic field gradients for microwave quantum logic.* PhD thesis, Imperial College London, 2016.

[68] D. Berkeland, J. Miller, J. C. Bergquist, W. M. Itano, and D. J. Wineland, "Minimization of ion micromotion in a paul trap," *Journal of applied physics*, vol. 83, no. 10, pp. 5025–5033, 1998.

[69] J. A. D. Randall, *High-Fidelity Entanglement of Trapped Ions using Long-Wavelength Radiation.* PhD thesis, Imperial College London, 2016.

[70] D. F. James, "Quantum dynamics of cold trapped ions with application to quantum computation," *Applied Physics B: Lasers and Optics*, vol. 66, no. 2, pp. 181–190, 1998.

[71] H. Kaufmann, T. Ruster, C. T. Schmiegelow, M. A. Luda, V. Kaushal, J. Schulz, D. von Lindenfels, F. Schmidt-Kaler, and U. G. Poschinger, "Fast ion swapping for quantum-information processing," *Phys. Rev. A*, vol. 95, p. 052319, May 2017.

[72] R. Bowler, J. Gaebler, Y. Lin, T. R. Tan, D. Hanneke, J. D. Jost, J. P. Home, D. Leibfried, and D. J. Wineland, "Coherent diabatic ion transport and separation in a multizone trap array," *Phys. Rev. Lett.*, vol. 109, p. 080502, Aug 2012.

[73] M. D. Hughes, B. Lekitsch, J. A. Broersma, and W. K. Hensinger, "Microfabricated ion traps," *Contemporary Physics*, vol. 52, no. 6, pp. 505–529, 2011.

[74] M. G. House, "Analytic model for electrostatic fields in surface-electrode ion traps," *Phys. Rev. A*, vol. 78, p. 033402, Sep 2008.

[75] Q. A. Turchette, Kielpinski, B. E. King, D. Leibfried, D. M. Meekhof, C. J. Myatt, M. A. Rowe, C. A. Sackett, C. S. Wood, W. M. Itano, C. Monroe, and D. J.

Wineland, "Heating of trapped ions from the quantum ground state," *Phys. Rev. A*, vol. 61, p. 063418, May 2000.

[76] D. A. Hite, Y. Colombe, A. C. Wilson, K. R. Brown, U. Warring, R. Jördens, J. D. Jost, K. McKay, D. Pappas, D. Leibfried, *et al.*, "100-fold reduction of electric-field noise in an ion trap cleaned with in situ argon-ion-beam bombardment," *Phys. Rev. Lett.*, vol. 109, no. 10, p. 103001, 2012.

[77] E. Kim, A. Safavi-Naini, D. Hite, K. McKay, D. Pappas, P. Weck, and H. Sadeghpour, "Electric-field noise from carbon-adatom diffusion on a au (110) surface: First-principles calculations and experiments," *Phys. Rev. A*, vol. 95, no. 3, p. 033407, 2017.

[78] D. T. C. Allcock, L. Guidoni, T. P. Harty, C. J. Ballance, M. G. Blain, A. M. Steane, and D. M. Lucas, "Reduction of heating rate in a microfabricated ion trap by pulsed-laser cleaning," *New Journal of Physics*, vol. 13, no. 12, p. 123023, 2011.

[79] J. Labaziewicz, Y. Ge, P. Antohi, D. Leibrandt, K. R. Brown, and I. L. Chuang, "Suppression of heating rates in cryogenic surface-electrode ion traps," *Phys. Rev. Lett.*, vol. 100, no. 1, p. 013001, 2008.

[80] L. Deslauriers, S. Olmschenk, D. Stick, W. K. Hensinger, J. Sterk, and C. Monroe, "Scaling and suppression of anomalous heating in ion traps," *Phys. Rev. Lett.*, vol. 97, p. 103007, Sep 2006.

[81] I. A. Boldin, A. Kraft, and C. Wunderlich, "Measuring anomalous heating in a planar ion trap with variable ion-surface separation," *Phys. Rev. Lett.*, vol. 120, p. 023201, Jan 2018.

[82] B. Lekitsch, *Development of Microfabricated Ion Traps for Scalable Microwave Quantum Technology.* PhD thesis, University of Sussex, 2013.

[83] R. C. Sterling, *Ytterbium ion trapping and microfabrication of ion trap arrays.* PhD thesis, University of Sussex, 2011.

[84] J. D. Siverns, *Yb ion trap experimental set-up and two-dimensional ion trap surface array design towards analogue quantum simulations.* PhD thesis, University of Sussex, 2011.

[85] C. Balzer, A. Braun, T. Hannemann, C. Paape, M. Ettler, W. Neuhauser, and C. Wunderlich, "Electrodynamically trapped yb^+ ions for quantum information processing," *Phys. Rev. A*, vol. 73, p. 041407, Apr 2006.

[86] N. Kjærgaard, L. Hornekær, A. Thommesen, Z. Videsen, and M. Drewsen, "Isotope selective loading of an ion trap using resonance-enhanced two-photon ionization," *Applied Physics B: Lasers and Optics*, vol. 71, no. 2, pp. 207–210, 2000.

[87] A. H. Nizamani, J. J. McLoughlin, and W. K. Hensinger, "Doppler-free yb spectroscopy with the fluorescence spot technique," *Phys. Rev. A*, vol. 82, no. 4, p. 043408, 2010.

[88] S. Weidt, J. Randall, S. Webster, E. Standing, A. Rodriguez, A. Webb, B. Lekitsch, and W. Hensinger, "Ground-state cooling of a trapped ion using long-wavelength radiation," *Phys. Rev. Lett.*, vol. 115, no. 1, p. 013002, 2015.

[89] D. Gerlich and G. Borodi, "Buffer gas cooling of polyatomic ions in rf multi-electrode traps," *Faraday discussions*, vol. 142, pp. 57–72, 2009.

[90] S. Chu, "Laser trapping of neutral particles," *Scientific American*, vol. 266, no. 2, pp. 70–77, 1992.

[91] W. D. Phillips, "Nobel lecture: Laser cooling and trapping of neutral atoms," *Reviews of Modern Physics*, vol. 70, no. 3, p. 721, 1998.

[92] C. Cohen-Tannoudji and W. D. Phillips, "New mechanisms for laser cooling," *Phys. Today*, vol. 43, no. 10, pp. 33–40, 1990.

[93] S. Stenholm, "The semiclassical theory of laser cooling," *Rev. Mod. Phys.*, vol. 58, pp. 699–739, Jul 1986.

[94] C. Foot, *Atomic physics*. Oxford master series in physics, Oxford University Press, 2005.

[95] S. Olmschenk, D. Hayes, D. N. Matsukevich, P. Maunz, D. L. Moehring, K. C. Younge, and C. Monroe, "Measurement of the lifetime of the $6p\ ^2P_{1/2}$ level of yb^+," *Phys. Rev. A*, vol. 80, p. 022502, Aug 2009.

[96] S. M. Olmschenk, *Quantum Teleportation Between Distant Matter Qubits*. PhD thesis, University of Michigan, 2009.

[97] P. Taylor, M. Roberts, S. V. Gateva-Kostova, R. B. M. Clarke, G. P. Barwood, W. R. C. Rowley, and P. Gill, "Investigation of the $^2S_{1/2}-^2D_{5/2}$ clock transition in a single ytterbium ion," *Phys. Rev. A*, vol. 56, pp. 2699–2704, Oct 1997.

[98] A. Härter, A. Krükow, A. Brunner, and J. H. Denschlag, "Long-term drifts of stray electric fields in a paul trap," *Applied Physics B*, vol. 114, no. 1-2, pp. 275–281, 2014.

[99] J. D. Siverns, L. R. Simkins, S. Weidt, and W. K. Hensinger, "On the application of radio frequency voltages to ion traps via helical resonators," *Applied Physics B*, vol. 107, no. 4, pp. 921–934, 2012.

[100] J. Randall, S. Weidt, E. Standing, K. Lake, S. Webster, D. Murgia, T. Navickas, K. Roth, and W. Hensinger, "Efficient preparation and detection of microwave dressed-state qubits and qutrits with trapped ions," *Phys. Rev. A*, vol. 91, no. 1, p. 012322, 2015.

[101] S. Weidt, *Towards microwave based ion trap quantum technology.* PhD thesis, University of Sussex, 2013.

[102] D. Meekhof, C. Monroe, B. King, W. M. Itano, and D. J. Wineland, "Generation of nonclassical motional states of a trapped atom," *Phys. Rev. Lett.*, vol. 76, no. 11, p. 1796, 1996.

[103] C. Gerry and P. Knight, *Introductory Quantum Optics.* Cambridge University Press, 2004.

[104] T. Harty, D. Allcock, C. J. Ballance, L. Guidoni, H. Janacek, N. Linke, D. Stacey, and D. Lucas, "High-fidelity preparation, gates, memory, and readout of a trapped-ion quantum bit," *Phys. Rev. Lett.*, vol. 113, no. 22, p. 220501, 2014.

[105] S. Wölk and C. Wunderlich, "Quantum dynamics of trapped ions in a dynamic field gradient using dressed states," *New Journal of Physics*, vol. 19, no. 8, p. 083021, 2017.

[106] H. C. Naègerl, D. Leibfried, H. Rohde, G. Thalhammer, J. Eschner, F. Schmidt-Kaler, and R. Blatt, "Laser addressing of individual ions in a linear ion trap," *Phys. Rev. A*, vol. 60, no. 1, p. 145, 1999.

[107] T. Ruster, C. T. Schmiegelow, H. Kaufmann, C. Warschburger, F. Schmidt-Kaler, and U. G. Poschinger, "A long-lived zeeman trapped-ion qubit," *Applied Physics B*, vol. 122, no. 10, p. 254, 2016.

[108] D. Farfurnik, N. Aharon, I. Cohen, Y. Hovav, A. Retzker, and N. Bar-Gill, "Experimental realization of time-dependent phase-modulated continuous dynamical decoupling," *Phys. Rev. A*, vol. 96, p. 013850, Jul 2017.

[109] E. T. Jaynes and F. W. Cummings, "Comparison of quantum and semiclassical radiation theories with application to the beam maser," *Proceedings of the IEEE*, vol. 51, no. 1, pp. 89–109, 1963.

[110] F. Schmidt-Kaler, H. Haffner, M. Riebe, S. Guide, *et al.*, "Realization of the ciraczoller controlled-not quantum gate," *Nature*, vol. 422, no. 6930, p. 408, 2003.

[111] W. M. Itano, J. C. Bergquist, J. J. Bollinger, and D. J. Wineland, "Laser colling of trapped ions," *Proceedings of thes international school of physics Enrico Fermi: Laser Manipulation of Atoms and Ions, Edité par North Holland*, p. 519, 1992.

[112] A. Sørensen and K. Mølmer, "Entanglement and quantum computation with ions in thermal motion," *Phys. Rev. A*, vol. 62, p. 022311, Jul 2000.

[113] R. W. Fox, C. W. Oates, and L. W. Hollberg, "1. stabilizing diode lasers to high-finesse cavities," *Experimental Methods in the Physical Sciences*, vol. 40, pp. 1 – 46, 2003. Cavity-Enhanced Spectroscopies.

[114] J. L. Hall, M. S. Taubman, and J. Ye, "Laser stabilization," *OSA Handbook v14*, 1999.

[115] J. C. Doyle, B. A. Francis, and A. R. Tannenbaum, *Feedback control theory*. Courier Corporation, 2013.

[116] K. Ogata, *Modern Control Engineering*. Upper Saddle River, NJ, USA: Prentice Hall PTR, 4th ed., 2001.

[117] D. Howe, D. Allan, and J. Barnes, "Properties of oscillator signals and measurement methods."

[118] A. Perot and C. Fabry, "On the application of interference phenomena to the solution of various problems of spectroscopy and metrology," *The Astrophysical Journal*, vol. 9, p. 87, 1899.

[119] B. Saleh and M. Teich, *Fundamentals of Photonics*. Wiley Series in Pure and Applied Optics, Wiley, 2007.

[120] R. L. Barger, M. Sorem, and J. Hall, "Frequency stabilization of a cw dye laser," *Applied Physics Letters*, vol. 22, no. 11, pp. 573–575, 1973.

[121] F. Hooge, "1/f noise," *Physica B+ C*, vol. 83, no. 1, pp. 14–23, 1976.

[122] R. W. P. Drever, J. L. Hall, F. V. Kowalski, J. Hough, G. M. Ford, A. J. Munley, and H. Ward, "Laser phase and frequency stabilization using an optical resonator," *Applied Physics B*, vol. 31, no. 2, pp. 97–105, 1983.

[123] C. E. Wieman and L. Hollberg, "Using diode lasers for atomic physics," *Review of Scientific Instruments*, vol. 62, no. 1, pp. 1–20, 1991.

[124] K. B. MacAdam, A. Steinbach, and C. Wieman, "A narrow-band tunable diode laser system with grating feedback, and a saturated absorption spectrometer for cs and rb," *American Journal of Physics*, vol. 60, no. 12, pp. 1098–1111, 1992.

[125] E. W. Streed, T. J. Weinhold, and D. Kielpinski, "Frequency stabilization of an ultraviolet laser to ions in a discharge," *Applied Physics Letters*, vol. 93, no. 7, p. 071103, 2008.

[126] M. W. Lee, M. C. Jarratt, C. Marciniak, and M. J. Biercuk, "Frequency stabilization of a 369 nm diode laser by nonlinear spectroscopy of ytterbium ions in a discharge," *Opt. Express*, vol. 22, pp. 7210–7221, Mar 2014.

[127] C. Foot, *Atomic physics*. Oxford master series in physics, Oxford University Press, 2005.

[128] A. J. Wallard, "Frequency stabilization of the helium-neon laser by saturated absorption in iodine vapour," *Journal of Physics E: Scientific Instruments*, vol. 5, no. 9, p. 926, 1972.

[129] J. E. Debs, N. P. Robins, A. Lance, M. B. Kruger, and J. D. Close, "Piezo-locking a diode laser with saturated absorption spectroscopy," *Appl. Opt.*, vol. 47, pp. 5163–5166, Oct 2008.

[130] B. Chéron, H. Gilles, J. Hamel, O. Moreau, and H. Sorel, "Laser frequency stabilization using zeeman effect," *J. Phys. III France*, vol. 4, no. 2, pp. 401–406, 1994.

[131] K. L. Corwin, Z.-T. Lu, C. F. Hand, R. J. Epstein, and C. E. Wieman, "Frequency-stabilized diode laser with the zeeman shift in an atomic vapor," *Appl. Opt.*, vol. 37, pp. 3295–3298, May 1998.

[132] J. Wang, S. Yan, Y. Wang, T. Liu, and T. Zhang, "Modulation-free frequency stabilization of a grating-external-cavity diode laser by magnetically induced sub-doppler dichroism in cesium vapor cell," *Japanese Journal of Applied Physics*, vol. 43, no. 3R, p. 1168, 2004.

[133] M. L. Harris, S. L. Cornish, A. Tripathi, and I. G. Hughes, "Optimization of sub-doppler davll on the rubidium d2 line," *Journal of Physics B: Atomic, Molecular and Optical Physics*, vol. 41, no. 8, p. 085401, 2008.

[134] W. Z. Zhao, J. E. Simsarian, L. A. Orozco, and G. D. Sprouse, "A computer-based digital feedback control of frequency drift of multiple lasers," *Review of Scientific Instruments*, vol. 69, no. 11, pp. 3737–3740, 1998.

[135] A. Rossi, V. Biancalana, B. Mai, and L. Tomassetti, "Long-term drift laser frequency stabilization using purely optical reference," *Review of Scientific Instruments*, vol. 73, no. 7, pp. 2544–2548, 2002.

[136] K. Matsubara, S. Uetake, H. Ito, Y. Li, K. Hayasaka, and M. Hosokawa, "Precise frequency-drift measurement of extended-cavity diode laser stabilized with scanning transfer cavity," *Japanese Journal of Applied Physics*, vol. 44, no. 1R, p. 229, 2005.

[137] B. Burghardt, W. Jitschin, and G. Meisel, "Precise rf tuning for cw dye lasers," *Applied physics*, vol. 20, no. 2, pp. 141–146, 1979.

[138] P. Bohlouli-Zanjani, K. Afrousheh, and J. D. D. Martin, "Optical transfer cavity stabilization using current-modulated injection-locked diode lasers," *Review of Scientific Instruments*, vol. 77, no. 9, p. 093105, 2006.

[139] J. Appel, A. MacRae, and A. I. Lvovsky, "A versatile digital ghz phase lock for external cavity diode lasers," *Measurement Science and Technology*, vol. 20, no. 5, p. 055302, 2009.

[140] E. Mount, D. Gaultney, G. Vrijsen, M. Adams, S.-Y. Baek, K. Hudek, L. Isabella, S. Crain, A. van Rynbach, P. Maunz, and J. Kim, "Scalable digital hardware for a trapped ion quantum computer," *Quantum Information Processing*, pp. 1–18, 2015.

[141] O. E. DeLange, "Optical heterodyne detection," *IEEE Spectr.*, vol. 5, pp. 77–85, Oct. 1968.

[142] "High finesse wavemeter specifications." `http://www.highfinesse.com/misc/miscfiles/HighFinesse_Wavemeter_web.pdf`.

[143] C. Reiser and R. B. Lopert, "Laser wavemeter with solid fizeau wedge interferometer," *Appl. Opt.*, vol. 27, pp. 3656–3660, Sep 1988.

[144] R. W. Fox, C. W. Oates, and L. W. Hollberg, "1. stabilizing diode lasers to high-finesse cavities," *Experimental Methods in the Physical Sciences*, vol. 40, pp. 1 – 46, 2003. Cavity-Enhanced Spectroscopies.

[145] P. Horowitz and W. Hill, *The Art of Electronics*. New York, NY, USA: Cambridge University Press, 2nd ed., 1989.

[146] N. Seymour-Smith, P. Blythe, M. Keller, and W. Lange, "Fast scanning cavity offset lock for laser frequency drift stabilization," *Review of Scientific Instruments*, vol. 81, no. 7, p. 075109, 2010.

[147] C. Balzer, A. Braun, T. Hannemann, C. Paape, M. Ettler, W. Neuhauser, and C. Wunderlich, "Electrodynamically trapped yb^+ ions for quantum information processing," *Phys. Rev. A*, vol. 73, p. 041407, Apr 2006.

[148] J. Eschner, G. Morigi, F. Schmidt-Kaler, and R. Blatt, "Laser cooling of trapped ions," *J. Opt. Soc. Am. B*, vol. 20, pp. 1003–1015, May 2003.

[149] C. Ballance, T. Harty, N. Linke, M. Sepiol, and D. Lucas, "High-fidelity quantum logic gates using trapped-ion hyperfine qubits," *Phys. Rev. Lett.*, vol. 117, no. 6, p. 060504, 2016.

[150] J. P. Gaebler, T. R. Tan, Y. Lin, Y. Wan, R. Bowler, A. C. Keith, S. Glancy, K. Coakley, E. Knill, D. Leibfried, *et al.*, "High-fidelity universal gate set for be 9+ ion qubits," *Phys. Rev. Lett.*, vol. 117, no. 6, p. 060505, 2016.

[151] NIST, "Basic atomic and spectroscopic data." `http://physics.nist.gov/PhysRefData/ASD/index.html`.

[152] L. Ricci, M. Weidemüller, T. Esslinger, A. Hemmerich, C. Zimmermann, V. Vuletic, W. König, and T. Hänsch, "A compact grating-stabilized diode laser system for atomic physics," *Optics Communications*, vol. 117, no. 5, pp. 541 – 549, 1995.

[153] M. Gharavipour, C. Affolderbach, S. Kang, T. Bandi, F. Gruet, M. Pellaton, and G. Mileti, "High performance vapour-cell frequency standards," *Journal of Physics: Conference Series*, vol. 723, no. 1, p. 012006, 2016.

[154] S. A. Schulz, *Scalable Microchip Ion Traps for Quantum Computation.* PhD thesis, University of Mainz, 2009.

[155] M. Kumph, *2D arrays of ion traps for large scale integration of quantum information processors.* PhD thesis, University of Innsbruck, 2016.

[156] "Corning code 7972 ultra low expansion glass datasheet." `https://www.corning.com/media/worldwide/csm/documents/D20FD2EA-7264-43DD-B544-E1CA042B486A.pdf`.

[157] J. Alnis, A. Matveev, N. Kolachevsky, T. Udem, and T. W. Hänsch, "Subhertz linewidth diode lasers by stabilization to vibrationally and thermally compensated ultralow-expansion glass fabry-pérot cavities," *Phys. Rev. A*, vol. 77, p. 053809, May 2008.

[158] S. Hirata, T. Akatsuka, Y. Ohtake, and A. Morinaga, "Sub-hertz-linewidth diode laser stabilized to an ultralow-drift high-finesse optical cavity," *Applied Physics Express*, vol. 7, no. 2, p. 022705, 2014.

[159] J. Fortágh and C. Zimmermann, "Magnetic microtraps for ultracold atoms," *Rev. Mod. Phys.*, vol. 79, pp. 235–289, Feb 2007.

[160] P. Kunert, D. Georgen, L. Bogunia, M. Baig, M. Baggash, M. Johanning, and C. Wunderlich, "A planar ion trap chip with integrated structures for an adjustable magnetic field gradient," *Applied Physics B*, vol. 114, no. 1-2, pp. 27–36, 2014.

[161] R. C. Sterling, H. Rattanasonti, S. Weidt, K. Lake, P. Srinivasan, S. C. Webster, M. Kraft, and W. K. Hensinger, "Fabrication and operation of a two-dimensional ion-trap lattice on a high-voltage microchip," *Nature Communications*, vol. 5, no. 3637, 2014.

[162] "Hardbake of photoresist structures." `http://www.microchemicals.com/technical_information/hardbake_photoresist.pdf`.

[163] C. R. Paul, *Inductance Loop and Partial.* John Wiley and Sons, Inc., 2009.

[164] E. D. Standing, *Design and fabrication of high magnetic field gradients towards fault tolerant two-qubit gates with trapped ions using long-wavelength radiation.* PhD thesis, University of Sussex, 2016.

[165] "Printed circuit boards for ultra high vacuum." `http://ific.uv.es/elec/files/PCB-UHV.pdf`.

[166] K. Singer, U. Poschinger, M. Murphy, P. Ivanov, F. Ziesel, T. Calarco, and F. Schmidt-Kaler, "Colloquium," *Rev. Mod. Phys.*, vol. 82, pp. 2609–2632, Sep 2010.

[167] G. Wilpers, P. See, P. Gill, and A. G. Sinclair, "A compact uhv package for microfabricated ion-trap arrays with direct electronic air-side access," *Applied Physics B*, vol. 111, no. 1, pp. 21–28, 2013.

[168] K. G. Johnson, J. D. Wong-Campos, A. Restelli, K. A. Landsman, B. Neyenhuis, J. Mizrahi, and C. Monroe, "Active stabilization of ion trap radiofrequency potentials," *Review of Scientific Instruments*, vol. 87, no. 5, p. 053110, 2016.

[169] J. M. Sage, A. J. Kerman, and J. Chiaverini, "Loading of a surface-electrode ion trap from a remote, precooled source," *Phys. Rev. A*, vol. 86, p. 013417, Jul 2012.

[170] D. R. Leibrandt, R. J. Clark, J. Labaziewicz, P. Antohi, W. Bakr, K. R. Brown, and I. L. Chuang, "Laser ablation loading of a surface-electrode ion trap," *Phys. Rev. A*, vol. 76, p. 055403, Nov 2007.

[171] A. Safavi-Naini, P. Rabl, P. F. Weck, and H. R. Sadeghpour, "Microscopic model of electric-field-noise heating in ion traps," *Phys. Rev. A*, vol. 84, p. 023412, Aug 2011.

[172] R. Dubessy, T. Coudreau, and L. Guidoni, "Electric field noise above surfaces: A model for heating-rate scaling law in ion traps," *Phys. Rev. A*, vol. 80, p. 031402, Sep 2009.

[173] D. A. Hite, Y. Colombe, A. C. Wilson, K. R. Brown, U. Warring, R. Jördens, J. D. Jost, K. S. McKay, D. P. Pappas, D. Leibfried, and D. J. Wineland, "100-fold reduction of electric-field noise in an ion trap cleaned with in situ argon-ion-beam bombardment," *Phys. Rev. Lett.*, vol. 109, p. 103001, Sep 2012.

[174] K. S. McKay, D. A. Hite, Y. Colombe, R. Jordens, A. C. Wilson, D. Slichter, D. T. C. Allcock, D. Leibfried, D. J. Wineland, and D. P. Pappas, "Ion-trap electrode preparation with ne+ bombardment," *arXiv:1406.1778 [physics.atom-ph]*.

[175] C. D. Bruzewicz, J. M. Sage, and J. Chiaverini, "Measurement of ion motional heating rates over a range of trap frequencies and temperatures," *Phys. Rev. A*, vol. 91, p. 041402, Apr 2015.

[176] Y. J. Lee, P. S. Lee, and S. K. Chou, "Hotspot mitigating with obliquely finned microchannel heat sink - an experimental study," *IEEE Transactions on components, packaging and manufacturing technology*, vol. 3, no. 8, pp. 1332–1341, 2013.

[177] A. H. Nizamani, J. J. McLoughlin, and W. K. Hensinger, "Doppler-free yb spectroscopy with the fluorescence spot technique," *Phys. Rev. A*, vol. 82, p. 043408, Oct 2010.

[178] J. Labaziewicz, *High Fidelity Quantum Gates with Ions in Cryogenic Microfabricated Ion Traps*. PhD thesis, Massachusetts Institute of Technology, 2003.

[179] J. Chiaverini, R. Blakestad, J. Britton, J. Jost, C. Langer, D. Leibfried, R. Eri, and D. Wineland, "Surface-electrode architecture for ion-trap quantum information processing," *Quantum Information and Computation*, vol. 5, no. 6, pp. 419–439, 2005.

[180] S. R. Trout and C. D. G. Jr., "High field magnetic measurements on sintered SmCo5 permanent magnets," *AIP Conference Proceedings*, vol. 29, no. 1, pp. 608–609, 1976.

[181] G. White and J. Collins, "Thermal expansion of copper, silver, and gold at low temperatures," *Journal of Low Temperature Physics*, vol. 7, no. 1, pp. 43–75, 1972.

[182] "Typical properties of sapphire wafers and substrates." `http://www.valleydesign.com/sappprop.htm`.

[183] "Metal - thermal properties." `http://www.goodfellow.com/catalogue/GFCat2C.php?ewd_token=tCrDMe3gOM5hw0e11Mt2uaGDLfza95&n=uXUlP89wh02MdaBEljRSi3s3y1vbkG&ewd_urlNo=GFCat24&type=00&prop=6`.

[184] T. Konaka, M. Sato, H. Asano, and S. Kubo, "Relative permittivity and dielectric loss tangent of substrate materials for high-tc superconducting film," *Journal of Superconductivity*, vol. 4, pp. 283–288, Aug 1991.

[185] J. Sambles and K. Elsom, "The temperature dependence of the electrical resistivity of gold films," *Solid state communications*, vol. 52, no. 4, pp. 367–370, 1984.

[186] F. R. Lebrun-Ricalens, "Scalable closed cycle helium cryostat and in-vacuum electronics for fast ion transport," Master's thesis, University of Sussex, 2016.

[187] W. Gifford and H. McMahon, "A low temperature heat pump," in *Proceedings. 10th International Congress of Refrigeration*, vol. 1, 1959.

[188] C. F. Bohren and D. R. Huffman, *Absorption and scattering of light by small particles*. John Wiley & Sons, 2008.

[189] "Table of emissivity of various surfaces." `http://www-eng.lbl.gov/~dw/projects/DW4229_LHC_detector_analysis/calculations/emissivity2.pdf`.

[190] R. Bird, W. Stewart, and E. Lightfoot, *Transport Phenomena*. A Wiley International edition, Wiley, 2007.

[191] S.-Y. Fu, "Cryogenic properties of polymer materials," in *Polymers at Cryogenic Temperatures*, pp. 9–39, Springer, 2013.

[192] A. Khromova, *Quantum Gates with Trapped Ions using Magnetic Gradient Induced Coupling*. PhD thesis, University of Siegen, 2012.

[193] S. J. Orfanidis, "Electromagnetic waves and antennas." `http://www.ece.rutgers.edu/~orfanidi/ewa/`.

[194] W. Cheung and F. Levien, *Microwaves Made Simple: Principles and Applications*. Artech House microwave library, Artech House, 1985.

[195] P. Colantonio, F. Giannini, and E. Limiti, *High efficiency RF and microwave solid state power amplifiers*. Wiley Online Library, 2009.